Direct evidence for fluid mixing processes during formation of post-Variscan, unconformity-related hydrothermal vein deposits

Dissertation

der Mathematisch-Naturwissenschaftlichen Fakultät

der Eberhard Karls Universität Tübingen

zur Erlangung des Grades eines

Doktors der Naturwissenschaften

(Dr. rer. nat.)

vorgelegt von

Dipl. Geol. Tobias Fußwinkel

aus Leverkusen

Tübingen

2013

Tag der mündlichen Qualifikation:	29.11.2013
Dekan:	Prof. Dr. Wolfgang Rosenstiel
1. Berichterstatter:	PD Dr. Thomas Wenzel
2. Berichterstatter:	Prof. Dr. Thomas Wagner
3. Berichterstatter:	Prof. Dr. Gregor Markl
4. Berichterstatter:	Prof. Dr. Philippe Muchez

Danksagung

Mein besonderer Dank gilt Prof. Dr. Thomas Wagner und PD Dr. Thomas Wenzel für die Vergabe des Dissertationsthemas und vor allem für die stets hervorragende Betreuung während der letzten Jahre sowie die immer zeitnahe Durchsicht meiner Manuskripte. Als weiterem Berichterstatter gebührt mein Dank ebenso Prof. Dr. Gregor Markl, besonders auch für die Unterstützung während des letzten Abschnitts der Doktorandenzeit. Prof. Dr. Christoph A. Heinrich danke ich für die überaus freundliche Aufnahme in seine Arbeitsgruppe an der ETH Zürich und die Unterstützung während meines Aufenthaltes dort. Ebenfalls ganz besonderer Dank gilt Joachim Lorenz für die Bereitstellung großer Mengen Probenmaterials aus Sailauf, seine Hilfsbereitschaft und Unterstützung während der Geländearbeit und die stets fachkundigen Auskünfte zu meinen Fragen.

Bei PD Dr. Thomas Wenzel möchte ich mich besonders für die Unterstützung während vieler Messtermine an der Elektronenstrahlmikrosonde bedanken. Dr. Markus Wälle danke ich für die immer kompetente Unterstützung bei den LA-ICPMS Messungen. Mein Dank gilt ebenso Indra Gill-Kopp für die Herstellung vieler hervorragender Dünn- und Dickschliffe aus oftmals sehr schwierig zu präparierendem Material, Udo Neumann für die Einführung in die Erzmikroskopie der Mn-Oxide, Bernd Steinhilber, Dr. Heinrich Taubald und Benjamin Walter für die Isotopenmessungen sowie Dr. Christoph Berthold und Melanie Keuper für die Unterstützung bei der Röntgendiffraktion und Ramanspektroskopie.

Weiterhin gilt mein Dank für viele Diskussionen, eine immer gute Arbeitsatmosphäre und viel Spaß während und nach der Arbeit meinen Kollegen in Tübingen und Zürich, Michael Marks, Linda Marks, Christopher Giehl, Sara Ladenburger, Yannick Hemberger, Nadja Huber, Sebastian Staude, Katharina Pfaff, Simon Kocher, Anselm Loges, Susanne Göb, Kai Hettmann, Julian Schilling, Benjamin Walter, Olga Apukhtina, Mathias Burisch, Marguerita Duchoslav, Jan-Erik Gühring, Gabriel Berni, Sam Scott, Maike Schubert, Achille Marsala, Niko Westphal, Daniela Gallhofer, Ferdinand Hingerl und vielen anderen.

Ganz besonderer Dank gilt darüber hinaus meinen Eltern Werner und Marianne Fußwinkel, die mir das Studium ermöglichten, und natürlich meiner Freundin Melanie Keuper!

Kurzzusammenfassung

Postvariszische, hydrothermale Gangmineralisationen sind in Zentraleuropa weitverbreitet und mit Elementanreicherungen wie Pb-Zn-Cu-(Ag), Mn-Fe und Co-Ni-Bi assoziiert. Ihre Bildung wird in der Regel durch Fluidmischungsprozesse erklärt, für deren Stattfinden auf der Skala einzelner Erzgänge aber meist nur indirekte Nachweise vorliegen bzw. deren Effizienz auf diesem Maßstab generell umstritten ist. Mit Hilfe von Laserablations-Massenspektrometrie (LA-ICPMS) wurden Multielementanalysen an einzelnen Fluideinschlüssen einer Quarz-Baryt-Pb-Zn Gangmineralisation im kristallinen Grundgebirge des Schwarzwalds durchgeführt. Die Fluide zeigen klare negative Korrelationen der Cl/Br Massenverhältnisse mit Konzentrationen von Pb und Zn, sowohl zwischen Gruppen kogenetischer Einschlüsse auf verschiedenen Wachstumszonen desselben Quarzkristalls, als auch innerhalb der Gruppen selbst. Dies belegt sehr kurzlebige und variable Mischungsvorgänge zwischen einem metallarmen Muschelkalk-Formationswasser, das seine hohe Salinität und hohes Cl/Br Verhältnis durch Halitlösung erhielt, mit einem metallreichen, hochsalinaren Grundgebirgsfluid während der Bildung der Mineralisation in Folge seismischer Aktivität. Diese Ergebnisse stellen den ersten direkten Nachweis für das Ablaufen von Fluidmischungsprozessen zwischen zwei hochsalinaren Fluiden auf dem Maßstab einzelner Gangartkristalle dar.

Die hydrothermale Mn-Fe-As Gangmineralisation in Sailauf (Spessart) durchschlägt einen unterpermischen Rhyolithkörper und umfasst eine komplexe Abfolge von Mn- und Fe-Oxiden, die mit Karbonaten unterschiedlicher Zusammensetzung assoziiert sind. Die Mineralisationsfolge belegt klare Fraktionierungen von Fe und Mn während zeitlich voneinander abgrenzbarer Vererzungsphasen. Die Mn-Oxid-Vererzungsphase umfasst Mn-Oxide und Calcit, während die Hämatit-Vererzungsphase durch Hämatit und Mn-Calcit gekennzeichnet ist. Thermodynamische Modellierungen zeigen, dass die Paragenesen deutliche Fluktuationen physikochemischer Parameter wie pH, f_{O2}, f_{CO2} und a_{SiO2} belegen. Mischungen von oxidierenden, neutralen Fluiden aus dem kristallinen Grundgebirge mit reduzierenden und alkalischen Fluiden aus den oberhalb der Gänge liegenden Zechsteindolomiten können diese Variationen erklären und werden auch durch Seltenerdelement-Verteilungsmustern der Karbonate angezeigt. Mit Hilfe von LA-ICPMS Analysen an Fluideinschlüssen mit petrographisch eindeutigen Altersbeziehungen können den paragenetisch klar abgrenzbaren Vererzungsphasen kompositionell unterschiedliche Fluide zugeordnet werden. Diese unterscheiden sich durch systematische Variationen ihrer Spurenelementgehalte von Li, B, K, Pb und Zn, während in Bezug auf Hauptelementchemie und Salinität praktisch keine Unterschiede bestehen. Die Fluide der Hämatit-Vererzungsphase zeigen Ähnlichkeiten zu Fluiden, die mit kristallinen Grundgebirgsgesteinen interagiert haben, während die hoch oxidierenden Fluide der Mn-Oxid Vererzungsphase Ähnlichkeiten zu Fluiden aus klastischen Sedimenten des Rotliegenden aufweisen. Diese Fluide mischten sich als Folge veränderter hydrologischer Rahmenbedingungen in zeitlich getrennten Phasen hydrothermaler Aktivität mit Formationswässern des Zechstein.

Abstract

Post-Variscan hydrothermal vein deposits are widespread in central Europe and are associated with enrichments in Pb-Zn-Cu-(Ag), Mn-Fe or Co-Ni-Bi. Their formation is commonly explained by fluid mixing processes. However, direct evidence for the occurrence of such processes on the scale of individual ore veins is rare, and as a result their efficiency on these scales is still disputed. Using laser ablation-inductively coupled plasma-mass spectrometry (LA-ICPMS), multi-element analyses of individual fluid inclusions hosted in quartz crystals from a basement-hosted quartz-baryte-Pb-Zn vein mineralization in the Schwarzwald district, SW Germany, were performed. Negative correlations between fluid Cl/Br mass ratios and base metal (Pb and Zn) concentrations were identified in fluid inclusion assemblages (FIA) on subsequent growth zones of the same quartz crystal and even within the same FIA. This indicates transient and variable fluid mixing processes between a metal-depleted halite dissolution brine with high Cl/Br ratio derived from evaporite-bearing Triassic limestones (Muschelkalk) and a metal-rich basement-interacted brine with low Cl/Br ratio. The dataset provides the first direct evidence for fluid mixing processes between similarly saline fluids on the scale of individual gangue minerals.

The hydrothermal Mn-Fe-As mineralization at Sailauf in the Spessart district, central Germany, is hosted by a Lower Permian rhyolite body and comprises a complex succession of Mn- and Fe-oxide minerals associated with several generations of carbonates of distinct major and trace element compositions. The paragenetic succession evidences a clear fractionation of Fe and Mn during discrete mineralization stages. The Mn-oxide mineralization stage comprises Mn-oxides and calcite, whereas the hematite stage is characterized by hematite and Mn-calcite. Thermodynamic modeling shows that these mineral associations evidence significant changes in the prevailing physicochemical conditions in terms of pH, f_{O2}, f_{CO2} and a_{SiO2}. Mixing processes between oxidizing and neutral to slightly acidic basement-interacted fluids with reducing and alkaline formation waters derived from Upper Permian (Zechstein) dolomites overlying the rhyolite body may explain these variations and are further evidenced by systematic changes in rare earth element distribution patterns of the different carbonate generations. LA-ICPMS microanalysis of petrographically well-constrained fluid inclusion assemblages within the carbonates reveals that chemically distinct fluid types can be related to the different mineralization stages. The fluids show systematic variation in their trace element compositions in terms of Li, B, K, Pb and Zn, whereas no differences exist in terms of their major element compositions or salinities. The fluids associated with the hematite stage are compositionally similar to fluids interacted with crystalline basement rocks, whereas the highly oxidizing Mn-oxide stage fluids show similarities to fluids derived from Lower Permian (Rotliegend) red bed sediments. These fluids were tapped during separate stages of hydrothermal activity under changed hydrological flow conditions and were mixed with Zechstein formation waters.

Table of Contents

Introduction

Hydrothermal fluid flow represents the principal mechanism facilitating metal enrichment and accumulation in the upper crust to concentration levels several orders of magnitude above crustal averages (BARNES and ROSE, 1998) in a large variety of geological settings. These include sedimentary basins (SANGSTER, 1990; HITZMAN et al., 2005; LEACH et al., 2005), crystallizing magmatic bodies (HEDENQUIST and LOWENSTERN, 1994) and collisional orogens (GROVES et al., 1998). Hot hydrothermal solutions can transport high amounts of metals in solution, depending on the prevailing physicochemical conditions like f_{O2} and pH and the availability of complexing ligands such as chlorine, sulfur and carbonate species (SEWARD and BARNES, 1997). Precipitation mechanisms may involve changes in fluid compositions induced by fluid mixing processes, phase separation or wall rock interaction (SEWARD and BARNES, 1997; WILKINSON, 2001). Therefore, knowledge about fluid compositions and the transient compositional changes associated with mineral precipitation mechanisms are essential in understanding ore forming processes. However, our knowledge on the variability of natural hydrothermal solutions and the processes governing their major and trace element inventory is still fragmentary. This is exemplified by an ongoing controversy whether any crustal fluid could potentially form economically viable ore deposits, given sufficiently efficient precipitation mechanisms (YARDLEY, 2005), or if formation of economic hydrothermal ore deposits requires anomalously metal-rich fluids (WILKINSON et al., 2009).

With the exception of surficial geothermal systems, hydrothermal processes at greater depths cannot be directly observed and studied. Instead, research is restricted to mineralization formed from fossil hydrothermal activity. Fluid inclusions in gangue minerals of ore deposits may contain samples of primary ore fluids preserved over geological timescales, long after the hydrothermal activity has ceased (ROEDDER, 1979). Recent analytical advances enable sampling of individual fluid inclusions by laser ablation drilling and subsequent chemical analysis of the liberated fluid by mass spectrometry (AUDÉTAT et al., 1998; GÜNTHER et al., 1998; HEINRICH et al., 2003). Application of this technique on the scale of petrographically well-constrained groups of cogenetic fluid inclusions, termed fluid inclusion assemblages (GOLDSTEIN and REYNOLDS, 1994), allows for reconstruction of small scale variations in fluid compositions and for their correlation with mineral precipitation processes (AUDÉTAT et al., 1998; WILKINSON et al., 2009).

In the course of this work, hydrothermal ore veins structurally related to unconformities between basement rocks and overlying sedimentary strata were studied. Unconformities represent interfaces between chemically contrasting fluid reservoirs and thus compositionally different fluid systems (e.g. DILL and NIELSEN, 1987; WAGNER et al., 2010). Seismic activity may trigger focused and episodic fluid flow in fault systems (COX et al., 1995) and facilitate mixing between ascending basement fluids and formation waters within the sedimentary sequence, causing mineral precipitation (SIBSON, 2001). Formation waters may possess very variable and high salinities, for example resulting from passive

evaporative enrichment of Cl, dissolution of halite in evaporitic strata by meteoric waters or diagenetic processes (CARPENTER, 1978; LAND, 1995). The ascending basement-interacted fluids often are Na-Ca dominated, highly saline brines of > 20 wt.% $NaCl_{eq}$, which are common in the upper continental crust and were found to depths of several km (FRAPE and FRITZ, 1987; PAUWELS et al., 1993; MÖLLER et al., 1997). Their mode of formation is, however, still controversial. A common model assumes density driven ingression of residual evaporitic brines from sedimentary sequences into the underlying basement rocks prior to seismically induced fault reactivation and fluid ascent (BANKS et al., 2000; GLEESON and YARDLEY, 2003). Other models assume magmatic sources of chlorinity (BANKS et al., 2000) or passive enrichment of chlorine via water consuming hydration reactions during fluid-rock interaction and alteration of basement rocks (STOBER and BUCHER, 1999).

Metals such as Pb, Zn, Cu, Co, Ni and Ag are strongly complexed by chloride complexes and thus highly mobile in saline hydrothermal fluids at moderate temperatures (SEWARD and BARNES, 1997; SHOCK et al., 1997; SVERJENSKY et al., 1997; WOOD and SAMSON, 1998). Accessory base metal sulfides in the crystalline basement rocks are thought to control high aqueous metal concentrations through solubility equilibria (YARDLEY, 2005). Basement-interacted fluids are therefore commonly invoked as the principal metal supplier for many different deposit types, for example for sediment- and basement-hosted Pb-Zn ore deposits (RUSSELL et al., 1981; KINNAIRD et al., 2002; MUCHEZ et al., 2005; LEACH et al., 2010; WILKINSON, 2010) and structurally controlled, unconformity-type U-deposits in Canada and Australia (DEROME et al., 2007; BOIRON et al., 2010). Conversely, metal sources for shale-hosted, stratabound Cu deposits like the Kupferschiefer in Germany and Poland or the deposits of the Zambian copper belt are disputed, with some authors favoring metal input through ascending basement-interacted fluids (BLUNDELL et al., 2003; MUCHEZ et al., 2005; KOZIY et al., 2009), while others advocate metal uptake via leaching of red bed clastic rocks by late diagenetic formation waters (JOWETT, 1986; OSZCZEPALSKI, 1999; HITZMAN, 2000; BROWN, 2009).

Many studies on these different deposit types inferred mixing processes between chemically contrasting fluids to have triggered ore formation. However, the hydrological efficiency and plausibility of fluid mixing is still controversial (APPOLD and GARVEN, 2000; BONS et al., 2012). Numerical modeling of Mississippi Valley-type sediment-hosted Pb-Zn deposits of the Southeastern Missouri District, USA, showed that even though ore precipitation in response to fluid mixing processes is highly efficient on thermodynamic grounds, the physical efficiency of such processes might in fact be much lower than expected (APPOLD and GARVEN, 2000). In light of this controversy it is important to note that evidence for fluid mixing processes in the past mostly came from regional scale studies, for example from systematic isotope studies on vein minerals of entire ore districts (DILL and NIELSEN, 1987; DILL, 1988; GOLDHABER et al., 1995; KINNAIRD et al., 2002; BAATARTSOGT et al., 2007; WAGNER et al., 2010; STAUDE et al., 2011; STAUDE et al., 2012a). Conversely, studies on individual ore veins, presumably formed by fluid mixing processes, using LA-ICPMS in-situ analysis of fluid inclusions are rare (RICHARD et al., 2010). Earlier studies often focused on the fluids' major

element chemistry, usually by microthermometry (BEHR et al., 1987; DUBOIS et al., 1996; DEROME et al., 2005; BAATARTSOGT et al., 2007; CATHELINEAU and BOIRON, 2010). Ion chromatography of fluid aliquots, obtained by crushing the host minerals, was used in many studies to determine bulk fluid compositions (BANKS et al., 1991; BANKS and YARDLEY, 1992; MCCAIG et al., 2000; HEIJLEN et al., 2003), but the significance of such bulk methods entirely depends on the homogeneity of fluid compositions in all inclusions contained within the leached sample (BANKS and YARDLEY, 1992). Thus, bulk analytical methods cannot resolve the possible occurrence of systematic variation in fluid chemistry on the scale of individual gangue crystals, which has already been demonstrated in other geological contexts (AUDÉTAT et al., 1998). The purpose of this work therefore was to study unconformity-related hydrothermal ore veins by coupling in-situ analysis of individual fluid inclusions with geochemical, mineralogical and isotopic studies and thermodynamic modeling to gain insight into the compositional evolution of ore fluids on the vein scale during the lifetime of hydrothermal systems, to study feedback mechanisms between ore fluid composition and precipitating mineral associations and to potentially provide new insight into the scale and efficiency of fluid mixing processes that could contribute to the ongoing debate on small scale fluid mixing processes.

Chapter 1 presents the major results of a study carried out on a hydrothermal vein mineralization in the Schwarzwald ore district, SW Germany. The district hosts more than 1000 known hydrothermal ore veins, formed by a long-lived, district scale hydrothermal system that has been active episodically since Variscan times. The article *„Fluid mixing forms basement-hosted Pb-Zn deposits: Insight from metal and halogen geochemistry of individual fluid inclusions"* (Appendix 1) published in *GEOLOGY* presents results from a comprehensive fluid inclusion study on zoned quartz crystals from a Pb-Zn quartz-baryte vein mineralization of Mesozoic age. For the first time, systematic changes in fluid Cl/Br ratios could be correlated with aqueous base metal concentrations in fluid inclusion assemblages on subsequent growth zones and even within the same growth zone of a single zoned quartz crystal, providing unambiguous evidence for very rapid and transient mixing processes between a metal-depleted halite dissolution brine and a metal-rich, saline basement fluid on this very small scale.

Chapter 2 summarizes results of a study carried out on a hydrothermal Mn-Fe-As vein mineralization near the village Sailauf in the Spessart district, central Germany. The veins comprise a complex paragenetic succession of Mn-oxides, hematite and compositionally different carbonates in several distinct mineralization phases. Details are given in the paper *"Evolution of unconformity-related Mn-Fe-As vein mineralization, Sailauf (Germany): Insight from major and trace elements in oxide and carbonate minerals"* (Appendix 2) which was published in *Ore Geology Reviews*. On the basis of major and trace element studies of several generations of vein carbonates and oxide ore minerals, thermodynamic modeling was carried out. The results indicate that the distinct mineral associations record drastic and episodic changes in prevailing physicochemical parameters (pH, f_{O2}, f_{CO2}, a_{SiO2}), most likely in response to transient mixing processes between formation waters derived from overlying Zechstein sedimentary strata and basement-interacted fluids.

In Chapter 3, results from fluid inclusion and stable isotope studies on the Sailauf Mn-Fe mineralization are summarized. The results are detailed in the manuscript *"Red bed and basement sourced fluids recorded in hydrothermal Mn–Fe–As veins, Sailauf (Germany): A LA-ICPMS fluid inclusion study"* (Appendix 3) which was published in *Chemical Geology*. Building on the paragenetic framework established in the preceding mineralogical and geochemical studies (Chapter 2) it was possible to allocate compositionally distinct fluids to the principal mineralization phases present at Sailauf. The fluids differ both in concentration levels of fluid-mobile trace elements (Li, B and K) and base metals (Pb, Zn) as well as in their stable isotopic composition (hydrogen and oxygen). The dataset provides clear evidence for episodic mixing processes between three end-member fluids during formation of the Sailauf mineralization, recorded on the scale of complexly intergrown carbonate generations. One of the end-member fluids possesses anomalous Li/B and Pb/Zn ratios, resembling fluids found in fracture fillings in Permian Rotliegend red bed sediments. By contrast, another fluid end-member has Li/B and Pb/Zn ratios typical of crustal fluids that interacted with crystalline basement rocks. Both fluids were modified by mixing processes with a common metal-depleted fluid, most likely a formation water derived from Zechstein sedimentary rocks overlying the Sailauf mineralization.

1. Fluid mixing processes relevant to formation of basement-hosted hydrothermal Pb-Zn ore veins, Schwarzwald district, Germany

1.1. Geological context

The Schwarzwald district in SW Germany is part of the internal zone of the Variscan orogenic belt (KRONER et al., 2008) and according to the classical subdivision of the European Variscides it belongs almost entirely to the Moldanubian zone (KOSSMAT, 1927). Minor occurrences of Saxothuringian units in the northernmost part of the Schwarzwald are separated from the Moldanubian rocks by the Baden-Baden zone, a former oceanic suture zone (KROHE and EISBACHER, 1988). Most of the Moldanubian units comprise partly migmatized para- and orthogneisses (KALT et al., 2000), whereas the Saxothuringian consists of orthogneisses, low grade metasediments and amphibolites that were intruded by gabbroic melts (ALTHERR et al., 1999). The Moldanubian part of the Schwarzwald is further subdivided into the Central Schwarzwald Gneiss Complex (CSGC) and Southern Schwarzwald Gneiss Complex (SSGC), which are separated by the Badenweiler-Lenzkirch suture zone (HANN et al., 2003; KRONER et al., 2008; Appendix 1, Fig. 1). Post-collisional extension resulted in decompressional melting of lower crustal metasedimentary rocks and led to the intrusion of large granitic bodies throughout the district (SCHLEICHER, 1994). During the waning stages of the Variscan orogen (Uppermost Carboniferous to Lowermost Permian), rhyolitic tuffs and ignimbrites were deposited locally (LIPPOLT et al., 1983; SCHLEICHER et al., 1983). Extensional tectonics during the Lower Permian (Rotliegend) led to formation of local pull-apart molasse basins and deposition of an up to 800 m thick series of clastic sediments under arid conditions, while other areas of the Schwarzwald district remained upland regions and subject to erosion (ZIEGLER, 1990). Between the Upper Permian (Zechstein) and Lower Triassic (Buntsandstein), clastic sediments were deposited throughout the entire district in arid climates (GEYER and GWINNER, 2011). Middle Triassic (Muschelkalk) subsidence led to formation of epicontinental shallow shelf sediments (limestones, clays and halite bearing evaporites) that are overlain by Upper Triassic (Keuper) terrestrial sandstones, marine clays and evaporite sequences (GEYER and GWINNER, 2011). Increasing rates of subsidence in Jurassic times resulted in deposition of shallow marine limestones and clays (GEYER and GWINNER, 2011). During the Cretaceous the region was subject to erosion, as is evidenced by local karstification of Jurassic limestones (GEYER and GWINNER, 2011). The onset of the Alpine orogeny is marked by the formation of the Upper Rhine Graben rift valley west of the Schwarzwald district during the Upper Cretaceous. Significant uplift along the rift shoulders led to W-E trending erosion of the sedimentary cover rock sequence and exhumation of basement rocks during the Paleogene (GEYER and GWINNER, 2011). Exhumation rates were highest in the Southern Schwarzwald, resulting in the exposure of formerly deeper seated basement rocks, while the Northern Schwarzwald is still covered by Mesozoic sediments (GEYER and GWINNER, 2011).

1.2. Hydrothermal vein mineralization in the Schwarzwald district

The Schwarzwald district hosts more than 1000 known hydrothermal vein deposits (METZ et al., 1957; BLIEDTNER and MARTIN, 1986). Mining activity began during the Neolithic, peaked in the Middle Ages and declined in modern times (GOLDENBERG et al., 2003; WERNER and DENNERT, 2004; MARKL, 2005). While most ore veins occur in basement rocks, some also extend into the cover rock sequence (BLIEDTNER and MARTIN, 1986). Different types of vein mineralization were classified into groups based on age data, paragenetic, geochemical and structural criteria (METZ et al., 1957; BLIEDTNER and MARTIN, 1986; BEHR and GERLER, 1987; SCHWINN et al., 2006; BAATARTSOGT et al., 2007; PFAFF et al., 2009; STAUDE et al., 2009). Locally, Sb-Ag-(Au)-quartz veins formed from cooling metamorphic fluids during the Permian (STAUDE et al., 2009). Most hydrothermal veins in the district were formed during a peak in hydrothermal activity during the Jurassic, which was caused by high subsidence rates resulting from changing stress patterns of the Tethyian and North Atlantic rift systems (ZIEGLER, 1987; WETZEL et al., 2003; PFAFF et al., 2009). The most common Jurassic mineralization style is Pb-Zn-(Ag) quartz-fluorite-baryte veins, while Co-Ni-Bi-Ag-U baryte-fluorite and Mn-Fe enriched quartz-baryte veins only occur locally (METZ et al., 1957; BLIEDTNER and MARTIN, 1986). Fluid inclusion studies on Jurassic veins identified apparently homogeneous Na-Ca dominated fluids with salinities around 25 wt.% $NaCl_{eq}$ throughout the district (BAATARTSOGT et al., 2007; STAUDE et al., 2007), in itself not immediately suggesting that fluid mixing processes played a role during vein formation. However, stable isotope studies (DILL and NIELSEN, 1987; DILL, 1988; SCHWINN et al., 2006; STAUDE et al., 2011; STAUDE et al., 2012a), ore mineralogy and thermodynamic modeling (STAUDE et al., 2007; STAUDE et al., 2010; STAUDE et al., 2012b) indicated that fluid mixing processes between basement brines and formation waters must have occurred. The constant salinities were therefore interpreted to indicate that both fluid end-members possessed comparable salinities prior to mixing (STAUDE et al., 2007).

Another major mineralization event during the Paleogene accompanied the opening of the Upper Rhine Graben rift and resulted in Pb-Zn-quartz-baryte vein formation on rift-parallel fault structures (METZ et al., 1957; STAUDE et al., 2009) and the formation of a minor sediment-hosted Mississippi Valley-type deposit north of the Schwarzwald district (PFAFF et al., 2010). Precipitation and ore formation was proposed to have been caused by fluid mixing processes between basement-interacted fluids and sedimentary formation waters (PFAFF et al., 2010). Other mineralization events are of local significance only and were related to fluid flow processes triggered by Miocene exhumation (STAUDE et al., 2009).

1.3. Direct evidence for fluid mixing processes

Formation of the Jurassic hydrothermal veins in the Schwarzwald is considered to have occurred in response to mixing processes between two highly saline fluids of similar major element chemistry but contrasting trace element inventory (STAUDE et al., 2007). In order to test this hypothesis, zoned quartz crystals were sampled from a Jurassic Pb-Zn quartz-baryte vein mineralization, located near the town of Sulzburg in the Southern Schwarzwald (Appendix 1, Fig. 1). Successive growth zones contain abundant primary fluid inclusions as well as subordinate galena and hematite crystals and thus provide clear age relationships between fluid inclusion assemblages (Appendix 1, Fig. 2). In-situ multi element analysis of individual fluid inclusions therefore provided insight into the chemical evolution of the ore fluids during crystal growth. Regardless of relative age, all fluid inclusions are of the two-phase liquid + vapor type and possess very similar salinities around 23 wt.% $(NaCl+CaCl_2)_{eq}$ and homogenization temperatures of 130 – 160 °C (Appendix 1, Fig. 3). Slight systematic variations in Na/Ca mass ratios of 2 to 6 were identified between FIA located on different growth zones as well as in fluid inclusions belonging to the same FIA, i.e. on the same growth zone. However, LA-ICPMS analysis reveals significant covariations in trace element compositions. Negative correlations were found between fluid Cl/Br ratios and aqueous base metal concentrations. Low Cl/Br mass ratios of ~80 were found in fluids with base metal concentrations (Pb+Zn) of over 1000 µg/g, while high Cl/Br mass ratios of up to 780 occur in fluids with very low base metal concentrations of 10-20 µg/g. A continuum of intermediate fluid compositions between these values was found along the succession of growth zones, but, even more importantly, variation within individual growth zones is significant as well (Appendix 1, Fig. 4b). Likewise, base metal concentrations are negatively correlated with increasing Na/Ca ratios (Appendix 1, Fig. 4a).

Chlorine and bromine are considered to be conservative tracer elements not affected by fluid-rock interaction processes, thus retaining the Cl/Br signature of the fluid source reservoir (RITTENHOUSE, 1967; BÖHLKE and IRWIN, 1992; KESLER et al., 1996; GLEESON et al., 2001; STOFFELL et al., 2008). Low Cl/Br mass ratios below the seawater value (290) are typical for basement-interacted fluids and are often interpreted to reflect an evaporative origin of these fluids (FRAPE and FRITZ, 1987; PAUWELS et al., 1993; GLEESON and YARDLEY, 2003). Halite formed during evaporation contains only trace amounts of Br, resulting in a passive enrichment of Br relative to Cl in the residual fluid (CARPENTER, 1978). Halogen ratios close to the seawater evaporation trajectory (FONTES and MATRAY, 1993) in hydrothermal basement brines are one of the cornerstones of the hypothesis that the high salinities in basement brines result from density-driven ingression of residual evaporitic fluids with low Cl/Br ratios into the basement (GLEESON and YARDLEY, 2003). Conversely, very high Cl/Br ratios in hydrothermal fluids can be attained through dissolution of Br-poor halite in evaporitic strata by meteoric fluids (CARPENTER, 1978). The cover rock sequence of SW Germany includes evaporitic units within the Middle Triassic Muschelkalk limestones (GEYER and GWINNER, 2011) which could

have been the source for formation waters with high Cl/Br ratios. Regional stable isotope studies also indicated that formation waters from Middle Triassic limestones were involved in the formation of the hydrothermal ore veins in the Schwarzwald district (SCHWINN et al., 2006; STAUDE et al., 2012a). The clear correlation of high base metal concentrations with low Cl/Br ratios indicates that the metals were provided by the basement brines. The data prove that systematic changes in fluid composition occurred in response to mixing of two chemically distinct fluids during growth of an individual quartz gangue crystal, providing the first direct evidence for mixing processes on this scale. Furthermore, the significant differences in fluid compositions within FIA hosted by the same growth are evidence for very transient and rapid mixing processes. The individual growth zones of the studied samples are on average 100-200 µm thick and full of 10–50 µm sized fluid inclusions. Therefore, the inclusions on a given growth zone cannot be entirely contemporaneous, which is reflected by the variability of fluid compositions on this scale that record rapid and variable mixing processes between two end-member fluids during an episode of fluid flow. Hydrologically, this rapid mixing model appears plausible if the mechanisms of hydrothermal fluid flow within fault zones are considered. Such flow is triggered by phases of seismic activity in response to variations in shear stress, local stress fields and fluid pressure at depth, resulting in episodic, short lived and focused fluid flow along preexisting fault structures (MUIR-WOOD and KING, 1993; COX, 1995; SIBSON, 2001). Dilatational jogs in such fault-valve systems provide a mechanism for efficient fluid mixing by causing fluids to flow into the fault from the surrounding fractured rock during coseismic slip (COX, 1995; SIBSON, 2001).

The data acquired in this study prove the transient and rapid nature of fluid mixing processes and provide clear constraints with regard to the scale of their occurrence, which will have to be accounted for in future hydrologic fluid flow models in similar structural settings. The results prove mixing processes between halite-dissolution formation brines and metal-rich basement-interacted brines on a scale where the geochemical indicators for the mixing processes would not have been detectable by any conventional bulk fluid analytical technique, such as ion chromatography. The results of this study were published in *GEOLOGY* in a paper titled *„Fluid mixing forms basement-hosted Pb-Zn deposits: Insight from metal and halogen geochemistry of individual fluid inclusions"* (Appendix 1).

2. Geochemistry and mineralogy of a hydrothermal Mn-Fe-As vein mineralization at Sailauf, Spessart district, Germany

2.1. Geological context and hydrothermal mineralization in the Spessart district

The Sailauf hydrothermal vein deposit is located directly beneath an unconformity separating the Spessart Crystalline Complex (SCC) from the Paleozoic and Mesozoic cover rock sequence. The Spessart district is part of the Mid German Crystalline Rise (MGCR), which, like the Schwarzwald, is part of the internal zone of the European Variscides (KRONER et al., 2008). The MGCR represents an active plate margin where SE-directed subduction caused closure of the Rheic ocean and collision of the Saxothuringian and Rhenohercynian terranes between Silurian and Carboniferous times (KRONER et al., 2008). The SCC consists of a series of NE-SW trending lithologic units comprising metasedimentary and metabasic rocks (OKRUSCH and WEBER, 1996). Two orthogneiss complexes are intercalated into the metasedimentary units. Their calc-alkaline, granodioritic to granitic protoliths were emplaced in an active continental margin setting between the Uppermost Silurian to Lowermost Devonian (DOMBROWSKI et al., 1995; OKRUSCH and WEBER, 1996). During the Variscan orogen the entire complex was subjected to medium grade amphibolite facies metamorphic conditions (OKRUSCH and WEBER, 1996) until uplift and cooling occurred between 325 – 315 Ma (DOMBROWSKI et al., 1994). Extension and basin formation during the Lower Permian resulted in widespread volcanic activity throughout the entire Central European Variscides, resulting in deposition of thick volcanoclastic sequences or emplacement of subvolcanic bodies (NEUMANN et al., 2004; MCCANN et al., 2008). In the Spessart district the Sailauf rhyolite body hosting the Mn-Fe-As vein mineralization was formed during this period (OKRUSCH et al., 2011). The crystalline rocks of the Spessart are unconformably overlain by Permian sedimentary rocks. During the Lower Permian parts of the Spessart formed an elongated, narrow NE-SW trending basement high (TRUSHEIM, 1964). NW and SE of this ridge thick red bed sequences (Rotliegend) were deposited in trough structures (TRUSHEIM, 1964; OKRUSCH et al., 2011). During the Upper Permian the Spessart was located on the southernmost extent of the Zechstein sea, resulting in deposition of the marginal Zechstein facies, which comprises basal manganiferous breccias and conglomerates, the Kupferschiefer black shale and bituminous dolomites of the Werra cycle (KÄDING, 2005). Temporary regressions in sea level led to deposition of clay and marls of the Aller and Leine Zechstein cycles, including a well defined claystone marking the Permian-Triassic boundary (KÄDING, 2005). The Permian rocks are conformably overlain by continental sandstones, conglomerates and mudrocks of the Lower Triassic Buntsandstein and Middle Triassic Muschelkalk (OKRUSCH et al., 2011). Middle Triassic to Upper Jurassic sedimentary rocks originally covering these units were eroded during regional uplift (OKRUSCH et al., 2011).

Hydrothermal ore veins are widespread throughout the Spessart district (Appendix 2, Fig. 1). Most are structurally related to a major post-Variscan NW-SE trending fault system that crosscuts both

the basement and the cover rock sequence. Post-Variscan extensional tectonics led to reactivation of the faults, fluid flow, fluid mixing processes and hydrothermal vein formation, comprising abundant barren baryte-quartz veins, base metal-rich veins and the Mn-Fe-As vein mineralization at Sailauf (ZIEGLER, 1987; WAGNER and LORENZ, 2002; OKRUSCH et al., 2007; LORENZ, 2010; WAGNER et al., 2010). Another major fault system striking NE-SW is only weakly mineralized (WAGNER et al., 2010).

2.2. The hydrothermal Mn-Fe-As vein-type mineralization at Sailauf

The hydrothermal vein mineralization at Sailauf, situated around 10 km NE of the city of Aschaffenburg (Appendix 2, Fig. 1), is hosted by a small Lower Permian subvolcanic rhyolite dome of roughly 400 x 200 m in size, which is being mined for gravel. The porphyritic rhyolite is emplaced in a small slab of biotite schist, which in turn is intercalated with orthogneisses (Appendix 2, Fig. 2). The roof of the rhyolite dome was part of the Lower Permian (Rotliegend) erosional land surface and later unconformably overlain by Upper Permian Zechstein dolomites (OKRUSCH et al., 2011). Although the Kupferschiefer is missing directly above the rhyolite dome, it appears beneath the dolomites only several hundred meters to the NE, the direction of the deepening Zechstein basin (LORENZ, 2010).

The hydrothermal vein mineralization comprises a set of five steeply dipping, NW-SE trending, discontinuously mineralized faults crosscutting the host rock. The veins range in thickness from 1 to 25 cm and are mineralized by a complex succession of carbonates, Mn- and Fe-oxides. A detailed account of the mineralization sequence is given in the paper "Evolution *of unconformity-related Mn-Fe-As vein mineralization, Sailauf (Germany): Insight from major and trace elements in oxide and carbonate minerals"* (Appendix 2) which was published in *Ore Geology Reviews*. The mineralization comprises four main stages (Appendix 2, Fig. 4): an early pre-ore stage, two main ore stages and a subsequent alteration stage. The onset of hydrothermal mineralization during the pre-ore stage is marked by widespread brecciation of the rhyolite host rock and cementation of breccia clasts by Ca-bearing rhodochrosite with subordinate fluorite, celadonite, illite and anhydrite. The first main ore stage ('ore stage 1' in Appendix 2) will for consistency with Chapter 3 be termed the 'Mn-oxide stage'. During the Mn-oxide stage different Mn-oxides (braunite, hausmannite, and manganite) were precipitated along with very pure calcite, subordinate fluorite, scheelite and anhydrite. Rhythmic cockade ores evidence sequential vein reactivation and mineral precipitation (Appendix 2, Fig. 6a). During the second major ore stage ('ore stage 2' in Appendix 2), in the following termed 'hematite stage', Mn-bearing calcite (Mn-calcite) along with several generations of hematite and quartz was precipitated. Subordinately, Fe-bearing calcite and celadonite accompany hematite stage mineralization. Commonly, the hematite stage assemblages replace preexisting Mn-oxide stage calcite along cleavage lamellae, fractures or grain boundaries (Appendix 2, Fig. 7a). In the alteration zones, Mn-calcite possessing Mn concentrations of around 10 mol.% (Appendix 2, Fig. 9) is accompanied by cogenetic hematite that is strictly confined to the altered areas (Appendix 2, Fig. 7b) and may be present in fine disseminations or large specularitic aggregates. The paragenetic age relations and

replacement textures between the carbonate generations are often too complex to interpret using transmitted light alone, hence most of the textural characterization was carried out using backscatter electron imaging to visualize the chemical contrasts. Occasionally, hematite stage mineralization also occurs in discrete veins not previously mineralized during the Mn-oxide stage. The later alteration stage affects mineral assemblages from both ore stages. Locally, Mn-oxide stage braunite and manganite are partly altered to Ca-bearing rhodochrosite. Carbonates from both ore stages are also partly altered to Ca-rhodochrosite, sometimes forming fine-grained pseudomorphs of Ca-rhodochrosite after scalenohedral calcite crystals (Appendix 2, Fig. 3e). Vugs are filled with a complex succession of secondary carbonates with compositions ranging from Mn-bearing calcite to Ca-bearing rhodochrosite, often finely intergrown with secondary arsenate phases like tilasite, sailaufite and arseniosiderite or secondary Mn-oxides (Appendix 2, Fig. 7e) (LORENZ, 1995; LORENZ, 2010). In addition, crusts of native arsenic occur on otherwise unmineralized fracture planes of the rhyolite (LORENZ, 1995). However, their genetic relation to the vein-type mineralization is unknown.

HAUTMANN et al. (1999) carried out (U-Th)/He dating on the main oxide ore minerals as well as K/Ar dating on clay minerals. Braunite ages are 156.9 to 158 Ma (±4.8), while hematite gave ages of 136.3 to 147.6 (±5) Ma. One hausmannite was dated at 130 Ma (no analytical error given), while K-Ar dating of illites gave ages of 156.4 to 160.5 (±4) Ma. Several, not clearly specified generations of celadonite yielded an age range of 98.2 to 119.9 Ma.

Accessory minerals and trace element compositions of all major oxide ore minerals and gangue carbonates show that the mineralization at Sailauf is enriched in Pb, Zn, Cu, W, As, Sr, Sb and U. Enrichment in this conspicuous element suite is commonly associated with terrestrial hydrothermal Mn-Fe vein deposits elsewhere (ROY, 1981; NICHOLSON, 1992) and stratabound sedimentary-exhalative Mn-Fe deposits like the Långban-type deposits in Sweden (HOLTSTAM, 2001; HOLTSTAM and MANSFELD, 2001) or the Val-Ferrara in Switzerland (BRUGGER and GIERÈ, 2000). HEIN et al. (2000) proposed that vein-type Mn-Fe deposits in marine sediments may represent feeder systems for stratabound sedimentary-exhalative deposit types. The geochemical similarities and the typical trace element enrichments in these different deposit types, irrespective of the very different geological contexts in which they occur, are thought to be lithologically controlled through fluid-rock interaction with felsic (and often volcanic) rocks (HEWETT, 1964; ROY, 1981; NICHOLSON, 1992; HOLTSTAM and MANSFELD, 2001; GLASBY et al., 2005). The Mn-Fe ore veins at Ilfeld (Harz Mountains, central Germany) and Ilmenau (Thuringia, eastern Germany) also occur in clastic or volcanoclastic red bed sediments of Lower Permian Rotliegend age, while the Sailauf mineralization is hosted by a Lower Permian rhyolite, situated only few km away from Rotliegend red bed successions in molasse basins (TRUSHEIM, 1964).

2.3. Genetic model for the Sailauf hydrothermal vein mineralization

The Sailauf mineralization is characterized by two very different main ore assemblages, one dominated by Mn-oxides and pure calcite, the other by hematite and Mn-bearing calcite. This indicates first order changes in the physicochemical parameters of the hydrothermal fluids. The solubilities of Mn and Fe are controlled by oxidation state, pH, temperature and relative concentrations of complexing ligands like chloride or sulfur, which significantly increase solubilities via formation of stable chloride complexes with Fe and Mn (KRAUSKOPF, 1957; HEM, 1972; CRERAR et al., 1980; BRUNO et al., 1992; WOLFRAM and KRUPP, 1996; WOOD and SAMSON, 1998; SULEIMENOV and SEWARD, 2000; TESTEMALE et al., 2009). Fractionation of Fe from Mn results mainly from the differences in redox potential. The redox transition of Fe^{2+}/Fe^{3+} occurs at much lower redox state than the Mn^{2+}/Mn^{3+} transition (KRAUSKOPF, 1957; CRERAR et al., 1980). Upon crossing of the Fe redox boundary, weakly soluble hematite would precipitate, while more soluble Mn^{2+}-chloro complexes would remain in solution (KRAUSKOPF, 1957; CRERAR et al., 1980). The stability of carbonates over oxide minerals would also be influenced by the CO_2 fugacity (CRERAR et al., 1980). Building on these considerations and the established paragenetic framework of the mineralization, thermodynamic modeling was carried out using the software GeochemistsWorkbench (BETHKE, 2008) to calculate the stability relations for the mineral phases as a function of f_{O2}, pH, f_{CO2} and a_{SiO2}. The stability diagrams were constructed at 150°C and saturated water vapor pressure, a reasonable approximation of the conditions during formation of the mineralization (see Chapter 3). The phases manganosite, hausmannite, braunite, pyrolusite, rhodochrosite, hematite, magnetite and siderite were considered. As no thermodynamic data are available for manganite, bixbyite data were accepted as best approximation of an Mn^{3+}-Mn-oxide. The results reflect the first order control of CO_2 fugacity on the stability of carbonates relative to Mn-oxides (Appendix 2, Fig. 14a). Low silica activities are a prerequisite to enable precipitation of hausmannite and manganite during the Mn-oxide mineralization stage. Hence, the occurrence of hematite and quartz during the hematite stage evidences a significant increase in silica activity, while missing Mn-oxides during this stage could indicate increased CO_2 fugacity. Mixing processes between fluids derived from two chemically contrasting reservoirs during ore formation could explain this major shift in the chemical parameters of the hydrothermal fluid. This is in good agreement with earlier sulfur isotope studies on other hydrothermal vein deposits the Spessart district, which also indicated fluid mixing processes to have facilitated ore formation (WAGNER et al., 2010). The most likely fluid source reservoirs are the basement rocks and the Zechstein sedimentary sequences. Ascending basement-interacted fluids would have been quartz saturated and possess a near neutral pH (YARDLEY, 2005), whereas fluids from bituminous Zechstein dolomite aquifers would most likely have been quartz undersaturated and more alkaline (WAGNER et al., 2010). The Mn-oxide stage was precipitated from a silica-undersaturated fluid, suggesting increased contribution of Zechstein fluids during their formation. Conversely, the hematite stage was precipitated from silica-saturated fluids, indicating increased influence of basement derived, quartz

saturated fluids. However, the mineral stability relations outlined above indicated that this fluid would also have had a higher CO_2 fugacity compared to the dolomite-derived Zechstein fluids to facilitate destabilization of Mn-oxides, which appears unlikely. The apparent contradiction can be resolved if the additional influence of pH variation on the solubilities of Mn-oxides and hematite is taken into account. At the assumed Fe/Mn ratios in the range of those observed in the Schwarzwald (see Chapter 1), Mn-oxides will be much more soluble than hematite at near neutral pH. Increasing the relative contribution of quartz-saturated basement-derived fluid over alkaline Zechstein fluids during precipitation of the hematite stage mineralization would have shifted the pH to lower values and increased Mn-oxide solubility (Appendix 2, Fig. 14c). This explains the lack of Mn-oxides in the hematite stage mineralization and is further corroborated by the increased Mn concentrations in hematite stage Mn-calcite, indicating that Mn was present in the divalent state during calcite and hematite precipitation. Subsequent mixing of this Fe-depleted fluid with higher proportions of Zechstein-derived, alkaline and quartz undersaturated fluids would have led to an increase in pH and a decrease in a_{SiO2}, eventually attaining conditions necessary to cause precipitation of the Mn-oxide stage mineral assemblage.

The stability relations indicate that progressive admixture of Zechstein fluids to a metal-bearing basement brines at near neutral pH and high silica activities would first precipitate the hematite stage mineral association and later the Mn-oxide paragenesis. In the context of a dynamic fault-hosted hydrothermal system, this could reflect a vertical redox zonation with hematite stage mineralization occurring in greater depths than the Mn-oxide assemblages. Such vertical redox gradients were described in other hydrothermal Mn-Fe deposits worldwide and also the vein-type deposits at Ilfeld and Ilmenau in Germany (SALZMANN, 1935; HEWETT, 1964; ROY, 1981; LEAL et al., 2008). Although both mineralization styles occur together at the same depth at Sailauf, the mineralization stages are clearly not contemporaneous. The hematite stage paragenesis crosscuts and replaces earlier formed Mn-oxide mineral assemblages, indicating discontinuous mineralization in episodic fluid flow events, most likely triggered by seismic activity as explained in Chapter 1. Discrete periods of seismic activity with different intensities could have caused fluid ascent of varying flow rates or tapping of different fluid reservoirs at depth with deviating physicochemical parameters. Therefore, the depths of the Fe and Mn redox boundaries relative to the mixing interface represented by the Permian unconformity would have been variable as well during each fluid flow event, which could explain the close spatial association of both major ore stages at Sailauf. Further evidence for redox variations between the major ore stages at Sailauf comes from systematic variations in Ce-anomalies in the rare earth element (REE) distribution patterns of the associated carbonate generations (Appendix 2, Fig. 12). Ce occurs in two oxidation states (+3 and +4) and may be removed from oxidized solutions by adsorptive fixation onto mineral surfaces or reductively mobilized from such surfaces, causing negative or positive Ce-anomalies in the fluids, respectively (WOOD, 1990; MÖLLER and DULSKI, 1999). Zechstein dolomites possess positive Ce-anomalies (FISCHER et al., 2006), as do the calcites from the Mn-oxide

mineralization stage at Sailauf, whereas hematite stage Mn-calcites do not. The positive anomalies in Mn-oxide stage calcites may indicate inheritance from Zechstein carbonates and therefore a stronger influence of Zechstein-derived fluids during this mineralization stage.

The results summarized above were published in the article *"Evolution of unconformity-related Mn-Fe-As vein mineralization, Sailauf (Germany): Insight from major and trace elements in oxide and carbonate minerals"*, published in Ore Geology Reviews. Building on the results and the established paragenetic framework, fluid inclusion and stable isotope studies were carried out on the Zechstein carbonates, in order to link the mineralogical features of the vein mineralization with real fluid compositions and to check whether the fluid chemistry is in support of the mixing model that was derived from the mineralogical and geochemical studies outlined in this Chapter. The results of the fluid and stable isotope study are summarized in the following Chapter.

3. Fluid geochemistry of the hydrothermal Mn-Fe-As mineralization at Sailauf

Fluid inclusion studies were carried out on representative carbonate samples from both major ore stages at Sailauf and fluorite samples of the hematite mineralization stage (see previous Chapter). Isotopic compositions were determined for carbonates (oxygen and carbon) from all mineralization stages, Mn- and Fe-oxides (oxygen) and celadonites (oxygen and hydrogen).

3.1. Stable isotope studies

The Mn-Fe-As mineralization at Sailauf is characterized by several distinct mineralization stages that are associated with very distinct carbonate compositions (Appendix 2, Fig. 9). The carbonates also show significant differences with regard to their oxygen isotopic compositions (Appendix 3, Fig. 8). Pure calcite of the Mn-oxide mineralization stage possesses very heavy isotopic compositions between +23.6 and +27.1 ‰ relative to V-SMOW. The $\delta^{18}O_{V\text{-}SMOW}$ values of hematite stage Mn-calcite and Ca-rhodochrosite from both the pre-ore and the alteration stage, on the other hand, are lower and vary between +14.7 and +17.6 ‰. In terms of carbon isotopic compositions all carbonate generations are relatively similar, with $\delta^{13}C_{V\text{-}PDB}$ values between -5.8 and -3.1 ‰. Hematite oxygen isotopic compositions are between -4.8 to -2.5 ‰ relative to V-SMOW. Pre-ore stage celadonites possess relatively constant $\delta^{18}O_{V\text{-}SMOW}$ values of +13.2 to +15.5 ‰; however, their $\delta D_{V\text{-}SMOW}$ compositions show significant variation and cover a range between -98 to -9 ‰ (Appendix 3, Fig. 12).

High calcite $\delta^{18}O_{V\text{-}SMOW}$ values can be caused by low temperature remobilization processes (ZHENG and HOEFS, 1993). Even though the Mn-oxide stage calcites from Sailauf possess unusually heavy $\delta^{18}O_{V\text{-}SMOW}$ values, their paragenetic association and fluid inclusion homogenization temperatures of around 155 °C rule out low temperature remobilization effects on their isotopic compositions and instead indicate isotopically heavy primary ore fluids. Calculation of fluid $\delta^{18}O_{V\text{-}SMOW}$ values using carbonate isotopic compositions, fluid inclusion homogenization temperatures and suitable calcite-H_2O fractionation factors (FRIEDMAN and O'NEIL, 1977) reveals that the ore fluids precipitating the Mn-oxide stage were indeed very different from those that formed the hematite stage mineral assemblages. Hematite stage fluids had $\delta^{18}O_{H2O}$ values of 2 – 5 ‰, whereas the Mn-oxide stage paragenesis formed from isotopically very heavy fluids with $\delta^{18}O_{H2O}$ of 13 – 17 ‰, relative to V-SMOW. High fluid $\delta^{18}O_{V\text{-}SMOV}$ values can for example be produced through intense evaporation processes or fluid-rock interaction (HOLSER, 1979; SHEPPARD, 1986). The oxygen and hydrogen isotopic composition of pre-ore stage fluids was calculated using celadonite-H_2O fractionation factors (ODIN et al., 1988; CAPUANO, 1992; SHEPPARD and GILG, 1996). Pre-ore stage celadonite $\delta^{18}O_{H2O}$ values are in good agreement with the values obtained for the hematite stage ore fluids. The origin of

very low fluid $\delta D_{V\text{-}SMOW}$ values, which at Sailauf were found to be as low as -80 ‰, is still debated (GLEESON et al., 1999). SHEPPARD (1986) proposed that interaction of fluids with organic rich sediments can result in very low fluid hydrogen isotopic composition, for example during diagenetic dehydration of kerogens. The high variability observed in $\delta D_{V\text{-}SMOW}$ values could then be interpreted as a mixing trend between fluids strongly influenced by such diagenetic processes, like formation waters derived from bituminous Zechstein sediments and another fluid that was not isotopically altered in this way.

3.2. Fluid inclusion petrography and fluid geochemistry

The carbonate gangue minerals at Sailauf possess virtually no growth zonation that could be used to establish unambiguous age relations between fluid inclusion assemblages. However, on the basis of the mineralogical and geochemical studies summarized in Chapter 2 it was possible to allocate FIAs to the two principal major ore stages. As explained in Chapter 2, hematite stage Mn-calcite replaces Mn-oxide stage pure calcite along cleavage lamellae, grain boundaries or cracks. Whereas the pure calcite is very clear, the replacement by Mn-calcite is accompanied by a significant increase in porosity and the occurrence of finely dispersed hematite flakes, providing workable age constraints for FIAs hosted in the different carbonate types (Appendix 3, Fig. 2). In cases where the extent of the alteration zones could not be determined unambiguously in transmitted light, backscatter electron imaging was used to allocate fluid inclusions to the chemically different carbonate compositions (Appendix 3, Fig. 5). All fluid inclusions are of the two-phase liquid + vapor type and contain aqueous, saline, Na-Ca dominated brines. Salinities determined by microthermometry are very constant around 26 wt.% $NaCl+CaCl_{2\ eq}$, while Na/Ca mass ratios vary slightly and rather unsystematically between 1 and 4 (Appendix 3, Fig. 4). No systematic differences in terms of salinity or cation ratios exist between FIAs belonging to the different mineralization stages. However, fluid inclusions occurring in Mn-oxide stage calcite homogenize at 155° ± 10°C into the aqueous phase, whereas inclusions hosted by hematite stage Mn-calcite do so at 135° ± 10°C.

LA-ICPMS analysis of individual fluid inclusions reveals very systematic differences and correlations in fluid trace element compositions, especially in concentrations of fluid mobile elements (K, Li, B, Rb, Cs) and base metals (Pb, Zn) (Appendix 3, Figs. 6, 7). As salinities are rather constant, differences in chlorinity cannot account for the systematic concentration differences in chloro-complexed cations. The fluid compositions form three positively correlating data arrays in K vs. Li space. The most Li-rich fluids are also most strongly enriched in the other fluid mobile elements (Appendix 3, Fig. 7). The host carbonate of the individual FIs controls their association to the different compositional trend lines, showing that the very systematic variations in trace element compositions can be directly related to the different mineralization stages identified at Sailauf (Appendix 3, Fig. 6b). Mn-oxide stage fluids form a distinctly less steep trend in K vs. Li space than hematite stage fluids. The third trend line is formed by fluid compositions obtained in a single sample. All data arrays converge towards a common

origin, indicating that each trend line represents a dilution vector of enriched end-member fluids by a common end-member fluid which were mixed in variable proportions. Despite the high fluid mobility of the elements in question, the rather similar homogenization temperatures between the fluids relevant to the two major ore stages make it appear unlikely that temperature effects caused the systematic differences in fluid composition. Instead, the best explanation for the observed differences would be fluids derived from chemically different source rocks.

This is further corroborated by Li-B systematics. The mobilization of Li and B during fluid-rock interaction is influenced by temperature but also by the source rock lithology. Li/B ratios can therefore serve to differentiate between fluid source reservoirs (SHAW and STURCHIO, 1992; REYES and TROMPETTER, 2012). Li/B ratios of hematite mineralization stage fluids from Sailauf are rather similar to other crustal fluids influenced by crystalline basement rocks in the Upper Rhine Graben (PAUWELS et al., 1993), the Schwarzwald district (own data, Chapter 1 and Appendix 1) or Irish-type Pb-Zn ore deposits in Ireland (WILKINSON et al., 2005). Fluids relevant to the formation of Mn-oxide stage mineralization, however, show similarities to fluid compositions found in hydrothermal calcite veins within Lower Permian (Rotliegend) red bed volcanoclastics of the North German Basin (Appendix 3, Fig. 9; LÜDERS et al., 2005).

Base metal concentrations also vary systematically between the different ore fluids. Pb and Zn concentrations are arranged on linear trend lines, reflecting controls on metal solubility by temperature, salinity and sulfide solubility equilibria at greater depth within the basement (YARDLEY, 2005). Some Mn-oxide stage and all hematite stage fluid Pb/Zn mass ratios (around 0.45) overlap with a trend commonly found in many crustal fluids related to Pb-Zn ore deposits or in basement brines (YARDLEY, 2005; STOFFELL et al., 2008; WILKINSON et al., 2009), including the data for the Pb-Zn mineralization in the Schwarzwald district (Chapter 1, Appendix 1). However, most Mn-oxide stage fluids have anomalously high Pb/Zn ratios, similar to Pb-enriched Rotliegend fluids of the North German Basin (Appendix 3, Fig. 10; LÜDERS et al., 2005). Cl/Br ratios in the different ore fluids are rather constant around mass ratios of 150 and do not show any systematic variation between the fluids relevant to the different ore stages (Appendix 3, Fig. 11).

3.3. Reconstruction of fluid sources

All fluids relevant to the formation of the Sailauf mineralization possess similar salinities and halogen ratios, indicating a common evaporitic origin. However, the ore fluids that precipitated the hematite stage mineral assemblages possess Li/B and Pb/Zn ratios similar to common crystalline basement-interacted fluids, whereas the Mn-oxide stage fluids are anomalous in terms of Li/B, Pb/Zn as well as their isotopic compositions. They are compositionally similar to fluids derived from clastic red bed sediments.

During the Lower Permian (Rotliegend) the Sailauf rhyolite dome was part of an elongated basement high. Rotliegend red bed clastics were deposited in trough structures only few km to the NW and SE of Sailauf (TRUSHEIM, 1964). The rhyolite body is unconformably overlain by Upper Permian (Zechstein) bituminous dolomites. Only a few hundred meters to the NE of the rhyolite (the direction of the deepening Zechstein basin) the Kupferschiefer black shale appears beneath the dolomites (LORENZ, 2010). The Kupferschiefer and the overlying dolomite are commonly mineralized by stratabound Cu-Pb-Zn-(Ag) ores (OKRUSCH et al., 2007; WAGNER et al., 2010). The dominant NW-SE striking, post-Variscan fault system was reactivated in Mesozoic times (ZIEGLER, 1987) and is frequently mineralized by Cu-Co-Ni-As-Fe-Bi ores whose occurrence is restricted to the uppermost parts of the basement or the immediately overlying Kupferschiefer (WAGNER et al., 2010). Similar fault-hosted ore veins also occur in stratabound Cu-Ag ores in the Mansfeld and Sangerhausen Kupferschiefer districts in the Harz Mountains, Central Germany (VAUGHAN et al., 1989). Furthermore, epigenetic veinlets or impregnations of Cu-As-Ag mineralization predating the major hydrothermal vein systems occur in the Spessart (OKRUSCH et al., 2007). Stable isotope data and mineral chemistry suggests that both mineralization styles were related to ascending, metal-bearing, acid and oxidizing brines (VAUGHAN et al., 1989; WAGNER et al., 2010).

The critical importance of post-depositional base metal enrichment in Kupferschiefer-type ore bodies by external metal-rich hydrothermal fluids has long been recognized and was emphasized by many geochemical studies, mass balance considerations and fluid flow models (RENTZSCH, 1974; BECHTEL and PÜTTMANN, 1991; CATHLES et al., 1993; OSZCZEPALSKI, 1999; BECHTEL et al., 2000). Kupferschiefer ore districts in Germany and Poland typically occur on basement highs above highly oxidized Permian Rotliegend red beds and volcanic rocks, the so called 'Rote Fäule' (JOWETT, 1986). A widely accepted genetic model suggests that metal-bearing brines convected through the Rotliegend red beds and were introduced into the reducing Kupferschiefer where Rotliegend rocks pinch out against the flanks of basement highs. The Kupferschiefer then acted as a geochemical trap and facilitated ore formation (JOWETT, 1986; OSZCZEPALSKI, 1999). The timing of the hydrothermal metal input, however, is still a matter of debate (see SYMONS et al., 2011 for an overview). Similarly, the ultimate source of the metals in sediment-hosted Cu deposits remains disputed. On the one hand, it was proposed that late-diagenetic Na-Ca red bed formation waters leached metals from Rotliegend clastics prior to injection into Kupferschiefer rocks and subsequent ore formation (JOWETT, 1986; BECHTEL and PÜTTMANN, 1991; OSZCZEPALSKI, 1999; BECHTEL et al., 2000). Conversely, BLUNDELL et al. (2003) argue that metal-rich basement brines were injected into the Rotliegend red beds prior to lateral updip flow towards the sites of deposition near basement highs. In this model, episodic fluid expulsion from the basement would have been induced normal fault reactivation during earthquake events (MUIR-WOOD and KING, 1993). A very similar dispute regarding metal sources of sediment-hosted Cu deposits in the Zambian Copper Belt also remains unresolved, with controversial

discussion whether metals were derived from red bed sequences (HITZMAN, 2000) or basement sources (KOZIY et al., 2009).

The Kupferschiefer-type Cu deposits of the Spessart district are not underlain by Rotliegend red bed sequences (WAGNER and LORENZ, 2002; OKRUSCH et al., 2007; WAGNER et al., 2010). Therefore, accepting the model of metal-bearing Rotliegend fluids as the principal metal supplier, formation of the Kupferschiefer-type deposits would have required significant lateral fluid flow along the major NW-SE striking fault zones that host the hydrothermal veins to transport fluid from the nearby Rotliegend basins to the sites of deposition on the flanks of the Spessart basement high. Such along-fault fluid flow could be analogous to the 'forced brine convection' model that has been proposed for the formation of the Mt. Isa Cu deposit in Australia (MATTHÄI et al., 2004). At Sailauf, the contrasting fluid compositions found in the two major mineralization stages resemble both red bed-interacted Rotliegend brines (Mn-oxide stage) as well as basement-interacted brines (hematite stage), indicating that along-fault fluid flow of Rotliegend brines did in fact occur during the hydrothermal fluid flow event that formed Mn-oxide stage mineralization. Conversely, the identification of basement-interacted fluids relevant to formation of hematite stage mineralization suggests that another fluid flow event occurred during seismically-induced normal fault reactivation (MUIR-WOOD and KING, 1993), resulting in focussed upward flow of deep-seated fluids within fault zones. The hydrothermal system at Sailauf thus recorded very distinct periods of fluid flow most likely related to changing hydrological regimes, providing insight into a protracted post-Variscan fluid flow system. At the site of deposition, the different fluids were mixed with a fluid possessing a composition defined by the point of convergence of the mixing trends observed in the K vs. Li concentration plots. Assuming this common end-member fluid to represent Zechstein formation waters appears geologically reasonable and is corroborated by the extremely low $\delta D_{V\text{-}SMOW}$ values found in pre-ore stage celadonites, which could indicate interaction with organic carbon within the bituminous Zechstein dolomite overlying the mineralization. The Sailauf Mn-Fe-As mineralization would thus represent a hydrothermal feeder system where both red bed- and basement-interacted fluids were episodically trapped prior to injection into the highly reactive lithologies of the Zechstein.

The identification of red bed-interacted fluids at Sailauf shows that lateral along-fault fluid flow from the nearby Rotliegend basins did occur. If Rotliegend fluids were the principal ore fluid of Kupferschiefer type Cu-deposits, the Mn-oxide stage fluids could then represent an analogue to these ore solutions. The Mn-oxide stage mineralization records extraordinarly oxidized conditions, as was deduced from the principal considerations on prevailing physicochemical conditions (Chapter 2 and Appendix 2), which also would be in agreement with the common association of Kupferschiefer-type mineralization with highly oxidized 'Rote Fäule' footwall rocks. However, Cu concentrations in all fluids observed at Sailauf appear very low (<10 µg/g), even though little is known about the chemical composition of Kupferschiefer ore fluids and their Cu concentrations are poorly constrained. Mass balance calculations still assumed concentrations of 60 to 130 ppm for the main Kupferschiefer ore

fluids (CATHLES et al., 1993; BLUNDELL et al., 2003), significantly in excess of the concentrations found at Sailauf. It has to be noted, however, that the Mn-oxide minerals at Sailauf contain up to 300 µg/g Cu (Appendix 2), up two orders of magnitude higher concentrations than in the associated fluids. Mn-oxides are capable of coprecipitating Cu from aqueous solutions very efficiently (HEWETT, 1972), so the Mn-oxide stage fluid trapped in cogenetic calcite may not be fully unmodified with regard to aqueous Cu concentrations. Nevertheless, even if the red bed-interacted Mn-oxide stage fluids do not represent unmodified primary Kupferschiefer ore fluids, the study shows that multi-element fluid inclusion microanalysis is capable of discerning red bed- and basement-interacted fluids, highlighting the methods' potential in resolving some of the controversy on fluid and metal sources of sediment-hosted Cu deposits.

The principal considerations with regard to the physicochemical factors (pH, f_{O2}, a_{SiO2}, f_{CO2}) controlling the mineral stabilities derived from the thermodynamic model outlined in Chapter 2 and Appendix 2 remain valid. In light of the additional insight gained through the fluid inclusion and stable isotope studies, however, the assumption of different mixing ratios between only two chemically contrasting fluid end-members has to be extended to include three end-member compositions. The results and conclusions summarized in this Chapter were submitted to Chemical Geology in a manuscript titled *„Red bed and basement sourced fluids recorded in hydrothermal Mn–Fe–As veins, Sailauf (Germany): A LA-ICPMS fluid inclusion study“* (Appendix 3).

Conclusions

This study provides first insight into the scale, efficiency and complexity of fluid mixing processes relevant to formation of unconformity-related hydrothermal ore veins. The results show that in-situ analysis of individual fluid inclusions in petrographically well-constrained fluid inclusion assemblages constitutes a very powerful tool in deciphering the compositional evolution of hydrothermal fluid systems during mineral precipitation. Using well-established halogen ratios as fluid source indicators in combination with aqueous base metal concentrations, it was possible to unambiguously prove fluid mixing processes on the scale of individual growth zones of a single quartz crystal from a basement-hosted hydrothermal Pb-Zn quartz-baryte vein in the Schwarzwald district, SW Germany. The process involved a metal-bearing basement-interacted brine with a halite-dissolution brine derived from the sedimentary cover rock sequence. Furthermore, evidence for fluid mixing processes relevant to the formation of a complex hydrothermal Mn-Fe-As vein mineralization in the Spessart district, Central Germany, was found using less well-established chemical tracers. Li/B and K/Li ratios clearly identify several end-member fluid compositions to have been involved in the formation of the mineralization, thus indicating significant changes in the prevailing hydrological regime during the lifetime of the hydrothermal system. The fluid end-members could be directly linked to different mineralization styles and are compositionally similar to red bed- and basement-interacted fluids. The study thus demonstrates that multi-element chemical analysis of individual fluid inclusions by LA-ICPMS enabled discrimination between these fluid reservoirs, providing a new approach for futures studies focusing on the disputed metal sources of sediment- and basement-hosted Cu- and Pb-Zn deposits.

All results were obtained from in-situ individual fluid inclusion analysis on the thin section scale, demonstrating the wealth of obtainable information given good petrographic and paragenetic constraints on age relations between fluid inclusion assemblages. In both localities the major element composition of all fluid inclusions determined by microthermometry was very similar and in itself did not clearly indicate mixing processes to have occurred. Consequently, while microthermometry certainly remains an indispensable part of any fluid inclusion study, more sophisticated analytical methods may yield additional genetic information that otherwise might be completely overlooked. Moreover, similar major element compositions of fluid inclusion populations is a common quality criterion to justify the application of bulk analytical techniques like ion chromatography (e.g. BANKS and YARDLEY, 1992; MCCAIG et al., 2000; GLEESON et al., 2001; BANKS et al., 2002; DEWAELE et al., 2004). In light of the data presented here, the validity of this conjecture in geological contexts where fluid mixing between similarly saline fluid end-members might have occurred may be questioned, although they certainly do not render all previous studies involving bulk methods meaningless. However, the scale at which fluid mixing processes were shown to occur would not have been detectable by any bulk analytical method and most of the genetic implications for the formation of hydrothermal ore veins derived in this study would have been overlooked.

References cited

ALTHERR, R., HENES-KLAIBER, U., HEGNER, E., SATIR, M., LANGER, C., 1999. Plutonism in the Variscan Odenwald (Germany): from subduction to collision. International Journal of Earth Sciences 88, 422-443.

APPOLD, M.S., GARVEN, G., 2000. Reactive Flow Models of Ore Formation in the Southeast Missouri District. Economic Geology 95, 1605-1626.

AUDÉTAT, A., GÜNTHER, D., HEINRICH, C.A., 1998. Formation of a Magmatic-Hydrothermal Ore Deposit: Insights with LA-ICP-MS Analysis of Fluid Inclusions. Science 279, 2091-2094.

BAATARTSOGT, B., SCHWINN, G., WAGNER, T., TAUBALD, H., BEITTER, T., MARKL, G., 2007. Contrasting paleofluid systems in the continental basement: a fluid inclusion and stable isotope study of hydrothermal vein mineralization, Schwarzwald district, Germany. Geofluids 7, 123-147.

BANKS, D.A., BOYCE, A.J., SAMSON, I.M., 2002. Constraints on the Origins of Fluids Forming Irish Zn-Pb-Ba Deposits: Evidence from the Composition of Fluid Inclusions. Economic Geology 97, 471-480.

BANKS, D.A., DAVIES, G.R., YARDLEY, B.W.D., MCCAIG, A.M., GRANT, N.T., 1991. The chemistry of brines from an Alpine thrust system in the Central Pyrenees: An application of fluid inclusion analysis to the study of fluid behaviour in orogenesis. Geochimica et Cosmochimica Acta 55, 1021-1030.

BANKS, D.A., GLEESON, S.A., GREEN, R., 2000. Determination of the origin of salinity in granite-related fluids: evidence from chlorine isotopes in fluid inclusions. Journal of Geochemical Exploration 69, 309-312.

BANKS, D.A., YARDLEY, B.W.D., 1992. Crush-leach analysis of fluid inclusions in small natural and synthetic samples. Geochimica et Cosmochimica Acta 56, 245-248.

BARNES, H.L., ROSE, A.W., 1998. Origins of Hydrothermal Ores. Science 279, 2064-2065.

BECHTEL, A., PÜTTMANN, W., 1991. The origin of the Kupferschiefer-Type mineralization in the Richelsdorf Hills, Germany, as deduced from stable isotope and organic geochemical studies. Chemical Geology 91, 1-18.

BECHTEL, A., SHIEH, Y.-N., ELLIOTT, W.C., OSZCZEPALSKI, S., HOERNES, S., 2000. Mineralogy, crystallinity and stable isotopic composition of illitic clays within the Polish Zechstein basin: implications for the genesis of Kupferschiefer mineralization. Chemical Geology 163, 189-205.

BEHR, H.J., GERLER, J., 1987. Inclusions of sedimentary brines in post-Variscan mineralizations in the Federal Republic of Germany — A study by neutron activation analysis. Chemical Geology 61, 65-77.

BEHR, H.J., HORN, E.E., FRENTZEL-BEYME, K., REUTEL, C., 1987. Fluid inclusion characteristics of the Variscan and post-Variscan mineralizing fluids in the Federal Republic of Germany. Chemical Geology 61, 273-285.

BETHKE, C.M., 2008. Geochemical and biogeochemical reaction modeling. Cambridge, Cambridge University Press, 564 p.

BLIEDTNER, M., MARTIN, M., 1986. Erz- und Minerallagerstätten des Mittleren Schwarzwaldes: eine bergbaugeschichtliche und lagerstättenkundliche Darstellung. Freiburg i. Br., Geologisches Landesamt Baden-Württemberg, 782 p.

BLUNDELL, D.J., KARNKOWSKI, P.H., ALDERTON, D.H.M., OSZCZEPALSKI, S., KUCHA, H., 2003. Copper mineralization of the Polish Kupferschiefer: a proposed basement fault-fracture system of fluid flow. Economic Geology 98, 1487-1495.

BÖHLKE, J.K., IRWIN, J.J., 1992. Laser microprobe analyses of Cl, Br, I, and K in fluid inclusions: Implications for sources of salinity in some ancient hydrothermal fluids. Geochimica et Cosmochimica Acta 56, 203-225.

BOIRON, M.-C., CATHELINEAU, M., RICHARD, A., 2010. Fluid flows and metal deposition near basement/cover unconformity: lessons and analogies from Pb-Zn-F-Ba systems for the understanding of Proterozoic U deposits. Geofluids 10, 270-292.

BONS, P.D., ELBURG, M.A., GOMEZ-RIVAS, E., 2012. A review of the formation of tectonic veins and their microstructures. Journal of Structural Geology 43, 33-62.

BROWN, A.C., 2009. A process-based approach to estimating the copper derived from red beds in the sediment-hosted stratiform copper deposit model. Economic Geology 104, 857-868.

BRUGGER, J., GIERÉ, R., 2000. Origin and distribution of some trace elements in metamorphosed Fe-Mn deposits, Val Ferrera, Eastern Swiss Alps. Canadian Mineralogist 38, 1075-1101.

BRUNO, J., STUMM, W., WERSIN, P., BRANDBERG, F., 1992. On the influence of carbonate in mineral dissolution: I. The thermodynamics and kinetics of hematite dissolution in bicarbonate solutions at T = 25°C. Geochimica et Cosmochimica Acta 56, 1139-1147.

CAPUANO, R.M., 1992. The temperature dependence of hydrogen isotope fractionation between clay minerals and water: Evidence from a geopressured system. Geochimica et Cosmochimica Acta 56, 2547-2554.

CARPENTER, A.B., 1978. Origin and chemical evolution of brines in sedimentary basins. Oklahoma Geological Survey Circular 79, 60-77.

CATHELINEAU, M., BOIRON, M.-C., 2010. Downward penetration and mixing of sedimentary brines and dilute hot waters at 5 km depth in the granite basement at Soultz-sous-Forêts (Rhine graben, France). Comptes Rendus Geoscience 342, 560-565.

CATHLES III, L.M., OSZCZEPALSKI, S., JOWETT, E.C., 1993. Mass balance evaluation of the late diagenetic hypothesis for Kupferschiefer Cu mineralization in the Lubin Basin of southwestern Poland Economic Geology 88, 948-956.

COX, S.F., SUN, S.-S., ETHERIDGE, M.A., WALL, V.J., POTTER, T.F., 1995. Structural and geochemical controls on the development of turbidite-hosted gold quartz vein deposits, Wattle Gully Mine, central Victoria, Australia. Economic Geology 90, 1722-1746.

CRERAR, D.A., CORMICK, R.K., BARNES, H.L., 1980. Geochemistry of manganese: An overview. In: I.M. Varentsov and G. Grasselly (Eds.), *Geology and geochemistry of manganese.* Stuttgart, Schweizerbart, pp. 293-334.

DEROME, D., CATHELINEAU, M., CUNEY, M., FABRE, C., LHOMME, T., BANKS, D.A., 2005. Mixing of Sodic and Calcic Brines and Uranium Deposition at McArthur River, Saskatchewan, Canada: A Raman and Laser-Induced Breakdown Spectroscopic Study of Fluid Inclusions. Economic Geology 100, 1529-1545.

DEROME, D., CATHELINEAU, M., FABRE, C., BOIRON, M.-C., BANKS, D.A., LHOMME, T., CUNEY, M., 2007. Paleo-fluid composition determined from individual fluid inclusions by Raman and LIBS: Application to mid-proterozoic evaporitic Na-Ca brines (Alligator Rivers Uranium Field, northern territories Australia). Chemical Geology 237, 240-254.

DEWAELE, S., MUCHEZ, P., BANKS, D.A., 2004. Fluid evolution along multistage composite fault systems at the southern margin of the Lower Palaeozoic Anglo-Brabant fold belt, Belgium. Geofluids 4, 341-356.

DILL, H.G., 1988. Geologic setting and age relationship of fluorite-barite mineralization in southern Germany with special reference to the Late Paleozoic unconformity. Mineralium Deposita 23, 16-23.

DILL, H.G., NIELSEN, H., 1987. Geochemical and geological constraints on the formation of unconformity-related vein baryte deposits of Central Europe. Journal of the Geological Society 144, 97-105.

DOMBROWSKI, A., HENJES-KUNST, F., HÖHNDORF, A., KRÖNER, A., OKRUSCH, M., RICHTER, P., 1995. Orthogneisses in the Spessart Crystalline Complex, north-west Bavaria: Silurian granitoid magmatism at an active continental margin. Geologische Rundschau 84, 399-411.

DOMBROWSKI, A., OKRUSCH, M., HENJES-KUNST, F., 1994. Geothermobarometry and geochronology on mineral assemblages of orthogneisses and related metapelites of the Spessart crystalline complex, NW Bavaria, Germany. Chemie der Erde / Geochemistry 54, 85-101.

DUBOIS, M., AYT-OUGOUGDAL, M., MEERE, P.A., ROYER, J.-J., BOIRON, M.-C., CATHELINEAU, M., 1996. Temperature of paleo-to modern self-sealing within a continental rift basin; the fluid inclusion data (Soultz-sous-Forets, Rhine Graben, France). European Journal of Mineralogy 8, 1065-1080.

FISCHER, M., BOTZ, R., SCHMIDT, M., ROCKENBAUCH, K., GARBE-SCHÖNBERG, D., GLODNY, J., GERLING, P., LITTKE, R., 2006. Origins of CO_2 in permian carbonate reservoir rocks (Zechstein, Ca2) of the NW-German Basin (Lower Saxony). Chemical Geology 227, 184-213.

FONTES, J.C., MATRAY, J.M., 1993. Geochemistry and origin of formation brines from the Paris Basin, France: 1. Brines associated with Triassic salts. Chemical Geology 109, 149-175.

FRAPE, S.K., FRITZ, P., 1987. Geochemical Trends for Groundwaters from the Canadian Shield. In: P. Fritz and S.K. Frape (Eds.), *Saline water and gases in crystalline rocks.* St. John's, Geological Association of Canada Special Paper, pp. 19-38.

FRIEDMAN, I., O'NEIL, J.R., 1977. Compilation of stable isotope fractionation factors of geochemical interest, US Geological Survey Special Paper (440-KK), 12 p.

GEYER, O.F., GWINNER, M.P., 2011. Geologie von Baden-Württemberg. Stuttgart, Schweizerbart, 482 p.

GLASBY, G.P., PAPAVASSILIOU, C.T., MITSIS, J., VALSAMI-JONES, E., LIAKOPOULOS, A., RENNER, R.M., 2005. The Vani manganese deposit, Milos island, Greece: A fossil stratabound Mn-Ba-Pb-Zn-As-Sb-W-rich hydrothermal deposit. In: M. Fytikas and G. Vougioukalakis (Eds.), *The South Aegean Volcanic Arc - Present Knowledge and Future Perspectives.* Amsterdam, Elsevier, pp. 255-291.

GLEESON, S.A., WILKINSON, J.J., BOYCE, A.J., FALLICK, A.E., STUART, F.M., 1999. On the occurrence and wider implications of anomalously low δD fluids in quartz veins, South Cornwall, England. Chemical Geology 160, 161-173.

GLEESON, S.A., WILKINSON, J.J., STUART, F.M., BANKS, D.A., 2001. The origin and evolution of base metal mineralising brines and hydrothermal fluids, South Cornwall, UK. Geochimica et Cosmochimica Acta 65, 2067-2079.

GLEESON, S.A., YARDLEY, B.W.D., 2003. Surface-derived fluids in basement rocks:inferences from palaeo-hydrothermal systems. Journal of Geochemical Exploration 78-79, 61-65.

GOLDENBERG, G., MAASS, A., STEFFENS, G., STEUER, H., 2003. Hematite mining during the linear ceramics culture in the area of the Black Forest, Southwest Germany. In: T. Stöllner, G. Körlin, G. Steffens and J. Cierny (Eds.), *Man and Mining: Mensch und Bergbau. Studies in honour of Gerd Weisgerber.* Bochum, Der Anschnitt Supplement 16, pp. 179-186.

GOLDHABER, M.B., CHURCH, S.E., DOE, B.R., ALEINIKOFF, J.N., BRANNON, J.C., PODOSEK, F.A., MOSIER, E.L., TAYLOR, C.D., GENT, C.A., 1995. Lead and Sulfur Isotope Investigation of Paleozoic Sedimentary Rocks from the Southern Midcontinent of the United States; Implications for Paleohydrology and Ore Genesis of the Southeast Missouri Lead Belts. Economic Geology 90, 1875-1910.

GOLDSTEIN, R.H., REYNOLDS, T.J., 1994. Systematics of fluid inclusions in diagenetic minerals - SEPM Short Course 31. Tulsa, Society for Sedimentary Geology, 199 p.

GROVES, D.I., GOLDFARB, R.J., GEBRE-MARIAM, M., HAGEMANN, S.G., ROBERT, F., 1998. Orogenic gold deposits: A proposed classification in the context of their crustal distribution and relationship to other gold deposit types. Ore Geology Reviews 13, 7-27.

GÜNTHER, D., AUDÉTAT, A., FRISCHKNECHT, R., HEINRICH, C.A., 1998. Quantitative analysis of major, minor and trace elements in fluid inclusions using laser ablation–inductively coupled plasma mass spectrometry. Journal of Analytical Atomic Spectrometry 13, 263-270.

HANN, H.P., CHEN, F., ZEDLER, H., FRISCH, W., LOESCHKE, J., 2003. The Rand Granite in the southern Schwarzwald and its geodynamic significance in the Variscan belt of SW Germany. International Journal of Earth Sciences (Geologische Rundschau) 92, 821-842.

HAUTMANN, S., BRANDER, H., LIPPOLT, H.J., LORENZ, J., 1999. K–Ar and (U+Th)–He chronometry of multistage alteration and mineralisation in the Hartkoppe rhyolite, Spessart, Germany. Journal of Conference Abstracts 4, 769.

HEDENQUIST, J.W., LOWENSTERN, J.B., 1994. The role of magmas in the formation of hydrothermal ore deposits. Nature 370, 519-527.

HEIJLEN, W., MUCHEZ, P., BANKS, D.A., SCHNEIDER, J., KUCHA, H., KEPPENS, E., 2003. Carbonate-hosted Zn-Pb deposits in Upper Silesia, Poland: Origin and Evolution of Mineralizing Fluids and Constraints on Genetic Models. Economic Geology 98, 911-932.

HEIN, J.R., STAMATAKIS, M.G., DOWLING, J.S., 2000. Trace metal-rich Quaternary hydrothermal manganese oxide and barite deposit, Milos Island, Greece. Transactions of the Institution of Mining and Metallurgy (Section B: Applied earth sciences) 109, 67-76.

HEINRICH, C.A., PETTKE, T., HALTER, W.E., AIGNER-TORRES, M., AUDÉTAT, A., GÜNTHER, D., HATTENDORF, B., BLEINER, D., GUILLONG, M., HORN, I., 2003. Quantitative multi-element analysis of minerals, fluid and melt inclusions by laser-ablation inductively-coupled-plasma mass-spectrometry. Geochimica et Cosmochimica Acta 67, 3473-3497.

HEM, J.D., 1972. Chemical Factors that Influence the Availability of Iron and Manganese in Aqueous Systems. Bulletin of the Geological Society of America 83, 443.

HEWETT, D.F., 1964. Veins of hypogene manganese oxide minerals in the southwestern United States. Economic Geology 59, 1429.

HEWETT, D.F., 1972. Manganite, Hausmannite, Nraunite; Features, Modes of Origin. Economic Geology 67, 83-102.

HITZMAN, M.W., 2000. Source basins for sediment-hosted stratiform Cu deposits: implications for the structure of the Zambian Copperbelt. Journal of African Earth Sciences 30, 855-863.

HITZMAN, M.W., KIRKHAM, R., BROUGHTON, D., THORSON, J., SELLEY, D., 2005. The sediment-hosted stratiform copper ore system. In: J.W. Hedenquist, J.F.H. Thompson, R.J. Goldfarb and J.P. Richards (Eds.), *Economic Geology - 100th Anniversary Volume*. Littleton, Society of Economic Geologists, pp. 609-642.

HOLSER, W.T., 1979. Trace elements and isotopes in evaporites. Marine Minerals 6, 295-436.

HOLTSTAM, D., 2001. W and V mineralization in Långban-type Fe-Mn deposits: Epigenetic or syngenetic? GFF 123, 29-33.

HOLTSTAM, D., MANSFELD, J., 2001. Origin of a carbonate-hosted Fe-Mn-(Ba-As-Pb-Sb-W) deposit of Långban-type in central Sweden. Mineralium Deposita 36, 641-657.

JOWETT, E.C., 1986. Genesis of Kupferschiefer Cu-Ag Deposits by Convective Flow of Rotliegende Brines during Triassic Rifting. Economic Geology 81, 1823-1837.

KÄDING, K.-C., 2005. Der Zechstein in der Stratigraphischen Tabelle von Deutschland 2002. Newsletters on Stratigraphy 41, 123-127.

KALT, A., ALTHERR, R., HANEL, M., 2000. The Variscan basement of the Schwarzwald. European Journal of Mineralogy 12, 1-43.

KESLER, S.E., MARTINI, A.M., APPOLD, M.S., WALTER, L.M., HUSTON, T.J., FURMAN, F.C., 1996. Na-Cl-Br systematics of fluid inclusions from Mississippi Valley-type deposits, Appalachian Basin: Constraints on solute origin and migration paths. Geochimica et Cosmochimica Acta 60, 225-233.

KINNAIRD, J.A., IXER, R.A., BARREIRO, B., NEX, P.A.M., 2002. Contrasting sources for lead in Cu-polymetallic and Zn-Pb mineralisation in Ireland: constraints from lead isotopes. Mineralium Deposita 37, 495-511.

KOSSMAT, F., 1927. Gliederung des varistischen Gebirgsbaues. Sächsisches Geologisches Landesamt - Abhandlungen 1, 1-39.

KOZIY, L., BULL, S., LARGE, R.R., SELLEY, D., 2009. Salt as a fluid driver, and basement as a metal source, for stratiform sediment-hosted copper deposits. Geology 37, 1107-1110.

KRAUSKOPF, K.B., 1957. Separation of manganese from iron in sedimentary processes. Geochimica et Cosmochimica Acta 12, 61-84.

KROHE, A., EISBACHER, G.H., 1988. Oblique crustal detachment in the Variscan Schwarzwald, southwestern Germany. Geologische Rundschau 77, 25-43.

KRONER, U., MANSY, J.L., MAZUR, S., ALEKSANDROWSKI, P., HANN, H.P., HUCKRIEDE, H., LACQUEMENT, F., LAMARCHE, J., LEDRU, P., PHARAOH, T.C., ZEDLER, H., ZEH, A., ZULAUF, G., 2008. Variscan Tectonics. In: T. McCann (Ed.), *The Geology of Central Europe.* London, The Geological Society, pp. 599-664.

LAND, L.S., 1995. Na-Ca-Cl saline formation waters, Frio Formation (Oligocene), south Texas, USA: Products of diagenesis. Geochimica et Cosmochimica Acta 59, 2163-2174.

LEACH, D.L., BRADLEY, D.C., HUSTON, D., PISAREVSKY, S.A., TAYLOR, R.D., GARDOLL, S.J., 2010. Sediment-Hosted Lead-Zinc Deposits in Earth History. Economic Geology 105, 593-625.

LEACH, D.L., SANGSTER, D.F., KELLEY, K.D., LARGE, R.R., GARVEN, G., ALLEN, C.R., GUTZMER, J., WALTERS, S., 2005. Sediment-hosted lead-zinc deposits: A global perspective. In: J.W. Hedenquist, J.F.H. Thompson, R.J. Goldfarb and J.P. Richards (Eds.), *Economic Geology - 100th Anniversary Volume.* Littleton, Society of Economic Geologists, pp. 561-607.

LEAL, P.R., CORREA, M.J., AMETRANO, S.J., ETCHEVERRY, R.O., DE BRODTKORB, M.K., 2008. The manganese deposits of the Pampean ranges, Argentina. Canadian Mineralogist 46, 1215-1233.

LIPPOLT, H.J., SCHLEICHER, H., RACZEK, I., 1983. Rb-Sr systematics of Permian volcanites in the Schwarzwald (SW-Germany). Part I: Space of time between plutonism and late orogenic volcanism. Contributions to Mineralogy and Petrology 84, 272-280.

LORENZ, J., 1995. Mineralisationen aus dem Rhyolith-Steinbruch von Sailauf einschließlich der Neufunde von ged. Arsen, Bertrandit, Humboldtin und Tilasit. Der Aufschluss 46, 105-122.

LORENZ, J., 2010. Spessartsteine. Spessartin, Spessartit und Buntsandstein – eine umfassende Geologie und Mineralogie des Spessarts. Aschaffenburg, Naturwissenschaftlicher Verein Aschaffenburg, 910 p.

LÜDERS, V., REUTEL, C., HOTH, P., BANKS, D.A., MINGRAM, B., PETTKE, T., 2005. Fluid and gas migration in the North German Basin: fluid inclusion and stable isotope constraints. International Journal of Earth Sciences (Geologische Rundschau) 94, 990-1009.

MARKL, G., 2005. Bergbau und Mineralienhandel im fürstenbergischen Kinzigtal. Filderstadt, Markstein Verlag, 392 p.

MATTHÄI, S.K., HEINRICH, C.A., DRIESNER, T., 2004. Is the Mount Isa copper deposit the product of forced brine convection in the footwall of a major reverse fault? Geology 32, 357-360.

MCCAIG, A.M., TRITLLA, J., BANKS, D.A., 2000. Fluid mixing and recycling during Pyrenean thrusting: Evidence from fluid inclusion halogen ratios. Geochimica et Cosmochimica Acta 64, 3395-3412.

MCCANN, T., KIERSNOWSKI, H., KRAINER, K., VOZÁROVÁ, A., PERYT, T.M., OPLUSTIL, S., STOLLHOFEN, H., SCHNEIDER, J., WETZEL, A., BOULVAIN, F., DUSAR, M., TÖRÖK, Á., HAAS, J., TAIT, J., KÖRNER, F., 2008. Permian. In: T. McCann (Ed.), *The Geology of Central Europe.* London, The Geological Society, pp. 531-597.

METZ, R., RICHTER, M., SCHÜRENBERG, H., 1957. Die Blei–Zink–Erzgänge des Schwarzwaldes. Hannover, Bundesanstalt für Geologie und Rohstoffe, 277 p.

MÖLLER, P., DULSKI, P., 1999. Rare earth elements and yttrium in mineral and geothermal waters from crystalline rocks. In: H. Ármannsson (Ed.), *Geochemistry of the Earth's Surface.* Rotterdam, A.A. Balkema, pp. 527-530.

MÖLLER, P., IRBER, W., GIESE, U., 1997. Element mobility in paragneisses and metabasites of the Continental Deep Drilling Project (KTB/Germany). Geologische Rundschau 86, 184-198.

MUCHEZ, P., HEIJLEN, W., BANKS, D.A., BLUNDELL, D.J., BONI, M., GRANDIA, F., 2005. Extensional tectonics and the timing and formation of basin-hosted deposits in Europe. Ore Geology Reviews 27, 241-267.

MUIR-WOOD, R., KING, G.C.P., 1993. Hydrological Signatures of Earthquake Strain. Journal of Geophysical Research: Solid Earth 98, 22035-22068.

NEUMANN, E.-R., WILSON, M., HEEREMANS, M., SPENCER, E.A., OBST, K., TIMMERMAN, M.J., KIRSTEIN, L., 2004. Carboniferous-Permian rifting and magmatism in southern Scandinavia, the North Sea and northern Germany: a review. In: M. Wilson, E.-R. Neumann, G.R. Davies, M.J. Timmerman, M. Heeremans and B.T. Larsen (Eds.), *Permo-Carboniferous Rifting and Magmatism in Europe.* London, The Geological Society, pp. 11-40.

NICHOLSON, K., 1992. Contrasting Mineralogical-Geochemical Signatures of Manganese Oxides: Guides to Metallogenesis. Economic Geology 87, 1253-1264.

ODIN, G.S., DESPRAIRIES, A., FULLAGAR, P.D., BELLON, H., DECARREAU, A., FRÖHLICH, F., ZELVELDER, M., 1988. Nature and Geological Significance of Celadonite. In: G.S. Odin (Ed.), *Developments in Sedimentology.* Elsevier, pp. 337-398.

OKRUSCH, M., GEYER, G., LORENZ, J., 2011. Spessart. Geologische Entwicklung und Struktur, Gesteine und Minerale. Sammlung Geologischer Führer Band 106. Stuttgart, Gebr. Bornträger, 368 p.

OKRUSCH, M., LORENZ, J., WEYER, S., 2007. The genesis of sulfide assemblages in the former Wilhelmine mine, Spessart, Bavaria, Germany. Canadian Mineralogist 45, 723-750.

OKRUSCH, M., WEBER, K., 1996. Der Kristallinkomplex des Vorspessart. Zeitschrift für Geologische Wissenschaften 24, 141-174.

OSZCZEPALSKI, S., 1999. Origin of the Kupferschiefer polymetallic mineralization in Poland. Mineralium Deposita 34, 599-613.

PAUWELS, H., FOUILLAC, C., FOUILLAC, A.-M., 1993. Chemistry and isotopes of deep geothermal saline fluids in the Upper Rhine Graben: Origin of compounds and water-rock interactions. Geochimica et Cosmochimica Acta 57, 2737-2749.

PFAFF, K., HILDEBRANDT, L., LEACH, D.L., JACOB, D.E., MARKL, G., 2010. Formation of the Wiesloch Mississippi Valley-type Zn-Pb-Ag deposit in the extensional setting of the Upper Rhinegraben, SW Germany. Mineralium Deposita 45, 647-666.

PFAFF, K., ROMER, R.L., MARKL, G., 2009. U-Pb ages of ferberite, chalcedony, agate, 'U-mica' and pitchblende: constraints on the mineralization history of the Schwarzwald ore district European Journal of Mineralogy 21, 817-836.

RENTZSCH, J., 1974. The Kupferschiefer in comparison with the deposits of the Zambian Copperbelt. In: P. Bartholomé (Ed.), *Gisements Stratiformes et Provinces Cuprifères.* Liege, Société Géologique de Belgique, pp. 395-418.

REYES, A.G., TROMPETTER, W.J., 2012. Hydrothermal water–rock interaction and the redistribution of Li, B and Cl in the Taupo Volcanic Zone, New Zealand. Chemical Geology 314-317, 96-112.

RICHARD, A., PETTKE, T., CATHELINEAU, M., BOIRON, M.-C., MERCADIER, J., CUNEY, M., DEROME, D., 2010. Brine-rock interaction in the Athabasca basement (McArthur River U deposit, Canada): consequences for fluid chemistry and uranium uptake. Terra Nova 22, 303-308.

RITTENHOUSE, G., 1967. Bromine in oil-field waters and its use in determining possibilities of origin of these waters. The American Association of Petroleum Geologists Bulletin 51, 2430-2440.

ROEDDER, E., 1967. Fluid inclusions as samples of ore fluids. In: H.L. Barnes (Ed.), *Geochemistry of Hydrothermal Ore Deposits*. New York, Holt, Rinehart and Winston, pp. 515-574.

ROY, S., 1981. Manganese deposits. London, Academic Press, 458 p.

RUSSELL, M.J., SOLOMON, M., WALSHE, J.L., 1981. The Genesis of Sediment-Hosted, Exhalative Zinc + Lead Deposits. Mineralium Deposita 16, 113-127.

SALZMANN, G., 1935. Untersuchungen im Ilfelder Manganerzbergbau. Zeitschrift für praktische Geologie 43, 171-174.

SANGSTER, D.F., 1990. Mississippi Valley-type and sedex lead-zinc deposits: A comparative examination. Transactions of the Institution of Mining and Metallurgy (Section B: Applied earth sciences) 99, 21-42.

SCHLEICHER, H., 1994. Collision-type granitic melts in the context of thrust tectonics and uplift history (Triberg granite complex, Schwarzwald, Germany). Neues Jahrbuch für Mineralogie - Abhandlungen 166, 211-237.

SCHLEICHER, H., LIPPOLT, H.J., RACZEK, I., 1983. Rb-Sr systematics of Permian volcanites in the Schwarzwald (SW-Germany). Part II: Age of eruption and the mechanism of Rb - Sr whole rock age distortions. Contributions to Mineralogy and Petrology 84, 281-291.

SCHWINN, G., WAGNER, T., BAATARTSOGT, B., MARKL, G., 2006. Quantification of mixing processes in ore-forming hydrothermal systems by combination of stable isotope and fluid inclusion analyses. Geochimica et Cosmochimica Acta 70, 965-982.

SEWARD, T.M., BARNES, H.L., 1997. Metal transport by hydrothermal ore fluids. In: H.L. Barnes (Ed.), *Geochemistry of hydrothermal ore deposits*. New York, John Wiley & Sons, pp. 435-486.

SHAW, D.M., STURCHIO, N.C., 1992. Boron-lithium relationships in rhyolites and associated thermal waters of young silicic calderas, with comments on incompatible element behaviour. Geochimica et Cosmochimica Acta 56, 3723-3731.

SHEPPARD, S.M.F., 1986. Characterization and isotopic variations in natural waters. Reviews in Mineralogy and Geochemistry 16, 165-183.

SHEPPARD, S.M.F., GILG, H.A., 1996. Stable isotope geochemistry of clay minerals. Clay Minerals 31, 1-24.

SHOCK, E.L., SASSANI, D.C., WILLIS, M., SVERJENSKY, D.A., 1997. Inorganic species in geologic fluids: Correlations among standard molal thermodynamic properties of aqueous ions and hydroxide complexes. Geochimica et Cosmochimica Acta 61, 907-950.

SIBSON, R.H., 2001. Seismogenic framework for hydrothermal transport and ore deposition. Society of Economic Geologists Reviews 14, 25-50.

STAUDE, S., BONS, P.D., MARKL, G., 2009. Hydrothermal vein formation by extension-driven dewatering of the middle crust: An example from SW Germany. Earth and Planetary Science Letters 286, 387-395.

STAUDE, S., GÖB, S., PFAFF, K., STRÖBELE, F., PREMO, W.R., MARKL, G., 2011. Deciphering fluid sources of hydrothermal systems: A combined Sr- and S-isotope study on barite (Schwarzwald, SW Germany). Chemical Geology 286, 1-20.

STAUDE, S., MORDHORST, T., NAU, S., PFAFF, K., BRÜGMANN, G., JACOB, D.E., MARKL, G., 2012a. Hydrothermal carbonates of the Schwarzwald ore district, southwestern Germany: Carbon source and conditions of formation using $\delta^{18}O$, $\delta^{13}C$, $^{87}Sr/^{86}Sr$, and fluid inclusions. Canadian Mineralogist 50, 1401-1434.

STAUDE, S., MORDHORST, T., NEUMANN, R., PREBECK, W., MARKL, G., 2010. Compositional variation of the tennantite-tetrahedrite solid-solution series in the Schwarzwald ore district (SW Germany): The role of mineralization processes and fluid source. Mineralogical Magazine 74, 309-339.

STAUDE, S., WAGNER, T., MARKL, G., 2007. Mineralogy, mineral compositions and fluid evolution at the Wenzel hydrothermal deposit, southern Germany: implications for the formation of Kongsberg-type silver deposits. Canadian Mineralogist 45, 1147-1176.

STAUDE, S., WERNER, W., MORDHORST, T., WEMMER, K., JACOB, D.E., MARKL, G., 2012b. Multi-stage Ag–Bi–Co–Ni–U and Cu–Bi vein mineralization at Wittichen, Schwarzwald, SW Germany: geological setting, ore mineralogy, and fluid evolution. Mineralium Deposita 47, 251-276.

STOBER, I., BUCHER, K., 1999. Origin of salinity of deep groundwater in crystalline rocks. Terra Nova 11, 181-185.

STOFFELL, B., APPOLD, M.S., WILKINSON, J.J., MCCLEAN, N.A., JEFFRIES, T.E., 2008. Geochemistry and Evolution of Mississippi Valley-Type Mineralizing Brines from the Tri-State and Northern Arkansas Districts Determined by LA-ICP-MS Microanalysis of Fluid Inclusions. Economic Geology 103, 1411-1435.

SULEIMENOV, O.M., SEWARD, T.M., 2000. Spectrophotometric measurements of metal complex formation at high temperatures: the stability of Mn(II) chloride species. Chemical Geology 167, 177-192.

SVERJENSKY, D.A., SHOCK, E.L., HELGESON, H.C., 1997. Prediction of the thermodynamic properties of aqueous metal complexes to 1000°C and 5 kb. Geochimica et Cosmochimica Acta 61, 1359-1412.

SYMONS, D.T.A., KAWASAKI, K., WALTHER, S., BORG, G., 2011. Paleomagnetism of the Cu–Zn–Pb-bearing Kupferschiefer black shale (Upper Permian) at Sangerhausen, Germany. Mineralium Deposita 46, 137-152.

TESTEMALE, D., BRUGGER, J., LIU, W., ETSCHMANN, B., HAZEMANN, J.-L., 2009. In-situ X-ray absorption study of Iron(II) speciation in brines up to supercritical conditions. Chemical Geology 264, 295-310.

TRUSHEIM, F., 1964. Über den Untergrund Frankens: Ergebnisse von Tiefbohrungen in Franken und Nachbargebieten, 1953-1960. München, Bayerisches Geologisches Landesamt, 92 p.

VAUGHAN, D.J., SWEENEY, M.A., FRIEDRICH, G., DIEDEL, R., HARANCZYK, C., 1989. The Kupferschiefer: An Overview with an Appraisal of the Different Types of Mineralization. Economic Geology 84, 1003-1027.

WAGNER, T., LORENZ, J., 2002. Mineralogy of complex Co-Ni-Bi vein mineralization, Bieber deposit, Spessart, Germany. Mineralogical Magazine 66, 385-407.

WAGNER, T., OKRUSCH, M., WEYER, S., LORENZ, J., LAHAYE, Y., TAUBALD, H., SCHMITT, R.T., 2010. The role of the Kupferschiefer in the formation of hydrothermal base metal mineralization in the Spessart ore district, Germany: insight from detailed sulfur isotope studies. Mineralium Deposita 45, 217-239.

WERNER, W., DENNERT, V., 2004. Lagerstätten und Bergbau im Schwarzwald. Freiburg im Br., Landesamt für Geologie, Rohstoffe und Bergbau; Baden-Württemberg, 334 p.

WETZEL, A., ALLENBACH, R., ALLIA, V., 2003. Reactivated basement structures affecting the sedimentary facies in a tectonically "quiescent" epicontinental basin: an example from NW Switzerland. Sedimentary Geology 157, 153-172.

WILKINSON, J.J., 2001. Fluid inclusions in hydrothermal ore deposits. Lithos 55, 229-272.

WILKINSON, J.J., 2010. A Review of Fluid Inclusion Constraints on Mineralization in the Irish Ore Field and Implications for the Genesis of Sediment-Hosted Zn-Pb Deposits. Economic Geology 105, 417-442.

WILKINSON, J.J., EVERETT, C.E., BOYCE, A.J., GLEESON, S.A., RYE, D.M., 2005. Intracratonic crustal seawater circulation and the genesis of subseafloor zinc-lead mineralization in the Irish orefield. Geology 33, 805-808.

WILKINSON, J.J., STOFFELL, B., WILKINSON, C.C., JEFFRIES, T.E., APPOLD, M.S., 2009. Anomalously Metal-Rich Fluids Form Hydrothermal Ore Deposits. Science 323, 764-767.

WOLFRAM, O., KRUPP, R.E., 1996. Hydrothermal solubility of rhodochrosite, Mn(II) speciation, and equilibrium constants. Geochimica et Cosmochimica Acta 60, 3983-3994.

WOOD, S.A., 1990. The aqueous geochemistry of the rare-earth elements and yttrium. 2. Theoretical predictions of speciation in hydrothermal solutions to 350°C at saturation water vapor pressure. Chemical Geology 88, 99-125.

WOOD, S.A., SAMSON, I.M., 1998. Solubility of ore minerals and complexation of ore metals in hydrothermal solutions. Reviews in Economic Geology 10, 33-80.

YARDLEY, B.W.D., 2005. 100th Anniversary Special Paper: Metal Concentrations in Crustal Fluids and Their Relationship to Ore Formation. Economic Geology 100, 613-632.

ZHENG, Y.-F., HOEFS, J., 1993. Stable Isotope Geochemistry of Hydrothermal Mineralizations in the Harz Mountains: I. Carbon and Oxygen Isotopes of Carbonates and Implications for the Origin of Hydrothermal Fluids. In: P. Möller and V. Lüders (Eds.), *Formation of Hydrothermal Vein Deposits – Case Study of the Pb-Zn, Barite and Fluorite Deposits of the Harz Mountains*. Berlin, Gebr. Bornträger, pp. 169-188.

ZIEGLER, P.A., 1987. Late cretaceous and cenozoic intra-plate compressional deformations in the Alpine foreland - a geodynamic model. Tectonophysics 137, 389-420.

ZIEGLER, P.A., 1990. Geological Atlas of Western and Central Europe. Shell International Petroleum Maatschappij. Den Haag, Elsevier, 239 p.

Appendix 1

Fluid mixing forms basement-hosted Pb-Zn deposits: Insight from metal and halogen geochemistry of individual fluid inclusions.

Authors

Tobias Fusswinkel, Thomas Wagner, Markus Wälle, Thomas Wenzel, Christoph A. Heinrich, Gregor Markl

Status

Published in *GEOLOGY* v.41 (2013), p. 679-682

Associate Editor

William Collins

Reviewer

Bruce Yardley, Antonin Richard and one anonymous reviewer

Contributions of the candidate

Scientific ideas	60 %
Data acquisition	100 %
Analysis and interpretation	80 %
Preparation of manuscript	80 %

Fluid mixing forms basement-hosted Pb-Zn deposits: Insight from metal and halogen geochemistry of individual fluid inclusions

Tobias Fusswinkel[1], Thomas Wagner[2], Markus Wälle[1], Thomas Wenzel[3], Christoph A. Heinrich[1], and Gregor Markl[3]
[1]Institute of Geochemistry and Petrology, ETH Zurich, Clausiusstrasse 25, CH-8092 Zürich, Switzerland
[2]Department of Geosciences and Geography, Division of Geology, University of Helsinki, Gustaf Hällströmin katu 2a, FI-00014 Helsinki, Finland
[3]Department of Geosciences, University of Tübingen, Wilhelmstrasse 56, D-72074 Tübingen, Germany

ABSTRACT

Fluid mixing across unconformities between crystalline basement and overlying sedimentary basins is commonly invoked as an efficient chemical mechanism for ore deposition, but the origin of basement brines and the process of ore formation have rarely been linked by direct evidence. Using laser ablation–inductively coupled plasma–mass spectrometry microanalysis of individual fluid inclusions with an improved detection approach for anion components, we determined simultaneously the ore metal concentrations and the Cl/Br ratio in texturally well constrained inclusion assemblages from a basement-hosted quartz-fluorite-barite-Pb-Zn vein system. An inverse correlation between the Pb + Zn concentrations and the Cl/Br mass ratios in the fluid inclusions provides clear evidence for mixing of a basement-derived metal-rich brine and a metal-poor formation water that acquired its salinity from halite dissolution in Triassic evaporites of the sedimentary cover. This mixing of two distinct brines with comparable salinity is recorded during the growth of individual quartz crystals containing small galena inclusions, demonstrating the transient and episodic nature of fluid mixing during mineral deposition.

INTRODUCTION

Na-Ca–rich basement brines are widespread in the crystalline continental crust (Frape and Fritz, 1987). Although their mode of formation and the source of their salinity are still debated, they are increasingly recognized as a major agent in the formation of many world-class hydrothermal ore deposit types, including sediment-hosted and vein-type Pb-Zn deposits (Gleeson et al., 2001; Muchez et al., 2005; Leach et al., 2010; Wilkinson, 2010), shale-hosted Cu deposits (Koziy et al., 2009), and unconformity-related U deposits (Derome et al., 2007; Boiron et al., 2010; Richard et al., 2012). Prominent examples where basement brines have been invoked as the major transporter of ore metals are the Irish-type Pb-Zn deposits (Russell et al., 1981; Wilkinson, 2010), the Cu deposits of the Central African copper belt, and the Kupferschiefer in Europe (Muchez et al., 2005; Koziy et al., 2009). Evidence for the diverse origins of basement brines and their role in ore deposit formation comes from geological relations and radiogenic isotope studies that were able to conclusively trace metal sources to basement rocks (Dixon et al., 1990; Goldhaber et al., 1995), and from fluid inclusion analysis for conservative components like halogen ratios (Banks et al., 2000) and stable isotope studies (Stoffell et al., 2008; Wilkinson, 2010). Fluid inclusion data demonstrate the presence of unusually metal-rich saline brines that record a high-temperature origin, compatible with fluid-rock interaction in the crystalline basement underlying the sedimentary basins that host the ore deposits (Wilkinson et al., 2009; Richard et al., 2012).

The hot chloride-rich brines are able to transport high concentrations of Pb, Zn, and Cu, to thousands of µg/g (Wilkinson et al., 2009), from the crystalline basement to shallow crustal levels, due to the enhanced stability of metal chloride complexes at elevated temperatures (Yardley, 2005). The formation of major sediment-hosted ore deposits also requires substantial fluid focusing and a mechanism that efficiently supplies reduced sulfur, which is essential for precipitating sulfide ore minerals (Goldhaber et al., 1995; Wilkinson et al., 2005; Leach et al., 2010). Fluid mixing between metal-rich basement brines and reduced sulfur-bearing sedimentary formation waters has been suggested as the most efficient process for Pb-Zn ore mineral precipitation. Evidence for fluid mixing comes from fluid inclusion data and bulk halogen systematics (Derome et al., 2007; Stoffell et al., 2008; Boiron et al., 2010), stable isotope geochemistry (Goldhaber et al., 1995), and paleohydrological modeling (Plumlee et al., 1994; Garven et al., 1999). Despite considerable advances in understanding the chemistry of base metal ore fluids and the physical and chemical processes that control their formation (Stoffell et al., 2008; Wilkinson et al., 2009), some discrepancy remains with regard to the hydrological efficiency of fluid mixing compared to its expected effectiveness on geochemical grounds (Appold and Garven, 2000). Thus, while many studies infer the importance of mixing processes for the formation of ore deposits on basinal or district scales, direct evidence on the scale of individual ore veins that could potentially resolve this discrepancy is lacking.

Here we report the results of a fluid inclusion study of basement-hosted Pb-Zn veins from the Schwarzwald in southwestern Germany that reconstructs the fluid sources based on a combination of detailed textural analysis of fluid inclusion assemblages and laser ablation–inductively coupled plasma–mass spectrometry (LA-ICPMS) microanalysis of the fluid composition. Reflecting recent advances in analytical techniques (Seo et al., 2011), it was possible to measure ore metal (Pb, Zn, Ag, As, Sb) and halogen (Cl, Br) concentrations simultaneously in the same fluid inclusions. This revealed clear correlations between Cl/Br ratios and total metal content at the scale of single growth zones in quartz crystals, providing the first direct evidence for fluid mixing processes at the scale of individually trapped fluid pulses.

Pb-Zn VEIN MINERALIZATION IN THE VARISCAN BASEMENT

Post-Variscan Mesozoic vein-type Pb-Zn mineralization is widespread in large parts of western and central Europe, including Variscan basement complexes of Germany, France, England, and Spain (Muchez et al., 2005). Typical examples of Pb-Zn-fluorite-barite veins that form part of a long-lived crustal-scale hydrothermal system are exposed in the crystalline basement of the Schwarzwald, Germany (Fig. 1). The Schwarzwald forms part of the European Variscan orogen, comprising Paleozoic gneiss complexes crosscut by syntectonic to late tectonic Variscan granitoids (Hann and Zedler, 2008). The crystalline basement is unconformably overlain by Permian and Lower Triassic redbed sedimentary rocks and Middle Triassic to Jurassic carbonates with intercalated claystones and evaporites. Comparable sedimentary rocks underlain by Variscan basement are host to major Mississippi Valley–type Pb-Zn deposits in Upper Silesia, Poland (Muchez et al., 2005). Large-scale extensional tectonics that commenced in the Tertiary resulted in the formation of the Upper Rhine Graben rift zone. Rifting caused exhumation of the crystalline basement and erosion of the post-Variscan sedimentary cover rocks. The Schwarzwald hosts ~1000 known hydrothermal veins, which are mostly confined to basement rocks and rarely extend into the overlying sediments. The veins occurring throughout the district have been classified into several groups based on age and metal inventory, the most common type being Mesozoic

GEOLOGY, June 2013; v. 41; no. 6; p. 679–682; Data Repository item 2013187 | doi:10.1130/G34092.1 | Published online 16 April 2013

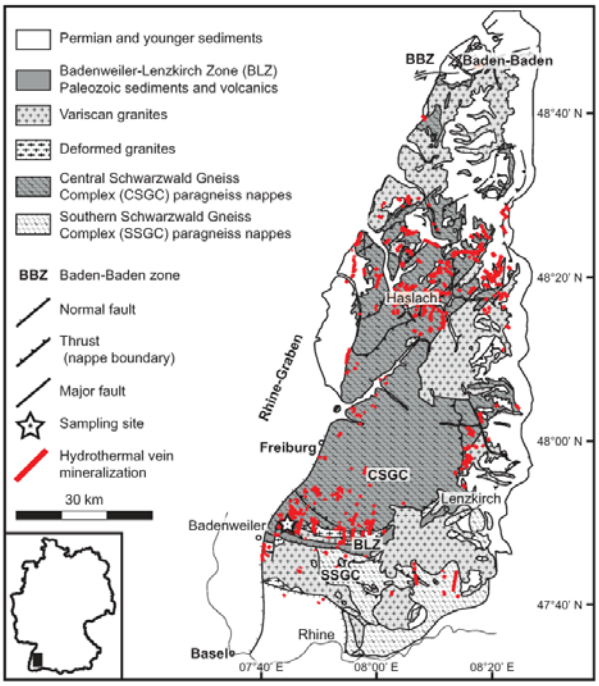

Figure 1. Geological map of Schwarzwald hydrothermal system (southwestern Germany) showing location of studied quartz-barite-fluorite-Pb-Zn vein mineralization (modified after Hann and Zedler, 2008).

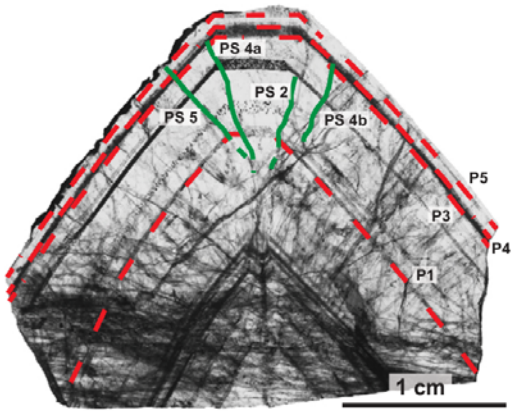

Figure 2. Fluid inclusion chronology in growth-zoned chevron quartz crystal. Growth zones hosting primary (P) fluid inclusions and pseudosecondary (PS) fluid inclusion trails are highlighted by dashed red lines and solid green lines, respectively.

quartz-fluorite-barite veins with Pb-Zn-Cu, Fe-Mn, or U-Bi-Ag-Co-Ni ore mineralization (Staude et al., 2009). The paleohydrological setting at the basement-cover interface makes the large-scale hydrothermal system of the Schwarzwald an ideal natural laboratory for investigating the interaction between basement-derived fluids and formation waters.

ANALYTICAL TECHNIQUES

Representative samples of quartz-barite-fluorite-Pb-Zn mineralization were selected for detailed texturally resolved fluid inclusion studies. The samples originate from a 10-m-thick cluster of hydrothermal veins north of the town Bad Sulzburg (southwestern Schwarzwald; Fig. 1). Massive barite veins are crosscut by hematite-bearing quartz veins, with euhedral chevron quartz crystals (to 5 cm in size) occurring inside open cavities. The crystals show pronounced growth zoning (Fig. 2) and several generations of well-preserved fluid inclusion assemblages. Galena inclusions occur along growth zones inside the quartz, whereas fluorite overgrows quartz and represents the latest hydrothermal mineral in this vein system.

Microthermometry was performed using a Linkam THMSG-600 cooling-heating stage, which was calibrated against synthetic fluid inclusion standards. LA-ICPMS microanalysis of individual fluid inclusions was performed with a Perkin Elmer Elan 6100 quadrupole ICPMS connected to a GeoLas 193 nm ArF excimer laser system. Analytical procedures were given by Heinrich et al. (2003) and Seo et al. (2011). LA-ICPMS analyses were done with two different element suites, the first containing 22 elements (Li, Na, K, Rb, Cs, Mg, Ca, Sr, Ba, B, Fe, Mn, Zn, Pb, Ag, Tl, As, Sb, S, Cl, Br, and Si). The second one was optimized for high-precision analysis of Cl/Br ratios and contained only 9 elements (Na, Ca, Fe, Mn, Zn, Pb, Cl, Br, and Si). The external standardization was based on Na concentrations calculated from microthermometric data using the model system H_2O-NaCl-$CaCl_2$ (Steele-MacInnis et al., 2011). Data reduction was carried out using the SILLS (Signal Integration for Laboratory Laser Systems) software package (Guillong et al., 2008).

MAJOR ELEMENT CHEMISTRY OF FLUID INCLUSIONS

The vein quartz samples show well-developed growth zoning with fluid inclusions trapped on each major growth surface (Fig. 2) and on trails that crosscut some growth zones, allowing a complete reconstruction of the relative timing of sequentially trapped fluid inclusion assemblages. The fluid inclusion assemblages situated on one growth zone or one pseudosecondary trail were taken as coeval and then grouped as primary (P) and pseudosecondary (PS) assemblage groups (Fig. 2), with increasing numbers denoting younger age. All fluid inclusions are aqueous two phase (liquid-vapor) with a vapor bubble size of ~5 vol%, and contain both ice and hydrohalite after freezing. Sequential freezing and low heating rates of 0.2 °C/min were used to account for sluggish dissolution behavior of hydrohalite, which invariably melts a few degrees before ice upon heating. Figure 3 shows the bulk composition of 174 fluid inclusions in the H_2O-NaCl-$CaCl_2$ phase diagram. The data are remarkably consistent for fluid inclusion assemblages trapped on individual growth zones and pseudosecondary inclusion trails. Total salinities are fairly constant at 23 wt% (NaCl + $CaCl_2$), whereas Na/Ca ratios vary. This variation is based on differences in hydrohalite melting temperature of ~4 °C, well outside the analytical uncertainty (0.5 °C). Homogenization temperatures are fairly constant throughout all fluid inclusion assemblages and are in the range of 130–160 °C.

TRACE ELEMENT GEOCHEMISTRY OF FLUID INCLUSIONS

Microanalysis with LA-ICPMS was carried out on fluid inclusions of at least 25 µm to ensure low detection limits and acceptable counting statistics for trace ore metals and Br. We conducted 70 successful measurements on inclusions from all assemblage groups with the full element suite and 28 with the reduced element suite. The microthermometric and concentration data for all elements analyzed are available in Table DR1 in the GSA Data Repository[1]. Figure DR1 (in the Data Repository) contains two representative LA-ICPMS signals of fluid inclusions and the

[1]GSA Data Repository item 2013187, Table DR1 (microthermometric and concentration data) and Figure DR1 (representative LA-ICPMS signals of fluid inclusions and adjacent host quartz), is available online at www.geosociety.org/pubs/ft2013.htm, or on request from editing@geosociety.org or Documents Secretary, GSA, P.O. Box 9140, Boulder, CO 80301, USA.

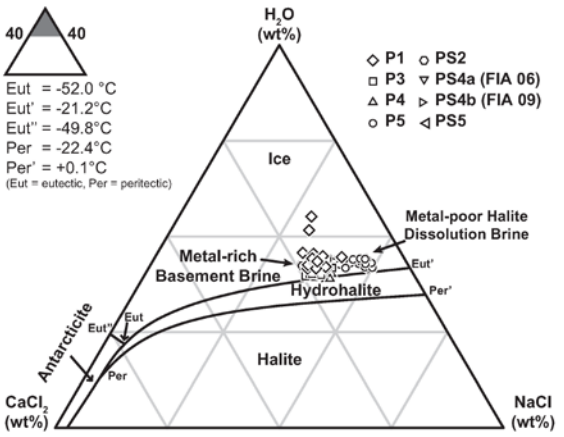

Figure 3. Fluid composition in ternary H_2O-NaCl-$CaCl_2$ system as determined by microthermometry, showing close overlap of two brine end members in terms of their major element composition. P—primary; PS—pseudosecondary; FIA—fluid inclusion assemblage.

adjacent host quartz. The LA-ICPMS data show that Zn, Pb, and Mn are the most important ore metals, with concentrations in the ranges of 10–770, 10–340, and 10–1650 µg/g, respectively. Sulfur concentrations were measured, but due to low signal to background ratios the analytical uncertainties are large, resulting in unsystematic variations in the range of 50–900 µg/g. Figure 4A shows Na/Ca ratios determined from microthermometry as a function of the concentration of Pb + Zn. Because accurate determination of Ca concentrations with LA-ICPMS is affected by mass interferences (Heinrich et al., 2003), we accepted the microthermometric data as the best estimate for the Na/Ca ratios. Combining the major and trace element data shows important correlations. The Na/Ca ratios are negatively correlated with the concentrations of Pb + Zn (Fig. 4A). Furthermore, the mass-based Cl/Br ratios show a distinct negative correlation with the concentration of Pb + Zn (Fig. 4B), whereas the Pb/Zn ratios are remarkably constant for all individual fluid inclusions and fluid inclusion assemblages regardless of their relative age (Fig. 4C).

The 1σ errors of measurements (relative standard deviation of element signals) with the full element suite are sometimes large for inclusions with high Cl/Br ratios, reflecting low absolute Br concentrations close to the detection limits. By contrast, the precision in Cl/Br ratios obtained with the reduced element suite is considerably better and the observed correlations are statistically significant.

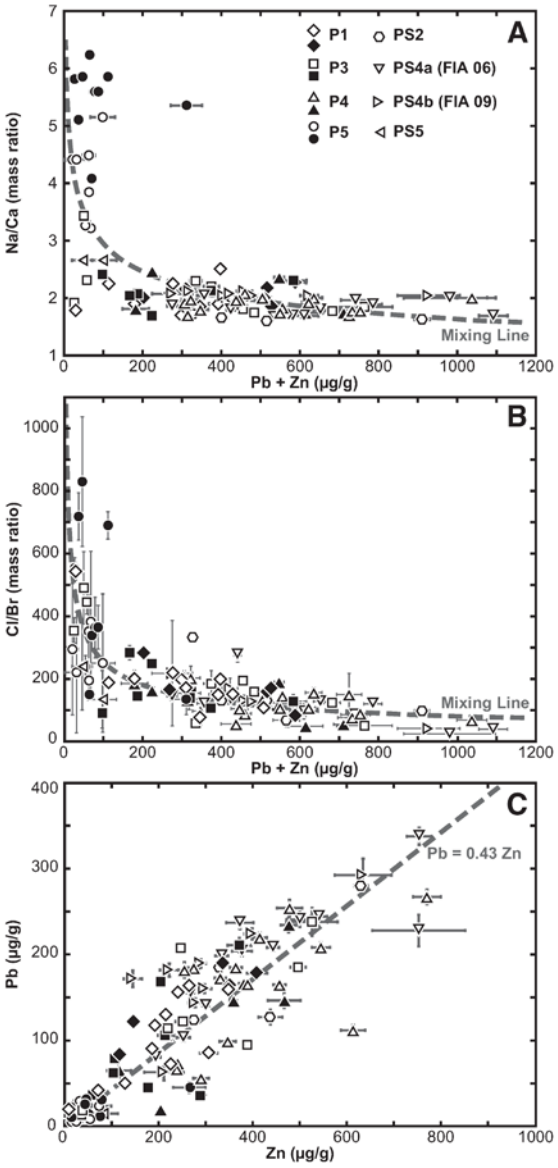

Figure 4. A: Microanalysis of single fluid inclusions shows close correlation between total base metal content (Pb + Zn) and Ca/Na ratio. P—primary; PS—pseudosecondary; FIA—fluid inclusion assemblage. B: Close correlation between Pb + Zn and Cl/Br ratio, resulting from mixing of two brines with similar total salinity (Fig. 3). C: Major variation of total metal content at constant Pb/Zn ratio reflects mixing of metal-bearing brine with metal-depleted fluid. Open and filled symbols denote analyses performed with full and reduced element suite, respectively.

DISCUSSION AND CONCLUSIONS

The fluid inclusion data show Cl/Br ratios between 80 and 780 that are negatively correlated with the ore metal concentrations. Low Cl/Br ratios (80–100) are typical of basement-derived brines that originated as residual brines after extensive evaporation of seawater, whereas high Cl/Br ratios above that of seawater (290) can be attained via halite dissolution when fluids percolate through evaporitic sequences (Frape and Fritz, 1987; Banks et al., 2000). The ore metal concentrations (Pb + Zn) are negatively correlated with the Cl/Br and Na/Ca ratios, both at the scale of different growth zones and within the same growth zone of individual quartz crystals. The data are best explained by fluid mixing processes that involve a metal-rich basement brine with low Cl/Br ratio and a metal-depleted halite dissolution brine with much higher Cl/Br ratio derived from evaporite-bearing Triassic sedimentary rocks. Elevated Ca concentrations in the latter are most likely related to Na-Ca exchange reactions along the flow path through the uppermost parts of the basement. The constant Pb/Zn ratios (Fig. 4C) support this interpretation, because crustal fluids typically show a linear correlation between both metals, which is controlled by sulfide saturation in the source aquifers and fluid salinity (Yardley, 2005). Dilution of a metal-bearing basement brine via mixing with a metal-depleted fluid would result in greater variation in the absolute concentrations of Pb and Zn without changing their ratio. The bulk salinity does not show large variations, suggesting that fluid mixing involved

two brines of very similar bulk properties but different Na/Ca ratios. This observation is in agreement with fluid inclusion data from post-Variscan basement-hosted vein mineralization (Staude et al., 2012) and the Soultz-sous-Forêts geothermal site in the Upper Rhine Graben, where brine inclusions with highly variable Cl/Br ratios were interpreted to record fluid mixing between a basement brine and formation water formed via halite dissolution (Boiron et al., 2010). The compositional variability we observe at the scale of individual growth zones and fluid inclusion trails suggests that the quartz crystals have trapped fluids that were not compositionally homogeneous and that fluid mixing processes are transient and can occur at a small scale. This supports earlier observations from unconformity-related ore deposits (U deposits in Canada, Australia, and Africa, and fluorite-barite-Pb-Zn mineralization in France), where variations in bulk salinity and homogenization temperatures of fluid inclusions trapped on individual microfractures were interpreted in terms of small-scale fluid mixing processes (Boiron et al., 2010).

In conclusion, our data clearly demonstrate that fluid mixing between a metal-bearing basement brine and a metal-depleted halite dissolution brine was responsible for formation of quartz-barite-fluorite-Pb-Zn vein mineralization. The data also show that geochemical signatures indicative of fluid mixing processes can be easily overlooked in conventional fluid inclusion data and bulk fluid analysis, and may require single-inclusion microanalytical data in order to be detected.

ACKNOWLEDGMENTS

This project was made possible by funding from the German Research Foundation (DFG), grant WA 1526/6-1. We thank Bruce Yardley, Antonin Richard, an anonymous reviewer, and William Collins for constructive comments.

REFERENCES CITED

Appold, M.S., and Garven, G., 2000, Reactive flow models of ore formation in the Southeast Missouri District: Economic Geology and the Bulletin of the Society of Economic Geologists, v. 95, p. 1605–1626, doi:10.2113/gsecongeo.95.8.1605.

Banks, D.A., Green, R., Cliff, R.A., and Yardley, B.W.D., 2000, Chlorine isotopes in fluid inclusions: Determination of the origins of salinity in magmatic fluids: Geochimica et Cosmochimica Acta, v. 64, p. 1785–1789, doi:10.1016/S0016-7037(99)00407-X.

Boiron, M.C., Cathelineau, M., and Richard, A., 2010, Fluid flows and metal deposition near basement/cover unconformity: Lessons and analogies from Pb-Zn-F-Ba systems for the understanding of Proterozoic U deposits: Geofluids, v. 10, p. 270–292, doi:10.1111/j.1468-8123.2010.00289.x.

Derome, D., Cathelineau, M., Fabre, C., Boiron, M.C., Banks, D., Lhomme, T., and Cuney, M., 2007, Paleo-fluid composition determined from individual fluid inclusions by Raman and LIBS: Application to mid-Proterozoic evaporitic Na-Ca brines (Alligator Rivers Uranium Field, northern territories Australia): Chemical Geology, v. 237, p. 240–254, doi:10.1016/j.chemgeo.2006.10.015.

Dixon, P.R., LeHuray, A.P., and Rye, D.M., 1990, Basement geology and tectonic evolution of Ireland as deduced from Pb isotopes: Geological Society of London Journal, v. 147, p. 121–132, doi:10.1144/gsjgs.147.1.0121.

Frape, S.K., and Fritz, P., 1987, Geochemical trends for groundwaters from the Canadian Shield, *in* Fritz, P., and Frape, S.K., eds., Saline water and gases in crystalline rocks: Geological Association of Canada Special Paper 33, p. 19–38.

Garven, G., Appold, M.S., Toptygina, V.I., and Hazlett, T.J., 1999, Hydrogeologic modeling of the genesis of carbonate-hosted lead-zinc ores: Hydrogeology Journal, v. 7, p. 108–126, doi:10.1007/s100400050183.

Gleeson, S.A., Wilkinson, J.A., Stewart, F.M., and Banks, D.A., 2001, The origin and evolution of base metal mineralising brines and hydrothermal fluids, south Cornwall, UK: Geochimica et Cosmochimica Acta, v. 65, p. 2067–2079, doi:10.1016/S0016-7037(01)00579-8.

Goldhaber, M.B., Church, S.E., Doe, B.R., Aleinikoff, J.N., Brannon, J.C., Podosek, F.A., Mosier, E.L., Taylor, C.D., and Gent, C.A., 1995, Lead and sulfur isotope investigation of Paleozoic sedimentary rocks from the southern midcontinent of the United States; implications for paleohydrology and ore genesis of the Southeast Missouri lead belts: Economic Geology and the Bulletin of the Society of Economic Geologists, v. 90, p. 1875–1910, doi:10.2113/gsecongeo.90.7.1875.

Guillong, M., Meier, D., Allan, M., Heinrich, C.A., and Yardley, B., 2008, SILLS: A MATLAB-based program for the reduction of laser ablation ICP-MS data of homogeneous materials and inclusions, *in* Sylvester, P., ed., Laser ablation ICP-MS in the Earth sciences: Current practices and outstanding issues: Mineralogical Association of Canada Short Course 40, p. 328–333.

Hann, H.P., and Zedler, H., 2008, Variscan Internides: Black Forest (Schwarzwald), *in* McCann, T., ed., The geology of Central Europe, Variscan tectonics, Volume 1: Precambrian and Palaeozoic: London, Geological Society of London, p. 599–665.

Heinrich, C.A., Pettke, T., Halter, W.E., Aigner-Torres, M., Audétat, A., Gunther, D., Hattendorf, B., Bleiner, D., Guillong, M., and Horn, I., 2003, Quantitative multi-element analysis of minerals, fluid and melt inclusions by laser-ablation inductively-coupled-plasma mass-spectrometry: Geochimica et Cosmochimica Acta, v. 67, p. 3473–3497, doi:10.1016/S0016-7037(03)00084-X.

Koziy, L., Bull, S., Large, R., and Selley, D., 2009, Salt as a fluid driver, and basement as a metal source, for stratiform sediment-hosted copper deposits: Geology, v. 37, p. 1107–1110, doi:10.1130/G30380A.1.

Leach, D.L., Bradley, D.C., Huston, D., Pisarevsky, S.A., Taylor, R.D., and Gardoll, S.J., 2010, Sediment-hosted lead-zinc deposits in Earth history: Economic Geology and the Bulletin of the Society of Economic Geologists, v. 105, p. 593–625, doi:10.2113/gsecongeo.105.3.593.

Muchez, P., Heijlen, W., Banks, D., Blundell, D., Boni, M., and Grandia, F., 2005, Extensional tectonics and the timing and formation of basin-hosted deposits in Europe: Ore Geology Reviews, v. 27, p. 241–267, doi:10.1016/j.oregeorev.2005.07.013.

Plumlee, G.S., Leach, D.L., Hofstra, A.H., Landis, G.P., Rowan, E.L., and Viets, J.G., 1994, Chemical reaction path modeling of ore deposition in Mississippi Valley-type Pb-Zn deposits of the Ozark region, U.S. Midcontinent: Economic Geology and the Bulletin of the Society of Economic Geologists, v. 89, p. 1361–1383, doi:10.2113/gsecongeo.89.6.1361.

Richard, A., Rozsypal, C., Mercadier, J., Banks, D.A., Cuney, M., Boiron, M.C., and Cathelineau, M., 2012, Giant uranium deposits formed from exceptionally uranium-rich acidic brines: Nature Geoscience, v. 5, p. 142–146, doi:10.1038/ngeo1338.

Russell, M.J., Solomon, M., and Walshe, J.L., 1981, The genesis of sediment-hosted exhalative zinc + lead deposits: Mineralium Deposita, v. 16, p. 113–127, doi:10.1007/BF00206458.

Seo, J.H., Guillong, M., Aerts, M., Zajacz, Z., and Heinrich, C.A., 2011, Microanalysis of S, Cl, and Br in fluid inclusions by LA-ICP-MS: Chemical Geology, v. 284, p. 35–44, doi:10.1016/j.chemgeo.2011.02.003.

Staude, S., Bons, P.D., and Markl, G., 2009, Hydrothermal vein formation by extension-driven dewatering of the middle crust: An example from SW Germany: Earth and Planetary Science Letters, v. 286, p. 387–395, doi:10.1016/j.epsl.2009.07.012.

Staude, S., Werner, W., Mordhorst, T., Wemmer, K., Jacob, D., and Markl, G., 2012, Multi-stage Ag-Bi-Co-Ni-U and Cu-Bi vein mineralization at Wittichen, Schwarzwald, SW Germany: Geological setting, ore mineralogy, and fluid evolution: Mineralium Deposita, v. 47, p. 251–276, doi:10.1007/s00126-011-0365-4.

Steele-MacInnis, M., Bodnar, R.J., and Naden, J., 2011, Numerical model to determine the composition of H_2O-NaCl-$CaCl_2$ fluid inclusions based on microthermometric and microanalytical data: Geochimica et Cosmochimica Acta, v. 75, p. 21–40, doi:10.1016/j.gca.2010.10.002.

Stoffell, B., Appold, M.S., Wilkinson, J.J., McClean, N.A., and Jeffries, T.E., 2008, Geochemistry and evolution of Mississippi Valley-type mineralizing brines from the Tri-State and northern Arkansas districts determined by LA-ICP-MS microanalysis of fluid inclusions: Economic Geology and the Bulletin of the Society of Economic Geologists, v. 103, p. 1411–1435, doi:10.2113/gsecongeo.103.7.1411.

Wilkinson, J.J., 2010, A review of fluid inclusion constraints on mineralization in the Irish ore field and implications for the genesis of sediment-hosted Zn-Pb deposits: Economic Geology, v. 105, p. 417–442, doi:10.2113/gsecongeo.105.2.417.

Wilkinson, J.J., Everett, C.E., Boyce, A.J., Gleeson, S.A., and Rye, D.M., 2005, Intracratonic crustal seawater circulation and the genesis of subseafloor zinc-lead mineralization in the Irish orefield: Geology, v. 33, p. 805–808, doi:10.1130/G21740.1.

Wilkinson, J.J., Stoffell, B., Wilkinson, C.C., Jeffries, T.E., and Appold, M.S., 2009, Anomalously metal-rich fluids form hydrothermal ore deposits: Science, v. 323, p. 764–767, doi:10.1126/science.1164436.

Yardley, B.W.D., 2005, Metal concentrations in crustal fluids and their relationship to ore formation: Economic Geology and the Bulletin of the Society of Economic Geologists, v. 100, p. 613–632.

Manuscript received 2 October 2012
Revised manuscript received 8 January 2013
Manuscript accepted 20 January 2013

Printed in USA

Table DR1. Summary of fluid inclusion concentration data (Sulzburg).

FIA	FI	Li (µg/g)	Na (µg/g)	K (µg/g)	Rb (µg/g)	Cs (µg/g)	Mg (µg/g)	Ca (µg/g)	Sr (µg/g)	Ba (µg/g)	B (µg/g)	Fe (µg/g)	Mn (µg/g)	Zn (µg/g)	Pb (µg/g)	Ag (µg/g)	Tl (µg/g)	As (µg/g)	Sb (µg/g)	S (µg/g)	Cl (LA) (µg/g)	Br (µg/g)	Cl (MT) (µg/g)	Tm (ice) (°C)	Tm (HH) (°C)	Th (tot.) (°C)	Inclusion size (µm)
P1	1	270	55080	2760	30	50	410	33000	1230	80	40	50	70	230	70	0.4	3	140	7.4	300	133800	570	142300	-22.1	-24.6		100
	2	290	55080	4390	30	60	350	38800	1140	170	80	<20	230	240	160	0.4	3.3	90	5.4	190	151400	760	144700	-22.8	-24.7		50
	3	260	56650	3550	30	60	350	25800	790	100	100		250	310	90	<0.2	1.9	10	<1		96700	650	140800	-21.7	-24.3		60
	4	340	56650	3920	40	50	290	17800	550	100	70	<15	340	270	160	0.2	3.9	140	25	920	97500	650	138500	-21.1	-24.2		70
	5	230	48390	2560	20	50	150	26900	930	50	30	<20	60	130	50	0.5	2.6	70	18	460	126100	630	119700	-16.6	-24.3		75
	6	510	60220	3880	60	80	500	32000	1030	90	90	160	200	190	120	0.1	3.7	300	11	120	147600	960	142600	-22.1	-24.0		50
	7	380	58380	4480	60	90	320	24300	940	190	50	<10	190	190	90	0.1	3.6	70	18	70	128700	590	136200	-20.5	-23.9		30
	8	440	56380	2260	20	80	10	29500	1040	60	30	30	20	70	40		1.9	40	16	150	126900	680	136200	-20.5	-23.9		30
	9	350	52180	6150	90	90	590	25200	900	140	80	70	410	350	160	0.4	4.2	180	12		116000	1070	126800	-18.2	-24.2		50
	10	540	55930	4830	50	70	470	36900	1290	110	50		10	10	20	0.5	3.6	60	6.1	90	130600	240	142000	-22.0	-24.5		75
	11	750	50330	3360	50	50	430	26900	990	60	50	<45	290	220	130	0.5	3	120	13		90800	1180	125900	-18.0	-24.4		75
	12		60650					27700				<15	300	350	160						140500	880	141900	-23.9	-21.9	143	70
	13		62100					22800				<55	640	410	180						130900	1570	143200	-23.8	-22.2	147	30
	14		55660					31400				100	470	340	190						101700	600	138100	-24.3	-21.0	133	40
	15		58020					24000				120	150	120	80						120500	430	139800	-24.1	-21.4	141	35
	16		46650					26500				110	80	150	120						93100	560	110800	-24.0	-14.6	100	55
Average		400	55650	3830	44	66	350	28090	980	100	60	90	210	220	110	0.3	3.2	110	13	290	120800	750	135594	-21.6	-23.0	133	
SD		150	4360	1130	21	16	180	5350	210	45	24	45	160	110	53	0.2	0.8	80	6	290	19520	310	9711	2.4	2.6	19	
P3	1	410	58370	6060	60	40	500	11800	470	40	40	110	10	40	10	<0.1	2.4	10	<0.2		98800	200	136000	-20.3	-23.1		100
	2	230	61190	1370	20	70	460	39200	1660	250	30		200	220	110	<0.2	3.5	50	1.5		122300	2100	144100	-22.4	-23.9		50
	3	300	59550	3820	60	70	150	27600	1040	160	60	<32	140	250	120	<0.2	2.5	<1	8		152000	820	115200	-15.6	-24.0		75
	4	280	57870	3210	40	70	1690	31000	800	270	70	170	520	250	210	0.4	3	110	24.7	330	105000	540	146100	-23.1	-24.5		30
	5	<4	56370	8550	130	100	1640	30100	890	130	130	400	710	500	190	1.4	4.8	170	<0.8		129600	1040	143400	-22.4	-24.5		40
	6	580	56100	3470	30	70	830	29300	900	130	50	20	260	390	90	0.3	3	110	47.3		132700	830	143700	22.5	24.6		50
	7	<14	59230	4720	90	90	850	23500	900	70	60	<240	150	530	240		4.4	80	<5.4		147400	2920	148500	-23.7	-24.4		90
	8	350	57620	1390	10	30	20	10500	540	40	10	<21	10	10	20	0.2	1.2	10	41.8		118800	340	142300	-22.1	-24.3		95
	9	440	60140	5480	50	40	730	16200	650	10	20	20	30	40	20	0.3	2	0	<0.1		112600	250	139100	-21.2	-23.9		90
	10		62530					23800				<45	290	370	210						121400	940	143500	23.8	22.3	149	25
	11		56350					36500				<8	50	180	50						129800	520	145000	-24.6	-22.8	130	50
	12		58650					31500				<25	100	290	40						127600	800	146200	-24.4	-23.6	128	50
	13		59880					33100				30	320	210	110						146200	1050	150000	-24.4	-24.1	134	30
	14		61010					15600				40	30	50	40						129800	1410	136000	-23.7	-20.9	154	60
	15		61510					31400				40	120	110	80						134500	930	146400	-24.1	-23.1	140	65
	16		62440					29400				30	180	210	170						121900	1150	147200	-24.0	-23.3	151	60
	17		62080					19100				40	140	100	60						120300	420	149500	-24.1	-23.6	141	40
Average		370	59470	4230	54	64	780	26860	870	120	52	90	190	220	100	0.5	3.0	68	25	330	126450	960	142659	22.7	23.6	141	
SD		120	2140	2290	37	24	580	8540	350	93	35	120	190	160	75	0.5	1.1	67	20		14120	590	8070	2.2	1.0	10	
P4	1	170	57060	1670	30	70	320	28800	730	100	60	<55	60	610	110		3.9	90	6.4		106200	710	146300	-23.2	-24.6		50
	2	340	58700	1500	30	90	130	34200	920	170	60	20	310	390	170	0.7	3.5	170	54.2	150	134200	920	146300	-23.1	-24.4		45
	3	260	57040	3460	40	90	430	26300	870	160	60		30	290	60		2.6	10	19.1		115000	1190	146600	-23.2	-24.5		60
	4	400	57040	950	10	70	210	31300	1030	100	50	<11	90	240	70	0.5	2.6	30	33.8	170	103100	780	146300	-23.2	-24.6		70
	5	340	60450	950	20	80	<0.3	33200	1100	300	40	<29	220	420	220	0.8	4	170	46.4	70	145100	930	146900	-23.2	-24.2		100
	6	490	59380	4510	60	100	350	26700	840	220	50	<15	160	460	170	0.5	5.4	90	16.7		141400	1310	146400	-23.1	-24.3		35
	7	1610	59980		810	220	1510	57500	1610	320	20	110	820	770	270	<0.4	37.8	350	<1.4		174000	2550	145700	-22.9	-24.2		50
	8	510	59980	2630	40	100	530	28100	900	80	40	70	160	330	170		3.2	70	11.5		138700	1050	145700	-22.9	-24.2		65
	9	400	60480	1700	20	30	220	22500	790	100	10	10	30	240	70	0.6	3.2	20	20.2	190	95100	460	149300	-23.9	-24.3		50
	10	<3	61180	2970	30	40	1540	25600	570	30	30		170	220	110	<0.2	1.6	80	9.5		120200	590	149500	-23.9	-24.2		60
	11	590	58740	2510	50	30	470	31500	800	110	<3	<32	480	450	250	1.3	4.9	90			147900	1940	149300	-23.9	-24.5		70
	12	560	58740	2180	50	60	480	24900	710	170	40	140	160	550	210	1.9	4.9	90	24.8		148800	1680	149300	-23.9	-24.5		60
	13	340	60890	750	20	70	2	26000	1070	190	40	<41	110	280	180	1.1	3.6	160	76.9		150800	1690	145800	-22.9	-24.1		30
	14	1600	58450	4180	60	80	1510	42600	1460	360	80	1110	390	350	190	16	4.6	240	72.5		156800	1460	149700	-24.0	-24.6		40
	15	880	59690	2760	50	80	630	30300	1150	50	70	<100	70	350	100	<0.3	3.8	30	<1.2		164500	1570	145900	-23.0	-24.2		30
	16	410	56830	2290	20	50	230	17500	530	80	60		290	260	180		2.3	180	50.8		109200	1950	146500	-23.1	-24.3		30
	17		60230					35300				<5	10	200	20						140400	860	146400	-23.7	-23.0	142	30
	18		56700					32700					500	480	230						115500	2120	144100	-24.5	-22.6	149	65
	19		65620					23200				170	230	380	170						133900	710	149500	-23.8	-23.8	140	70
	20		57480					32900					1000	470	160						177800	3650	146000	-24.6	-23.1	151	50
	21		58200					13100				<85	40	120	70						125200	980	145700	-24.5	-23.0	138	45
	22		59600					23300				230	310	360	150						107800	870	142800	-24.2	-22.7	150	45
Average		590	59570	6790	84	79	570	29430	940	160	50	230	260	380	150	2.8	5.7	120	34	150	134160	1350	146818	-23.6	-24.0	145	
SD		440	2310	17850	190	44	520	8900	290	91	19	360	260	150	67	5.7	8.6	97	24	50	23320	760	1856	0.6	0.7	6	

FIA	FI	Li (µg/g)	Na (µg/g)	K (µg/g)	Rb (µg/g)	Cs (µg/g)	Mg (µg/g)	Ca (µg/g)	Sr (µg/g)	Ba (µg/g)	B (µg/g)	Fe (µg/g)	Mn (µg/g)	Zn (µg/g)	Pb (µg/g)	Ag (µg/g)	Tl (µg/g)	As (µg/g)	Sb (µg/g)	S (µg/g)	Cl (LA) (µg/g)	Br (µg/g)	Cl (MT) (µg/g)	Tm (ice) (°C)	Tm (HH) (°C)	Th (tot.) (°C)	Inclusion size (µm)
P5	1	490	67670	3730	30	50	220	20900	330	40	50		<2	40	30	<0.2	3.9	<1.5	33		128900	340	140600	-21.4	-23.2		40
	2	420	68060	2190	30	30	110	14000	580	50	0	<28	20	40	20		2.1	10	56.3		153600	640	142100	-21.8	-23.2		50
	3	<7	72430	3000	20	30	120	16600	690	90	20	<48	30	30	30	<0.3	1.8	<1.7	64.1		139900	400	140400	-21.3	-22.7		45
	4	560	68660	5790	60	40	220	12500	350	80	<6	<74	20	60	10	<0.5	1.5	20			154700	790	137700	-20.7	-22.9		55
	5	380	70940	4480	40	30	190	15900	620	50	20		<10	20	10		1.1	10	8.4		95100	320	138000	-20.7	-22.7		35
	6	1020	72130	9370	80	40	370	21200	930	70	<9		<15	30	10	<0.9		10			110900	500	140300	-21.3	-22.7		30
	7	980	71140	240	30		<4	14400	820	40	60	<122	40	70	20	<0.9	5.5				107600	430	137500	-20.6	-22.5		35
	8		78550					13000				<29	20	50	10						134000	890	142400	-22.3	-21.7	109	55
	9		74210					11100				120	20	80	10						162800	450	136900	-22.5	-20.4	175	40
	10		75360					17500				<191	<15	270	50						130100	960	140100	-22.5	-21.2		40
	11		78030					12800				<29	10	30	10						148400	180	137200	-22.4	-20.5	160	45
	12		78030					11700				160	<5	50	30						131000	360	144000	-22.5	-22.1	152	25
	13		74440					12600				510	30	80	30						147000	210	136300	-22.4	-20.3	153	75
	14		70090					14900				<50	40	50	30						133200	390	137500	-22.8	-20.6	160	45
	15		75830					11700				<17	10	20	20						149600	210	142200	-22.5	-21.7	128	50
	16		75320					9500				<8	<1	20	10						141900	260	138100	-22.3	-20.7	175	35
Average		640	73180	4110	41	37	210	14390	620	60	30	260	24	59	21		2.7	13	40		135540	460	139456	-21.9	-21.8	152	
SD		280	3580	2910	21	8	94	3330	220	20	24	210	11	60	12		1.7	5	25		18470	240	2359	0.8	1.1	23	
PS2	1	280	54910	8020	110	110	810	32200	1120	200	90	60	470	630	280	0.7	6	350	11.3		123700	1260	143400	-22.4	-24.8		40
	2	360	54940	7970	110	90	470	33200	1200	160	100	10	130	290	40	0.5	3.8	50	3.6	160	149700	450	140500	-21.6	-24.6		90
	3	260	54870	6800	80	90	550	27800	840	90	80	20	160	280	120	0.3	3	50	8.6		109500	840	142300	-22.1	-24.7		50
	4	310	54510	5230	80	90	760	21400	970	120	110	<11	610	330	190	0.6	6.2	390	31.3	50	115300	880	143400	-22.4	-24.8		50
	5	250	55080	8210	120	90	270	22800	970		<7		60	440	130		5.4			890	125200	1840	142000	-22.0	-24.6		40
Average		290	54860	7250	100	94	570	27480	1020	140	100	30	290	390	150	0.5	4.9	210	14	370	124680	1050	142320	-22.1	-24.7		
SD		44	210	1260	19	9	220	5340	140	48	13	26	240	150	89	0.2	1.4	190	12	460	15380	520	1199	0.3	0.1		
PS4a	1	300	57190	4280	60	50	210	11300	590	50	40		140	190	80		3.5	60	<0.7		121500	830	142800	-22.2	-24.4		30
	2	260	57030	7460	90	90	90	23100	860	160	70		90	300	140		3.2	100	81.5	170	118100	430	142400	-22.1	-24.4		60
	3	430	54370	7980	80	90	590	28500	930	190	50		130	330	200		5	20	5		125900	1190	141800	-22.0	-24.7		80
	4	200	56680	6420	70	80	300	24700	870	180	80		490	500	240		3.6	240	13.6		161600	1880	138800	-21.1	-24.3		65
	5	330	56710	6930	80	80	820	29500	910	260	90		550	540	240		4.2	350	29.2		127000	1060	140900	-21.7	-24.4		40
	6	<41	57600	6350	100	150	2460	60200	1360	650	90		1470	750	230			440	275.4		160800	6530	140000	-21.4	-24.2		50
	7	200	58370	2070	60	90	350	22000	610	130	50	90	190	250	100	0.9	3.5	120	<0.5		118500	970	140800	-21.6	-24.2		35
	8	240	56310	5780	60	70	90	12200	510	80	40	<23	260	270	160		3.3	30	11		88100	650	142700	-22.2	-24.5		55
	9	300	54370	10010	90	100	660	24700	850	160	90	120	390	440	210	0.9	4	180	16.5	140	126900	990	142700	-22.0	-24.7		70
	10	390	54820	7590	150	110	230	22600	750	130	200	<33	1650	750	340	1.5	10.8	590	17		146200	3700	142300	-22.1	-24.7		75
	11	310	54890	5690	70	60	560	17900	730	140	50		480	370	240	1.8	3.4	150	<2.4		110900	1150	142500	-22.1	-24.7		70
	12	310	54590	5690	80	70	480	22600	770	150	60	<48	390	380	200	<0.3	3.6	180	4.3		112400	930	141700	-21.9	-24.7		45
Average		300	56080	6350	83	87	570	24940	810	190	76	110	520	420	200	1.3	4.4	210	50	160	126490	1690	141617	-21.9	-24.5		
SD		72	1400	1980	25	26	640	12420	220	150	44	21	510	180	71	0.5	2.2	170	88	15	21050	1740	1257	0.3	0.2		
PS4b	1	260	58620	5370	80	80	460	22400	760	110	40	<38	170	220	180		5.6	50			123900	910	141400	-21.8	-24.2		50
	2	260	59350	8480	100	90	460	28300	1080	180	80		530	300	160	<0.3	3.4	210	<1.8		127400	970	141300	-21.8	-24.1		45
	3	320	58210	8190	90	90	400	29000	1060	150	70	70	320	290	190	0.6	3.4	140	19		122400	950	140400	-21.5	-24.2		50
	4	400	61190	9560	130	100	840	37800	1020	150	140		380	630	290	<1.2	9.8	260	60.8		144800	3480	140800	-21.6	-24.2		75
	5	330	58730	7660	90	90	770	28300	1010	130	80	<44	500	280	140	1	2.8	180	11.5		115300	680	140900	-21.7	-24.1		35
	6	250	58730	7040	70	100	830	25600	1040	220	50	<128	100	210	60	<1		40			133600	610	140900	-21.7	-24.1		30
	7	230	59350	3030	20	80	20	18300	760	110	20	<92	70	150	170		3.5	90	257.5		114100	740	141300	-21.8	-24.1		70
	8	300	58370	9640	130	80	420	35300	1530	220	10	<17	60	400	220	1.5	5.9	20	4.7		152400	1470	140800	-21.6	-24.2		30
Average		290	59070	7370	89	89	530	28130	1030	160	61	70	270	310	180	1.0	4.9	120	71		129240	1230	140975	-21.7	-24.1		
SD		56	950	2230	35	8	280	6340	240	44	41		190	150	66	0.5	2.5	88	110		13630	950	337	0.1	0.0		
PS5	1	430	62410	6250	20	50	50	10800	130		80	200	60	30	10	<0.5		40	166.2		138100	580	138000	-20.9	-23.6		75
	2	250	62410	4370	40	40	120	12500	420		<12	<218	70	80	10	<1.1	2.8	10	62.5		119600	890	138000	-20.9	-23.6		60
Average		340	62410	5310	30	45	85	11650	280		80	200	65	55	10		2.8	25	110		128850	740	138000	-20.9	-23.6		
SD		130	0	1330	14	7	49	1200	210				7	35	0			21	73		13080	220	0	0.0	0.0		

1sigma errors (calculated with SILLS data reduction software)

FIA	FI	Li (µg/g)	Na (µg/g)	K (µg/g)	Rb (µg/g)	Cs (µg/g)	Mg (µg/g)	Ca (µg/g)	Sr (µg/g)	Ba (µg/g)	B (µg/g)	Fe (µg/g)	Mn (µg/g)	Zn (µg/g)	Pb (µg/g)	Ag (µg/g)	Tl (µg/g)	As (µg/g)	Sb (µg/g)	S (µg/g)	Cl (LA) (µg/g)	Br (µg/g)	Inclusion size (µm)
P1	1	5.8	40	10	0.7	0.6	3.7	170	3.8	2.5	2.2	6.5	1.2	3.8	1.1	0.06	0.2	1.9	0.7	20	870	20	100
	2	10	70	50	1.5	1.5	6.9	390	7.6	7.9	7		4.1	7.9	3.3	0.2	0.4	3.3	1.4	70	2100	60	50
	3	30	150	100	2.8	3	10	670	10	10	10	40	8.5	20	5.1		0.7	3.2		140	3600	130	60
	4	10	70	40	1.4	1.3	6.4	290	5.2	5.8	5.5		4.5	7.8	3	0.1	0.4	3.7	1.8	50	1600	50	70
	5	9.1	60	40	1	1.2	4.2	300	6.3	3.6	4.7		2.3	5	1.7	0.1	0.3	2.6	1.7	60	1700	50	75
	6	7.5	50	20	1.4	1.3	5.4	250	5.5	4.4	3.6	10	2.4	5.3	2.1	0.07	0.4	3.9	0.9	20	1200	30	50
	7	6.4	50	30	1.6	1.5	4.9	250	5.7	6.9	3.1		2.6	5.7	2	0.08	0.4	2.2	1	30	1200	30	30
	8	7.4	50	20	1.1	1.5	1.9	270	6.5	4.3	2.7	8.5	1.3	4.1	1.5	0.09	0.3	1.6	1	20	1300	30	30
	9	20	90	60	3.2	2.5	10	480	9.8	9.7	7.7	40	6.5	10	4.7	0.2	0.7	5.8	2.4		2300	70	50
	10	4.6	30	10	0.9	0.8	4	180	4.2	3.1	2.1	4.5	0.5	1	0.6	0.06	0.2	1.2	0.4	10	770	10	75
	11	20	60	60	1.7	1.2	7	450	6.4	5.2	4.8		4.4	8.5	2.8	0.1	0.4	3.4	2.5	90	1800	70	75
	12		60					330					3.9	8.6	2.9						1200	20	70
	13		140					970					10	20	6.1						3000	70	30
	14		70					310				20	2.8	8.7	3.6						1200	20	40
	15		60					390				30	3	6.5	2.2						1300	30	35
	16		80					480				30	3.6	8.2	3.6						1600	30	55
P3	1	10	70	30	2.3	1.5	8.7	280	5.7	4.6	5	20	2	4.3	1.2		0.4	1.4			1700	40	100
	2	30	90	40	1.6	2.1	9.1	530	10	10	6	20	5.1	10	4.1		0.6	3.4	2.1		2300	80	50
	3	20	100	100	2.9	2.5	6.8	690	10	10	8.6		8.2	20	4.5		0.7		3.5		3600	170	75
	4	10	50	20	1.1	1.2	10	260	4.6	6.9	3.5	10	3.5	5.6	2.7	0.09	0.3	2.4	2	30	1000	30	30
	5		90	70	4	2.8	20	620	9.6	10	10	50	9.2	20	5.2	0.4	0.7	6.6			2800	100	40
	6	7.5	30	10	0.6	0.8	4.4	150	3	3	2	6.4	1.7	4.3	1.2	0.05	0.2	1.5	1.3		700	20	50
	7		260	340	9.4	7.2	40	2000	20	20	20		30	50	20	1.1	1.6	20		570	10800	530	90
	8	10	50	20	0.7	0.8	1.1	180	4	3.1	1.5		1.6	2.3	0.8	0.1	0.2	1.1	2.7	40	1200	30	95
	9	7.5	50	20	1.3	0.9	6.9	180	4.4	1.4	2.2	7.1	1.1	2.4	0.9	0.07	0.3	0.6			1100	20	90
	10		160					1200					10	30	8.4						4300	120	25
	11		30					170					1	3.9	1.2						610	10	50
	12		60					520					4.9	9.4	3.5						2200	60	50
	13		100					520				20	5.5	10	4.1						1900	30	30
	14		70					320				20	2.3	4.1	1.5						1400	30	60
	15		50					250				10	2	4	1.7						910	10	65
	16		70					380				20	3.5	7.2	3.6						1400	30	60
	17		90					430				30	4.3	7.4	2.5						1700	30	40
P4	1	60	150	140	2.7	3.3	10	970	10	10	20		10	30	6.4	0.5	1.1	9.7	7		4500	290	50
	2	7.8	40	10	0.7	1	2.4	190	3.9	4.6	3	6.7	2.4	5.7	1.9	0.08	0.2	2.5	1.3	10	980	30	45
	3	10	140	210	3	3.2	20	820	10	10	20	80	6.3	20	3.7	0.3	0.7	4.5	3.1		5600	490	60
	4	5.8	50	20	0.6	1	4.2	230	4.4	3.6	3.5		1.6	4.8	1.5	0.09	0.2	1.3	1	40	1200	50	70
	5	30	90	50	1.7	2.4		530	10	20	5.8		5.6	20	5.7	0.3	0.7	6.3	4.8	70	2500	80	100
	6	20	70	40	2.2	2.2	7.4	380	8.2	10	5.4		4.8	10	3.8	0.2	0.6	3.7	2.1		2000	60	35
	7	70	140	190	10	5.9	30	1100	20	20	10	80	20	30	8.7		2.8	10		190	4500	170	50
	8	20	80	50	2.1	2.4	10	410	8.4	7.3	5.2	30	4.4	10	4.2	0.2	0.5	3.7	2.7		2200	70	65
	9	10	60	30	1.2	1	5.4	250	5.7	5.8	3	20	2.5	7.3	2	0.1	0.3	1.5	1.6	40	1300	40	50
	10		140	60	3.1	2.9	40	810	10	20	8.8	30	8.3	20	6.3		0.7	6.5	6.9	90	3300	100	60
	11	50	150	80	4.5	4	20	900	20	20			10	30	9.7	0.5	1.2	8.5	6.4		4400	130	70
	12	40	100	70	2.7	2.6	10	550	9.6	10	7.4	40	6.4	20	5.9	0.4	0.9	5.4	5.1	120	3200	130	60
	13	30	80	70	1.3	2	1	460	9.2	10	5.3		3.6	10	4.4	0.3	0.6	5	4.2		2500	100	30
	14	40	80	50	2.6	2.3	20	560	10	10	7.3	60	6.4	10	4.8	1	0.7	6.4	4.5		2400	90	40
	15	30	100	130	2.6	2.6	10	750	10	7.4	9.3		9.1	20	4.1		0.7	4.9			4100	190	30
	16	60	180	200	4.6	4.4	20	1100	20	20	20	160	20	30	9.1	0.7	1.1	10	7.4		6200	320	30
	17		40					190					0.6	4.1	0.7						660	10	30
	18		100					570				2400	8.4	20	8.5						2200	60	65
	19		60					340				30	3.6	9.3	3						1300	30	70
	20		190					1900				220	20	30	8.7						6500	150	50
	21		290					1800					10	30	8						6100	120	45
	22		50					230				20	2.9	7.4	2.2						840	10	45

FIA	FI	Li (µg/g)	Na (µg/g)	K (µg/g)	Rb (µg/g)	Cs (µg/g)	Mg (µg/g)	Ca (µg/g)	Sr (µg/g)	Ba (µg/g)	B (µg/g)	Fe (µg/g)	Mn (µg/g)	Zn (µg/g)	Pb (µg/g)	Ag (µg/g)	Tl (µg/g)	As (µg/g)	Sb (µg/g)	S (µg/g)	Cl (LA) (µg/g)	Br (µg/g)	Inclusion size (µm)
P5	1	20	160	90	2.9	2.7	10	570	8.5	7.2	10	40		6.5	2.8		0.9		3.3	120	3700	190	40
	2	20	90	70	1.8	1.5	4.9	420	7.3	5.5	4.9		2.3	6.8	1.7	0.2	0.5	2.9	7.9	90	2500	80	50
	3		150	120	2.8	2.3	8.5	840	10	10	10		4.2	10	3.3		0.7		20		4000	140	45
	4	40	130	90	3.8	2.6	10	1100	9.2	8.7			4.5	9.8	3		0.7	4.5	7.1	140	3500	110	55
	5	60	210	170	4.9	3.2	10	1000	20	10	20			10	2.3		0.9	5.7	10	270	4800	210	35
	6	90	280	350	10	4.8	50	1900	30	20		230		30	3.7		1.4	8.4	20		8300	400	30
	7	150	330	300	10	4.9		1700	30	20	30		20	30	6		2.1	10	30		7900	350	35
	8		90					400					2.3	4	1.1						1500	40	55
	9		120					580				50	4.3	8.1	1.5						2700	80	40
	10		270					2700						30	6						8400	290	40
	11		100					360					2.6	4.2	1.2						1800	40	45
	12		190					980				90		9.5	3.5						4100	80	25
	13		60					200				20	1.4	3.6	1.1						980	10	75
	14		70					450					4	4	1.2						1800	40	45
	15		80					250					1.7	2.2	1.2						1400	20	50
	16		60					170						1.9	0.7						1000	10	35
PS2	1	10	80	50	3	2.3	10	430	9	10	8.3	20	6.3	10	5	0.2	0.7	7.2	2		2100	80	40
	2	4.4	40	20	1.3	0.9	4	170	4	3.8	3.3	4.9	1.4	4.4	0.9	0.07	0.2	1.2	0.4	20	950	20	90
	3	9.5	80	50	2.7	2.2	10	390	8.4	7.4	8	30	4.3	10	3.5	0.1	0.5	3.6	2.2	60	2000	70	50
	4	7.4	60	40	1.8	1.5	8.2	260	5.7	5.6	6.3		4.7	7.4	2.9	0.1	0.5	5.3	1.4	60	1500	70	50
	5	20	170	190	5.9	3.9	20	800	20	60		410	7.6	30	8.6	0.5	1.2	10	8.4	320	5700	470	40
PS4a	1	10	70	50	2.3	1.6	6.1	330	6.3	5.3	4.2		3.4	10	2.8		0.5	3.3			2000	80	30
	2	4.7	40	30	1.8	1.3	2.3	210	4.8	5.5	3.2		1.6	6.7	2.3		0.3	2.4	3	30	1100	30	60
	3	20	90	50	3.3	2.7	10	490	9.8	10	5.1		3.7	10	5.5		0.8	2.5	2.3	60	2300	70	80
	4	20	130	120	4.6	3.8	20	940	20	20	10		10	30	8.7		1	9.3	3.5	160	4300	170	65
	5	30	80	60	3.2	2.4	10	550	10	10	6.8		7.5	20	5.4		0.7	8.3	5.1		2200	80	40
	6		230	600	10	8.7	60	4600	30	50	40	360	40	100	20	2.4	3.3	30	90	880	16400	900	50
	7	10	90	60	2.9	2.9	9.8	480	8.7	10	6.1	30	5.1	10	4.4	0.3	0.7	5.5		70	2400	80	35
	8	6.6	50	40	1.7	1.4	2.9	230	4.5	4.9	3.5		3.5	7.6	2.8	0.08	0.4	1.6	2.3	50	1300	50	55
	9	9.6	70	50	2.6	2.3	9.9	360	7.5	8.7	6.6	20	5.4	10	4.4	0.2	0.5	5	3.5	60	1900	60	70
	10	20	120	80	5.7	3.9	9.3	690	10	10	20		20	30	10	0.5	1.4	20	2.7	120	3800	150	75
	11	40	120	150	4.6	3.5	20	1200	10	10	10	110	10	30	7.7	0.7	0.8	10			4800	240	70
	12	30	100	70	3.9	2.9	20	680	10	20	10		10	20	6		0.6	7.3	1.3	120	2700	100	45
PS4b	1	20	130	110	4.7	3.6	10	710	10	10	8.1		7.3	20	7.6	0.5	1.3	7.4	4.7	120	3700	130	50
	2	10	90	100	4.2	2.7	10	600	10	10	8.1	40	8.2	10	5.1		0.7	8.4		110	2800	110	45
	3	10	80	50	3	2.3	9	440	9.4	9.7	6.8	30	5.7	10	4.8	0.3	0.6	5.1	1.9		2100	60	50
	4	70	270	350	10	8.3	40	2600	30	30	30	240	30	60	20		2.8	20	30	710	11600	630	75
	5	20	100	70	3.7	2.8	20	610	10	10	9.9		9.7	10	5	0.4	0.6	7.3	4.4	130	2700	110	35
	6	50	280	270	10	8.7	40	1900	30	40	30		20	40	9.6		2.3	10	10		9600	430	30
	7	30	180	150	3.3	4.8	5.5	950	20	20	8.5		10	20	9.7	0.6	1.2	9.5	10		5200	220	70
	8	10	100	60	4.4	3.3	10	650	10	10	4.1		3.7	20	6.5	0.3	0.9	3	1.2	90	3000	80	30
PS5	1	30	260	220	5.1	5.5	10	1200	10	9.4	20	150	10	20	3.8		2.3	8.3	10		7900	300	75
	2	30	240	380	6.4	4.9	10	1900	20	10			20	30	4.7		1.4	10	10		10900	530	60

Figure DR1

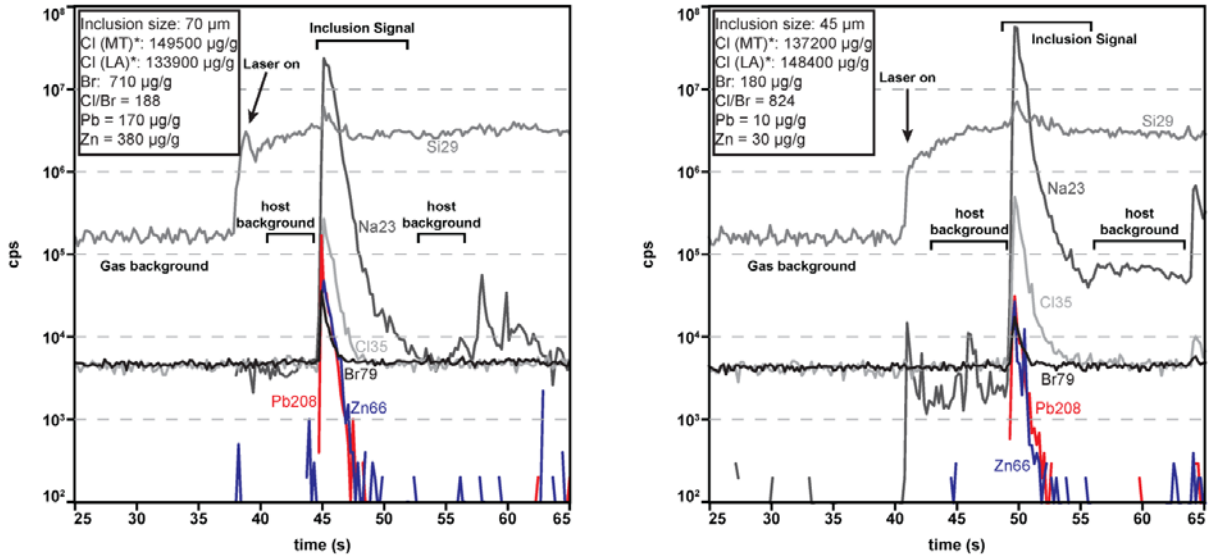

*Cl(MT) refers to Cl concentration as determined by microthermometry, Cl(LA) is Cl concentration as determined by LA-ICPMS

Appendix 2

Evolution of unconformity-related Mn-Fe-As vein mineralization, Sailauf (Germany): Insight from major and trace elements in oxide and carbonate minerals

Authors

Tobias Fusswinkel, Thomas Wagner, Thomas Wenzel, Markus Wälle, Joachim Lorenz

Status

Published in *Ore Geology Reviews* v.50 (2013), p. 28-51

Associate Editor

Albert Gilg

Reviewer

Two anonymous reviewers

Contributions of the candidate

Scientific ideas	50 %
Data acquisition	90 %
Analysis and interpretation	60 %
Preparation of manuscript	70 %

Ore Geology Reviews 50 (2013) 28–51

Contents lists available at SciVerse ScienceDirect

Ore Geology Reviews

journal homepage: www.elsevier.com/locate/oregeorev

Evolution of unconformity-related Mn – Fe – As vein mineralization, Sailauf (Germany): Insight from major and trace elements in oxide and carbonate minerals

Tobias Fusswinkel [a,*], Thomas Wagner [b], Thomas Wenzel [a], Markus Wälle [b], Joachim Lorenz [c]

[a] Fachbereich Geowissenschaften, Eberhard Karls Universität Tübingen, Wilhelmstrasse 56, D-72074 Tübingen, Germany
[b] Institute of Geochemistry and Petrology, ETH Zurich, NW F 82.4, Clausiusstrasse 25, CH-8092 Zürich, Switzerland
[c] Graslitzer Strasse 5, D-63791 Karlstein am Main, Germany

ARTICLE INFO

Article history:
Received 4 January 2012
Received in revised form 26 June 2012
Accepted 14 August 2012
Available online 23 August 2012

Keywords:
Mn – Fe – As mineralization
LA-ICPMS
Trace elements
Mn oxides
Carbonates
REE geochemistry

ABSTRACT

The Sailauf Mn – Fe – As vein mineralization, located in the Spessart district (central Germany), is characterized by complex hydrothermal carbonate and oxide assemblages. The mineralization is hosted by a Permian rhyolite body and is structurally related to the Variscan unconformity that separates Permian sedimentary rocks from the underlying Variscan crystalline basement. The hydrothermal vein system has been studied by optical microscopy, electron-microprobe and LA-ICPMS analysis of major and trace elements (including the REE). Four distinct mineralization stages that are characterized by diagnostic carbonate-oxide assemblages are identified, which are (1) pre-ore stage, (2) ore stage 1, (3) ore stage 2, and (4) the replacement stage. Hydrothermal carbonates show complex compositional trends in Ca – Mn – (Fe + Mg) space, and comprise calcite, Mn-calcite, Fe – Mg calcite, Ca-rhodochrosite, and Ca-kutnahorite. Oxide assemblages are dominated by braunite and hematite, with minor amounts of manganite and hausmannite. The mineralization is enriched in a distinct suite of trace elements, including As, W, Pb, Zn and Cu. Analysis of the paragenetic evolution, in conjunction with the major and trace element data, allows to reconstruct the fluid evolution of the hydrothermal system. The first order change in mineralogy between the two main ore stages (Mn oxides and calcite evolving into hematite and Mn-rich calcite) records a pronounced shift in fluid pH and silica activity of the system. This interpretation is also supported by variations in the behavior of Ce in different carbonate generations. The late stage replacement carbonates relate to destabilization of the primary ore assemblages. The distinct geological setting immediately below the Permian unconformity, in conjunction with the mineralogical and chemical data, suggests that dynamic fluid mixing processes involving basement-derived brines and more shallow groundwaters were important in the formation of the Sailauf Mn – Fe – As mineralization. The significant enrichment in the As – W – Pb – Zn – Cu element suite resembles that of other Mn – Fe deposits, and points to felsic lithologies as the main metal source of the mineralization.

1. Introduction

Hydrothermal Mn – Fe oxide deposits represent a widespread mineralization style, which occurs in diverse geological settings and different depositional environments. The geological settings range from volcanogenic deposits at mid-ocean spreading centers to sedimentary–exhalative deposits in arc settings, and hot spring and hydrothermal vein type deposits, sometimes associated with epithermal base metal sulfide or Ag – Au mineralization (Hewett, 1964; Roy, 1981). In systems that are closely associated with volcanic rocks, boiling of fluids at greater depths has been invoked for sulfide precipitation, while the metal inventory that is associated with the Mn – Fe mineralization is then transported to shallower levels by the residual liquid phase (Hein et al., 2000). Hydrothermal vein deposits in marine settings are commonly interpreted as feeder zones for submarine–exhalative deposits (Hein et al., 2000). Irrespective of the large variability in geological settings in which these deposits occur, earlier studies have shown that consistent similarities in trace element enrichment (As – W – Pb – Zn – Cu) exist between sedimentary–exhalative and terrestrial deposits. These have been essentially related to interaction with felsic (and often volcanic) source rock lithologies (Glasby et al., 2005; Hewett, 1964; Holtstam and Mansfeld, 2001; Nicholson, 1992; Roy, 1981). The driving force for fluid convection and migration in most hydrothermal Mn – Fe deposits is considered to be an anomalously high heat flow due to volcanic activity (Roy, 1981).

Precipitation of ore minerals in Mn – Fe deposits is commonly linked to mixing of metal bearing hydrothermal brines with stagnant groundwaters or seawater, which typically results in the separation of Fe from Mn (Hewett, 1964; Roy, 1981). Both metals are highly soluble in

* Corresponding author.
E-mail address: tobias.fusswinkel@uni-tuebingen.de (T. Fusswinkel).

0169-1368/$ – see front matter © 2012 Elsevier B.V. All rights reserved.
http://dx.doi.org/10.1016/j.oregeorev.2012.08.001

aqueous brines in the divalent form due to formation of stable chloride complexes (Krauskopf, 1957), whereas oxidation leads to rapid precipitation of Fe and Mn oxide or oxyhydroxide minerals (Krauskopf, 1957; Roy, 1981). Because both elements show significant differences in their redox potential, the transition between the divalent and more oxidized forms will be crossed at different times along fluid evolution paths, resulting in spatial separation of Fe and Mn oxide minerals. Therefore, both metals are sensitive redox and pH indicators, making them ideally suited to reconstruct the depositional conditions and precipitation mechanisms of hydrothermal vein mineralization or of fluid controlled alteration processes affecting pre-existing Mn – Fe ore bodies (Gutzmer and Beukes, 1995; Jonsson and Broman, 2002). Many geologically old Mn – Fe ore deposits have been affected by metamorphic, diagenetic or supergene modification, obliterating much of the primary mineral assemblages that recorded the physicochemical properties of the primary mineralizing fluids (Brugger and Gieré, 2000; Glasby et al., 2005; Hein et al., 2000; Holtstam and Mansfeld, 2001; Leal et al., 2008).

The structurally controlled Mn – Fe – As vein mineralization at Sailauf (Spessart, central Germany) has recorded and preserved a complete sequence of changes in fluid chemistry in the mineral assemblages and trace element inventory. Multiple hydrothermal pulses with evolving pH and redox conditions have resulted in a complex but paragenetically and texturally well constrained assemblage of carbonates, Mn and Fe oxides, and As and W bearing mineral phases. The vein mineralization is hosted by a porphyritic subvolcanic rock body of rhyolitic composition (Hartkoppe rhyolite) of lower Permian age, and occurs as a set of five distinct veins immediately below the unconformity separating the Variscan crystalline basement and the overlying Permian to Triassic sedimentary rocks. A large number of other hydrothermal deposits were described in close proximity to Sailauf throughout the Spessart district, the formation of which was ascribed to fluid mixing processes controlled by the basement–cover interface (Okrusch et al., 2007; Wagner et al., 2010). On a larger scale, the formation of many other post Variscan vein mineralizations in central Europe has been related to the Variscan unconformity (Dill, 1988; Dill and Nielsen, 1987). The Sailauf mineralization, despite not being an economically viable ore deposit, provides an important window into the evolution of the fluid composition and depositional conditions during the protracted history of a high oxidation state hydrothermal system. The present study reports the results of a comprehensive mineralogical, major and trace element study of hydrothermal oxide and carbonate minerals. The data are used to reconstruct the evolution of the fluid composition, and to establish the first order factors that have controlled the mineral deposition processes.

2. Geological setting

The Spessart district (Fig. 1) is composed of two distinct geological units, which are the basement of the Spessart crystalline complex (SCC) and the Paleozoic to Mesozoic cover comprising sedimentary rocks of lower Permian (Rotliegend) to Triassic (Bunter Sandstone) age. The SCC is part of the Mid German Crystalline High, the internal zone of the central European Variscan orogen (Franke, 2000). The SCC consists of metamorphosed sedimentary rocks of Proterozoic, Cambro-Ordovician and Silurian ages, intercalated with amphibolites and orthogneisses (Okrusch and Weber, 1996). During the Variscan orogeny, peak metamorphism attained medium-pressure amphibolite grade conditions (Okrusch and Weber, 1996) and was accompanied by large scale compressional deformation. Rapid uplift and cooling occurred between 325 and 315 Ma (Nasir et al., 1991). During the Lower Permian, the crystalline complex was intruded by felsic magmas, forming several subvolcanic bodies that included the Hartkoppe rhyolite close to Sailauf. No radiometric age data are available for the Sailauf rhyolite, although indirect evidence for its minimum age comes from rhyolitic detritus found in Lower Permian red bed sedimentary rocks (Okrusch et al., 2011).

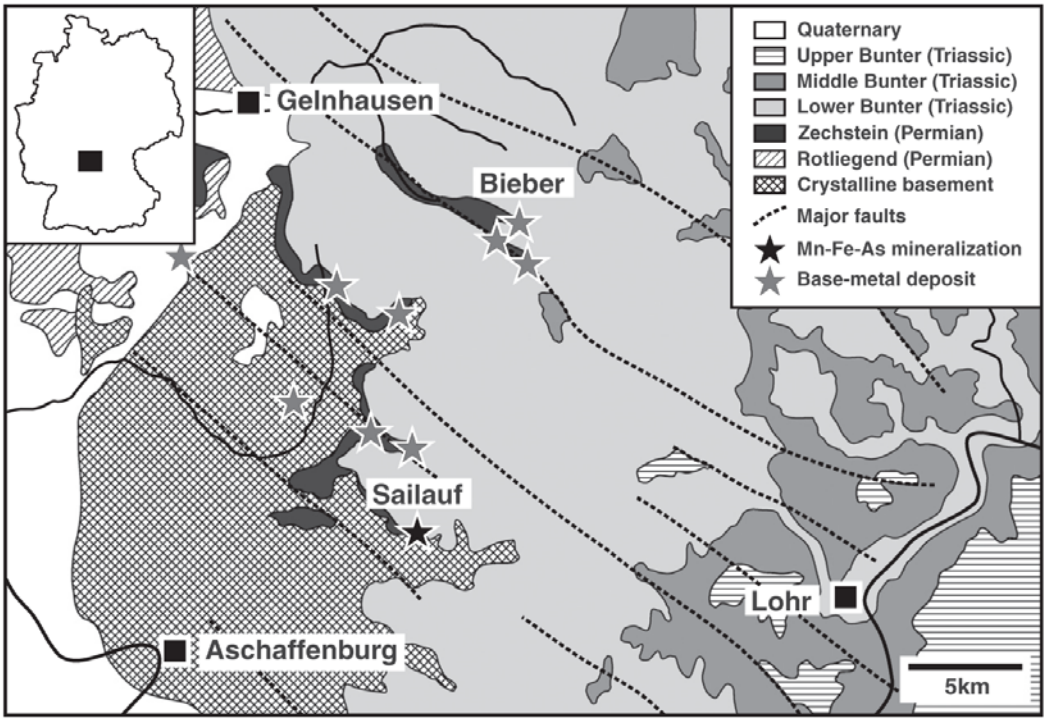

Fig. 1. Geological sketch map of the Spessart district, showing the location of base metal deposits and the Sailauf Mn – Fe – As mineralization. Modified after Okrusch et al. (2011).

The crystalline basement is unconformably overlain by red bed sedimentary rocks of the Rotliegend (Lower Permian), which are only locally preserved. These comprise conglomerates, sandstones and siltstones, which formed as erosion products of the Variscan mountain range. The red beds are overlain by sequences of the Upper Permian (Zechstein), which comprise (from bottom to top) basal manganiferous conglomerates and breccias, black shales (i.e. the Kupferschiefer), bituminous dolomites of the Werra cycle and clay and marlstones of the Leine and Aller cycles (Kading, 2005; Menning et al., 2005). The uppermost stratigraphic unit contains a well-defined claystone (Bröckelschiefer). The Zechstein is conformably overlain by continental sand- and siltstones, conglomerates and sandy mudstones of Triassic age, which constitute the Bunter Sandstone (Okrusch et al., 2011). Lower Middle Triassic limestones (Muschelkalk) represent the stratigraphically youngest unit preserved in the Spessart district, while the Middle Triassic to Upper Jurassic sedimentary rocks originally covering the area have been entirely eroded during regional uplift (Okrusch et al., 2011).

Basement and cover lithologies are crosscut by two major fault systems, a predominant system striking NW–SE and dipping steeply to the NE or SW, and a subordinate system striking NE–SW. Both fault systems were activated during post-Variscan extensional tectonics (Ziegler, 1987) and provided important fluid pathways, reflected by the frequent occurrence of barite–quartz mineralization (Wagner et al., 2010). Several types of hydrothermal base metal deposits, both structurally controlled and stratabound, occur throughout the Spessart district. Their formation has been related to fluid mixing processes at the basement–cover interface (Okrusch et al., 2007; Wagner et al., 2010), which explains the occurrence of all major deposits close to this first order structural feature (Fig. 1).

2.1. The Sailauf Mn – Fe – As mineralization

The vein-type Mn – Fe – As mineralization is hosted by a Lower Permian rhyolite body, which is exposed in a 50 m deep quarry at the Hartkoppe hill (Fig. 2). The rhyolite body has a size of approximately 400 m length and 200 m width. The basement-cover unconformity is exposed at the top of the quarry, where the crystalline basement and the rhyolite are overlain by sequences of Upper Permian Zechstein. The rhyolite is emplaced in a small slab of mica schists, which forms an intercalation in orthogneisses (Rotgneiss complex; Dombrowski et al., 1995). Parts of the rhyolite body display irregular (sub)-vertical to horizontal jointing, whereas other parts of the rhyolite form compact rock masses with well-developed flow textures. Both observations suggest a complex emplacement process, possibly during subvolcanic lava dome formation. The rhyolite is a compact, matrix dominated, mostly porphyritic rock containing phenocrysts of quartz and K-feldspar in a fine grained groundmass of purple-grayish color. Clay alteration and hematitization of the rhyolite is widespread, the latter resulting in the commonly pronounced red color. A striking feature of the Hartkoppe rhyolite is the abundance of dark grey crusts of native arsenic, uraninite and subordinate sulfides, reaching diameters of up to 25 cm (Lorenz, 1995). The crusts appear to be localized on otherwise unmineralized fracture planes where they form individual irregular round patches, sometimes surrounded by bleaching halos of up to 2 cm in size. The transition between the halo and the non-bleached rhyolite is remarkably sharp.

The massive rhyolite body is crosscut by five parallel, NW–SE striking fault systems, which host discontinuously mineralized hydrothermal veins with thicknesses ranging from about 1 to 25 cm (Fig. 3). The mineralized parts of the veins are numbered as A to E, from NE to SW (Fig. 2). Four distinct stages of hydrothermal mineralization can be distinguished macroscopically, the texturally earliest being dominated by celadonite, carbonates and minor hematite and fluorite. The subsequent assemblage composed of carbonates and Mn oxides such as braunite, hausmannite and manganite makes up the bulk of the mineralization, whereas a later generation of carbonate–hematite dominated vein fillings with minor fluorite and celadonite is less common. Brecciation of the host rock in the vicinity of the veins is widespread and often associated with a pronounced black color of rhyolite clasts incorporated into the breccia matrix. The black color is mainly due to impregnation with very fine-grained Mn oxides.

Previously published geochronologic data of different ore and gangue minerals yielded exclusively Mesozoic ages. Hautmann et al. (1999) carried out (U + Th) – He dating of braunite, hausmannite and hematite, as well as K – Ar dating of illite and celadonite. Braunite yielded ages of 157–158 Ma, whereas hematites were dated at 136–148 Ma. Hausmannites gave crystallization ages of approximately 130 Ma. Illite yielded K – Ar ages of 156–161 Ma, whereas different generations of celadonite gave a range in ages from 98 to 120 Ma.

3. Samples and methods

The mineralization was systematically documented and sampled by one of the authors (JL) since 1984, and a complete suite of samples representing all known mineralization types is available. The sample suite was further augmented by few additional samples collected on the present mining levels. A total number of 120 samples were studied petrographically, and Table 1 lists the samples that were selected for further electron-microprobe and LA-ICPMS analysis of major and trace elements.

3.1. Electron-microprobe analysis

The major element composition of carbonate minerals, braunite, hausmannite, manganite, hematite and arsenate minerals was determined with a JEOL JXA-8900RL instrument in Tübingen. Natural and synthetic standards were used for calibration. Carbonates, Mn ore minerals, hematite and arsenates were analyzed with specifically developed analytical protocols. The instrument settings, standard materials and integration times are summarized in Appendix A. For carbonate analysis, an overlap correction between the As – Lα and Mg – Kα lines was required. Overlaps between As – Lα and Fe – Kα were corrected in both carbonate and Mn mineral data. Element distribution maps of Si, As, Mn, and Ca were acquired at 20 kV acceleration voltage and 100 nA beam current. The samples were scanned with a pixel size of 0.5 µm and acquisition times of 100 ms on each pixel.

3.2. Trace element analysis with LA-ICPMS

LA-ICPMS analysis was performed at ETH Zurich with an excimer ArF laser ablation system operating at 193 nm wavelength (Geolas, ETH prototype), coupled to a Perkin Elmer Elan 6100 DRC quadrupole ICP mass spectrometer (Günther et al., 1997). Selected major and trace elements were analyzed in braunite, hausmannite and hematite, as well as in different carbonate generations. The REE concentrations in carbonates and hematite were determined separately with laser parameters specifically adjusted. Ablation was performed in polished thin and thick sections on mineral grains which had previously been analyzed by electron microprobe. Mn oxides and hematite were analyzed in standard polished thin sections, whereas for the carbonates 300 µm thick polished sections were used. Use of polished thick sections allowed to greatly improving the detection limits and standard errors for the REE, by increasing the laser repetition rate and maintaining ablation times of at least 60 s. Mn oxides and hematite were ablated with laser repetition rates of 5 Hz and laser spot sizes of 20 or 40 µm, depending on the grain size. Ablation spot sizes for carbonate analysis were varied between 40 and 115 µm, depending on grain size, although preferentially larger grains were analyzed. Repetition rates were increased to 10 Hz for carbonate analysis to improve counting rates. During some of the carbonate measurements, small amounts of H_2 were added to the carrier gas flow to increase the sensitivity of the instrument (Guillong and Heinrich, 2007).

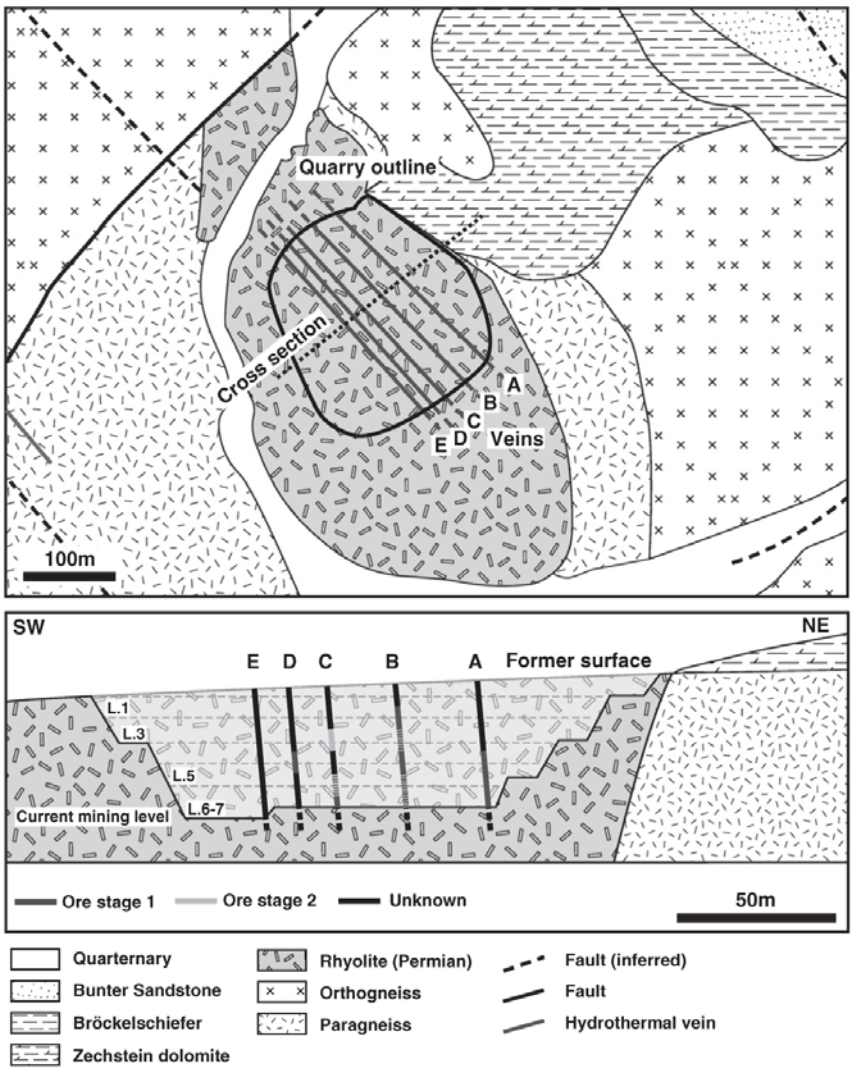

Fig. 2. Geological map showing the geological setting of the Sailauf quarry and the location of hydrothermal Mn–Fe–As veins and sulfide mineralization.

Data reduction was carried out with the SILLS software package (Guillong et al., 2008), using NIST SRM610 as the external standard. Internal standardization was based on the major element concentrations determined by electron microprobe. Mn oxides were internally standardized against MnO concentration, calcitic carbonates against CaO, whereas MnO concentrations were used to standardize Mn-rich carbonates. Hematite was standardized against Fe_2O_3 contents. During data reduction, a special treatment was necessary to address potential contamination of sample signals by inclusions of other minerals. When analyzing carbonate samples, carbonate phases with grossly differing chemistry were frequently intersected when laser ablation penetrated into deeper parts of the sections. This issue was particularly relevant in carbonate assemblages that display replacement features. Because all major elements of the carbonate minerals (Ca, Mg, Fe, Mn) were monitored during LA-ICPMS analysis, significant changes in composition could be clearly detected in the time-resolved signals. Appropriate selection of integration intervals would then ensure that only trace element signals from the phase exposed at the surface would be considered for data reduction and quantification.

4. Mineralogy and textures

The hydrothermal vein mineralization at Sailauf records a complex history of distinct pulses of ore deposition, brecciation, and superposed alteration and remobilization. In general, the vein mineralization in all five veins is very discontinuous along strike and dip, with zones extremely enriched in Mn oxide minerals or hematite alternating with almost barren vein sections within just a few meters. Based on crosscutting relationships and textural observations, four main hydrothermal stages can be distinguished, clearly separated by major vein opening and brecciation events. These stages are (1) the pre-ore stage, (2) ore stage 1, (3) ore stage 2, and (4) the alteration stage (Fig. 4). Hydrothermal carbonates constitute the most abundant gangue minerals in the Mn–Fe–As vein mineralization.

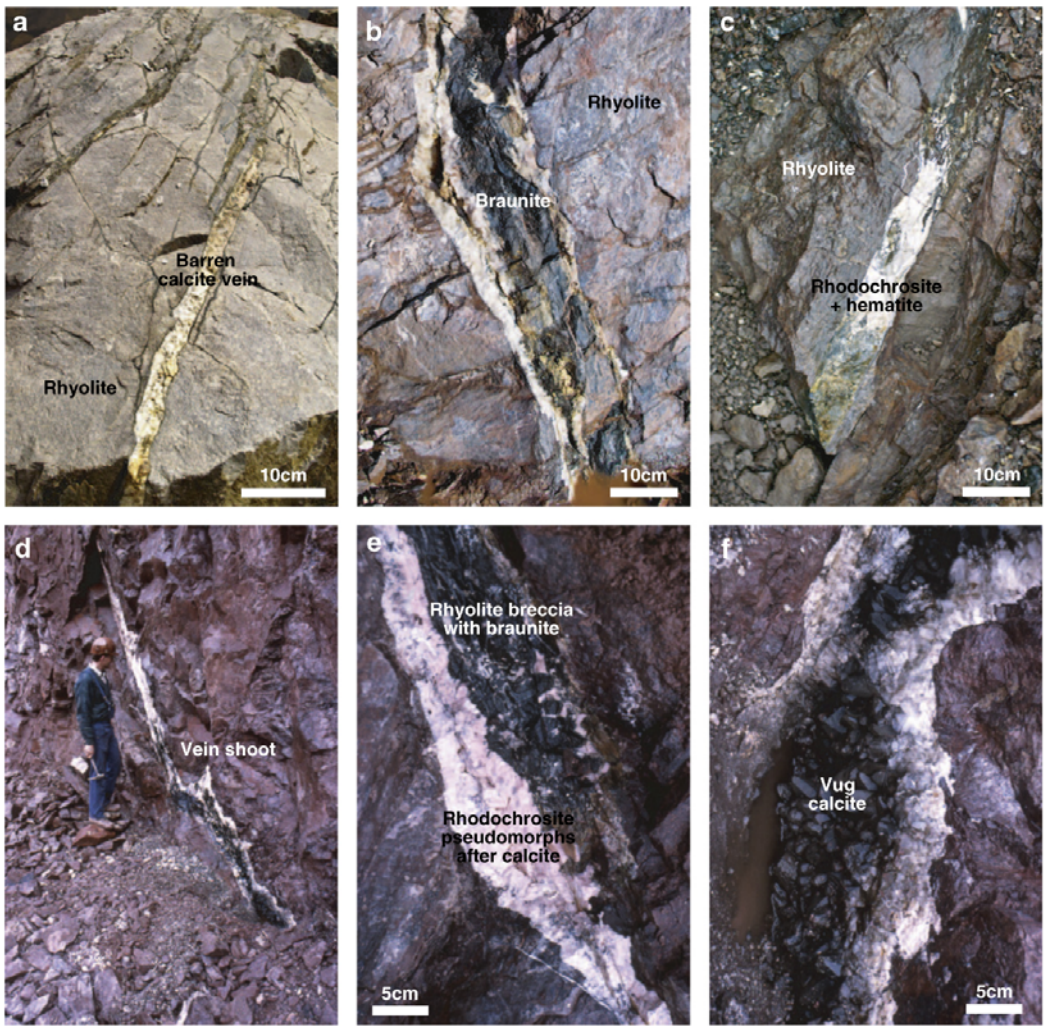

Fig. 3. Field relationships of Mn – Fe – As veins. (a) Set of barren calcite veins. (b) Multistage calcite–braunite vein, containing rhyolite clasts impregnated with braunite. Reopening of the vein resulted in formation of open fissures. (c) Rhodochrosite–hematite–celadonite vein mineralization. (d) Calcite–Mn-oxide vein shoot, with euhedral calcite crystals in open fissures covered by secondary Mn-oxides. (e) Pseudomorphic replacement of calcite crystals by rhodochrosite. Dark rhyolite clasts impregnated with braunite are overgrown by braunite cockade ore. (f) Vug filling calcite crystals with dispersed braunite.

They are characterized by substantial compositional variation in Ca – Mn – Fe – Mg space and can be classified into several distinct groups, each being related to a particular paragenetic stage. Discrimination of most carbonate types based on optical properties and textural features has not always been possible, and the textural classification of carbonate generations has been supported by chemical data obtained from EPMA analysis. A noteworthy feature of the Sailauf vein mineralization is the complete lack of sulfide minerals, which is in remarkable contrast to all other hydrothermal mineralization styles in the Spessart district. Subordinate sulfides only occur together with the patches of native Arsenic on otherwise unmineralized fracture planes. The latter represent an interesting mineral assemblage, but no clear relation to the vein mineralization could be established. Table 2 gives a summary of all mineral phases observed in the Sailauf mineralization, including those from hydrothermal veins and the native arsenic mineralization.

4.1. Primary hydrothermal assemblages

The paragenetic sequence of the vein mineralization is illustrated in Fig. 4. Following a first vein opening and brecciation event, the earliest recognizable mineralization (assigned to the pre-ore stage) comprises crusts of greenish celadonite with minor illite surrounding rhyolite clasts in breccia bodies (Fig. 5a, b). Larger cavities within the breccias are filled with Ca-rhodochrosite I (Fig. 5a), which occurs as lenticular, scaling shaped aggregates, and subordinate purple fluorite I, as well as pseudomorphs of late stage carbonates phases after lath-shape anhydrite crystals.

The first major ore mineralization (ore stage 1) comprises cockade ore, which is composed of braunite (braunite Ia), calcite, subordinate hausmannite Ia (Fig. 6a) and minor amounts of needle-shaped manganite and bixbyite. Coeval braunite impregnation has resulted in a distinct blackening of rhyolite clasts (Fig. 5d), although this feature

Table 1
Description of the investigated samples from the Sailauf Mn–As vein mineralization.

Sample	Vein	Location	Paragenesis/description
Sai-001	A	Level 5, center-NW	Celadonite cockade ore, vug filling fine grained Ca-rhodochrosite I. Minor fluorite and relicts of anhydrite laths.
Sai-002	A	Level 5, center-NW	Celadonite cockade ore, vug filling fine grained Ca-rhodochrosite I. Minor fluorite and relicts of anhydrite laths.
Sai-003	B	Level 5, NW	Braunite Ia cockade ores cementing clasts of blackened rhyolite. Larger vein filled by calcite I and braunite Ib. Small veinlet of Mn-calcite I and hematite crosscutting older vein.
Sai-004	B	Level 5, NW	Blackened rhyolite breccia clasts, seamed by braunite Ia cockade ores with some minor ore stage 1 hematite. Clasts cemented by barren calcite I. Thin veinlets of Ca-rhodochrosite III crosscut calcite I and breccia clasts.
Sai-005	B	Level 5, center	Braunite Ia cockade ores, larger vein filled by abundant braunite Ib, hausmannite Ib and calcite I. Calcite I strongly altered and partly replaced by fine grained Ca-rhodochrosite I.
Sai-006	B	Level 5, center	Braunite Ia cockade ores, larger vein filled by abundant braunite Ib, hausmannite Ib and calcite I. Calcite I strongly altered and partly replaced by fine grained Ca-rhodochrosite I.
Sai-007	B	Level 5, center-SE	Calcite I vein with subordinate braunite Ib. Calcite I is strongly altered by Mn-rich carbonates. Abundant relictic laths of anhydrite II filled by secondary carbonates and arsenates.
Sai-011	B	Level 5, center-SE	Barren calcite I mineralization, strongly altered by Mn-rich carbonates. In altered zones minor hematite Ib.
Sai-013	B	Level 5, center-NW	Barren calcite I mineralization, strongly altered by Mn-rich carbonates. Some hematite Ib occurs together with Mn-calcite I
Sai-014	B	Level 5, center-SE	Braunite Ia cockade ores, larger vein filled by abundant braunite Ib, hausmannite Ib and calcite I. Calcite I strongly altered and replaced
Sai-015	B	Level 5, center	Braunite Ib mineralization with partly replaced calcite I. Hematite Ib occurs with replacive Mn-calcite I along grain boundaries
Sai-016	B	Level 5, center	Massive calcite I mineralization, almost completely replaced by Mn-rich carbonates. Minor braunite Ib and hematite with Mn-calcite I along grain boundaries.
Sai-026	D	Level 6, SE	Massive mineralization of Ca-rhodochrosite II after calcite I. Close to the vein wall massive mineralization of fine grained Mn-calcite I.
Sai-056	B	Level 3, SE	Calcite I with abundant braunite and hausmannite. Braunites are commonly altered to brownish carbonate.
Sai-061	B	Level 3, center	Braunite Ia cockade ores rimming blackened rhyolite breccia clasts. Larger vug filled by calcite I and abundant braunite Ib as well as hausmannite Ib.
Sai-062	B	Level 3, NW	braunite Ia cockade ores rimming black rhyolite breccia clasts. Larger vug filled by calcite I and abundant braunite Ib as well as hausmannite Ib.
Sai-065	C	Level 3, NW	Barren calcite I mineralization, partly replaced by Mn-calcite I. Abundant hematite Ib in Mn-calcite I rich areas.
Sai-074	B	Level 4, center	Celadonite and Ca-rhodochrosite I pre ore stage mineralization around brecciated rhyolite. A younger vein of calcite I with abundant braunite cuts the mineralization, proving it's younger relative age.
Sai-075	C	Level 4, SE	Calcite I mineralization with abundant braunite Ib.
Sai-079	C	Level 4, NW	Calcite I vein mineralization, almost no braunite present. Mn-calcite I replaces calcite I along grain boundaries and is intergrown with hematite Ib. Fe–Mg calcite with additional later hematite Ib in interstitial space of earlier hematite Ib
Sai-080	D	Level 4, center	Calcite I almost completely replaced by fine grained Ca-rhodochrosite II. Remnants of cleavage and twinning lamellae preserved in scale-like, lenticular rhodochrosite.
Sai-083	A	Level 5, center	Massive braunite Ib and calcite mineralization. Calcite I is commonly replaced by fine grained Mn-rich carbonates
Sai-084	A	Level 5, NW	Calcite I vein mineralization, almost no braunite present. Mn-calcite I replaces calcite I along grain boundaries and is intergrown with hematite Ib. Minor celadonite II and colloform hematite II are also present.
Sai-100	D	Level 6, SE	Calcite-I mineralization with abundant braunite Ia in cockade ore and braunite Ib in massive vein mineralization.

is not everywhere present. Hematite only occurs in subordinate amounts within some cockade ores. Comb textures in braunite I record a sequential opening of fractures to form larger veins (Figs. 5d, 6a), where the cockade ore grades into more massive mineralization. This is composed of calcite I (Table 3) and braunite Ib that display pronounced growth zoning. The massive mineralization also contains lath-shaped anhydrite crystals, which are only preserved in the interstices between braunite crystals, along with minor amounts of celestite. In places where these anhydrite laths were not isolated and sealed off from later alteration events, they are entirely replaced by late stage carbonates, arsenate phases and minor quartz.

Reopening of the vein system must have been associated with a period of tectonic rupturing, as is demonstrated by delaminated braunite–calcite cockade ore that is now present as fragments within massive mineralization of calcite I and braunite (Fig. 5c, f). Thin, closely spaced pressure twin lamellae within calcite I are indicative of low temperature deformation (Burkhard, 1993). Euhedral scheelite grains, commonly intergrown with braunite Ia and Ib, occur within cockade ore and the massive vein mineralization. Relicts of tabular manganite that are present in interstices between braunite Ib crystals indicate a slightly later timing of manganite deposition (Fig. 6b, c). Hausmannite Ib and secondary pyrolusite texturally postdate both braunite Ib and manganite. The entire ore stage 1 assemblage is extensively altered. Crystals of largely replaced manganite are traced by brownish carbonate, braunite II and hausmannite II (Fig. 6b). Braunite is commonly replaced by a carbonate of rhodochrositic composition. The alteration and replacement features are typically restricted to specific growth zones of the braunite (Fig. 6c), while other areas within the same crystals are entirely unaffected. Braunite alteration is concomitant with the formation of veinlets of Ca-rhodochrosite III. In addition, purple fluorite II, intimately intergrown with calcite I, occurs scarcely in samples of this ore stage.

Ore stage 2 is largely coeval with the precipitation of manganoan calcite (Mn-calcite I). Vein portions that are only mineralized by this ore stage regularly contain hematite Ia in cockade ores (Fig. 6d). This hematite is distinct from the minor amount of hematite that occurs in stage 1 mineralization. The cockade ores present in ore stage 2 mineralization contain much larger aggregates of hematite. It was classified as hematite Ia, even though strictly speaking it does not represent the very first occurrence of hematite within the vein mineralization. Mn-calcite I occurs either in small subhedral grains or, more commonly, as replacement of calcite I. This replacement is epitactic along grain boundaries, cleavage or twin lamaellae in calcite I (Fig. 7a). Mn-calcite I that has formed by replacement of calcite I is often intergrown with specularitic hematite (hematite Ib) that is strictly confined to the replacement zones (Fig. 7b). Thus, hematite Ib likely represents a product of the replacement process. In large grains of hematite Ib, a weakly developed chevron-shaped growth zoning is visible (Fig. 6e). Rarely, colloform and very porous aggregates of a texturally late hematite (hematite II) can be observed (Fig. 6f). Interstitial spaces within specularitic hematite Ib are commonly filled by Fe–Mg-bearing calcite (Fe–Mg calcite), which is also intergrown with hematite II and subordinate siderite. Thus, hematite appears to be a ubiquitous phase during ore stage 2, while the principal carbonate composition changed from Mn-bearing to Mg–Fe bearing calcite. Additionally, quartz, barite and celadonite II locally accompany hematite in this ore stage (Fig. 5e). Ore stage 2 is not restricted to pre-existing veins mineralized during

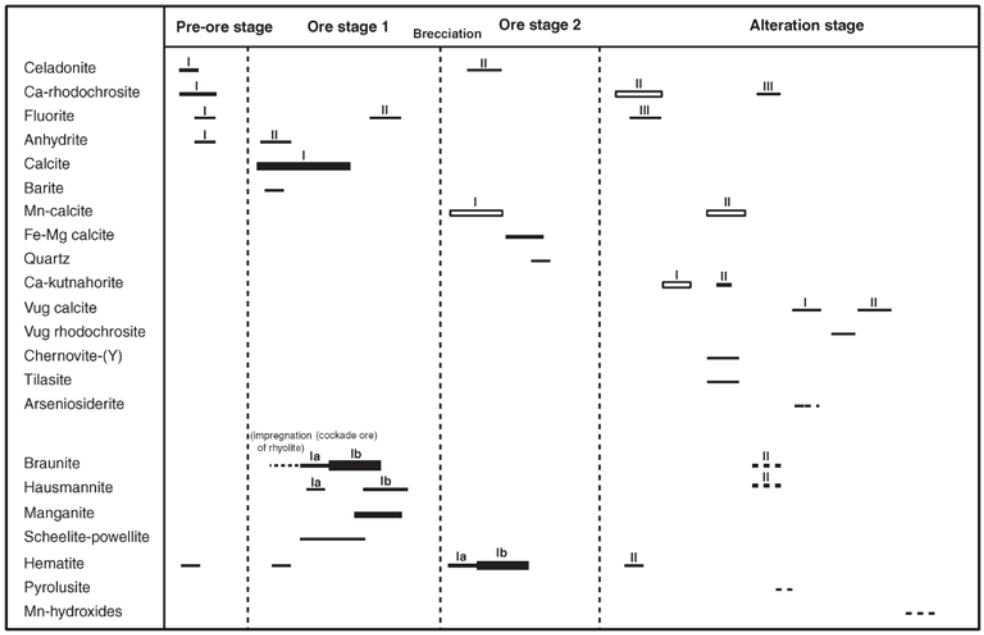

Fig. 4. Paragenetic sequence of the Sailauf Mn – Fe – As mineralization. Open symbols represent carbonates which have formed by replacement reactions. See text for further explanation.

ore stage 1, but may also occur in newly opened vein portions. Here, intergrowths of hematite Ib, Mn-calcite I and Fe – Mg calcite constitute the only mineralization present (Fig. 5e).

4.2. Alteration and remobilization features

In addition to the primary mineralization, almost all samples exhibit complex alteration and replacement textures. Most of these involve carbonate minerals having variable compositions. They replace older carbonate precursors, such as Mn-calcite I (that in turn commonly replaces calcite I at the onset of ore stage 2). Because of the textural complexity and small grain sizes, backscatter electron imaging (BSE) and chemical microanalysis was essential to identify the phases and to reconstruct the relative time sequence of alteration and replacement reactions. Table 3 lists the principal features of each carbonate generation, including those that formed by replacement of older carbonate precursors. (Mn)-calcite formed in both main ore stages is commonly replaced by calcian rhodochrosite (Ca-rhodochrosite II; Figs. 5f, 7c, d,). Like Ca-rhodochrosite I of the pre-ore stage, Ca-rhodochrosite II mainly forms irregular aggregates, and is only rarely present as filling of small veinlets (Fig. 7d). Texturally, Ca-rhodochrosite II closely resembles saddle dolomites which typically form at temperature conditions between 90 and 160 °C, often replacing other carbonate precursors (Spötl and Pitman, 1998). Where Ca-rhodochrosite II replaces calcite I, the cleavage or grain boundaries of the precursor are commonly preserved as relicts in rhodochrosite. Such textural evidence for replacement is entirely lacking in pre-ore stage samples that contain Ca-rhodochrosite I. Growth of an intermediate Ca – Mn carbonate phase at the expense of all earlier carbonates (including Ca-rhodochrosite II) represents the next alteration reaction (Fig. 7c). Compositionally, this intermediate carbonate conforms to a Ca-dominated kutnahorite (Frondel and Bauer, 1955; Peacor et al., 1987). This interpretation is supported by X-ray powder diffraction data. Therefore, we have classified this mineral as Ca-kutnahorite I. Interestingly, Ca-kutnahorite I is epitactically intergrown with earlier calcite I, as confirmed by the extinction behavior in polarized light.

All earlier carbonates were subject to localized replacement by manganoan calcite II (Mn-calcite II), which occurs as brownish, blade-shaped and very porous aggregates or as small veinlets (Fig. 7d). Rarely, Mn-calcite II is intergrown with another generation of calcian kutnahorite (Ca-kutnahorite II), while intergrowths with the arsenates tilasite and arseniosiderite are more common. A third generation of rhodochrosite (Ca-rhodochrosite III) is present in the Mn-oxide rich assemblages of ore stage 1, where it occurs as veinlets or oriented along cleavage lamellae (Fig. 7f). These veinlets appear to be related to a widespread alteration of ore braunite, which resulted

Table 2
Mineralogical summary of the Sailauf mineralization. Parentheses denote phases or assemblages that were not further investigated in this study. For descriptions of secondary minerals and native arsenic containing crusts see Lorenz (1995).

Assemblage	Paragenetic stage	Minerals
Vein mineralization	Pre ore stage	Celadonite, (illite), Ca-rhodochrosite, fluorite, anhydrite, ± hematite
Vein mineralization	Ore stage 1	Calcite, braunite, hausmannite, manganite, anhydrite, hematite, fluorite, barite, ± scheelite–powellite
Vein mineralization	Ore stage 2	Mn-calcite, hematite , celadonite, quartz, ± Fe – Mg calcite
Vein mineralization	Alteration stage	Ca-rhodochrosite, Mn-calcite, Ca-kutnahorite, vug filling carbonates, fluorite, arseniosiderite, tilasite, chernovite-(Y), ± hematite, ± braunite, ± hausmannite, (± todorokite), (± pyrolusite), (± cryptomelane), (± brandtite), (± sailaufite), (± bertrandite)
(Crusts on fracture planes)	Unknown	(Native arsenic), (± uraninite), (± pyrite), (± chalcopyrite), (± arsenopyrite), (± realgar), (± zeunerite), (± uranospinite), (± fluorite), (± illite)

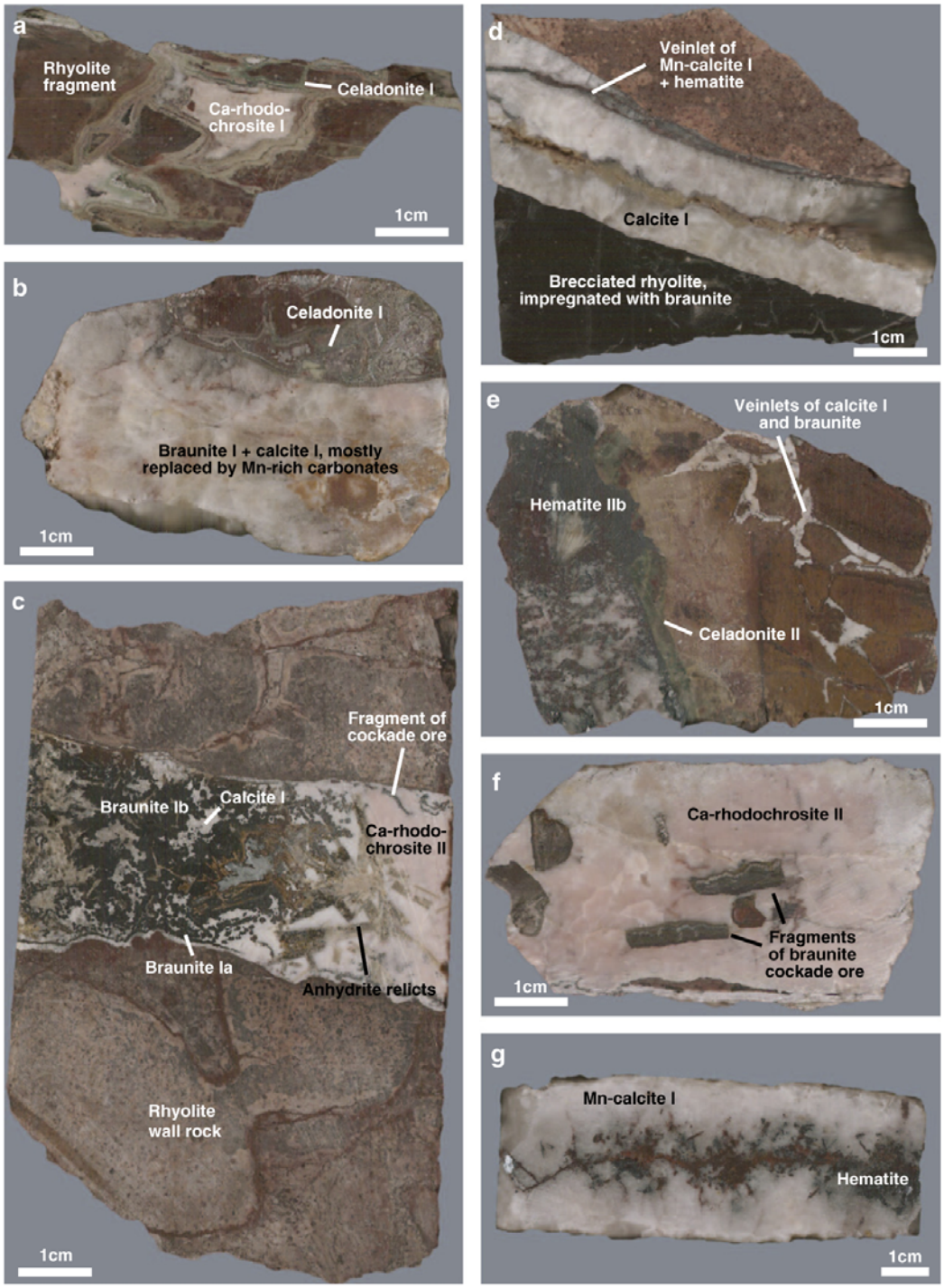

Fig. 5. Photographs of representative ore hand specimens. (a) Pre-ore stage celadonite I rimming rhyolite clasts, cemented by Ca-rhodochrosite I. Sample: Sai-001. (b) Ore stage 1 vein filled by calcite I. The vein wall is made up of an older celadonite I rich breccia of the pre-ore stage. Sample: Sai-031. (c) Ore stage 1 mineralization, containing abundant calcite I with braunite Ia and Ib. Pinkish Ca-rhodochrosite II replaces calcite I. Sample: Sai-005. (d) Vein of Calcite I (ore stage 1) in rhyolite impregnated with braunite. The reddish veinlet is composed of Mn-calcite I and hematite (ore stage 2). Sample: Sai-003. (e) Small veinlets of ore stage 1, crosscut by a larger vein of hematite rich carbonate (ore stage 2). Sample: Sai-118. (f) Ca-rhodochrosite II completely replacing calcite I. Isolated fragments of cockade are present as inclusions in Ca-rhodochrosite II. Sample: Sai-094. (g) Relicts of calcite I (ore stage 1) replaced by pinkish Mn-calcite I during ore stage 2. Former calcite I grain boundaries acted as fluid pathways for ore stage 2 fluids along which hematite precipitated. Sample: Sai-079.

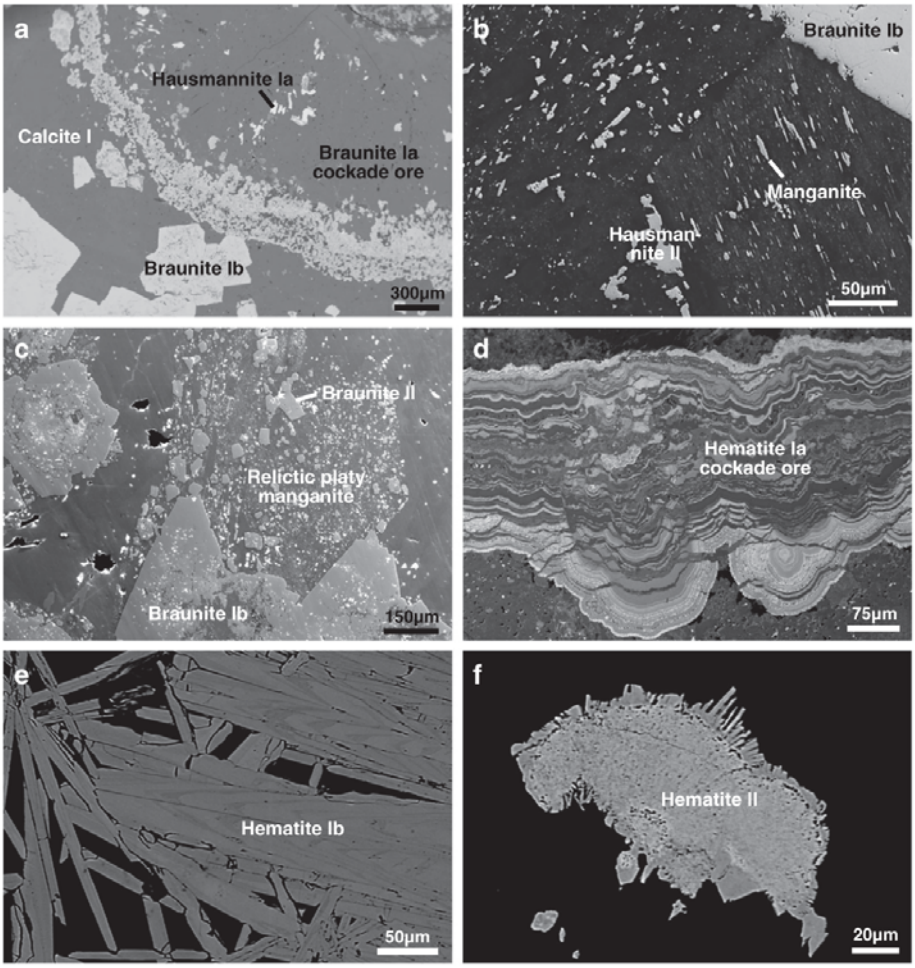

Fig. 6. BSE images and microphotographs (d) of the principal ore minerals. (a) Fine grained Mn-oxide calcite cockade ore grading into massive calcite I and braunite Ib mineralization (ore stage 1). Sample: Sai-014. (b) Elongated manganite, relictic after large platy manganite. The assemblage is present in interstices of braunite Ib and hausmannite II (ore stage 1). Sample: Sai-083. (c) Relictic platy manganite (ore stage 1) with abundant braunite II. Note alteration of zoned braunite Ib grain. Sample: Sai-100. (d) Hematite Ia cockade ore (ore stage 2), crosscut by veinlets of younger carbonates of the alteration stage. Sample: Sai-016. (e) Chevron zoning in hematite Ib (ore stage 2). Sample: Sai-079. (f) Porous, colloform aggregate of hematite II. Sample: Sai-084.

Table 3
Textural and paragenetic characteristics of the different carbonate generations.

Generation	Occurrence	Ore stage	Textural features/intergrowths
Ca-rhodochrosite I	Together with celadonite and fluorite	Pre-ore	Fine grained, scale-like texture
Calcite I	Main gangue mineral	Stage 1	Coarse grained, pressure twinning lamellae. Intergrown with Mn oxides
Mn-calcite I	Replaces calcite I along favorable fluid pathways or in discrete veinlets	Stage 2 early	Often intergrown with specularitic hematite
Fe-Mg-calcite	Together with Mn-calcite I, also in discrete veinlets	Stage 2 late	Also associated with specularitic hematite
Ca-rhodochrosite II	Replaces earlier carbonates, often pseudomorphic	Post-ore	Fine grained, scale-like texture
Ca-kutnahorite I	Replaces especially rhodochrosite I,	Post-ore	Epitactic intergrowths with calcite I
Mn-calcite II	Replaces all earlier carbonates, often intergrown with kutnahorite II	Post-ore	Porous, blade-like, brownish masses. Often intergrown with arsenates
Ca-kutnahorite II	Intergrown with Mn-calcite II	Post-ore	Small patches in porous Mn-calcite II
Ca-rhodochrosite II	Restricted to Mn-Ores of ore stage 1.	Post-ore	Small veinlets crosscutting older phases
Vug calcite I	Radial-fibrous vug infilling aggregates	Post ore	Intergrown with arsenates, rimmed by vug-rhodochrosite
Vug rhodochrosite	Rims around vug calcite I	Post ore	
Vug calcite II	Radial-fibrous vug infilling aggregates	Post ore	

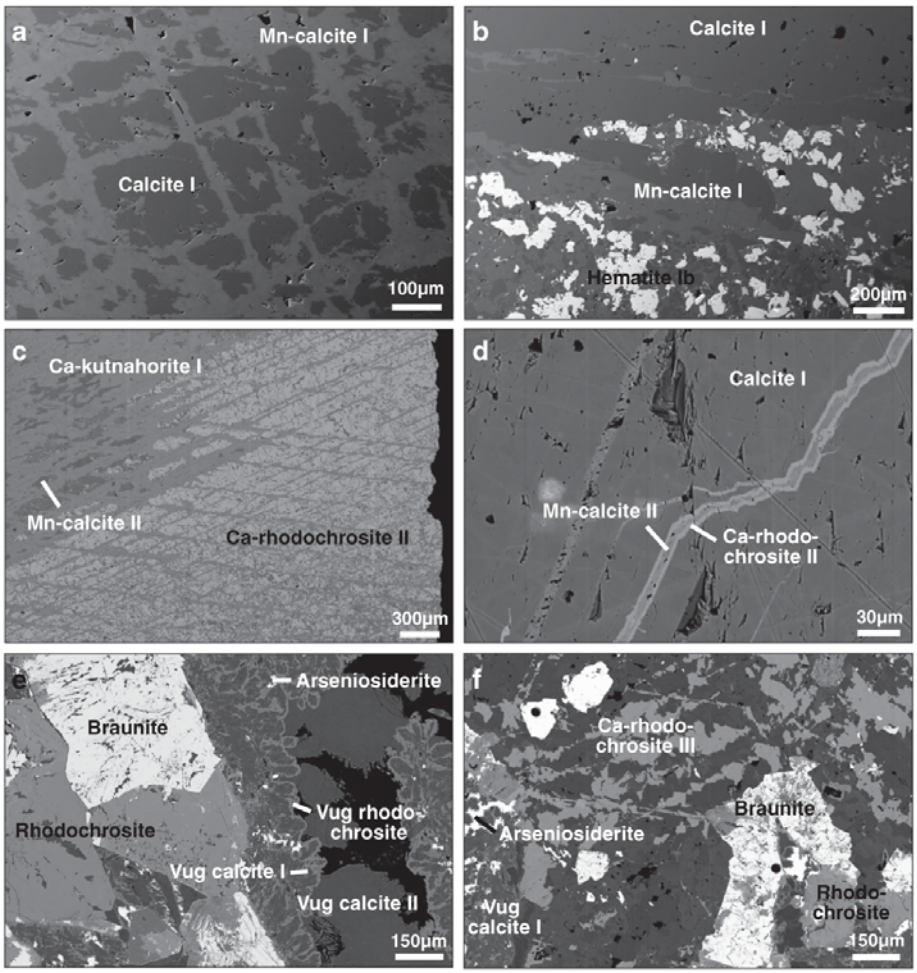

Fig. 7. BSE images of the principal carbonate generations, including replacement and alteration textures. (a) Replacement of dark calcite I (ore stage 1) by Mn-calcite I (ore stage 2). Sample: Sai-003. (b) Replacement of dark calcite I by Mn-calcite I and hematite which exclusively occurs within the Mn-calcite I. Sample: Sai-003. (c) Complex alteration stage assemblage. Relict lamellae of calcite I were preserved after replacement by Ca-rhodochrosite II. Along these lamellae, Ca-kutnahorite I replaced rhodochrosite. Sample: Sai-013. (d) Younger veinlets within calcite I. Ca-rhodochrosite II veinlet was reactivated and filled by Mn-calcite II (central portion). Sample: Sai-011. (e) Braunite Ib (ore stage 1) pseudomorphically replaced by rhodochrosite. The assemblage is overgrown by vug filling late stage carbonates, associated with arsenate minerals (bright white). Sample: Sai-005. (f) Complex replacement texture. Veinlets of Ca-rhodochrosite III related to alteration of braunite Ib occur along cleavage lamellae in calcite I. Vugs are filled by late stage vug calcite I and arseniosiderite. Sample: Sai-005.

in the formation of carbonates having rhodochrosite composition. The veinlets crosscut porous Mn-calcite II, proving their younger age. Thus, they have to be distinguished from Ca-rhodochrosite II, which is texturally older than Mn-calcite II (Fig. 7d).

Two distinct generations of calcite that fill open vugs in the center of the veins (vug calcite I and II) represent the texturally youngest carbonates (Fig. 7e, f). The first generation is rimmed by a seam of calcian rhodochrosite (vug rhodochrosite). Both vug calcites occur as radial-fibrous aggregates and are commonly intergrown with reddish arseniosiderite, and slightly younger quartz and barite. This mineral assemblage is also present as pseudomorphic replacement after lath-shaped anhydrite crystals. In addition to the late stage arsenates, Mn hydroxides constitute the youngest minerals that formed, being present as radial-fibrous aggregates in the vugs. In addition to the minerals described from the alteration stage, open vugs host a large number of rare late stage and supergene minerals (e.g. brandtite, sailaufite, bertrandite, Mn-hydroxides) (Lorenz, 1995), which were not further investigated in this study.

5. Major and trace element composition of Mn and Fe oxides

5.1. Braunite

Braunite is the most abundant ore mineral in the Sailauf mineralization. Braunite has an ideal stoichiometry of Mn_7SiO_{12}, but is known to be part of a polysomatic series (Thompson, 1978) which further includes bixbyite (Mn_2O_3), braunite-II ($Ca_{0.5}Mn_7Si_{0.5}O_{12}$), neltnerite ($CaMn_6SiO_{12}$) and up to 17 theoretically predicted polysomes (Abs-Wurmbach et al., 1983; Baudracco-Gritti, 1985; De Villiers and Buseck, 1989). The major element composition of braunite resembles the chemical variability reported in the literature (Table 5). According to De Villiers and Buseck (1989), stoichiometric braunite (sensu stricto) contains 10 wt.% SiO_2, whereas braunite-II contains 5 wt.% SiO_2. With the exception of a single analysis (SAI-100a III-58), all data conform to braunite. The single datapoint may represent a 3- or 6-module polysome (De Villiers and Buseck, 1989), which would

have a theoretical SiO_2 concentration of 6.7 wt.%. Even though CaO concentrations up to 2.7 wt.% were detected, no stoichiometric braunite-II is present. The pronounced growth zoning of braunite Ib results from variations in the Mn, Ca, Al and Si contents, although systematic chemical trends from cores to rims are not observable. The different braunite generations show subtle but systematic variations in their major element composition. Braunites from cockade ores (braunite Ia) have CaO contents in the range of 0.1–2.5 wt.%, with a clear mode around 1.7 wt.%. Braunite Ib contains between 0.3 and 2.4 wt.% of CaO, with a mode around 1.4 wt.%. Later braunite II that is present as inclusions in carbonate minerals contains more elevated CaO concentrations in the range of 1.0–2.5 wt.%. The Fe_2O_3 contents in braunite Ia are in the range of 0.1 to 4.0 wt.%, with a mode around 0.2 wt.%, whereas in braunite Ib and II the concentrations are much lower, ranging from below the detection limit to 0.9 wt.%. The silica content in most braunites is close to the stoichiometric value, although growth zones with both silica deficiency and excess do occur throughout all generations. The As_2O_5 concentrations vary substantially, ranging between values close to detection limit (about 200 ppm) to maximum values of up to 0.8 wt.%. The median As values of braunites from generations Ia and II are 800 and 750 ppm, respectively. In braunite Ib, the median As_2O_5 content is 300 ppm, although concentrations exceeding 1000 ppm were found.

5.2. Hausmannite

Microprobe data of hausmannite (Mn_3O_4) show elevated concentrations of Zn, Ca, Fe and Al (Table 6). The Fe_2O_3 concentrations reach values of up to 3.3 wt.% in hausmannite Ia, whereas hausmannite Ib and II never contain more than a few hundred ppm iron. Negative correlations exist between Mn^{2+} and (Zn + Ca), and Mn^{3+} and (Al + Fe^{3+}). Thus, substitution of these elements in tetrahedral (divalent cations) and octahedral (trivalent cations) coordination sites are likely, as has been previously reported (Frenzel, 1980; Roy, 1981). The As_2O_5 contents in hausmannite are consistently below the detection limit.

5.3. Manganite

Manganite typically occurs as small elongated stringers parallel to the c-axis of former large tabular manganite crystals, which have been largely altered to brownish carbonates containing abundant oriented inclusions of braunite II. Trace amounts of Al_2O_3 and Fe_2O_3 were detectable in some manganite grains (Table 7). Large manganite grains contain low CaO contents that do not exceed 0.1 wt.%. Higher concentrations that were found in small grains likely result from contamination by the surrounding carbonates. The As_2O_5 concentrations in manganite are consistently below the detection limit.

5.4. Hematite

Representative hematite data are listed in Table 8. Fine intergrowth with carbonates results in often low analytical totals (around 95%) for cockade ore hematites (hematite Ia), rendering interpretation of minor element contents difficult. Hematites from this generation contain up to 0.4 wt.% of WO_3, which cannot result from carbonate contamination. Specularitic hematite Ib yielded very good analytical totals. WO_3 contents vary between the detection limit (about 350 ppm) and 1.0 wt.%. The chevron zoning observable in sufficiently large grains (Fig. 6e) corresponds to variations in WO_3 concentrations. Additionally, CaO and Mn_2O_3 are present in significant quantities, reaching maximum concentrations of 2.0 and 0.1 wt.%, respectively. Colloform aggregates of hematite II contain even larger concentrations of minor elements. Most remarkable are rather constant Mn_2O_3 contents of around 1.0 wt%, substantial WO_3 concentrations of 0.4–1.5 wt.% and CaO concentrations of 0.1–1.0 wt.%. The W enrichment in hematite was explained by the substitution scheme 2 Fe^{3+}=W^{6+} (Tarassov et al., 2002). Mn^{3+} possesses a limited solubility in hematite (Singh et al., 2000), thus the simple homovalent substitution may explain the detected Mn_2O_3 contents in hematite Ib.

5.5. Arsenate minerals

Late stage arsenate phases are common in all samples, often intergrown with manganoan calcite II (Mn-calcite II) or the later, vug calcite I. Three different arsenate phases could be distinguished, and selected data are reported in Table 9. Tilasite with minor Mn and Fe occurs intergrown with porous Mn-calcite II. The second As-rich phase is arseniosiderite. This phase occurs as inclusions in late stage vug calcite I and as perimorphs after lath-shaped anhydrite crystals that are common in samples from both main ore stages. Another As-rich phase occurring in Mn-calcite II contains only Y and As in significant quantities, while the concentrations of MnO, F and CaO are very low. The only known mineral that would conform to this phase is chernovite-(Y) ($YAsO_4$). Concentrations of Y_2O_3 lower than the stoichiometric value (around 34 wt.%) may be readily explained by substitution of Y by trivalent REE (Ondrejka et al., 2007), which were not analyzed by electron microprobe due to complicated peak interferences.

5.6. Trace elements in Fe and Mn oxides

The trace element composition of the main oxide minerals (braunite, hausmannite and hematite) was analyzed by LA-ICPMS, with focus on covering the different main generations (Fig. 4). Fig. 8 shows boxplots of selected element concentrations within the Mn oxides and hematite. Due to the small grain size of braunite Ia and II, hausmannite and hematite Ia and II, only few data could be obtained from these minerals. The Mn oxides contain elevated concentrations of As, U, W, Zn, Cu, Pb and Sb that can amount to several 100 to 10,000 ppm. Marked differences in trace metal contents exist between the different generations of hematite, especially with regard to As, W, U and Pb. The concentrations of these elements vary between several 100 to 10,000 ppm. Hematite Ia contains high concentrations of As, whereas U, W and Sb are enriched in both hematite Ia and hematite II compared to hematite Ib. The two generations of braunite and hausmannite show much smaller differences in their trace element content. Both As and U appear to be preferentially incorporated into braunite, whereas Zn and Pb are enriched in hausmannite. The Zn concentrations in hausmannite Ia reach a maximum value of roughly 6.8 wt.% (LA-ICPMS data). In some braunite data, variable Zn signals are observed, indicating considerable sample heterogeneity. This observation is also supported by the EMPA data, which revealed strongly different ZnO concentrations even within individual hausmannite grains (see Table 6, columns 2 and 3).

The most striking feature of the trace element data is the large variation even within individual samples, sometimes approaching two orders of magnitude (Fig. 8). In order to understand whether this variability is correlated with the visible growth zoning, the distribution of selected minor and trace elements was mapped with the electron microprobe. The spatial distribution of As, being one of the most highly enriched trace elements in braunite and hematite, was determined in several crystals covering all main generations of braunite (Fig. 11). Braunite Ib exhibits a pronounced As zoning pattern that does not strictly correspond to the major element variations which are responsible for the growth zoning visible in the BSE images. Braunite II that is present as inclusions in carbonates lacks zoning in major and trace elements, in agreement with the much lower variation in As concentration determined with LA-ICPMS. Although not directly confirmed by element mapping, the large variation in all trace elements within braunite Ib can be attributed to similar zoning effects.

Table 4
Representative EPMA and LA-ICPMS data of carbonate minerals (CO_2 was calculated by stoichiometry), excluding the REE.

Sample	Sai-001 TS-007	Sai-011 TS-001	Sai-100 TS-011	Sai-006c TS-003	Sai-014a TS-001	Sai-065 TS-005	Sai-079 TS-006	Sai-026 TS-013	Sai-011 TS-012	Sai-080 III-006	Sai-005c TS-014	Sai-014a TS-004	Sai-005c TS-012	Sai-005c TS-016	Sai-080 TS-007	Sai-005a TS-007	Sai-015 VI-008	Sai-005a III-027	Sai-005a TS-010	Sai-006c TS-004
Generation	Ca-rhodo-chrosite I	Calcite-I	Calcite-I	Mn--calcite I	Mn -calcite I	Fe – Mg-calcite	Fe – Mg-calcite	Ca-rhodo-chrosite II	Ca-kutna-horite I	Ca-kutna-horite I	Mn-calcite II	Mn-calcite II	Ca-kutna-horite II	Ca-rhodo-chrosite II	Vug Calcite I	Vug Calcite I	Vug-rhodo-chrosite	Vug-rhodo-chrosite	Vug- calcite II	Vug-calcite II
Wt.%																				
SiO_2	b.d.	b.d.	b.d.	0.01	0.01	0.01	b.d.	b.d.	0.01	b.d.	b.d.	0.01	b.d.	b.d.	b.d.	b.d.	0.02	b.d.	0.01	0.02
As_2O_5	b.d.	b.d.	b.d.	b.d.	b.d.	b.d.	b.d.	b.d.	b.d.	b.d.	b.d.	b.d.	b.d.	0.08	b.d.	b.d.	0.33	0.22	0.12	b.d.
MnO	53.6	b.d.	b.d.	3.68	4.25	1.32	1.56	51.59	25.99	27.68	11.21	12.08	24.83	50.11	20.13	17.48	43.46	40.28	12.77	10.91
CaO	6.63	55.24	54.39	54.35	53.85	52.10	52.44	8.13	29.38	28.87	46.40	45.84	31.87	9.37	36.03	39.08	12.93	16.57	45.48	47.86
MgO	0.16	0.64	0.38	0.01	0.02	0.20	0.18	0.23	2.04	0.18	0.05	0.09	0.26	b.d.	0.69	0.66	2.29	1.73	0.58	0.31
FeO	0.05	b.d.	0.02	b.d.	b.d.	2.73	2.96	0.04	0.03	b.d.	b.d.	b.d.	0.02	0.03	0.17	0.48	0.05	0.31	0.19	0.11
SrO	0.03	0.04	b.d.	0.04	0.05	0.05	b.d.	b.d.	0.02	b.d.	b.d.	0.04	b.d.	b.d.	0.02	b.d.	0.02	b.d.	0.04	0.06
ZnO	b.d.	b.d.	b.d.	b.d.	b.d.	b.d.	b.d.	b.d.	b.d.	0.02	0.03	b.d.	b.d.	b.d.	b.d.	b.d.	b.d.	0.02	0.03	b.d.
BaO	b.d.	0.04	b.d.	b.d.	b.d.	b.d.	b.d.	b.d.	b.d.	b.d.	b.d.	b.d.	b.d.	b.d.	b.d.	b.d.	b.d.	b.d.	b.d.	b.d.
CO_2	38.67	44.08	43.11	44.97	44.96	43.63	44.13	38.67	41.44	40.04	43.45	43.59	40.72	38.49	41.64	42.53	39.80	40.17	44.45	44.76
Total	60.47	55.97	54.81	58.09	58.20	56.42	57.14	60.00	57.47	56.76	57.72	58.05	57.00	59.60	57.07	57.71	59.12	59.14	59.22	59.25
Total*	99.14	100.05	97.92	103.06	103.17	100.05	101.26	98.67	98.91	96.80	101.17	101.64	97.71	98.09	98.71	100.24	98.92	99.31	103.67	104.02
Formula (O = 3)																				
Si	0.00	0.00	0.00	0.00	0.00	0.00	0.00	0.00	0.00	0.00	0.00	0.00	0.00	0.00	0.00	0.00	0.00	0.00	0.00	0.00
As	0.00	0.00	0.00	0.00	0.00	0.00	0.00	0.00	0.00	0.00	0.00	0.00	0.00	0.00	0.00	0.00	0.00	0.00	0.00	0.00
Mn	0.86	0.00	0.00	0.05	0.04	0.02	0.02	0.83	0.39	0.43	0.16	0.17	0.38	0.81	0.30	0.25	0.67	0.62	0.18	0.15
Ca	0.13	0.98	0.99	0.95	0.96	0.94	0.93	0.17	0.56	0.57	0.84	0.83	0.61	0.19	0.68	0.72	0.25	0.32	0.80	0.84
Mg	0.00	0.02	0.01	0.00	0.00	0.01	0.00	0.01	0.05	0.00	0.00	0.00	0.01	0.00	0.02	0.02	0.06	0.05	0.01	0.01
Fe	0.00	0.00	0.00	0.00	0.00	0.04	0.04	0.00	0.00	0.00	0.00	0.00	0.00	0.00	0.00	0.01	0.00	0.01	0.00	0.00
Sr	0.00	0.00	0.00	0.00	0.00	0.00	0.00	0.00	0.00	0.00	0.00	0.00	0.00	0.00	0.00	0.00	0.00	0.00	0.00	0.00
Zn	0.00	0.00	0.00	0.00	0.00	0.00	0.00	0.00	0.00	0.00	0.00	0.00	0.00	0.00	0.00	0.00	0.00	0.00	0.00	0.00
Ba	0.00	0.00	0.00	0.00	0.00	0.00	0.00	0.00	0.00	0.00	0.00	0.00	0.00	0.00	0.00	0.00	0.00	0.00	0.00	0.00
ppm																				
Co	0.38	0.13	0.05	0.11	0.16	0.13	0.06	1.6	0.49	n.a.	0.39	0.2	n.a.	0.08	0.34	0.66	n.a.	n.a.	0.35	0.22
Zn	8.2	16	0.13	4.9	2.7	1.8	1.7	10	6.1	n.a.	8.8	4.5	n.a.	0.8	41	12	n.a.	n.a.	18	8.9
As	28	21	0.11	41	b.d.	0.36	0.2	24	9.5	n.a.	53	20	n.a.	321	857	319	n.a.	n.a.	1229	241
Sr	18	46	86	188	112	225	130	34	44	n.a.	248	283	n.a.	2.6	173	221	n.a.	n.a.	229	163
Sb	0.06	b.d.	0.01	0.39	b.d.	0.01	b.d.	b.d.	0.05	n.a.	0.23	0.07	n.a.	b.d.	0.39	2	n.a.	n.a.	0.08	b.d.
Ba	1.2	b.d.	0.02	1.3	0.12	0.59	0.21	3.6	5.1	n.a.	13	5.4	n.a.	1.4	4.2	3.3	n.a.	n.a.	0.19	0.88
W	1.9	b.d.	0.12	2.9	0.06	0.16	0.18	0.1	b.d.	n.a.	1.1	0.21	n.a.	3.3	8.8	1.6	n.a.	n.a.	1.9	3.4
Pb	2	0.39	0.51	5.7	1.5	4.6	8.5	1.2	0.6	n.a.	5.9	4.2	n.a.	2	1.9	3.2	n.a.	n.a.	1	2.5
Bi	0.06	b.d.	0	0.02	b.d.	b.d.	0	0.01	0.02	n.a.	0.06	0.03	n.a.	0.03	0.01	0.05	n.a.	n.a.	0.01	0.01
U	0.97	10	0	0.61	0	0.02	11	0.48	0.26	n.a.	0.27	0.11	n.a.	0.13	20	2.3	n.a.	n.a.	77	1.5

Table 5
Representative EPMA and LA-ICPMS data of braunite (*Mn_2O_3 was calculated from charge balance).

Sample	Sai-014a V-092	Sai-014a V-094	Sai-100 V-022	Sai-100a III-058	Sai-005a V-004	Sai-005a V-016	Sai-007 I-014	Sai-005b V-041	Sai-014a V-016	Sai-014a V-025	Sai-056 V-027	Sai-075 III-034	Sai-100 V-003	Sai-075 V-015	Sai-100 V_038	Sai-083 III-008	Sai-100a III-080
Generation	Ia	Ia	Ia	Ia	Ib	Ib	Ib	Ib	Ib	Ib	Ib	Ib	Ib	II	II	II	II
wt%																	
SiO_2	9.92	9.88	10.55	6.75	9.71	8.93	11.14	10.06	10.12	10.06	9.92	9.11	10.31	9.59	10.10	9.62	9.91
As_2O_5	b.d.	0.15	0.07	0.07	b.d.	0.04	b.d.	b.d.	0.02	0.09	b.d.	b.d.	0.02	0.13	0.10	0.23	0.07
MnO	9.71	10.39	9.98	5.93	8.98	8.70	9.98	9.33	10.39	9.69	10.69	8.89	10.22	10.27	10.18	9.59	9.27
Mn_2O_3*	77.00	78.18	75.98	84.84	78.91	80.40	74.56	78.32	78.03	78.98	79.47	81.42	78.01	77.42	78.37	78.21	80.89
SO_3	0.02	0.01	b.d.	b.d.	0.01	0.01	0.10	b.d.	0.01	0.01	0.02	b.d.	0.01	0.02	0.02	b.d.	b.d.
Al_2O_3	0.57	0.44	2.04	0.68	0.43	0.27	b.d.	0.13	0.04	0.26	0.66	0.22	0.18	0.14	0.25	0.67	0.43
Fe_2O_3	0.06	0.07	0.12	0.39	0.07	0.07	0.15	0.10	0.11	0.08	0.06	0.07	0.11	0.05	0.31	0.07	0.11
K_2O	b.d.	b.d.	b.d.	b.d.	b.d.	b.d.	b.d.	b.d.	b.d.	b.d.	b.d.	b.d.	b.d.	b.d.	b.d.	b.d.	b.d.
MgO	0.03	b.d.	b.d.	b.d.	b.d.	0.01	0.01	b.d.	0.01	0.02	b.d.	b.d.	0.01	0.03	0.02	0.03	b.d.
ZnO	0.05	0.02	b.d.	b.d.	0.04	0.02	0.01	0.04	b.d.	b.d.	0.01	b.d.	0.01	0.02	b.d.	b.d.	b.d.
CaO	1.56	1.17	2.03	1.67	1.96	1.48	2.68	1.99	1.26	1.81	0.83	1.46	1.56	0.95	1.47	1.58	1.98
BaO	b.d.	b.d.	b.d.	b.d.	b.d.	0.01	b.d.	b.d.	0.01	b.d.	0.01	0.02	0.01	b.d.	0.01	b.d.	0.02
Total	98.94	100.29	100.78	100.33	100.11	99.93	98.63	99.97	99.99	100.99	101.67	101.19	100.46	98.62	100.83	100.02	99.05
Formula (O = 12)																	
Si	1.00	0.99	1.03	0.68	0.97	0.90	1.12	1.01	1.01	1.00	0.98	0.91	1.03	0.98	1.00	0.96	1.00
As	0.00	0.01	0.00	0.00	0.00	0.00	0.00	0.00	0.00	0.00	0.00	0.00	0.00	0.01	0.00	0.01	0.00
Mn^{2+}	0.83	0.88	0.83	0.51	0.76	0.74	0.85	0.79	0.88	0.81	0.89	0.75	0.86	0.89	0.86	0.81	0.90
S	0.00	5.94	0.00	0.00	0.00	0.00	0.01	0.00	0.00	0.00	0.00	0.00	0.00	0.00	0.00	0.00	0.00
Al	0.07	0.00	0.24	0.08	0.05	0.03	0.00	0.02	0.00	0.03	0.08	0.03	0.02	0.02	0.03	0.08	0.06
Fe^{3+}	0.00	0.05	0.01	0.03	0.01	0.01	0.01	0.01	0.01	0.01	0.00	0.00	0.01	0.00	0.02	0.01	0.01
K	0.00	0.01	0.00	0.00	0.00	0.00	0.00	0.00	0.00	0.00	0.00	0.00	0.00	0.00	0.00	0.00	0.00
Mg	0.00	0.00	0.00	0.00	0.00	0.00	0.00	0.00	0.00	0.00	0.00	0.00	0.00	0.01	0.00	0.00	0.00
Zn	0.00	0.00	0.00	0.00	0.00	0.00	0.00	0.00	0.00	0.00	0.00	0.00	0.00	0.00	0.00	0.00	0.00
Ca	0.17	0.12	0.21	0.18	0.21	0.16	0.29	0.21	0.13	0.19	0.09	0.16	0.17	0.10	0.16	0.17	0.10
Ba	0.00	0.00	0.00	0.00	0.00	0.00	0.00	0.00	0.00	0.00	0.00	0.00	0.00	0.00	0.00	0.00	0.00
Mn^{3+}	5.92	0.00	5.67	6.52	6.00	6.16	5.72	5.96	5.95	5.95	5.96	6.16	5.91	6.00	5.92	5.95	5.93
A: (Mn^{2+} + Ca)	1.00	1.00	1.04	0.69	0.97	0.90	1.14	1.00	1.02	1.00	0.98	0.90	1.03	0.99	1.01	0.98	1.00
B: (Mn^{3+} + Fe^{3+} + Al)	5.99	6.00	5.92	6.63	6.06	6.19	5.73	5.99	5.97	5.99	6.04	6.19	5.94	6.02	5.98	6.04	6.00
Si	1.00	0.99	1.03	0.68	0.97	0.90	1.12	1.01	1.01	1.00	0.98	0.91	1.03	0.98	1.00	0.96	1.00
Ppm																	
Co	7.2	6.7	n.a.	n.a.	4.4	4.5	1.3	3.9	6	6	37	n.a.	3.2	8.4	5.8	7.2	6.7
Ni	b.d.	b.d.	n.a.	n.a.	b.d.	b.d.	b.d.	b.d.	14	b.d.	b.d.	n.a.	b.d.	7.1	b.d.	b.d.	b.d.
Cu	284	278	n.a.	n.a.	237	244	13	201	239	260	170	n.a.	41	46	43	284	278
Zb	118	94	n.a.	n.a.	51	50	20	55	61	62	159	n.a.	50	56	83	118	94
As	4195	4452	n.a.	n.a.	174	287	1825	359	580	1653	1370	n.a.	56	1062	1356	4195	4452
Se	b.d.	b.d.	n.a.	n.a.	b.d.	b.d.	b.d.	b.d.	b.d.	b.d.	b.d.	n.a.	b.d.	b.d.	b.d.	b.d.	b.d.
Mo	b.d.	b.d.	n.a.	n.a.	22	18	10	b.d.	b.d.	b.d.	b.d.	n.a.	b.d.	b.d.	b.d.	b.d.	b.d.
Sb	62	43	n.a.	n.a.	56	38	89	35	60	21	166	n.a.	25	41	20	62	43
Ba	1.6	1.4	n.a.	n.a.	1.3	0.46	0.87	1.7	0.3	0.57	1	n.a.	0.51	0.27	b.d.	1.6	1.4
W	255	480	n.a.	n.a.	233	248	189	213	148	281	781	n.a.	49	152	213	255	480
Pb	74	138	n.a.	n.a.	223	118	23	106	109	35	128	n.a.	84	6.7	62	74	138
Bi	44	38	n.a.	n.a.	0.3	0.37	5.1	6.6	3.2	17	22	n.a.	0.48	77	28	44	38
Th	0.16	b.d.	n.a.	n.a.	b.d.	b.d.	b.d.	b.d.	b.d.	0.09	b.d.	n.a.	b.d.	b.d.	b.d.	0.16	b.d.
U	87	98	n.a.	n.a.	91	96	59	66	171	100	164	n.a.	86	35	117	87	98

Table 6
Representative EPMA and LA-ICPMS data of hausmannite (*Mn_2O_3 was calculated from charge balance).

Sample	Sai-014a V-064	Sai-014a V-111	Sai-014a V-112	Sai-014a V-127	Sai-100a III-045	Sai-005b V-006	Sai-005b V-020	Sai-056 III-005	Sai-061 III_007	Sai-056 V-012	Sai-075 V-001	Sai-100 III-009	Sai-100a III-027
Generation	Ia	Ia	Ia	Ia	Ia	Ib	Ib	Ib	Ib	II	II	II	II
Wt.%													
SiO_2	0.13	0.00	0.08	0.60	b.d.	0.31	0.24	0.14	0.05	0.36	b.d.	0.22	0.34
As_2O_5	b.d.	0.00	0.00	b.d.	b.d.	b.d.	b.d.	b.d.	b.d.	b.d.	b.d.	b.d.	b.d.
MnO	31.41	29.37	30.74	31.39	30.70	28.95	30.52	28.06	29.46	30.02	31.04	29.69	29.16
Mn_2O_3*	68.18	69.55	69.22	66.58	69.24	67.88	68.40	68.43	69.82	68.66	69.54	68.29	68.72
SO_3	b.d.	0.00	0.00	b.d.	b.d.	b.d.	b.d.	b.d.	b.d.	b.d.	b.d.	b.d.	b.d.
Al_2O_3	0.16	0.08	0.05	b.d.	0.27	0.15	0.01	0.28	0.17	0.25	0.11	0.09	0.09
Fe_2O_3	0.98	0.30	0.35	0.67	0.12	0.08	0.10	0.07	0.11	0.08	0.10	0.06	0.09
K_2O	b.d.	0.00	0.00	b.d.	b.d.	b.d.	b.d.	b.d.	b.d.	b.d.	b.d.	b.d.	b.d.
MgO	b.d.	0.00	0.00	b.d.	b.d.	b.d.	b.d.	b.d.	b.d.	b.d.	b.d.	0.02	b.d.
ZnO	0.05	1.77	0.16	0.05	0.03	2.21	0.90	3.72	2.48	1.27	0.15	1.32	2.67
CaO	0.03	0.41	0.48	0.20	0.49	0.41	0.08	0.03	b.d.	0.67	0.18	0.37	0.22
BaO	b.d.	0.01	0.00	b.d.	0.02	b.d.	b.d.	b.d.	b.d.	b.d.	0.02	b.d.	b.d.
Total	100.96	101.49	101.06	99.52	100.89	100.03	100.26	100.73	102.13	101.36	101.15	100.10	101.30
Formula (O = 4)													
Si	0.00	0.00	0.00	0.02	0.00	0.01	0.01	0.01	0.00	0.01	0.00	0.01	0.01
As	0.00	0.00	0.00	0.00	0.00	0.00	0.00	0.00	0.00	0.00	0.00	0.00	0.00
Mn^{2+}	1.00	0.93	0.98	1.01	0.98	0.93	0.98	0.90	0.93	0.95	0.99	0.96	0.93
S	0.00	0.00	0.00	0.00	0.00	0.00	0.00	0.00	0.00	0.00	0.00	0.00	0.00
Al	0.01	0.00	0.00	0.00	0.01	0.01	0.00	0.01	0.01	0.01	0.01	0.00	0.00
Fe^{3+}	0.03	0.01	0.01	0.02	0.00	0.00	0.00	0.00	0.00	0.00	0.00	0.00	0.00
K	0.00	0.00	0.00	0.00	0.00	0.00	0.00	0.00	0.00	0.00	0.00	0.00	0.00
Mg	0.00	0.00	0.00	0.00	0.00	0.00	0.00	0.00	0.00	0.00	0.00	0.00	0.00
Zn	0.00	0.05	0.00	0.00	0.00	0.06	0.03	0.10	0.07	0.04	0.00	0.04	0.07
Ca	0.00	0.02	0.02	0.01	0.02	0.02	0.00	0.00	0.00	0.03	0.01	0.02	0.01
Ba	0.00	0.00	0.00	0.00	0.00	0.00	0.00	0.00	0.00	0.00	0.00	0.00	0.00
Mn^{3+}	1.96	1.99	1.98	1.93	1.98	1.97	1.98	1.97	1.99	1.96	1.99	1.98	1.97
A: $(Mn^{2+} + Ca)$	1.00	0.95	1.00	1.02	1.00	0.95	0.98	0.90	0.93	0.98	1.00	0.97	0.94
B: $(Mn^{3+} + Fe^{3+} + Al)$	1.99	2.00	1.99	1.95	2.00	1.98	1.98	1.99	2.00	1.97	2.00	1.98	1.97
ppm													
Co	3	6	n.a.	2.1	n.a.	b.d.	4.1	13	5	1.6	5.8	10	6.5
Ni	b.d.	b.d.	n.a.	b.d.	n.a.	b.d.	b.d.	b.d.	b.d.	b.d.	b.d.	b.d.	b.d.
Cu	29	b.d.	n.a.	2	n.a.	b.d.	15	21	12	26	14	5.3	4.4
Zn	132	7306	n.a.	599	n.a.	21440	14300	25100	37790	14146	25207	18412	44185
As	85	6	n.a.	272	n.a.	252	418	283	191	2085	413	197	38
Se	b.d.	b.d.	n.a.	b.d.	n.a.	b.d.	b.d.	b.d.	b.d.	b.d.	b.d.	b.d.	b.d.
Mo	b.d.	b.d.	n.a.	b.d.	n.a.	b.d.	b.d.	b.d.	b.d.	b.d.	b.d.	b.d.	b.d.
Sb	52	6	n.a.	17	n.a.	104	104	206	25	1309	94	b.d.	55
Ba	b.d.	b.d.	n.a.	b.d.	n.a.	b.d.	b.d.	b.d.	16	b.d.	b.d.	0.72	b.d.
W	144	85	n.a.	31	n.a.	163	129	191	310	87	797	113	44
Pb	138	65	n.a.	201	n.a.	8347	5400	210	360	1887	3507	130	1116
Bi	2.3	7	n.a.	17	n.a.	11	84	0.71	2	2.4	3.2	6.8	1.1
Th	b.d.	b.d.	n.a.	0.66	n.a.	b.d.	b.d.	b.d.	b.d.	b.d.	b.d.	b.d.	b.d.
U	18	6	n.a.	7.4	n.a.	6.7	11	17	13	3.2	3.1	2.2	7.2

6. Major and trace element composition of carbonate minerals

The major and trace element composition of the primary carbonates is listed in Table 4, and their compositional variation in Ca – Mn – (Fe + Mg) space is depicted in Fig. 9. The carbonates exhibit a significant compositional variability, and the carbonate phases associated with both main ore stages have distinct compositions. Some carbonate generations (calcite I, Fe – Mg calcite and Ca-rhodochrosite II) are characterized by low variability in their Mn and Ca content. With the exception of Fe – Mg calcite, Fe is generally low in all carbonate types. In calcite I, Fe is below the detection limit in most samples, whereas in Ca-rhodochrosite II low Fe concentrations with a clear mode around 500 ppm were measured. Fe – Mg calcite contains up to 4 wt.% FeO, with a mode around 3 wt.%. The MgO concentrations in these carbonate generations typically exceed average FeO and vary between 0.2 and 1 wt.%.

Ca-rhodochrosite I and III as well as both generations of Mn-calcite and Ca-kutnahorite display a larger variability in their major constituents (MnO and CaO). FeO contents are also low, in most samples they are just above the detection limit (150 ppm). Only the Ca-rhodochrosite I of the pre-ore stage contains somewhat higher FeO (mode around 500 ppm). MgO displays a larger variability in these carbonate types. While in Ca-rhodochrosite I, Ca-rhodochrosite III, Mn-calcite I and Mn-calcite II the MgO concentrations rarely exceed 1000 ppm, Ca-kutnahorite I and II contain much higher MgO between 0.1 and 0.5 wt.%. The late stage carbonates (vug calcite I and II, and vug rhodochrosite) also display significant variability in CaO and MnO. The FeO content varies between 0.1 and 1 wt.%, with modes at 0.5 and 0.2 wt.% in vug calcite I and II, whereas MgO values cluster around 0.7 and 0.5 wt.% for these calcite generations. Vug rhodochrosite has the highest MgO concentrations between 1.3 and 2.8 wt.%.

6.1. Trace elements in carbonate minerals

The trace element composition of 104 carbonate samples was determined. Representative carbonate trace element compositions are listed in Table 4 along with the major element data. Ca-kutnahorite II and Ca-rhodochrosite III veinlets could not be analyzed, because of their small grain sizes. Rare earth element abundances in most carbonate generations were found to be rather low, especially in the case of calcite I, and REE distribution patterns could only be determined for 84 data

Table 7
Representative EPMA data of manganite (*H_2O was calculated by stoichiometry).

Sample	Sai-005b III-001	Sai-056 III-016	Sai-056 III-027	Sai-061 III-012	Sai-061 III-040	Sai-075 III-001	Sai-075 III-023	Sai-083 III-007	Sai-083 III-031	Sai-100a III-028	Sai-100a III-037
Generation	I	I	I	I	I	I	II	II	II	II	II
Wt.%											
SiO_2	0.00	0.00	0.00	0.00	0.00	0.00	0.01	0	0	0.01	0
As_2O_5	0.01	0.06	0.02	0.02	0.02	0.02	0.03	0	0	0	0
Mn_2O_3	87.24	88.33	88.64	89.47	88.80	88.95	89.12	87.98	88.71	89.03	88.99
SO_3	0.01	0.02	0.00	0.00	0.00	0.00	0.02	0.01	0	0.01	0
Al_2O_3	0.10	0.07	0.17	0.01	0.08	0.04	0.31	0.17	0.07	0.25	0.01
Fe_2O_3	0.04	0.07	0.07	0.10	0.04	0.11	0.08	0.06	0.12	0.13	0.19
K_2O	0.00	0.00	0.00	0.00	0.00	0.00	0	0	0	0	0
MgO	0.01	0.00	0.00	0.01	0.02	0.00	0	0	0	0	0
ZnO	0.00	0.01	0.01	0.02	0.00	0.03	0	0	0	0.02	0.01
CaO	1.26	1.83	1.62	0.13	1.15	1.90	1.04	1.36	0.89	0.64	0.44
BaO	0.00	0.01	0.00	0.00	0.00	0.01	0.01	0	0	0.03	0.01
H_2O^*	10.18	10.40	10.42	10.25	10.34	10.48	10.41	10.29	10.29	10.33	10.44
Total	98.92	100.63	100.77	99.99	100.35	101.30	100.86	99.82	100.02	100.36	99.90
Formula (O = 1.5)											
Si	0.00	0.00	0.00	0.00	0.00	0.00	0.00	0.00	0.00	0.00	0.00
As	0.00	0.00	0.00	0.00	0.00	0.00	0.00	0.00	0.00	0.00	0.00
Mn^{2+}	0.00	0.00	0.00	0.00	0.00	0.00	0.00	0.00	0.00	0.00	0.00
S	0.00	0.00	0.00	0.00	0.00	0.00	0.00	0.00	0.00	0.00	0.00
Al	0.00	0.00	0.00	0.00	0.00	0.00	0.01	0.00	0.00	0.00	0.00
Fe^{3+}	0.00	0.00	0.00	0.00	0.00	0.00	0.00	0.00	0.00	0.00	0.00
K	0.00	0.00	0.00	0.00	0.00	0.00	0.00	0.00	0.00	0.00	0.00
Mg	0.00	0.00	0.00	0.00	0.00	0.00	0.00	0.00	0.00	0.00	0.00
Zn	0.00	0.00	0.00	0.00	0.00	0.00	0.00	0.00	0.00	0.00	0.00
Ca	0.02	0.03	0.03	0.00	0.02	0.03	0.02	0.02	0.01	0.01	0.01
Ba	0.00	0.00	0.00	0.00	0.00	0.00	0.00	0.00	0.00	0.00	0.00
Mn^{3+}	0.98	0.98	0.98	1.00	0.99	0.98	0.98	0.98	0.99	0.99	0.99

Table 8
Representative EPMA and LA-ICPMS data of hematite, excluding the REE.

Sample	Sai-065 IV_011	Sai-065 V_028	Sai-065 V_001	Sai-065 V-025	Sai-079 IV_006	Sai-079 V-007	Sai-084 IV_035	Sai-084 V_045	Sai-084 IV_030	Sai-084 V-001	Sai-084 IV_014
Generation	Ia	Ia	Ib	Ib	Ib	Ib	Ib	Ib	Ib	II	II
Wt.%											
SiO_2	0.81	0.61	b.d.	0.07	b.d.	b.d.	0.09	b.d.	0.08	0.17	0.28
MgO	0.01	0.03	b.d.	b.d.	0.02	0.02	b.d.	0.04	b.d.	0.01	0.04
Fe_2O_3	94.06	95.89	99.33	99.87	99.16	99.97	98.30	100.52	97.84	98.13	96.24
V_2O_3	0.01	0.03	b.d.	b.d.	0.38	b.d.	b.d.	b.d.	b.d.	0.03	0.01
CaO	0.42	0.07	0.01	0.09	0.06	0.01	0.07	0.02	0.49	0.36	0.12
Mn_2O_3	0.83	0.79	0.01	0.02	0.68	0.01	0.01	b.d.	0.02	0.66	0.82
WO_3	0.02	0.01	0.03	0.06	0.10	0.06	0.18	b.d.	0.15	0.73	0.86
Total	96.16	97.44	99.38	100.11	100.41	100.07	98.64	100.57	98.58	100.17	98.36
Formula (O = 3)											
Si	0.02	0.02	0.00	0.00	0.00	0.00	0.00	0.00	0.00	0.00	0.01
Mg	0.00	0.00	0.00	0.00	0.00	0.00	0.00	0.00	0.00	0.00	0.00
Fe^{3+}	1.94	1.96	2.00	1.99	1.98	2.00	1.99	2.00	1.99	1.97	1.96
V	0.00	0.00	0.00	0.00	0.01	0.00	0.00	0.00	0.00	0.00	0.00
Ca	0.01	0.00	0.00	0.00	0.00	0.00	0.00	0.00	0.01	0.01	0.00
Mn^{3+}	0.02	0.02	0.00	0.00	0.01	0.00	0.00	0.00	0.00	0.01	0.02
W	0.00	0.00	0.00	0.00	0.00	0.00	0.00	0.00	0.00	0.01	0.01
ppm											
Co	2.4	3	1.5	1.1	0.76	1.1	0.35	1.2	b.d.	1.7	1.9
Ni	b.d.	b.d.	b.d.	b.d.	b.d.	9.6	b.d.	b.d.	b.d.	b.d.	b.d.
Cu	38	30	b.d.	b.d.	2.7	1.5	1.9	b.d.	b.d.	4	b.d.
Zn	303	246	5.1	b.d.	21	3.7	b.d.	b.d.	2.2	34	40
As	7064	7138	893	271	b.d.	415	350	669	118	915	1137
Se	b.d.	b.d.	b.d.	b.d.	b.d.	b.d.	b.d.	b.d.	b.d.	b.d.	b.d.
Sb	915	811	205	77	168	124	198	177	44	2335	2489
Ba	72	58	2	3.4	5.9	2.2	6.1	3.4	2.2	244	161
W	887	923	202	2896	123	113	1830	18	1605	9067	10292
Pb	907	842	5.1	2.9	6.6	3.1	3.8	5.3	2.1	154	187
Bi	34	27	8	2.7	2.9	1.9	4.4	3.8	2.9	69	95
Th	25	25	b.d.	b.d.	b.d.	0.05	0.82	b.d.	0.28	1.3	0.54
U	470	437	8.6	15	40	17	16	21	7.9	266	221

Table 9
Representative EPMA analyses of arsenate minerals (*H_2O in arseniosiderite calculated by stoichiometry).

Sample	Sai-006a As-01	Sai-006a As-03	Sai-015 As-03	Sai-015 As-13	Sai-006a As-07	Sai-006a As-09	Sai-016 As-04	Sai-016 As-06
Mineral	Arsenio-siderite	Arsenio-siderite	Arsenio-siderite	Arsenio-siderite	Tilasite	Tilasite	Cherno-vite-(Y)	Cherno-vite-(Y)
Wt.%								
F	b.d.	b.d.	b.d.	0.02	8.82	8.46	0.16	0.27
As_2O_5	43.96	43.10	44.33	45.15	48.24	48.10	45.63	42.74
Mn_2O_3	0.03	1.09	0.33	0.33	0.61	2.44	0.59	0.41
Fe_2O_3	30.51	28.87	30.92	30.73	0.23	0.33	0.03	0.03
MgO	b.d.	b.d.	b.d.	b.d.	20.18	18.58	b.d.	b.d.
CaO	14.41	14.44	14.88	14.06	26.40	26.33	0.77	1.30
Y_2O_3	b.d.	b.d.	b.d.	b.d.	b.d.	b.d.	35.94	34.21
(O=F)	0	0	0	0	−3.71	−3.56	0	0
H_2O^*	6.90	6.81	7.04	6.98	0	0	0	0
Total	95.81	94.32	97.50	97.26	100.76	100.67	83.12	78.97
Formula								
F	0.00	0.00	0.00	0.01	1.03	0.99	0.02	0.04
As	3.00	2.99	2.97	3.03	0.93	0.93	1.06	1.05
Mn^{3+}	0.00	0.11	0.03	0.03	0.02	0.07	0.02	0.01
Fe^{3+}	2.99	2.88	2.98	2.97	0.01	0.01	0.00	0.00
Mg	0.00	0.00	0.00	0.00	1.11	1.02	0.00	0.00
Ca	2.01	2.05	2.04	1.93	1.04	1.04	0.04	0.07
Y	0.00	0.00	0.00	0.00	0.00	0.00	0.85	0.86

points. While Bi, Sb, and Co concentrations in all carbonates are very low (sometimes below the detection limit), the concentrations of Zn, Ba, W, Pb and U are slightly higher but do not exhibit significant variations within analytical uncertainty. Sr and As, however, are present in much higher concentrations in most carbonates and vary significantly throughout the paragenetic sequence and as a function of major element composition.

Fig. 10 shows boxplots of As and Sr concentrations of the different carbonate minerals. With the exception of Ca-rhodochrosite I and III, the Sr concentrations in all carbonates vary between 30 and 500 ppm. Ca-rhodochrosite II (that replaces calcite I) contains Sr concentrations that are intermediate between those of the calcitic carbonates and Ca-rhodochrosite I that does not occur as replacement of precursor phases. This points to at least partial inheritance of Sr from the precursor carbonates during formation of Ca-rhodochrosite II. Even though Mn-calcite I displays a considerable spread in Sr concentration comparable to that of calcite I, the median value is significantly higher than in calcite I. Ca-rhodochrosite I and II both contain significantly less Sr, only between 2 and 40 ppm. In cases, the arsenic concentrations in calcite I, Mn-calcite I and Fe–Mg calcite were below the detection limit of LA-ICPMS analysis. In general, all carbonate phases belonging to both the pre-ore stage and the two main ore stages, as well as the major replacement carbonates of the alteration stage, contain As concentrations only rarely in excess of 100 ppm. With the onset of braunite alteration and subsequent precipitation of Ca-rhodochrosite III, the As concentrations increase significantly to values between 200 and 1000 ppm. Elevated As concentrations are also shown for the vug filling carbonates.

7. REE distribution in carbonates and hematite

The REE concentration data were normalized against Post Archean Australian Shale (PAAS) (McLennan, 1989) which represents a typical upper crustal composition. PAAS-normalized REE distribution patterns of all analyzed carbonates and hematite are shown in Fig. 12, grouped according to their paragenetic position. Fig. 13 shows scatter plots of important anomalies and element ratios (Ce anomaly versus La anomaly and Y/Ho ratio) that can be used for further discriminating the REE data. Because of low absolute La concentrations in the samples, Ce anomalies were calculated by extrapolation from Nd and Pr according to log $(Ce/Ce^*)_{sn} = \log((Ce_{sn} \cdot Nd_{sn})/Pr^2_{sn})$ (Masuda and Nagasawa, 1975). La anomalies were calculated as log $(La/La^*)_{sn} = \log((La_{sn} \cdot Nd^2_{sn})/Pr^3_{sn})$. With the exception of Mn-calcite II and Fe–Mg calcite, the total REE concentrations of the carbonate minerals are very low. The REE patterns of all carbonates, independent of carbonate chemistry, are characterized by elevated LREE, a pronounced negative Eu anomaly, and flat to slightly elevated MREE and HREE distributions. La anomalies were found to be present in most of the analyzed carbonates (Fig. 13a).

The variability of the REE patterns as a function of their paragenetic position is quite significant. Particularly noteworthy are the differences for the ore stage carbonate phases. While pre-ore stage Ca-rhodochrosite I (Fig. 12a) has comparably flat REE patterns with only a slight LREE depletion, the LREE depletion in all subsequent ore stage carbonates (calcite I, Mn-calcite I, Fe–Mg calcite) is much more developed. Hematites that are cogenetic with Mn-calcite I have distinct REE patterns that show only a slight depletion in LREE, a flat MREE and HREE distribution, and a weak negative Eu anomaly (Fig. 12i). Another striking feature is the strongly contrasting behavior of Ce. Ca-rhodochrosite I, calcite I and Fe–Mg calcite display positive anomalies, whereas Mn-calcite I shows a larger variability with Ce anomalies being slightly negative. Likewise, systematic differences in the Y/Ho ratios are present. Calcite I and Fe–Mg calcite are characterized by Y/Ho ratios that are much larger than 1, whereas Mn-calcite I again is more variable and has Y/Ho ratios ranging from about 1 to slightly greater values (Fig. 13b).

Carbonates of the alteration stage also show significant variability in their REE patterns. Ca-rhodochrosite II (Fig. 12b), which replaces calcite I, is less strongly depleted in LREE than the calcitic precursor. The distribution patterns differ significantly from those of pre-ore stage Ca-rhodochrosite I (Fig. 12a), reflecting systematic changes in formation conditions as the hydrothermal system evolved with time. The REE patterns of Ca-kutnahorite I (Fig. 12d) are very similar to those of Ca-rhodochrosite II, whereas Mn-calcite II (Fig. 12f) has the largest negative La and slightly positive Ce anomalies. The Y/Ho ratios of Mn-calcite II are around 1. The late stage vug filling carbonates also display large negative La anomalies and positive Ce anomalies (Fig. 12h, j). In contrast to Mn-calcite II, their Y/Ho ratios are much larger than 1.

8. Discussion and conclusions

The vein type Mn–Fe–As mineralization at Sailauf is characterized by two distinct ore assemblages and subsequent complex replacement and alteration features. The systematic changes in mineral assemblages

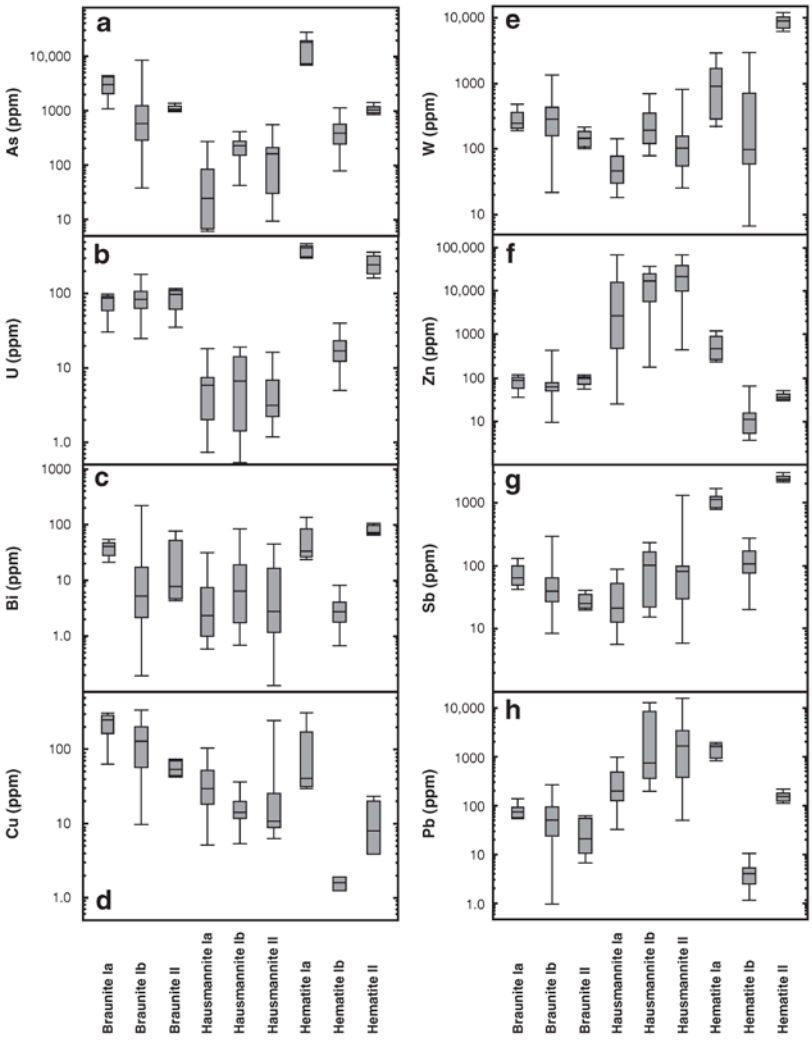

Fig. 8. Boxplots of selected trace element concentrations in Mn oxides and hematite. Horizontal lines inside the boxes represent the median values. The box limits mark the upper and lower quartile of data, and the outer brackets the maximum and minimum concentrations.

in each mineralization stage are reflected by the trace element and REE distribution in carbonate and oxide phases. The mineral assemblages and compositions have recorded progressive changes in fluid chemistry throughout the lifetime of the hydrothermal system. This information, in conjunction with constraints from mineral stability diagrams, will be used to reconstruct the depositional conditions and the main processes controlling the formation of the Sailauf Mn–Fe–As deposit. The results of this process analysis will then be compared to other Mn–Fe deposits in different settings with the aim to identify common features.

8.1. Fluid evolution of the hydrothermal system

The most striking feature of the Sailauf mineralization is the occurrence of two different ore assemblages, the first dominated by Mn-oxides and calcite, and the second by Fe-oxides, manganoan calcite, and minor quartz and barite. This substantial shift in the stable mineral assemblages likely reflects first-order changes in key parameters of the hydrothermal fluids. The solubility and fractionation behavior of Fe and Mn in hydrothermal systems are largely controlled by temperature, pH, oxidation state, and the relative concentrations of important complexing ligands (Crerar et al., 1980; Hem, 1972; Krauskopf, 1957; Wood and Samson, 1998). The hydrothermal solubility of Fe and Mn is greatly enhanced in chloride solutions due to the formation of stable chloride complexes (Heinrich and Seward, 1990; Palmer and Hyde, 1993; Suleimenov and Seward, 2000; Testemale et al., 2009). The formation of carbonate and bicarbonate complexes in carbonate-rich aqueous solutions can also affect the transport and deposition of Fe and Mn (Bruno et al., 1992; Wolfram and Krupp, 1996; Wood and Samson, 1998).

The stability of chloride species of Fe and Mn in hydrothermal fluids up to 300 °C is rather well studied (Gammons and Seward, 1996; Liu et al., 2006; Suleimenov and Seward, 2000; Tagirov et al., 2000; Testemale et al., 2009), whereas thermodynamic data for carbonate and bicarbonate species are only available up to moderate temperatures. Reliable experimental data are available up to temperatures of 55 °C, and stability constants up to 300 °C are based on limited experimental data and

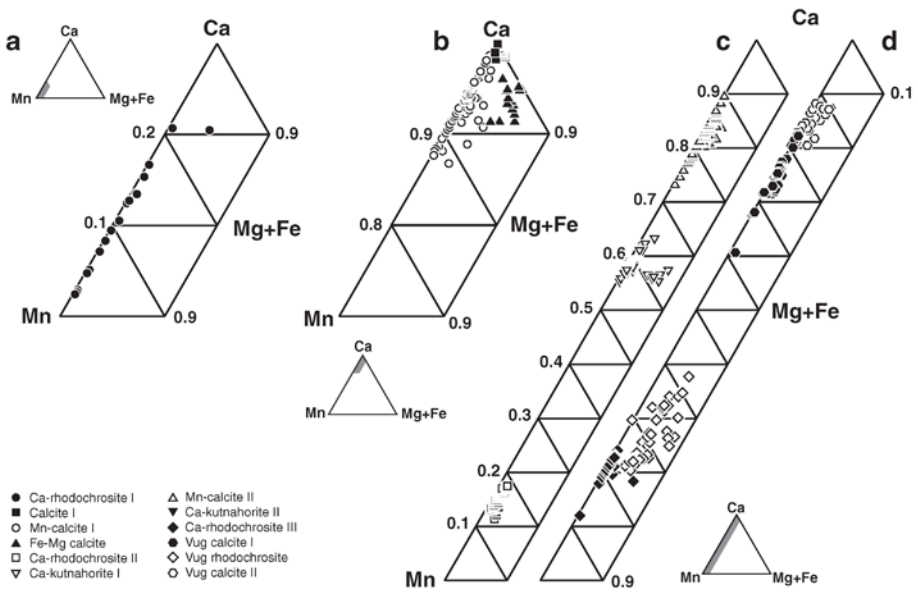

Fig. 9. Major element composition of hydrothermal carbonates in Ca – Mn – (Fe + Mg) space. (a) Variation within Ca-rhodochrosite I of the pre-ore stage. (b) Main carbonate types from ore stages 1 and 2. (c) Early carbonates of the alteration stage. (d) Late-stage vug filling carbonates.

extrapolations (Böttcher and Usdowski, 1990; Wolfram and Krupp, 1996). The stability of Fe and Mn carbonates relative to the oxide phases is strongly dependent on the activity of CO_2 (Crerar et al., 1980; French, 1971). Of particular importance for the transport and deposition of Fe and Mn is the large difference in their redox potential, with the Fe^{3+}/Fe^{2+} transition located at much lower oxidation state than the redox transition for Mn (Crerar et al., 1980; Hem, 1972; Krauskopf, 1957).

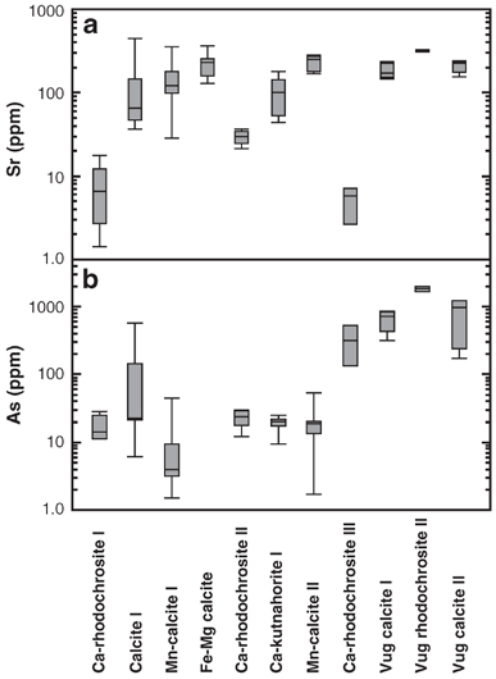

Fig. 10. Boxplots of As and Sr concentrations in the different hydrothermal carbonate generations.

Considering the major controls on Fe and Mn solubility, the changes in mineral assemblages in the different ore stages in the Sailauf vein systems can be interpreted in terms of the depositional conditions. The transition between the two main ore stages records a change from Mn oxides and Mn-free calcite (ore stage 1) to hematite and manganoan calcite (ore stage 2). In the alteration stage that postdates the main ore mineral deposition, different compositionally variable carbonates (calcian rhodochrosite, kutnahorite, different types of manganoan calcite) have formed. Fig. 14 shows activity diagrams, where the stability fields of Fe and Mn minerals is plotted as function of pH, log (f_{O2}), log (f_{CO2}) and log (a_{SiO2}). The diagrams were constructed at 150 °C and saturated water vapor pressure, which is well within the T–P range reported for other post-Variscan hydrothermal vein deposits (Baatartsogt et al., 2007; Lüders and Möller, 1992; Staude et al., 2007). The mineral stability diagrams consider the Mn oxide phases manganosite, hausmannite, braunite, bixbyite and pyrolusite, and the Mn carbonate rhodochrosite (Fig. 14). Because no thermodynamic data are available for manganite, its stability field could not be calculated, and bixbyite which also contains trivalent Mn will serve as a proxy for manganite. The stability diagrams show that CO_2 fugacity largely controls the stability of rhodochrosite and siderite compared to the oxide phases (Fig. 14a), and that the silica activity determines whether braunite or other Mn oxides are stable (Fig. 14b). The occurrence of hausmannite and manganite in ore stage 1 requires that the silica activity has been rather low (the system was quartz undersaturated), whereas the coexistence of hematite with minor quartz in ore stage 2 indicates a substantially larger silica activity. In ore stage 2, Mn is only present as minor constituent in Mn-calcite I, which is approximated by the stability of the rhodochrosite component. In order to stabilize the mineral assemblage of ore stage 2, requires an increase in silica activity and CO_2 fugacity (Fig. 14).

A possible mechanism to cause major changes in the key parameters of the hydrothermal system are variations in the mixing ratios of two chemically contrasting fluids, which was proposed as the essential

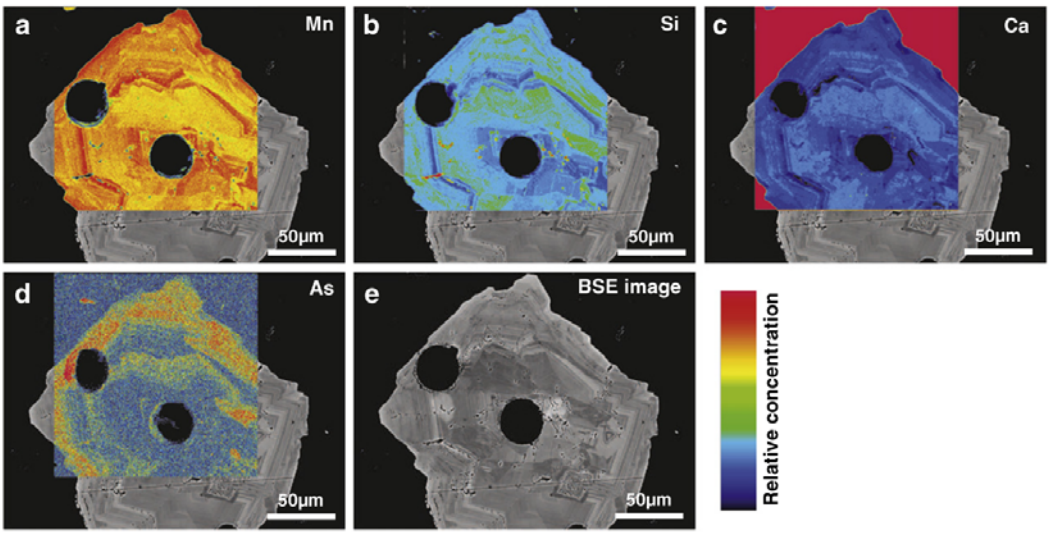

Fig. 11. Element maps of a braunite-Ib crystal, illustrating the distribution of (a) Mn, (b) Si, (c) Ca, (d) As concentrations in relation to the growth zoning visible in (e) the BSE image. The maps reveal a considerable zoning in the major element concentrations and arsenic. Note that the arsenic enrichments appears to be not correlated with the major element chemistry.

depositional mechanism for hydrothermal mineralization in the Spessart and many other post-Variscan ore deposits in central Europe (Baatartsogt et al., 2007; Behr et al., 1987; Dill, 1988; Dill and Nielsen, 1987; Muchez et al., 2005; Staude et al., 2007; Wagner et al., 2010). In the Spessart district, fluid mixing would have involved fluids derived from the crystalline basement and formation waters originating from the Zechstein dolomite sequence. The basement fluids would be saline, have a near neutral pH and would be quartz saturated, whereas formation waters from Zechstein carbonates are expected to be more alkaline and probably quartz undersaturated.

During the formation of ore stage 1, the mineral assemblage was precipitated from silica undersaturated fluids, suggesting that the contribution of fluids from the Zechstein dolomite must have been dominant. Conversely, the transition to ores stage 2 then reflects a change towards conditions where the basement derived fluids were more important. Because Mn oxides do not occur in ore stage 2, it would also be necessary to decrease the oxidation state and increase the CO_2 fugacity to stabilize carbonates minerals over the oxides. This, in turn, would lead to the conclusion that the basement derived fluids would have been more reducing and CO_2 rich than those from the Zechstein aquifer, which appears geologically unreasonable. The apparent contradiction can be resolved when considering the effect of pH on the relative solubility of Fe and Mn oxide minerals. For reasonable Mn/Fe ratios in the post-Variscan hydrothermal fluids, the Mn oxides will be more soluble at near-neutral to slightly acidic pH than the Fe oxides (Fig. 14c). Increasing the contribution of basement fluids to the hydrothermal system, which could be related to tectonic activation of the fault systems hosting the veins, would drive the pH from slightly alkaline to near-neutral or slightly acidic. This would make Mn oxides more soluble compared to Fe oxides, resulting in precipitation of hematite–quartz assemblages during ore stage 2.

The mineral stability constraints would explain the distinct separation of Fe and Mn oxides between both ore stages. Considerable pH increase due to initial mixing of basement derived fluids with the Zechstein groundwaters would efficiently precipitate hematite first. This is evidenced by the presence of early hematite in cockade ores formed during the initial stages of ore stage 1, which is then overgrown by Mn oxides (Fig. 4). The ore stage 2 would be essentially dominated by basement derived fluids, resulting in somewhat lower pH and higher silica activity, promoting deposition of hematite and quartz. Manganese would be largely retained in solution in ore stage 2, and would only become incorporated into Mn-bearing calcite. The depositional conditions during the alteration stage carbonates are much more difficult to assess. The availability of dissolved Mn for incorporation into manganoan calcites or rhodochrosite, in conjunction with the rare occurrence of secondary Mn oxides and hematite, suggests that this stage was characterized by large fluctuations in f_{O2}, f_{CO2} and pH.

8.2. Significance of REE patterns of carbonate minerals

This interpretation is supported by the distinct differences in the REE patterns of the carbonate minerals. All hydrothermal carbonates display a pronounced negative Eu anomaly. At temperatures below about 200 °C, Eu anomalies can only be inherited from the host rocks, which in the case of felsic rocks should cause negative anomalies due to chloritization of biotite (Lüders et al., 1993; Möller and Dulski, 1999). Shales of the Kupferschiefer basin possess weakly positive to weakly negative Eu anomalies (Bechtel et al., 2001). Negative Ce anomalies result from oxidation of Ce^{3+}, which may be selectively removed as Ce^{4+} by adsorption to mineral surfaces (Möller and Dulski, 1999; Wood, 1990). Conversely, more reducing fluids reacting with preexisting Ce enriched mineral surfaces may acquire positive anomalies (Möller and Dulski, 1999). The strong LREE depletion that is observed in our samples would be consistent with fluids rich in dissolved bicarbonate and carbonate, which form stronger complexes with HREE than with LREE and thus preferentially remove HREE from the source material (Bau, 1991; Haas et al., 1995; Wood, 1990).

Carbonates of the different ore stages all have systematically different REE patterns, in qualitative agreement with changes in pH and oxidation state. Diagenetic and hydrothermally influenced carbonates from sediments of the Zechstein basin have been analyzed for their REE distribution by Fischer et al. (2006). They have positive Ce anomalies, which was explained by reductive Ce release from degraded marine particles within the Zechstein sediments and Y/Ho ratios in excess of 1 in both types of carbonates. The slightly positive Ce anomalies and Y/Ho ratios larger than 1 in calcite I may therefore indicate an inheritance by fluids that percolated through diagenetically

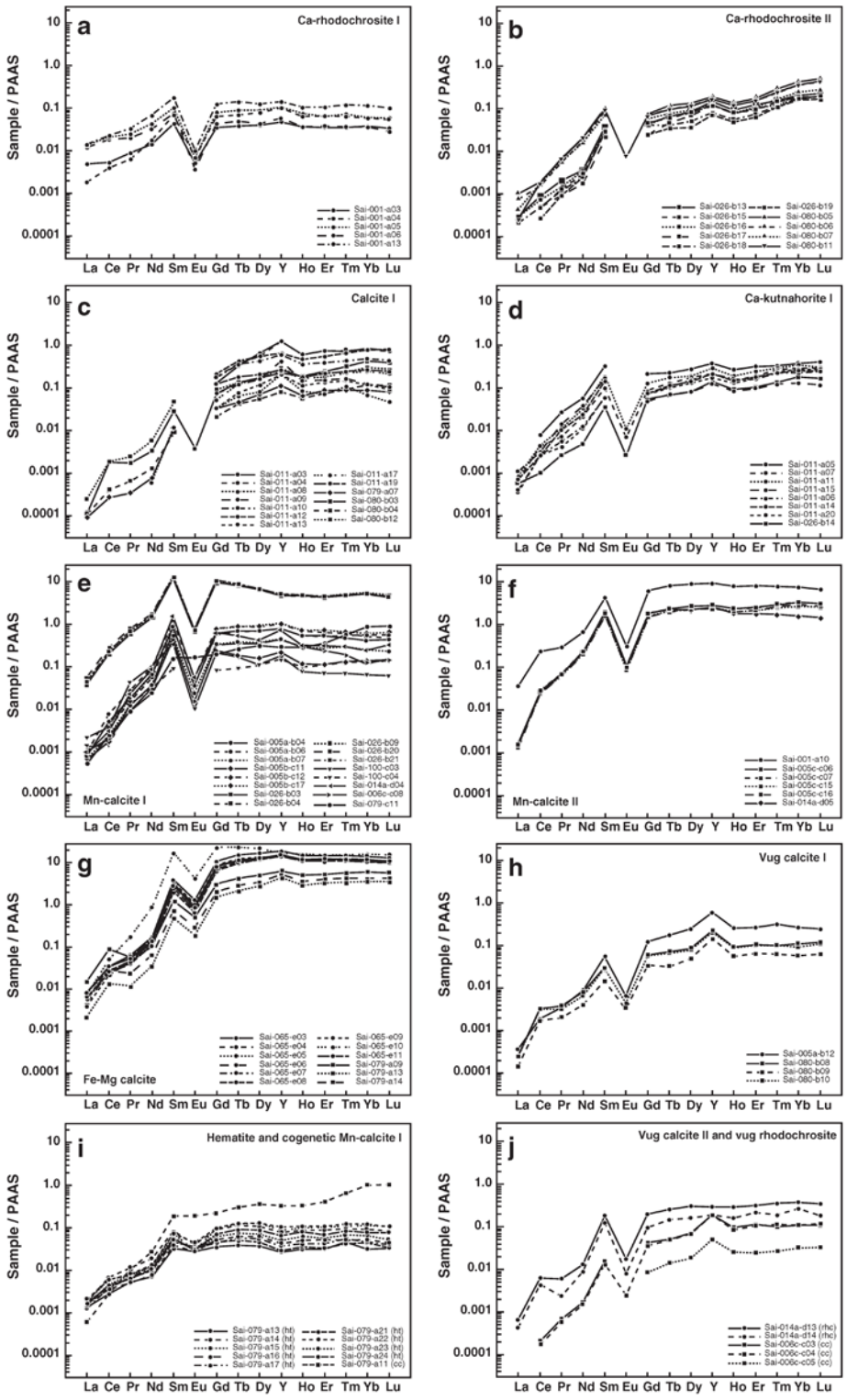

Fig. 12. REE distribution patterns of carbonate minerals, normalized to PAAS (McLennan, 1989).

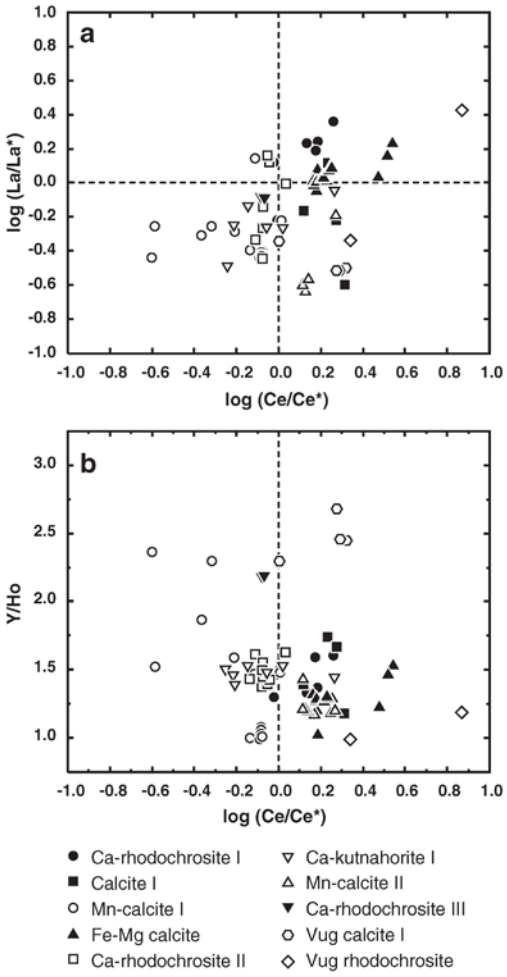

Fig. 13. Discrimination plots of Ce-anomalies versus La anomaly (a) and Y/Ho ratio (b). Some carbonate data could not be plotted in these diagrams, because the Ce concentrations were below the detection limit.

influenced Zechstein carbonates. The REE patterns of Mn-calcite I (ore stage 2) lack positive Ce anomalies and the Y/Ho ratios are generally lower (Fig. 13b).

Although we do not have good control on the REE budget of the crystalline basement rocks, leachates of Variscan gneisses and granites had no significant Ce anomaly (Möller et al., 1997a, 1997b). Accepting this source feature, dominance of fluids derived from the crystalline basement during ore stage 2 would also result in REE patters that would display no or weak Ce anomalies. Interpreting the REE patterns of the carbonate phases that formed during the replacement stage additionally requires to consider inheritance effects. Recrystallization and

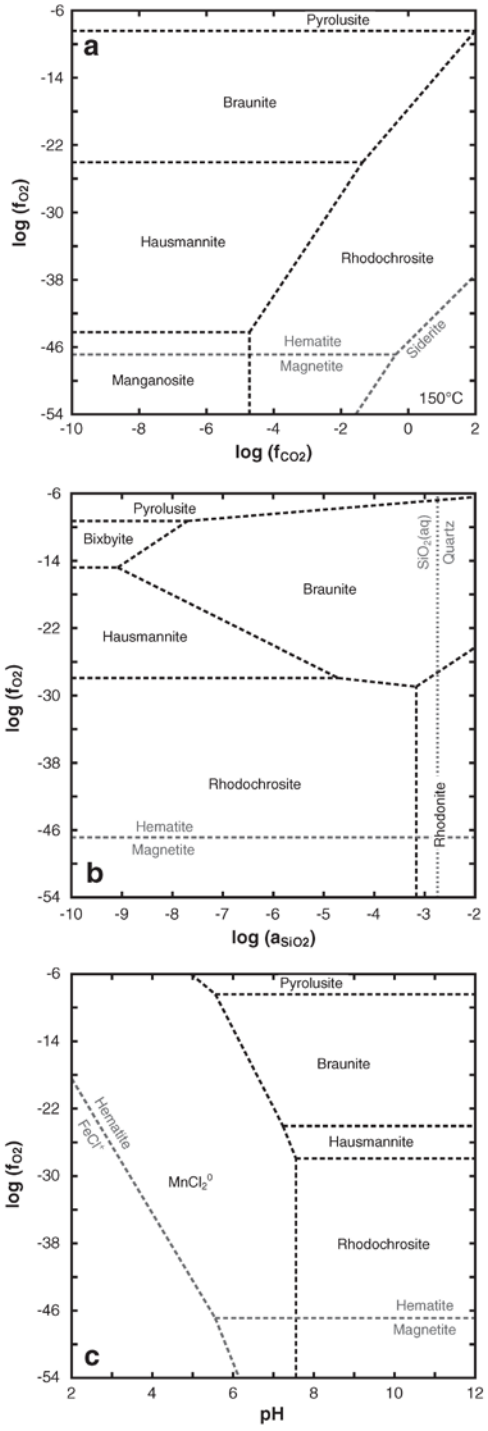

Fig. 14. Phase diagrams constructed at 150 °C and saturated water vapor pressure, showing stability relationships of Fe and Mn minerals as function of oxygen fugacity, CO_2 fugacity, silica activity and pH. (a) log (f_{O2}) vs. log (f_{CO2}) diagram, with log (a_{SiO2}) fixed at −6.0. (b) log (f_{O2}) vs. log (a_{SiO2}) diagram, with log(f_{CO2}) fixed at −2.0. (c) log (f_{O2}) vs. pH diagram, with log (a_{SiO2}) and log (f_{CO2}) fixed at −6.0 and −2.0, respectively. The concentrations of Fe and Mn were assumed to be 65 and 195 ppm, and were converted into aqueous species activities using the HCh speciation code (Shvarov and Bastrakov, 1999). The mineral stability diagrams were constructed with the GeochemistsWorkbench software (Bethke, 2007). Thermodynamic data for aqueous species were taken from the SUPCRT database and subsequent updates (Johnson et al., 1992; Shock et al., 1989, 1997; Sverjensky et al., 1997). Data for rock-forming minerals came from Holland and Powell (1998) and those for braunite, hausmannite, bixbyite and pyrolusite from Chatterjee et al. (1998).

replacement of carbonates would typically occur under conditions where fluid/mineral ratios are rather small, and hence the REE budget of new carbonate phases should be largely inherited from the precursor phase. The REE patterns of kutnahorite and rhodochrosite are further complicated by crystallographic control on REE fluid-mineral partitioning. Minerals that mainly contain cations with ionic radii smaller than Ca (Mg, Fe^{2+} and Mn^{2+}) will favor HREE incorporation (Morgan and Wandless, 1980). The REE patterns of Ca-rhodochrosite II may be largely explained by this effect, because they display a constant increase in HREE not observable in any of the other carbonate types. Yet, their LREE distribution is quite similar to that of the precursor carbonates and may therefore reflect inheritance from the precursor.

8.3. Source and origin of Mn–Fe deposits

The Sailauf vein-type Mn–Fe–As mineralization is structurally related to the basement-cover unconformity, which is a common feature with many post-Variscan Pb–Zn-fluorite-barite ore deposits of Mesozoic age in central Europe. Fluid mixing processes are commonly invoked to explain mineral precipitation (Baatartsogt et al., 2007; Behr et al., 1987; Dill, 1988; Dill and Nielsen, 1987; Muchez et al., 2005; Staude et al., 2007; Wagner et al., 2010), and the structural setting of the Sailauf mineralization and the available mineralogical and geochemical evidence would suggest a similar depositional environment. Although unconformity related Mn–Fe deposits are not described in the literature, the Sailauf mineralization displays striking mineralogical and geochemical similarities with Mn–Fe deposits in widely differing geologic settings. These similarities point to common fluid sources and depositional processes, and process analysis of the Sailauf system will contribute to understanding the controls on essential features of Mn–Fe deposits such as element zoning, redox transitions, variation in silica activity, and the trace element inventory typically associated with Mn and Fe.

Manganiferous vein deposits have been described from many localities worldwide (Glasby et al., 2005; Hein et al., 2000; Leal et al., 2008; Nicholson, 1986; Roy, 1981). Examples in Germany can be found in Ilfeld (Harz) and Ilmenau (Thüringen). The hydrothermal veins at Ilfeld contain Mn and Fe oxides in carbonate, quartz and barite gangue, and are hosted by Lower Permian rhyodacitic lavas and ignimbrites (Hewett, 1972; Salzmann, 1935). Salzmann (1935) reports the occurrence of spatially separated Fe and Mn oxide veins, and an increase in hematite abundance with depth. The hydrothermal veins at Ilmenau contain Mn oxides associated with calcite or barite gangue, which occur in Permian quartz porphyries and red beds of the Lower Permian (Hewett, 1972). Some authors considered vein type deposits that are associated with marine sediments as subsurface feeder systems of stratabound sedimentary exhalative Mn–Fe deposits (Hein et al., 2000). Prominent examples of stratabound sedimentary–exhalative orebodies include the Långban and Sjögruvan deposits, central Sweden (Boström et al., 1979; Holtstam and Mansfeld, 2001), the Franklin and Sterling Hill ore bodies, USA (Frondel and Baum, 1974; Johnson and Skinner, 2003; Peck et al., 2009), and the Boléo district, Mexico (Conly et al., 2011).

The Sailauf Mn–Fe–As veins show a considerable enrichment in the same trace element suite that is commonly found in other Mn–Fe deposits, notably As, W, Sr, Zn, Sb, Cu, Pb, Zn and U (Fig. 8). The only exception is Ba, which is often present at high concentrations in a variety of deposits, whereas the enrichment in Sailauf oxides is rather low, although the occurrence of barite (see Fig. 4) indicates that Ba was also present in the hydrothermal fluid. Nicholson (1992) proposed that the element association As–Ba–Cu–Li–Mo–Pb–Sb–Sr–V–Zn is typical for Mn oxide deposits of hydrothermal origin, and W and Tl were identified to be enriched in hydrothermal Mn–Fe vein deposits in the southwestern USA and Argentina (Leal et al., 2008; Roy, 1981). Enrichment in this element suite have also been identified in stratiform sedimentary–exhalative deposits of the Långban type in the Bergslagen province in Sweden (Holtstam, 2001; Holtstam and Mansfeld, 2001) as well as at the Val Ferrara deposit in Switzerland (Brugger and Gieré, 2000). At Långban, Nysten et al. (1999) additionally described enrichments in Be, which at Sailauf is also observed in late stage assemblages (bertrandite and bergslagite).

The similarities in trace metal associations found in Fe–Mn deposits of very different origin was already observed in other studies and was explained as being largely controlled by the source rock lithologies of the hydrothermal systems, irrespective of the specific ore precipitation mechanism (Glasby et al., 2005; Hein et al., 2000; Hewett, 1964, 1972; Lüders et al., 2001). For the majority of these deposits, a genetic link with felsic lithologies has been proposed. The Långban and Sjögruvan deposits in Bergslagen have been related to felsic arc-related volcanic rocks (Boström et al., 1979; Holtstam and Mansfeld, 2001), and rhyolite and orthogneisses are considered as the metal source of the Val Ferrara deposit in Switzerland (Brugger and Gieré, 2000). The geochemical similarity between vein type deposits, ferromanganoan deposits in back-arc settings, and terrestrial hot-spring systems and the Mn–Fe–As mineralization at Sailauf points to a common link with felsic lithologies. Potential source rock candidates at Sailauf are the Permian rhyolites and the granitic orthogneisses, which would provide large volumes of rock that could have supplied the characteristic element suite.

In terrestrial Mn-rich hydrothermal systems, a clear zonation of Mn minerals with increasing depth has been documented (Roy, 1981). The deepest parts of the vein systems contain Mn^{2+} bearing minerals (rhodochrosite, rhodonite, tephroite) (Hewett, 1964; Roy, 1981). These comparatively reduced ore associations then grade into shallower zones dominated by mixed valence oxides (bixbyite, braunite) and finally to tetravalent Mn oxides in the uppermost zones. This systematic mineral zoning reflects increasing oxidation via fluid mixing with shallow oxygenated groundwater at decreasing deposition temperatures. Similar redox gradients may also develop during alteration of Mn ores by interaction with late-stage fluids, as recorded in the fissure hosted mineralization at Långban (Jonsson and Broman, 2002) or the fault-controlled metasomatic alteration of the Proterozoic marine-sedimentary Kalahari Manganese Fields, South Africa (Gutzmer and Beukes, 1995). In both cases, the Mn oxide minerals have been extensively modified in response to changes in fluid composition, resulting in replacement of precursor ore assemblages.

The Sailauf Mn–Fe–As vein mineralization provides direct evidence for multistage fluid processes that have resulted in separation of Mn and Fe, likely due to progressive or episodic changes in key state parameters. As opposed to other Mn–Fe deposits which show systematic changes in Mn and Fe oxide mineralogy as a function of depth below the paleosurface or proximity to a hydrothermal vent, the Sailauf hydrothermal system records comparable changes as a function of time. The clear association with felsic rock lithologies and the geological setting immediately below the Variscan unconformity suggest that the Sailauf Mn–Fe–As mineralization has likely formed through fluid mixing processes that caused major variations in pH, CO_2 fugacity, oxidation state and silica activity. Fluid mixing involved basement-derived fluids that had picked up their metal inventory by interaction with felsic source rocks, and shallow groundwaters or formation waters from Zechstein sediments.

Acknowledgments

This project was made possible by funding from the German Research Council (DFG). Indra Gill-Kopp is thanked for preparing polished thin sections of excellent quality. Constructive comments by two anonymous reviewers and AE Albert Gilg greatly helped to improve this paper.

Appendix A. Analytical conditions for electron-probe microanalysis

Minerals	Elements	Acceleration voltage (kV)	Probe current (nA)	Beam diameter (μm)	Standard materials	Integration times (s)
Carbonates	Mg, Si, Ca, Mn, Fe, Zn, As, Sr, Ba	20	20	5	Periclase (Mg – Kα) Diopside (Si – Kα) Dolomite (Ca – Kα) Rhodonite (Mn – Kα) Hematite (Fe – Kα) Zn (Zn – Kα) GaAs (As – Lα) SrTiO3 (Sr – Lα) Barite (Ba – Lα)	16/8 (Mg, Si, Ca, Fe, Zn, As, Ba) 30/15 (Mn, Sr)
Braunite, hausmannite, manganite	Mg, Al, Si, S, K, Ca, Mn, Fe, Zn, As, Ba	20	20	Focused	Diopside (Mg – Kα, Si – Kα, Ca – Kα) Al2O3 (Al – Kα) Pyrite (S – Kα) Sanidine (K – Kα) Bustamite (Mn – Kα) Hematite (Fe – Kα) Zn (Zn – Kα) GaAs (As – Lα) Barite (Ba – Lα)	16/8 (Mg, Al, Si, S, K, Ca, Mn, Zn, As, Ba) 30/15 (Fe)
Hematite	Mg, Si, Ca, V, Mn, Fe, W	20	20	focused	Diopside (Si – Kα, Mg – Kα) Scheelite (Ca – Kα, W – Kα) V (V – Kα) Bustamite (Mn – Kα) Hematite (Fe – Kα)	16 / 8 (all)
Arsenates	F, Mg, Ca, Mn, Fe, As, Y	15	20	5	Fluorite (F – Kα) Periclase (Mg – Kα) Dolomite (Ca – Kα) Bustamite (Mn – Kα) Hematite (Fe – Kα) GaAs (As – Lα) Y2O3 (Y – Lα)	16/8 (Mg, Ca, Mn, Fe, As) 30/15 (F, Y)

References

Abs-Wurmbach, I., Peters, T., Langer, K., Schreyer, W., 1983. Phase relations in the system Mn – Si – O: an experimental and petrological study. N. Jahrb. Mineral. Abh. 146, 258–279.

Baatartsogt, B., Schwinn, G., Wagner, T., Taubald, H., Beitter, T., Markl, G., 2007. Contrasting paleofluid systems in the continental basement: a fluid inclusion and stable isotope study of hydrothermal vein mineralization, Schwarzwald district, Germany. Geofluids 7, 123–147.

Bau, M., 1991. Rare-earth element mobility during hydrothermal and metamorphic fluid–rock interaction and the significance of the oxidation state of europium. Chem. Geol. 93, 219–230.

Baudracco-Gritti, C., 1985. Substitution of bivalent manganese by calcium in the minerals of the group—braunite, neltnerite, braunite-II. Bull. Mineral. 108, 437–445.

Bechtel, A., Ghazi, A.M., Elliot, W.C., Oszczepalski, S., 2001. The occurrences of the rare earth elements and the platinum group elements in relation to base metal zoning in the vicinity of Rote Faule in the Kupferschiefer of Poland. Appl. Geochem. 16, 375–386.

Behr, H.J., Horn, E.E., Frentzel-Beyme, K., Reutel, C., 1987. Fluid inclusion characteristics of the Variscan and post-Variscan mineralizing fluids in the Federal Republic of Germany. Chem. Geol. 61, 273–285.

Bethke, C.M., 2007. Geochemical and Biogeochemical Reaction Modeling. Cambridge University Press, New York.

Boström, K., Rydell, H., Joensuu, O., 1979. Långban, an exhalative sedimentary deposit? Econ. Geol. 74, 1002–1011.

Böttcher, M., Usdowski, E., 1990. An estimation of dissociation constants for manganese (II) complexes in aqueous solutions up to 300°C. Z. Phys. Chem. Neue Folge 167, 81–86.

Brugger, J., Gieré, R., 2000. Origin and distribution of some trace elements in metamorphosed Fe – Mn deposits, Val Ferrera, Eastern Swiss Alps. Can. Mineralog. 38, 1075–1101.

Bruno, J., Wersin, P., Stumm, W., 1992. On the influence of carbonate in mineral dissolution: II. The solubility of $FeCO_3$ (s) at 25 °C and 1 atm total pressure. Geochim. Cosmochim. Acta 56, 1149–1155.

Burkhard, M., 1993. Calcite twins, their geometry, appearance and significance as stress–strain markers and indicators of tectonic regime: a review. J. Struct. Geol. 15, 351–368.

Chatterjee, N.D., Krüger, R., Haller, G., Olbricht, W., 1998. The Bayesian approach to an internally consistent thermodynamic database: theory, database, and generation of phase diagrams. Contrib. Mineral. Petrol. 133, 149–168.

Conly, A.G., Scott, S.D., Bellon, H., 2011. Metalliferous manganese oxide mineralization associated with the Boleo Cu – Co – Zn district, Mexico. Econ. Geol. 106, 1173–1196.

Crerar, D., Cormick, R., Barnes, H., 1980. Geochemistry of manganese: an overview. In: Varentsov, I., Grasselly, G. (Eds.), Geology and geochemistry of manganese, pp. 293–334.

De Villiers, P., Buseck, P.R., 1989. Stacking variations and nonstoichiometry in the bixbyite–braunite polysomatic mineral group. Am. Mineralog. 74, 1325–1336.

Dill, H.G., 1988. Geologic setting and age relationship of fluorite–barite mineralization in southern Germany with special reference to the late paleozoic unconformity. Miner. Deposita 23, 16–23.

Dill, H.G., Nielsen, H., 1987. Geochemical and geological constraints on the formation of unconformity-related vein baryte deposits of Central Europe. J. Geol. Soc. Lond. 144, 97–105.

Dombrowski, A., Okrusch, M., Richter, P., Henjes-Kunst, F., Höhndorf, A., Kröner, A., 1995. Orthogneisses in the Spessart Crystalline Complex, north–west Bavaria: Silurian granitoid magmatism at an active continental margin. Geol. Rundsch. 84, 399–411.

Fischer, M., Botz, R., Schmidt, M., Rockenbauch, K., Garbe-Schönberg, D., Glodny, J., Gerling, P., Littke, R., 2006. Origins of CO_2 in Permian carbonate reservoir rocks (Zechstein, Ca2) of the NW-German Basin (Lower Saxony). Chem. Geol. 227, 184–213.

Franke, W., 2000. The mid-European segment of the Variscides: tectonostratigraphic units, terrane boundaries and plate tectonic evolution. Geol. Soc. Lond. Spec. Publ. 179, 35–61.

French, B.M., 1971. Stability relations of siderite ($FeCO_3$) in the system Fe – C – O. Am. J. Sci. 271, 37–78.

Frenzel, G., 1980. The manganese ore minerals. In: Varentsov, I., Grasselly, G. (Eds.), Geology and Geochemistry of Manganese, pp. 25–157.

Frondel, C., Bauer, L., 1955. Kutnahorite: a manganese dolomite: $CaMn(CO_3)_2$. Am. Mineralog. 40, 748–760.

Frondel, C., Baum, J.L., 1974. Structure and mineralogy of the Franklin zinc–iron–manganese deposit, New Jersey. Econ. Geol. 69, 157–180.

Gammons, C.H., Seward, T.M., 1996. Stability of manganese(II) chloride complexes from 25 to 300 °C. Geochim. Cosmochim. Acta 60, 4295–4311.

Glasby, G., Papavassiliou, C., Mitsis, J., Valsami-Jones, E., Liakopoulos, A., Renner, R., 2005. The Vani manganese deposit, Milos island, Greece: a fossil stratabound Mn – Ba – Pb – Zn – As – Sb – W-rich hydrothermal deposit. Dev. Volcanol. 7, 255–291.

Guillong, M., Heinrich, C.A., 2007. Sensitivity enhancement in laser ablation ICP-MS using small amounts of hydrogen in the carrier gas. J. Anal. At. Spectrom. 22, 1488–1494.

Guillong, M., Meier, D.L., Allan, M.M., Heinrich, C.A., Yardley, B.W.D., 2008. SILLS: a Matlab-based program for the data reduction of laser ablation ICP-MS data of homogeneous materials and inclusions. In: Sylvester, P. (Ed.), Laser Ablation ICP-

MS in the Earth Sciences: Current Practices and Outstanding Issues: Mineral. Assoc. Can. Short Course Ser., 40, pp. 328–333.
Günther, D., Frischknecht, R., Heinrich, C.A., Kahlert, H.J., 1997. Capabilities of an argon fluoride 193 nm excimer laser for laser ablation inductively coupled plasma mass spectometry microanalysis of geological materials. J. Anal. At. Spectrom. 12, 939–944.
Gutzmer, J., Beukes, N., 1995. Fault-controlled metasomatic alteration of early Proterozoic sedimentary manganese ores in the Kalahari manganese field, South Africa. Econ. Geol. 90, 823–844.
Haas, J.R., Shock, E.L., Sassani, D.C., 1995. Rare-earth elements in hydrothermal systems—estimates of standard partial molal thermodynamic properties of aqueous complexes of the rare-earth elements at high-pressures and temperatures. Geochim. Cosmochim. Acta 59, 4329–4350.
Hautmann, S., Brander, H., Lippolt, H., Lorenz, J., 1999. K–Ar and (U+Th) –He chronometry of multistage alteration and mineralisation in the Hartkoppe rhyolite, Spessart, Germany. J. Conf. Abstr. 4, 769.
Hein, J., Stamatakis, M., Dowling, J., 2000. Trace metal-rich Quaternary hydrothermal manganese oxide and barite deposit, Milos Island, Greece. Trans. Inst. Min. Metall. B Appl. Earth. Sci. 109, 67–76.
Heinrich, C., Seward, T., 1990. A spectrophotometric study of aqueous iron (II) chloride complexing from 25 to 200 °C. Geochim. Cosmochim. Acta 54, 2207–2221.
Hem, J.D., 1972. Chemical factors that influence the availability of iron and manganese in aqueous systems. Geol. Soc. Amer. Bull. 83, 443–450.
Hewett, D.F., 1964. Veins of hypogene manganese oxide minerals in the southwestern United States. Econ. Geol. 59, 1429–1472.
Hewett, D.F., 1972. Manganite, hausmannite, braunite; features, modes of origin. Econ. Geol. 67, 83–102.
Holland, T.J.B., Powell, R., 1998. An internally consistent thermodynamic data set for phases of petrological interest. J. Metamorph. Geol. 16, 309–343.
Holtstam, D., 2001. W and V mineralization in Långban-type Fe–Mn deposits: epigenetic or syngenetic? GFF 123, 29–33.
Holtstam, D., Mansfeld, J., 2001. Origin of a carbonate-hosted Fe–Mn– (Ba–As–Pb–Sb–W) deposit of Långban-type in central Sweden. Miner. Deposita 36, 641–657.
Johnson, C.A., Skinner, B.J., 2003. Geochemistry of the furnace magnetite bed, Franklin, New Jersey, and the relationship between stratiform iron oxide ores and stratiform zinc oxide-silicate ores in the New Jersey highlands. Econ. Geol. 98, 837–854.
Johnson, J.W., Oelkers, E.H., Helgeson, H.C., 1992. SUPCRT92: a software package for calculating the standard molal thermodynamic properties of minerals, gases, aqueous species, and reactions from 1 to 5000 bar and 0 to 1000 °C. Comp. Geosci. 18, 899–947.
Jonsson, E., Broman, C., 2002. Fluid inclusions in late-stage Pb–Mn–As–Sb mineral assemblages in the Långban deposit, Bergslagen, Sweden. Can. Mineralog. 40, 47–65.
Kading, K.C., 2005. The Zechstein in the stratigraphical scale of Germany 2002. Newsl. Stratigr. 41, 123–127.
Krauskopf, K.B., 1957. Separation of manganese from iron in sedimentary processes. Geochim. Cosmochim. Acta 12, 61–84.
Leal, P.R., Correa, M.J., Ametrano, S.J., Etcheverry, R.O., De Brodtkorb, M.K., 2008. The manganese deposits of the Pampean ranges, Argentina. Can. Mineralog. 46, 1215–1233.
Liu, W., Etschmann, B., Brugger, J., Spiccia, L., Foran, G., McInnes, B., 2006. UV–vis spectrophotometric and XAFS studies of ferric chloride complexes in hyper-saline LiCl solutions at 25–90 °C. Chem. Geol. 231, 326–349.
Lorenz, J., 1995. Mineralisationen aus dem Rhyolith-Steinbruch von Sailauf einschliesslich der Neufunde von ged. Arsen, Bertrandit, Humboldtin und Tilasit. Aufschluss 46, 105–122.
Lüders, V., Möller, P., 1992. Fluid evolution and ore deposition in the Harz mountains (Germany). Eur. J. Mineral. 4, 1053–1068.
Lüders, V., Möller, P., Dulski, P., 1993. REE fractionation in carbonates and fluorite. Monogr. Ser. Miner. Depos. 30, 133–150.
Lüders, V., Pracejus, B., Halbach, P., 2001. Fluid inclusion and sulfur isotope studies in probable modern analogue Kuroko-type ores from the JADE hydrothermal field (Central Okinawa Trough, Japan). Chem. Geol. 173, 45–58.
Masuda, A., Nagasawa, S., 1975. Rocks with negative cerium anomalies, dredged from Shatsky Rise. Geochem. J. 9, 227–233.
McLennan, S.M., 1989. Rare-earth elements in sedimentary-rocks—influence of provenance and sedimentary processes. Rev. Mineral. Geochem. 21, 169–200.
Menning, M., Gast, R., Hagdorn, H., Kading, K.C., Simon, T., Szurlies, M., Nitsch, E., 2005. Time scale for the Permian and Triassic groups in the Stratigraphical Scale of Germany 2002, cyclostratigraphic calibration of the Dyassic and Germanic Triassic groups and the age of the strata Roadium to Rhaetium 2005. Newsl. Stratigr. 41, 173–210.
Möller, P., Stober, I., Dulski, P., 1997a. Seltenerdelement-, Yttrium-Gehalte und Bleiisotope in Thermal- und Mineralwässern des Schwarzwaldes. Grundwasser 2, 118–132.
Möller, P., Irber, W., Giese, U., 1997b. Element mobility in paragneisses and metabasites of the Continental Deep Drilling Project (KTB/Germany). Geol. Rundsch. 86, S184–S198.
Möller, P., Dulski, P., 1999. Rare earth elements and yttrium in mineral and geothermal waters from crystalline rocks. In: Ármannsson, H. (Ed.), Geochemistry of the Earth's Surface. A.A. Balkema, Rotterdam, pp. 527–530.
Morgan, J., Wandless, G., 1980. Rare earth element distribution in some hydrothermal minerals: evidence for crystallographic control. Geochim. Cosmochim. Acta 44, 973–980.
Muchez, P., Heijlen, W., Banks, D., Blundell, D., Boni, M., Grandia, F., 2005. Extensional tectonics and the timing and formation of basin-hosted deposits in Europe. Ore Geol. Rev. 27, 241–267.
Nasir, S., Okrusch, M., Kreuzer, H., Lenz, H., Höhndorf, A., 1991. Geochronology of the Spessart Crystalline Complex, Mid-German Crystalline Rise. Mineral. Petrol. 44, 39–55.
Nicholson, K., 1986. Mineralogy and geochemistry of manganese and iron veins, Arndilly, Banffshire. Scot. J. Geol. 22, 213–224.
Nicholson, K., 1992. Contrasting mineralogical–geochemical signatures of manganese oxides; guides to metallogenesis. Econ. Geol. 87, 1253–1264.
Nysten, P., Holtstam, D., Jonsson, E., 1999. The Långban Minerals. In: Holtstam, D., Langhof, J. (Eds.), Langban. Tha Mines, Their Minerals, Geology and Explorers. Raster förlag & Naturhistoriska riksmuseet, Stockholm, pp. 89–183.
Okrusch, M., Weber, K., 1996. Der Kristallinkomplex des Vorspessart. Z. Geol. Wiss. 24, 141–174.
Okrusch, M., Lorenz, J., Weyer, S., 2007. The genesis of sulfide assemblages in the former Wilhelmine mine, Spessart, Bavaria, Germany. Can. Mineralog. 45, 723–750.
Okrusch, M., Geier, G., Lorenz, J., 2011. Spessart. Geologische Entwicklung und Struktur, Gesteine und Minerale. : Sammlung Geologischer Führer, v. 106 . 368 pp.
Ondrejka, M., Uher, P., Pršek, J., Ozdín, D., 2007. Arsenian monazite-(Ce) and xenotime-(Y), REE arsenates and carbonates from the Tisovec-Rejkovo rhyolite, western Carpathians, Slovakia: composition and substitutions in the (REE, Y)XO4 system (X = P, As, Si, Nb, S). Lithos 95, 116–129.
Palmer, D.A., Hyde, K., 1993. An experimental determination of ferrous chloride and acetate complexation in aqueous solutions to 300 °C. Geochim. Cosmochim. Acta 57, 1393–1408.
Peacor, D., Essene, E., Gaines, A., 1987. Petrologic and crystal-chemical implications of cation order–disorder in kutnahorite [$CaMn(CO_3)_2$]. Am. Mineralog. 72, 319–328.
Peck, W.H., Volkert, R.A., Mansur, A.T., Doverspike, B.A., 2009. Stable isotope and petrologic evidence for the origin of regional marble-hosted magnetite deposits and the zinc deposits at Franklin and Sterling Hill, New Jersey Highlands, United States. Econ. Geol. 104, 1037–1054.
Roy, S., 1981. Manganese Deposits. Academic Press, London . 458 pp.
Salzmann, G., 1935. Untersuchungen im Ilfelder Manganerzbergbau. Z. Prakt. Geol. 43, 171–174.
Shock, E.L., Helgeson, H.C., Sverjensky, D.A., 1989. Calculation of the thermodynamic and transport properties of aqueous species at high pressures and temperatures: standard partial molal properties of inorganic neutral species. Geochim. Cosmochim. Acta 53, 2157–2183.
Shock, E.L., Sassani, D.C., Willis, M., Sverjensky, D.A., 1997. Inorganic species in geological fluids: correlations among standard molal thermodynamic properties of aqueous ions and hydroxide complexes. Geochim. Cosmochim. Acta 61, 907–950.
Shvarov, Y.V., Bastrakov, E., 1999. HCh: a software package for geochemical equilibrium modeling. Australian Geological Survey Organization. 61 pp.
Singh, B., Sherman, D.M., Gilkes, R.J., Wells, M., Mosselmans, J.F.W., 2000. Structural chemistry of Fe, Mn, and Ni in synthetic hematites as determined by extended X-ray absorbtion fine structure spectroscopy. Clays Clay Miner. 48, 521–527.
Spötl, C., Pitman, J., 1998. Saddle (baroque) dolomite in carbonates and sandstones: a reappraisal of a burial-diagenetic concept. Spec. Publ. Int. Ass. Sedimentol. 26, 437–460.
Staude, S., Wagner, T., Markl, G., 2007. Mineralogy, mineral compositions and fluid evolution at the Wenzel hydrothermal deposit, southern Germany: implications for the formation of Kongsberg-type silver deposits. Can. Mineralog. 45, 1147–1176.
Suleimenov, O., Seward, T., 2000. Spectrophotometric measurements of metal complex formation at high temperatures: the stability of Mn (II) chloride species. Chem. Geol. 167, 177–192.
Sverjensky, D.A., Shock, E.L., Helgeson, H.C., 1997. Prediction of the thermodynamic properties of aqueous metal complexes to 1000 °C and 5 kb. Geochim. Cosmochim. Acta 61, 1359–1412.
Tagirov, B.R., Diakonov, I.I., Devina, O.A., Zotov, A.V., 2000. Standard ferric-ferrous potential and stability of $FeCl^{2+}$ to 90 °C. Thermodynamic properties of $Fe^{3+}_{(aq)}$ and ferric-chloride species. Chem. Geol. 162, 193–219.
Tarassov, M., Mihailova, B., Tarassova, E., Konstantinov, L., 2002. Chemical composition and vibrational spectra of tungsten-bearing goethite and hematite from Western Rhodopes, Bulgaria. Eur. J. Mineral. 14, 977–986.
Testemale, D., Brugger, J., Liu, W., Etschmann, B., Hazemann, J.L., 2009. In-situ X-ray absorption study of Iron (II) speciation in brines up to supercritical conditions. Chem. Geol. 264, 295–310.
Thompson, J., 1978. Biopyriboles and polysomatic series. Am. Mineralog. 63, 239–249.
Wagner, T., Okrusch, M., Weyer, S., Lorenz, J., Lahaye, Y., Taubald, H., Schmitt, R., 2010. The role of the Kupferschiefer in the formation of hydrothermal base metal mineralization in the Spessart ore district, Germany: insight from detailed sulfur isotope studies. Miner. Deposita 45, 217–239.
Wolfram, O., Krupp, R., 1996. Hydrothermal solubility of rhodochrosite, Mn(II) speciation, and equilibrium constants. Geochim. Cosmochim. Acta 60, 3983–3994.
Wood, S., 1990. The aqueous geochemistry of the rare-earth elements and yttrium: 2. Theoretical predictions of speciation in hydrothermal solutions to 350 °C at saturation water-vapor pressure. Chem. Geol. 88, 99–125.
Wood, S., Samson, I., 1998. Solubility of ore minerals and complexation of ore metals in hydrothermal solutions. Rev. Econ. Geol. 10, 33–80.
Ziegler, P., 1987. Late cretaceous and cenozoic intra-plate compressional deformations in the Alpine foreland—a geodynamic model. Tectonophys 137, 389–420.

Appendix 3

Red bed and basement sourced fluids recorded in hydrothermal Mn–Fe–As veins, Sailauf (Germany): A LA-ICPMS fluid inclusion study

Authors

Tobias Fusswinkel, Thomas Wagner, Thomas Wenzel, Markus Wälle, Joachim Lorenz

Status

Published in *Chemical Geology* v.363 (2014), p. 22-39

Associate Editor

David Hilton

Reviewer

Kalin Kouzmanov and one anonymous reviewer

Contributions of the candidate

Scientific ideas	50 %
Data acquisition	95 %
Analysis and interpretation	60 %
Preparation of manuscript	80 %

Chemical Geology 363 (2014) 22–39

Contents lists available at ScienceDirect

Chemical Geology

journal homepage: www.elsevier.com/locate/chemgeo

Red bed and basement sourced fluids recorded in hydrothermal Mn–Fe–As veins, Sailauf (Germany): A LA-ICPMS fluid inclusion study

Tobias Fusswinkel [a,*], Thomas Wagner [a], Thomas Wenzel [b], Markus Wälle [c], Joachim Lorenz [d]

[a] Department of Geosciences and Geography, Division of Geology, University of Helsinki, Gustaf Hällströmin katu 2a, FI-00014 Helsinki, Finland
[b] Department of Geosciences, Eberhard Karls University Tübingen, Wilhelmstrasse 56, D-72074 Tübingen, Germany
[c] Institute of Geochemistry and Petrology, ETH Zurich, Clausiusstrasse 25, CH-8092 Zürich, Switzerland
[d] Graslitzer Strasse 5, D-63791 Karlstein am Main, Germany

ARTICLE INFO

Article history:
Received 21 May 2013
Received in revised form 16 October 2013
Accepted 20 October 2013
Available online 30 October 2013

Editor: David R. Hilton

Keywords:
Mn–Fe–As mineralization
Fluid mixing
LA-ICPMS
Kupferschiefer
Red beds
Sediment hosted Pb–Zn deposits

ABSTRACT

The hydrothermal Mn–Fe–As vein mineralization at Sailauf (Germany) hosts a complex sequence of oxide and carbonate minerals that record a protracted fluid history. The mineralization is related to a major unconformity that separates Permian (Zechstein) sedimentary rocks from underlying Variscan crystalline basement. The hydrothermal veins contain two principal mineralization stages, which are Mn oxides associated with calcite and hematite associated with Mn-calcite. The fluid evolution of the hydrothermal system has been reconstructed from fluid inclusion petrography, microthermometry, and LA-ICPMS microanalysis, coupled with stable isotope geochemistry of carbonate and oxide minerals. The fluid inclusions are high salinity sodic–calcic brines and the bulk fluid properties show no major differences between the Mn oxide and the hematite stage. LA-ICPMS analysis of major and trace elements demonstrates that the mineralization formed from chemically distinct fluid pulses characterized by variations in their K, Li, B, Pb and Zn concentrations. The fluid that precipitated the Mn oxide stage has anomalous Pb/Zn and Li/B ratios, which closely resemble fluids found in fracture fillings in red beds of the Permian Rotliegend basin. By contrast, the fluids associated with the hematite stage have Pb/Zn and Li/B ratios typical of crustal fluids that were derived from interaction with crystalline basement. Both fluids possess characteristic element ratios including Cl/Br, but variable absolute concentrations of most metals. This suggests that both fluids were modified by mixing with a common metal-depleted brine that had a similar Cl/Br ratio, most likely a formation water from the overlying Zechstein sedimentary rocks. The Sailauf mineralization provides insight into the protracted post-Variscan fluid evolution at the basement–cover interface. The compositionally anomalous fluid that precipitated the Mn oxides is comparable to brines derived from interaction with red beds and likely represents the ore fluid of Kupferschiefer-type sediment-hosted Cu deposits. Conversely, the fluid that deposited the hematite mineralization resembles fluids that typically form basement- and sediment-hosted Pb–Zn deposits.

1. Introduction

Aqueous fluids drive formation of hydrothermal ore deposits in a wide range of crustal settings, including large sedimentary basins (Sangster, 1990; Hitzman et al., 2005; Leach et al., 2005), crystallizing shallow hydrous intrusions (Hedenquist and Lowenstern, 1994), and collisional orogens (Groves et al., 1998). Despite considerable research, our understanding of the controls on the major and trace elements composition of crustal fluids remains incomplete because only recently microanalytical techniques became available that make it possible to obtain multi-element data for fluid inclusions (Günther et al., 1998; Heinrich et al., 2003). Understanding the dynamics of hydrothermal systems requires insight into the time–space evolution of ore fluids which might reflect transient processes such as changes in fluid sources, fluid mixing and phase separation. Major progress in understanding the feedback between variations in fluid composition and mineral precipitation in hydrothermal systems comes from in-situ microanalysis of fluid inclusions using LA-ICPMS coupled with well-constrained reconstruction of mineral paragenesis and textural evolution (Audétat et al., 1998; Wilkinson et al., 2009; Fusswinkel et al., 2013a).

The importance of fluid mixing processes across basement–cover unconformities for formation of sediment-hosted hydrothermal ore deposits has been recognized in many geological settings worldwide (Raffensperger and Garven, 1995; Garven et al., 1999). Prominent examples include post-Variscan fluorite–barite–Pb–Zn vein deposits throughout central and western Europe (Behr and Gerler, 1987; Behr et al., 1987; Lüders and Möller, 1992; Staude et al., 2009; Fusswinkel et al., 2013a), carbonate-hosted Pb–Zn deposits of the Mississippi-Valley Type (Muchez et al., 2005; Stoffell et al., 2008), shale-hosted Cu deposits of the Permian Kupferschiefer and in the Central African Copper belt (Rentzsch, 1974; Jowett, 1986; Sweeney et al., 1991), and

* Corresponding author.
E-mail address: tobias.fusswinkel@helsinki.fi (T. Fusswinkel).

0009-2541/$ – see front matter © 2013 Elsevier B.V. All rights reserved.
http://dx.doi.org/10.1016/j.chemgeo.2013.10.026

the world-class U deposits of the Athabasca basin in Canada (Kotzer and Kyser, 1995; Derome et al., 2005; Richard et al., 2011, 2012). Recent fluid inclusion and stable isotope studies of these ore deposit types have increasingly emphasized the importance of basement rocks as major source of ore metals (Goldhaber et al., 1995; Boiron et al., 2010; Wilkinson, 2010; Fusswinkel et al., 2013a), although in the case of Kupferschiefer-type Cu deposits the potential role of continental red beds as key metal supply is controversially debated (see Blundell et al., 2003 for an overview).

The structurally controlled hydrothermal vein-type Mn–Fe–As mineralization at Sailauf (Spessart, central Germany) is located at the unconformity between Variscan crystalline basement and overlying Permian sedimentary rocks. The mineralization records a complex sequence of hydrothermal carbonate minerals associated with Fe and Mn oxide minerals and subordinate arsenate phases (Fusswinkel et al., 2013b). Most importantly, the vein system hosts two texturally distinct mineralization stages with Mn oxides and calcite evolving into hematite and Mn-rich calcite (Fusswinkel et al., 2013b). This shift in mineral assemblages records substantial changes in pH and oxidation state of the fluid system involved, which can be related to dynamic fluid mixing processes between oxidized basement-derived fluids and reducing fluids originating in the sedimentary cover rocks (Fusswinkel et al., 2013b). Fluid inclusions from the Sailauf mineralization have therefore great potential to provide detailed insight into the chemistry of fluid mixing processes at basement–cover interfaces.

This study reports the results of a detailed fluid inclusion study of the Sailauf Mn–Fe–As mineralization, combining fluid inclusion petrography, microthermometry and LA-ICPMS microanalysis of individual fluid inclusions. The fluid inclusion data are combined with stable isotope data (carbon, oxygen, hydrogen) of carbonates, Fe and Mn oxides and sheet silicates. The fluid inclusion dataset comprises the concentrations of major cations, trace ore metals and sulfur, and the Cl/Br ratios, and is used to reconstruct the fluid evolution of the hydrothermal system. We observe significant chemical differences in terms of base metal and other cation ratios between fluids of the early Mn mineralization stage and those of the later Fe oxide stage, which are used to trace the fluid sources.

2. Geological setting

The Sailauf Mn–Fe–As mineralization is located at the unconformity between the Variscan basement of the Spessart Crystalline Complex (SCC) and the Paleozoic to Mesozoic cover comprising sedimentary rocks of Lower Permian to Triassic age (Fig. 1). The SCC is part of the Mid-German Crystalline Rise (MGCR), the internal zone of the European Variscan orogen (Kroner et al., 2008). It comprises a sequence of NE–SW trending metasedimentary, metagranitic and metabasic lithologies (Okrusch and Weber, 1996). The MGCR represents a former active plate margin along which the Rheic ocean basin was closed by SE directed subduction between the Silurian and Carboniferous (Kroner et al., 2008). In the SCC, this is evidenced by intercalations of metapelitic to metapsammitic paragneiss units with two orthogneiss complexes, whose granodioritic to granitic protoliths were emplaced in an active continental margin setting during the uppermost Silurian to lowermost Devonian (Okrusch and Richter, 1986; Dombrowski et al., 1995).

During the Variscan orogeny, the crystalline rock units attained metamorphic grades of medium pressure amphibolite facies conditions (Okrusch and Weber, 1996). Uplift and cooling of the SCC occurred between 325 and 315 Ma (Dombrowski et al., 1994). Extension and basin formation during the Lower Permian was associated with widespread bimodal volcanic activity in central Europe (McCann et al., 2008). Thick volcaniclastic sequences were deposited in northern Germany (Neumann et al., 2004) and inside Permo-Carboniferous basins (McCann et al., 2008), while more localized subvolcanic bodies intruded crystalline basement rocks in southern Germany, among them the Hartkoppe rhyolite (Okrusch et al., 2011) which hosts the Sailauf Mn–Fe mineralization.

The SCC is unconformably overlain by Permian sedimentary rocks. Most parts of the Spessart area were geographic highs during the Lower Permian (Okrusch et al., 2011), and the Lower Permian red beds of the Rotliegend are therefore restricted to the NW part. During the Upper Permian, sedimentary rocks of the marginal facies of the Zechstein basin were deposited, which comprise the basal manganiferous breccia and conglomerate, the Kupferschiefer black shale (only occurring in the NE part) and bituminous dolomites of the Werra cycle. An intermittent regression of the Zechstein Sea led to deposition of clay- and marlstones of the Aller and Leine cycle. These include the uppermost stratigraphic unit, a well-defined claystone (Käding, 2005). Continental mudstones, sandstones and conglomerates of the Lower Triassic Bunter Sandstone and limestones of the Lower Middle Triassic Muschelkalk conformably overly the Permian rocks (Okrusch et al., 2011). Middle Triassic to Upper Jurassic sedimentary rocks originally covering the area were completely eroded during regional uplift (Okrusch et al., 2011).

Both the crystalline basement and the sedimentary cover rocks are crosscut by two major systems of post-Variscan faults. The predominant system strikes NW–SE and hosts most of the hydrothermal veins, while a subordinate system striking NE–SW is only weakly mineralized. Large-scale post-Variscan extensional tectonics activated both fault systems and caused significant fluid flow, as evidenced by the frequent occurrence of barite-quartz and base metal vein mineralization (Ziegler, 1987; Wagner and Lorenz, 2002; Okrusch et al., 2007; Wagner et al., 2010).

3. The Sailauf Fe–Mn–As mineralization

The hydrothermal vein-type Mn–Fe–As mineralization comprises a set of 5 NW–SE trending, steeply dipping, discontinuously mineralized fault systems that crosscut the Lower Permian Hartkoppe rhyolite dome (Fusswinkel et al., 2013b). The porphyritic subvolcanic rock is exposed over an area of approximately 400 by 200 m and is emplaced within a small slab of biotite schist that is intercalated with orthogneisses of the Rotgneiss complex (Dombrowski et al., 1995). The top of the rhyolite marks the unconformity to the Permian Zechstein sediments and is directly overlain by bituminous dolomites of the Upper Permian Zechstein. The hydrothermal veins range in thickness between 1 and 25 cm and are mineralized by a complex sequence of different hydrothermal carbonates that are associated with Mn and Fe oxides. Reflecting the present level of erosion, it is not possible to confirm if the veins originally extended into the cover rock sequence.

The paragenesis and mineral chemistry of the Sailauf Mn–Fe–As mineralization was described by Fusswinkel et al. (2013b), and a summary diagram showing the most important minerals is given in Fig. 3. Four stages of mineralization can be distinguished, which are (1) the pre-ore stage, (2) ore stage 1 (Mn oxide stage), (3) ore stage 2 (hematite stage) and (4) the late alteration stage. The pre-ore stage contains calcian rhodochrosite, fluorite and subordinate amounts of celadonite, illite, and anhydrite. The Mn oxide stage hosts abundant Mn-oxides (braunite, hausmannite, manganite and bixbyite) along with calcite and subordinate fluorite. The hematite stage is dominated by specularitic hematite associated with Mn-calcite, whereas Mn oxides are completely absent. Rarely, a second calcite generation enriched in Fe and subordinate Mg (Fe-calcite) along with small amounts of quartz occurs in the hematite stage, postdating the Mn-calcite. The hematite stage mineralization appears both as discrete veins and as replacement of calcite from the Mn oxide stage. In the latter case, the occurrence of hematite is strictly confined to the alteration zones (Fusswinkel et al., 2013b). The final alteration stage comprises several generations of carbonates associated with arsenate minerals that locally replace and overgrow the primary mineralization.

The paragenetic sequence that is characterized by the distinct mineral assemblages of the Mn oxide stage and the hematite stage

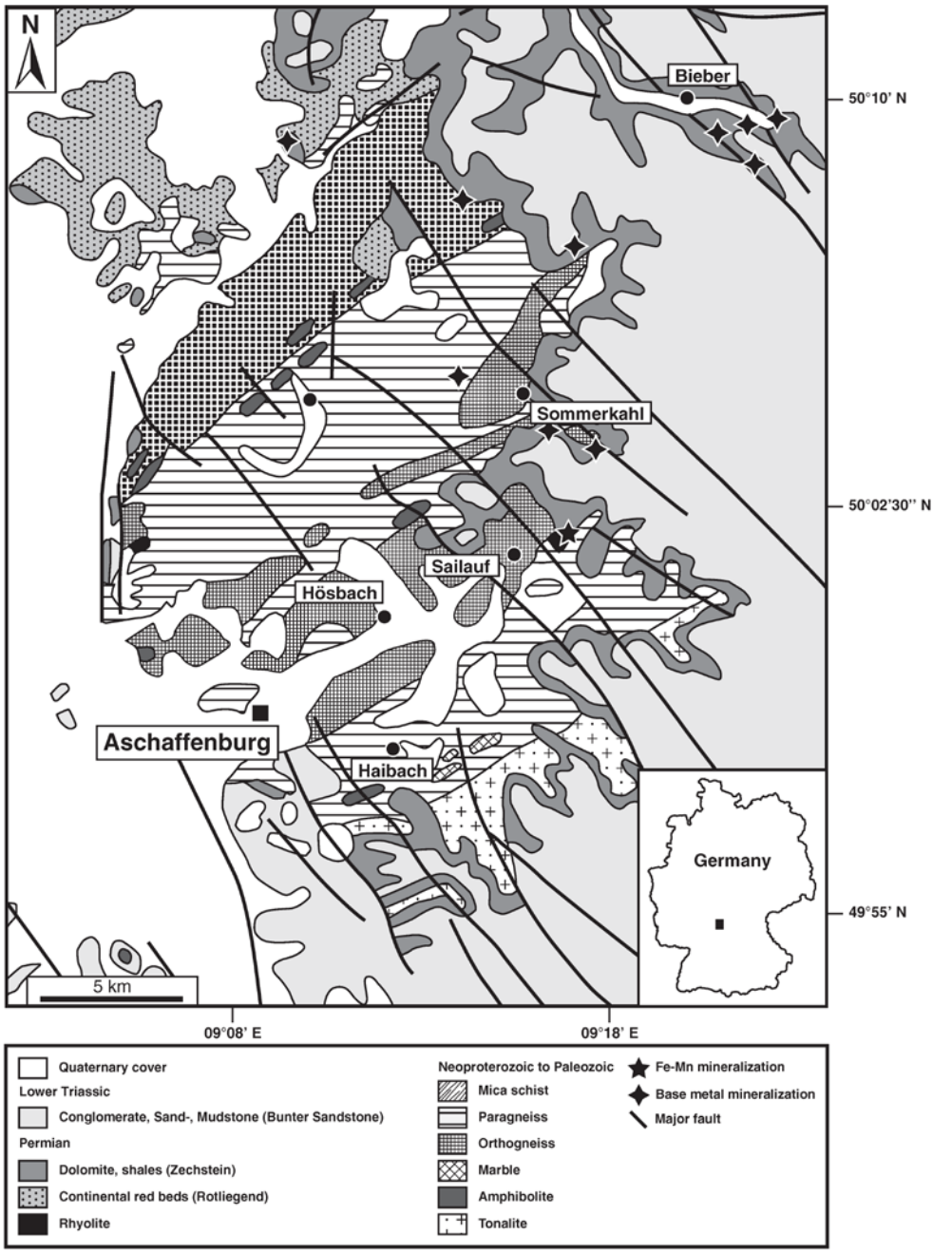

Fig. 1. Geological map of the Spessart showing the location of the Sailauf Mn–Fe–As mineralization as well as of known base—metal deposits. The map is based on the 1:500,000 map sheet provided by the Bavarian Environment Agency (Bayerisches Geologisches Landesamt, 1996).

demonstrates a clear separation of Fe from Mn during the evolution of the hydrothermal system at Sailauf. On the basis of thermodynamic modeling, this was interpreted in terms of variations of the prevailing physicochemical conditions, notably pH, $aSiO_2$, fO_2, and fCO_2 during ore precipitation. These variations, in turn, were related to dynamic fluid mixing processes across the basement-cover interface that involved oxidized fluids derived from the crystalline basement and reducing fluids likely originating in the sedimentary cover rocks (Fusswinkel et al., 2013b).

4. Samples and methods

The samples of this study originate from the active quarry that exposes the hydrothermal Mn–Fe–As veins over a vertical extent of

45 m. They are a sub-set of the samples that were investigated previously (Fusswinkel et al., 2013b) and are briefly described in Table 1. Nine representative samples containing carbonates and fluorite from the Mn oxide and hematite stage were selected for detailed fluid inclusion studies with microthermometry and LA-ICPMS. The carbonates from the pre-ore and alteration stage contained no fluid inclusions of suitable size for microthermometric and LA-ICPMS analysis.

4.1. Backscatter electron imaging with electron-microprobe

Backscatter electron (BSE) imaging was used to resolve the complex textural relations of hydrothermal carbonates and to relate fluid inclusion generations to their respective host carbonates. BSE imaging was performed with the JEOL JXA-8900RL instrument at the University of Tübingen, using 15 kV acceleration voltage and 10 nA beam current.

4.2. Fluid inclusion microthermometry

Doubly polished wafers of 200–300 μm thickness were prepared for petrographic investigation of fluid inclusion assemblages (FIAs) and subsequent microthermometric analysis with a Leica DM 2500P microscope equipped with a Linkam THMSG-600 heating-freezing stage. Calibration of the heating–freezing stage was performed using synthetic fluid inclusions of CO_2 (melting: −56.6 °C), H_2O–NaCl (eutectic melting of ice and hydrohalite: −21.2 °C), H_2O (ice melting: 0.0 °C, critical homogenization: 374.1 °C). True NaCl and $CaCl_2$ salinities were calculated from melting temperatures of ice and hydrohalite using the model for the H_2O–NaCl–$CaCl_2$ system of Steele-MacInnis et al. (2011). The analytical precision of all freezing experiments is 0.1 °C, and the precision of heating experiments is about 1 °C.

4.3. LA-ICPMS microanalysis of fluid inclusions

LA-ICPMS microanalysis of fluid inclusions was performed at ETH Zürich with a Perkin Elmer Elan 6100 quadrupole ICPMS instrument connected to a prototype GeoLas 193 nm ArF excimer laser ablation system (Günther et al., 1997). Instrumental parameters of the LA-ICPMS system are listed in Table 2. Ablation pit sizes were adjusted to the size of each fluid inclusion using an aperture to ensure complete ablation of the entire inclusion. H_2 gas was added to the He carrier gas flow to increase sensitivity for most elements (Guillong and Heinrich, 2007). To account for instrumental drift, sample measurements were bracketed by ablation of reference materials. These were NIST610 and an in-house scapolite standard for quantification of Cl and Br (Seo et al., 2011). Following acquisition of the time integrated count rate signals, each spectrum was then quantified against NIST and scapolite internal standards, yielding concentration data for the full element suite. The internal standardization and calculation of concentrations

Table 1
Description of the investigated samples from the Sailauf Mn–Fe–As vein mineralization.

Sample	Paragenesis/description
Sai-001	Breccia clasts of red rhyolite, cemented by celadonite and Ca-rhodochrosite (pre-ore stage)
Sai-002	Breccia clasts of red rhyolite, cemented by celadonite and Ca-rhodochrosite (pre-ore stage)
Sai-003	Calcite vein (Mn oxide stage) separating red rhyolite and braunite-impregnated rhyolite; calcite is crosscut and partly altered by Mn-calcite + hematite (hematite stage)
Sai-005	Calcite vein in red rhyolite, containing abundant Mn-oxides (Mn oxide stage); calcite is partly altered to Mn-calcite (hematite stage) and Ca-rhodochrosite (alteration stage)
Sai-010a	Breccia clast of braunite-impregnated rhyolite in barren calcite (Mn oxide stage); partly altered to Mn-calcite + hematite (hematite stage)
Sai-011	Barren calcite (Mn oxide stage) brecciating red rhyolite; partly altered by Mn-calcite (hematite stage)
Sai-013	Relictic calcite (Mn oxide stage) in braunite-impregmated rhyolite, strongly altered by Mn-calcite + hematite (hematite stage) and Ca-rhodochrosite (alteration stage)
Sai-014a	Braunite impregnated rhyolite clasts cemented by calcite + abundant Mn-oxides (Mn oxide stage)
Sai-015	Calcite associated with Mn oxides (Mn oxide stage); partly altered to Mn-calcite (hematite stage) and Ca-rhodochrosite (alteration stage) in red rhyolite
Sai-026	Vein of Mn-calcite + hematite (hematite stage); partly altered calcian rhodochrosite (alteration stage) in red rhyolite
Sai-027	Breccia clasts of red rhyolite cemented by celadonite + Ca-rhodochrosite (pre-ore stage); cut by a vein of calcite (Mn oxide stage); altered by Mn-calcite + hematite (hematite stage)
Sai-028	Breccia clasts of red rhyolite cemented celadonite + Ca-rhodochrosite + hematite (pre-ore stage)
Sai-030	Clast of red rhyolite coated by celadonite cockade ore (pre-ore stage) in veinlet of calcite (Mn oxide stage); altered by Mn-calcite (hematite stage)
Sai-031	Breccia clasts of rhyolite cemented by pre-ore stage assemblage; cut by vein of calcite (Mn oxide stage); altered by Mn-calcite (hematite stage) and Ca-rhodochrosite (alteration stage)
Sai-033	Vein of calcite (Mn oxide stage); almost completely altered by Mn-calcite + hematite (hematite stage) and Ca-rhodochrosite (alteration stage)
Sai-039	Veinlet of calcite with fluorite (Mn oxide stage)
Sai-044	Very hematite-rich veinlets with Fe-calcite (hematite state) in red rhyolite
Sai-051	Vein of calcite + fluorite (Mn oxide stage); partly replaced by Mn-calcite + hematite (hematite stage) in red rhyolite
Sai-052	Calcite vein + fluorite (Mn oxide stage); partly replaced by Mn-calcite + hematite (hematite stage) in red rhyolite
Sai-058	Calcite + Mn-oxides (Mn oxide stage); partly replaced by Mn-calcite (hematite stage) and Ca-rhodochrosite (alteration stage)
Sai-061	Calcite vein + abundant Mn-oxides (Mn oxide stage); partly altered by Mn-calcite (hematite stage) in braunite-impregnated black rhyolite
Sai-065	Veinlets of Fe-calcite + hematite (hematite stage) in red rhyolite
Sai-071	Euhedral scalenohedral crystals of calcite from a vug filling, with weak growth zonation (Mn oxide stage); partly replaced by Mn-calcite + hematite (hematite stage)
Sai-075	Calcite + abundant Mn-oxides (Mn oxide stage) in red rhyolite
Sai-076	Botryoidal hematite (hematite stage)
Sai-079	Mn-calcite and Fe-calcite with abundant hematite and celadonite (hematite stage)
Sai-080	Brecciated red rhyolite, cemented by calcite (Mn oxide stage); completely altered to Ca-rhodochrosite (alteration stage)
Sai-084	Mn-calcite + celadonite (hematite stage) replacing calcite (Mn oxide stage)
Sai-086	Euhedral scalenohedral calcite crystals from a vug filling (Mn oxide stage)
Sai-087	Euhedral scalenohedral calcite crystals (Mn oxide stage); basal parts altered by Mn-calcite + hematite (hematite stage)
Sai-092	Vein of calcite + abundant Mn-oxides (Mn oxide stage) cutting red rhyolite
Sai-094	Vein of calcite (Mn oxide stage), almost completely altered Mn-calcite (hematite stage) and Ca-rhodochrosite (alteration stage)
Sai-100	Braunite cockade ore surrounding braunite impregnated blackened rhyolite crusts, cut by vein of calcite + braunite (Mn oxide stage); partly altered by Mn-calcite (hematite stage)
Sai-102	Euhedral scalenohedral calcite crystals from vug filling (Mn oxide stage)
Sai-114	Euhedral scalenohedral calcite crystals (Mn oxide stage); basal parts altered Mn-calcite + hematite (hematite stage)
Sai-116	Breccia clasts of red rhyolite; cemented by celadonite and Ca-rhodochrosite (pre-ore stage)
Sai-117	Breccia clasts of red rhyolite; cemented by celadonite and Ca-rhodochrosite (pre-ore stage); crosscut by later Mn-calcite + abundant hematite (hematite stage)
Sai-118	Breccia clasts of red rhyolite; cemented by celadonite and Ca-rhodochrosite (pre-ore stage); crosscut by later Mn-calcite + abundant hematite (hematite stage)
Sai-131	Vein of calcite + fluorite (Mn oxide stage); mostly altered to Ca-rhodochrosite (alteration stage)

Table 2
Instrumental parameters of the LA-ICPMS system used in this study.

Laser type	ArF excimer laser (193 nm, Coherent Germany) with homogenized beam path
Laser energy for mineral ablation	>30 J/cm^2
Laser pulse frequency	10 Hz
Ablation pit diameter	Adjusted to inclusion size with an iris aperture
ICPMS	Elan 6100 DRC quadrupole ICPMS (Perkin Elmer, USA)
Carrier gas and flow rate	He, 1.1 l/min
Auxiliary gas	H_2, 5 ml/min
Dwell times	Ag: 30 ms; Cu, Br: 20 ms; Fe: 15 ms; all other elements: 10 ms
External standards	NIST610 for all elements except Cl and Br. In house Scapolite standard for Cl and Br

(reported as ppm on mass basis, i.e. μg/g) was carried out using absolute NaCl concentrations as determined from microthermometry using the model system H_2O–NaCl–$CaCl_2$. For calcic–sodic brines, this approach significantly improves the data accuracy compared to using NaCl equivalent salinity and empirical salt correction procedures (Heinrich et al., 2003; Schlegel et al., 2012). Matrix correction was performed against Ca concentrations as determined by microthermometry as second internal standard (Halter et al., 2002). This method provides a more precise host correction, because it takes into account that the Ca signal in the transient LA-ICPMS signal contains contributions from the host mineral and the fluid inclusions. Although the difference is negligible for most cases, this approach is preferable over host correction methods that assume an element to be present only in the matrix. This is clearly is not the case for calcite or fluorite that host sodic–calcic brine fluid inclusions. Data reduction was carried out with the SILLS software package (Guillong et al., 2008).

During data reduction, the transient time-resolved signals of each measured isotope were carefully inspected and only considered significant if the peak appeared synchronously with the main Na and Cl signals. The Na and Cl signals and their return to background values were used to define the integration interval lengths used for calculation of concentration data. These were closely bracketed by integration intervals for matrix correction using the Ca concentrations in the host minerals. This is important for elements with high background count rates like Br, because Ca count rates diminish as the ablation pit deepens and less material is ablated. The count rates for Br never exceed the gas background during matrix ablation and after background correction only noise is contributing to the Br signal during host ablation. This noise remains constant in terms of the absolute count rate, and consequently the uncertainty in the Br/Ca ratios increases as ablation proceeds. Applying the matrix correction to a time interval much later than the fluid signal interval (i.e. deeper in the host) would then result in higher apparent background concentrations of Br and thus underestimate the Br content of the fluid after matrix correction.

4.4. Stable isotope analysis

Reflecting the complex textures of carbonate-oxide assemblages, carbonate mineral separates were obtained by microdrilling with a 2 mm core drill and subsequent hand-picking under UV light. The bright pink UV luminescence of Mn-calcite from the hematite stage allowed to clearly discriminate this phase from unaltered Mn-oxide stage calcite, which is almost completely Mn-free (Fusswinkel et al., 2013b) and does not show any UV luminescence. Ca-rhodochrosite from both the pre-ore and the alteration stage occurs as fine grained, pink aggregates that could be easily separated from the calcites. The carbonate samples were cleaned in doubly distilled water, powdered and treated with 3 M NaOCl in order to dissolve organic contaminants. After dissolution in phosphoric acid, the isotopic composition of CO_2 was measured with a Finnigan MAT-252 Gasbench II mass spectrometer at the University of Tübingen, using international standards NBS18 ($\delta^{13}C_{V\text{-}PBD}$: −5.0‰, $\delta^{18}O_{V\text{-}PDB}$: −23.0‰) and NBS19 ($\delta^{13}C_{V\text{-}PDB}$: 2.0‰, $\delta^{18}O_{V\text{-}PDB}$: −2.2‰). The reproducibility of the isotope ratios was ±0.1‰ for both $\delta^{13}C$ and $\delta^{18}O$ analysis. The isotopic composition of carbonates is reported in conventional delta notation relative to Vienna Pee Dee Belemnite (V-PDB) for carbon and to Vienna Standard Mean Ocean Water (V-SMOW) for oxygen.

Following careful handpicking under a binocular microscope, hematite and celadonite were cleaned in doubly distilled water. Oxygen isotope analysis was performed by laser extraction following the procedures of Sharp (1990) and Rumble and Hoering (1994). Approximately 7 mg sample material were placed in Pt sample holders and loaded into the sample chamber. After evacuation and prefluorination, the samples were heated with a CO_2 laser at a F_2 partial pressure of 50 mbar. The extracted O_2 was collected on a molecular sieve and then expanded. The $^{18}O/^{16}O$ isotope ratio was measured on a Finnigan MAT-252 Gasbench II mass spectrometer. Reproducibility was monitored through replicate analysis of the international standard NBS-28 ($\delta^{18}O_{V\text{-}SMOW}$: 9.6‰). The analytical 1σ precision was ±0.2‰. All hematite and celadonite oxygen isotope data are reported in standard delta notation relative to V-SMOW.

Extraction of water from celadonite samples was done following the method of Vennemann and O'Neil (1993). The celadonite samples (40 mg) were degassed in the vacuum line at 110 °C overnight. The samples were then heated until fusion to quantitatively liberate the water, and any H_2 was oxidized to water with a CuO trap. Water and CO_2 were separated using liquid N_2 and ethanol cold traps. Subsequently, the water was converted to hydrogen by reduction with zinc metal. The hydrogen isotope composition was measured using a Finnigan MAT-252 gas source mass spectrometer. Hydrogen isotope compositions are given in delta notation, expressed relative to V-SMOW. Accuracy was monitored through replicate measurements of an internal kaolinite standard (δD: −64‰) that was calibrated against international standards (NBS-30). The external reproducibility of the δD values, reported relative to V-SMOW, is better than ±5‰.

5. Fluid inclusion studies

5.1. Fluid inclusion petrography

The fluid inclusions from the two main ore stages (Mn oxide and hematite stage) were investigated by careful fluid inclusion petrography that followed the approach of using fluid inclusion assemblages (FIAs), i.e. groups of fluid inclusions that were trapped together on temporally constrained growth features (such as growth zones and single healed fractures) (Goldstein and Reynolds, 1994). With the exception of sample Sai-071, none of the calcite samples contained clearly developed growth zones that would have provided well-defined time markers for establishing relative age relations between different FIAs. Instead, in the remaining samples the fluid inclusions appear in healed fractures that intersect each other with complex time relationships. However, the distinct paragenetic sequence of the different carbonate types at Sailauf that correlate with the main ore mineral assemblages allows for a clear allocation of fluid inclusions to the two principal ore stages (i.e., Mn oxide and hematite stage). In three samples (Sai-010a, Sai-014a and Sai-100), the replacement of early calcite from the Mn oxide stage by Mn-calcite of the hematite stage along fractures and cleavage planes is recognized by a significant increase in porosity and the appearance of small hematite flakes that are strictly confined to the altered areas. While unaltered and clear calcite crystals contain large fluid inclusions in clusters, fluid inclusions within the altered zones are typically smaller and much more abundant (see Fig. 2). Therefore, the distribution of fluid inclusions between the different carbonate types provides workable relative age constraints for the FIAs in these samples. A single sample (Sai-071) showed visible growth zonation as well as zones of alteration of hematite stage Mn-calcite along healed fractures, providing

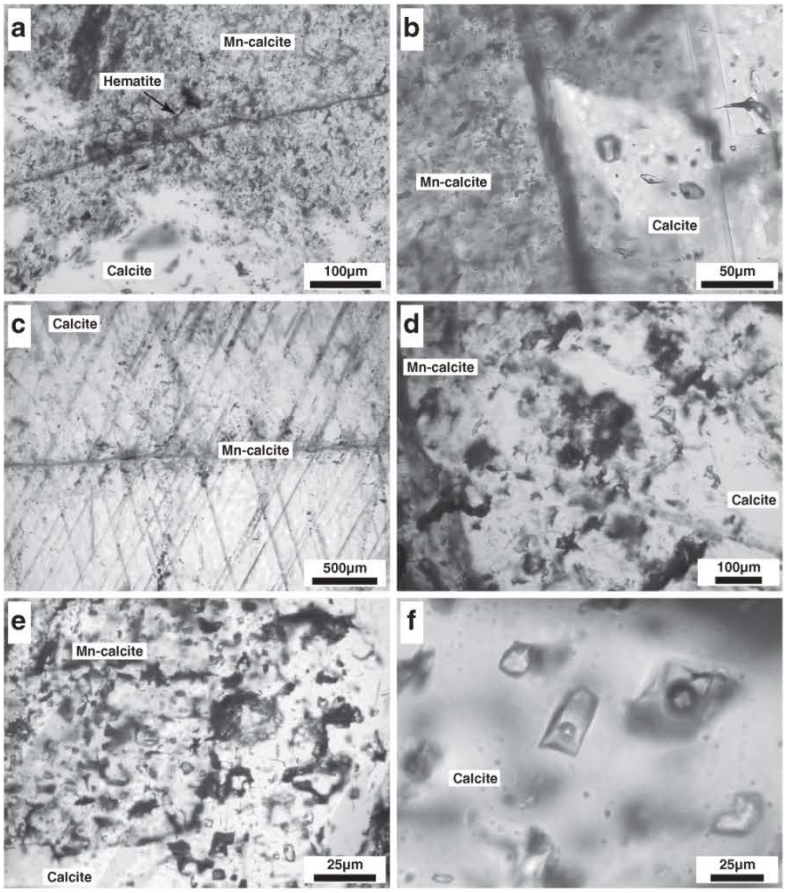

Fig. 2. Photographs illustrating typical carbonate mineral textures and related fluid inclusion assemblages. (a) Relicts of clear calcite from the Mn oxide stage, replaced by porous Mn-calcite from the hematite stage that contains numerous fluid inclusions associated with fine-grained hematite. Sample: Sai-010a. (b) Group of fluid inclusions hosted by clear calcite from the Mn oxide stage. The calcite is bordered by brownish Mn-calcite from the hematite stage that contains numerous very small FI. Sample: Sai-010a. (c) Fracture in calcite from the Mn oxide stage that is surrounded by a narrow alteration halo of Mn-calcite related to reaction with fluids from the hematite stage. Note that the original twinning lamellae in the altered calcite have been obliterated. Sample: Sai-114. (d) Group of fluid inclusions that record a complex growth history. The textural evolution can only be resolved by BSE imaging. Some of the FIs are hosted by calcite from the Mn oxide stage, while others are hosted by Mn-calcite from the hematite stage. Sample: Sai-114. (e) Two-phase aqueous brine inclusions hosted by Mn-calcite of the hematite stage that replaces pure calcite from the Mn oxide stage. Sample: Sai-100. (f) Group of fluid inclusions hosted by clear calcite from the Mn oxide stage. Sample: Sai-100.

clear age relationships as well. In the remaining carbonate samples (Sai-028, Sai-058 and Sai-114), the replacement textures were so complex that no clear petrographic correlation between the carbonate types and the FIAs could be established. Therefore, the replacement textures of these samples and their relation to the fluid inclusions were studied by BSE imaging (see Section 5.3). Fluid inclusions hosted in Mn oxide stage fluorite (sample Sai-131) occur in secondary trails along healed fractures which crosscut the entire fluorite crystals, but do not extend into the surrounding carbonates. Fig. 3 shows a simplified paragenetic sequence of the mineralization at Sailauf and additionally lists the association of FIAs with the different carbonate generations.

5.2. Microthermometry

At room temperature, all fluid inclusions are two-phase aqueous (liquid-vapor) with vapor bubbles of approximately 5 vol.%. Upon cooling, the inclusion content freezes at approximately −90 °C and first melting is observed at around −50 °C, indicating that the fluids belong to the H_2O–NaCl–$CaCl_2$ system that has an eutectic temperature of −52 °C (Steele-MacInnis et al., 2011 and references therein). Further heating results in ice melting between −27.6 °C and −22.1 °C, followed by hydrohalite melting between −12.1 °C and −0.2 °C. Only few inclusions showed hydrohalite melting temperatures of −24.9 °C to −20.0 °C. In two fluid inclusions, ice was the last phase to melt at −14.5 and −12.6 °C, after hydrohalite melting had occurred at −24.7 °C and −24.9 °C, respectively. Sequential heating and freezing was routinely done to ensure growth of larger individual crystals that would increase the accuracy of melting temperature determinations. The microthermometric measurements were complicated by the very common tendency of hydrohalite to fail nucleating when freezing the fluid inclusions. Fortunately, such metastable absence is recognized during microthermometry because it enlarges the stability field of ice to lower temperatures (Bakker and Baumgartner, 2012). This resulted in a depression of ice melting temperatures by about 10 °C in the case of the inclusions investigated. Sequential freezing and heating between −50 and −100 °C would eventually result in hydrohalite nucleation from the supersaturated liquid. With these procedures, melting temperatures for both ice and hydrohalite were reliably obtained for every fluid inclusion using heating rates of 0.1 °C/min.

Salinities and fluid compositions in the ternary model system H_2O–NaCl–$CaCl_2$ were calculated using the procedures given in Steele-MacInnis et al. (2011). Fig. 4 shows the compositions of the fluid

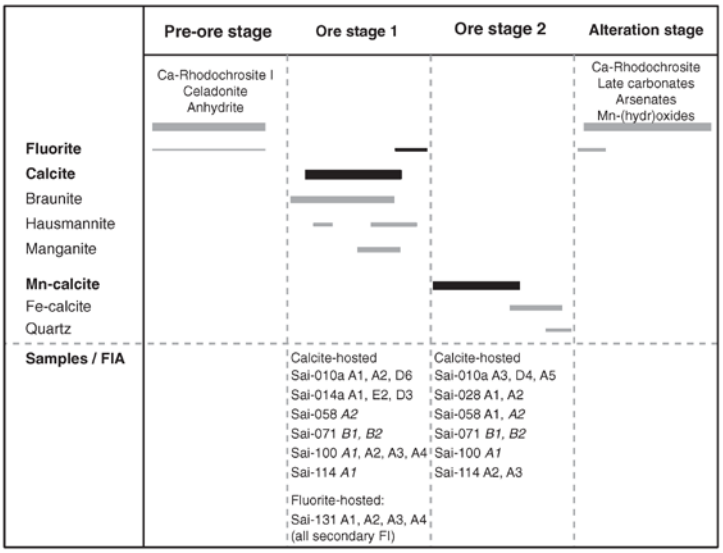

Fig. 3. Simplified paragenetic sequence diagram of the Sailauf Mn–Fe–As mineralization based on Fusswinkel et al. (2013b), listing the most important mineral phases. Black bars indicate the two main carbonate generations that host the studied fluid inclusion assemblages. The bottom part of the diagram relates samples and fluid inclusion assemblages (FIA) to host minerals and the major ore stages. FIA labeled in italics contained fluid inclusions hosted by carbonate types from the Mn oxide and hematite stage.

inclusions from all samples in ternary space. The melting temperature data for every inclusion along with the variation within a given FIA is included in the electronic supplementary material. Table 3 lists only average values of fluid inclusion assemblages. All FIAs have very consistent, high salinities of approximately 25 wt.% at Na/Ca mass ratios of 1 to 4, with most data clustering at a mass ratio of 1.5. No systematic difference exists between inclusions that could be petrographically allocated to the Mn oxide and hematite stage of mineralization. In some FIAs, the final hydrohalite melting temperatures varied by up to 8 °C, yet such seemingly large absolute temperature differences translate into only minor compositional differences due to the very densely spaced isotherms in this portion of the ternary phase diagram.

Some of the final melting temperatures were flagged as metastable phase transitions by the calculation procedure of Steele-MacInnis et al. (2011). The temperatures were higher than the peritectic reaction point between hydrohalite and halite, corresponding to the Na/Ca ratio defined by the ice melting temperature. Based on the phase rule, these fluid inclusions should have peritectically nucleated halite at the

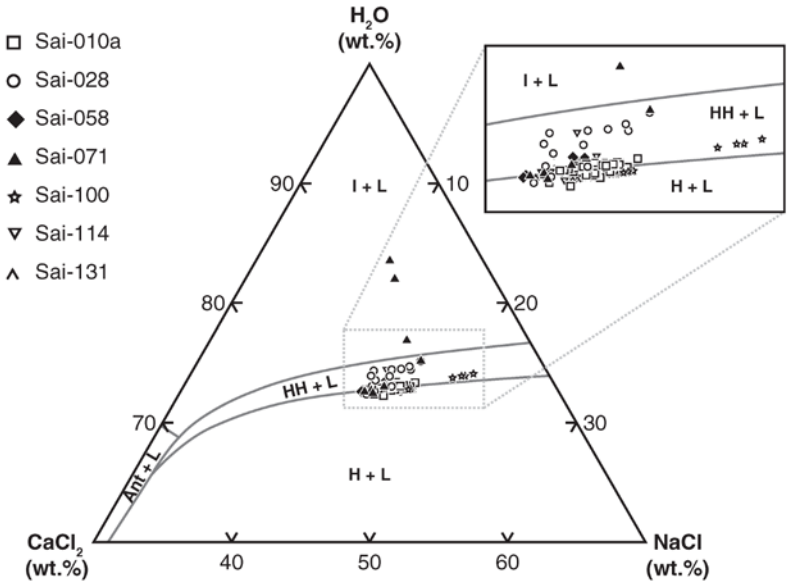

Fig. 4. Ternary H_2O–NaCl–$CaCl_2$ phase diagram showing the bulk composition of fluid inclusions from the Sailauf Mn–Fe–As mineralization as determined by microthermometry. The fluid compositions were calculated from ice and hydrohalite melting temperatures using the model of Steele-MacInnis et al. (2011).

Table 3
Average elemental composition, ice and hydrohalite dissolution temperatures and temperatures of total homogenization of all analyzed fluid inclusion assemblages (FIA).

FIA	No. FI	Li (ppm)	Na (ppm)	K (ppm)	Rb (ppm)	Cs (ppm)	Mg (ppm)	Ca (ppm)	Sr (ppm)	Ba (ppm)	B (ppm)	Fe (ppm)	Mn (ppm)	Zn (ppm)	Pb (ppm)	Cu (ppm)	Ag (ppm)	Tl (ppm)	As (ppm)	Sb (ppm)	S (ppm)	Cl (ppm)	Br (ppm)	Tm_{ice} (°C)	Th_{HH} (°C)	Th_{total} (°C)
Carbonate (calcite, Mn-calcite) hosted fluid inclusions																										
Sai-010a A1	8	940	62,160	4940	130	66	940	40,940	2190	90	180			850	400	0.7		6.7	8.3			197,610	4460	−25.8	−3.7	156
Sai-010a A2	6	780	59,670	4330	89	47	1160	43,930	2060	89	160			750	330			5.2	17			160,520	2900	−26.3	−2.5	
Sai-010a A3	2	450	60,800	10,450	80	33	1420	42,500	2450	110	130			400	150	5.0		3.1	370			234,700	6480	−26.0	−3.4	
Sai-010a A5	2	280	58,900	8170	52	26	2280	43,200	1900	110	69			360	120		0.3	1.9	200	1.1		179,500	2910	26.2	3.7	
Sai-010a D4	8	390	58,960	8190	72	29	1080	43,430	2050	92	120			330	130	4.0		2.8	280			212,730	4400	−26.1	−7.0	132
Sai 010a D6	1	860	63,300	5270	130	56	10,300	38,800	3680	18	110			2540	370	6.0		6.5	6.9			194,400	4790	−25.4	−7.0	
Sai-014a A1	7	800	56,760	4020	140	63	380	46,060	1730	58	120			470	620	4.0		7.0				199,890	3790	−26.6	−7.3	150
Sai-014a D3	5	950	62,620	5540	140	67	480	39,380	1850	120	130			540	730	5.6		7.7				221,100	3470	−25.5	−7.4	
Sai-014a E2	7	950	63,170	5390	140	65	310	39,230	1920	66	130			570	640	4.5		7.6			360	214,430	3720	−25.5	−6.2	153
Sai-028 A1	9	320	57,410	2470	54	19	4920	40,030	1950	29	81			590	210	3.0		3.2				197,260	4450	−25.5	−18.9	
Sai-028 A2	6	360	55,750	3320	86	33	2660	47,230	1900	33	58			410	490	2.2		5.7	4.7		74	187,870	4810	−26.8	−5.7	
Sai-058 A1	6	450	55,770	5180	88	33	870	46,700	1780	120	87			300	470	2.9		5.1	550			205,450	4100	−26.7	−7.6	
Sai-058 B2	6	400	58,820	6550	85	37	600	43,200	2080	130	120			280	260	3.3		3.7				203,430	5070	−26.1	−7.8	
Sai-071 B1	4	270	49,800	4570	61	20	4770	28,150	1400	33	74			400	160			6.6				131,450	4000	−18.4	−24.0	
Sai-071 B3	4	480	54,300	6260	74	32	2210	48,150	1180	21	98			220	110			6.0	48			182,330	2980	27.0	6.4	
Sai-071 B4	1	80	54,900	1730	46	13		48,600	1160					190	240			4.3				133,800	3100	−27.1	−2.6	
Sai-100 A1	13	460	70,990	9440	85	36	23	31,060	1570	54	130			9	49	8.3		2.7	7.0			190,900	5080	−24.6	−5.2	
Sai-100 A2	23	620	64,030	7100	91	49	41	39,390	2140	93	170			20	140	9.3		3.5	5.3			189,940	4440	−25.6	−2.3	
Sai-100 A3	5	580	64,140	7470	89	46	35	39,340	2260	180	170			6	120	7.3		4.1	1.8			188,360	3770	−25.6	−2.1	
Sai-100 A4	9	490	60,460	6900	79	43	44	43,180	1520	62	160			150	180	6.0		3.3	17			183,840	4120	−26.2	−2.2	
Sai-114 A1	18	490	57,260	6190	74	37	1990	45,790	1720	65	110			490	230	4.6		3.2	24			189,960	4170	−26.6	−4.8	138
Sai-114 A2	10	430	57,880	6150	68	31	9160	45,150	1750	110	110			500	220	5.2		3.1	97			187,440	3760	−26.5	−4.7	
Sai-114 A3	1	280	55,400	6780	47	20	15,400	41,900	1190		110			580	87			1.8				182,900	3460	−25.7	−19.6	
Fluorite-hosted fluid inclusions																										
Sai-131 A1	3	210	60,430	5050	40	11	1680	41,900	1600	27	29		380	110					3.6		320	226,730	1070	−25.9	−6.8	136
Sai-131 A2	5	210	57,560	3680	41	12	1720	44,960	1630	26	28	280	290	140	60			2.5			220	205,820	1600	−26.4	−6.9	
Sai-131 A3	9	340	56,600	6880	61	30	530	47,080	1830	130	110		1330	280	140	4.4		2.4	9.0		66	187,630	1770	−26.8	−2.9	
Sai-131 A4	6	220	57,580	5390	41	11	1290	45,020	1700	29	34		260	140	55			2.0				205,850	2330	−26.4	−6.8	

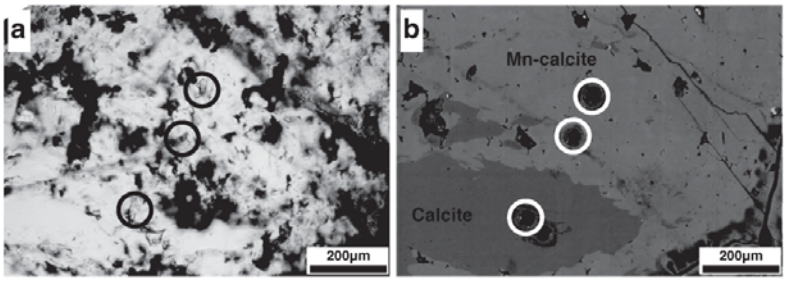

Fig. 5. Comparison of (a) transmitted-light and (b) BSE image of a complex carbonate mineral assemblage that hosts fluid inclusions related to sequential fluid pulses. BSE imaging reveals clear color contrast between unaltered calcite (dark grey) from the Mn oxide stage and Mn-calcite (light grey) of the hematite stage. Circles highlight fluid inclusions analyzed by LA-ICPMS.

expense of hydrohalite, which was never observed. Inclusions showing this behavior were left at constant temperatures slightly below the supposedly metastable melting temperatures for several hours to check for sluggish reaction phenomena, but the melting temperatures were always reproducible and halite never nucleated. Thus, the predicted metastability likely reflects small deviations of the fitted empirical equations in the model of Steele-MacInnis et al. (2011) from the true melting and reaction curves. They report an average deviation of 4% in total salinity between their empirical equations and experimental data at the hydrohalite–halite peritectic that could well explain our observations. In addition, the presence of additional solutes in the fluid inclusions could result in a small shift of the reaction curves compared to the pure H_2O–NaCl–$CaCl_2$ system. Reflecting these sources of uncertainty, we accepted extrapolations from the microthermometric data as best estimates for fluid inclusion salinity and Na/Ca ratio.

Preliminary heating experiments revealed that calcite hosted fluid inclusions from Sailauf would be somewhat affected by post-entrapment modifications through leakage or stretching at elevated temperatures. Because highly accurate Na concentrations are required for internal standardization and quantification of LA-ICPMS data, we did not perform homogenization experiments on fluid inclusions (and wafers) before LA-ICPMS microanalysis. Instead, homogenization temperatures of inclusions belonging to the same FIAs as those used for LA-ICPMS were determined afterwards. Fluid inclusions hosted in fluorite were homogenized prior to ablation, because they did not show any signs of post-entrapment modification. Fluid inclusions related to the Mn oxide stage homogenize at temperatures of 155 ± 10 °C, whereas inclusions hosted by the Mn-calcite of the hematite stage homogenize at slightly lower temperatures of 135 ± 10 °C.

5.3. BSE imaging constraints on fluid inclusion assemblages

In order to verify the FIA chronology established using carbonate replacement textures and to provide clearer petrographic criteria for those samples which have replacement textures too complex to interpret using transmitted light microscopy alone, we carried out BSE imaging on selected fluid inclusion wafers. BSE imaging is the most reliable method to discriminate between the complexly intergrown carbonate

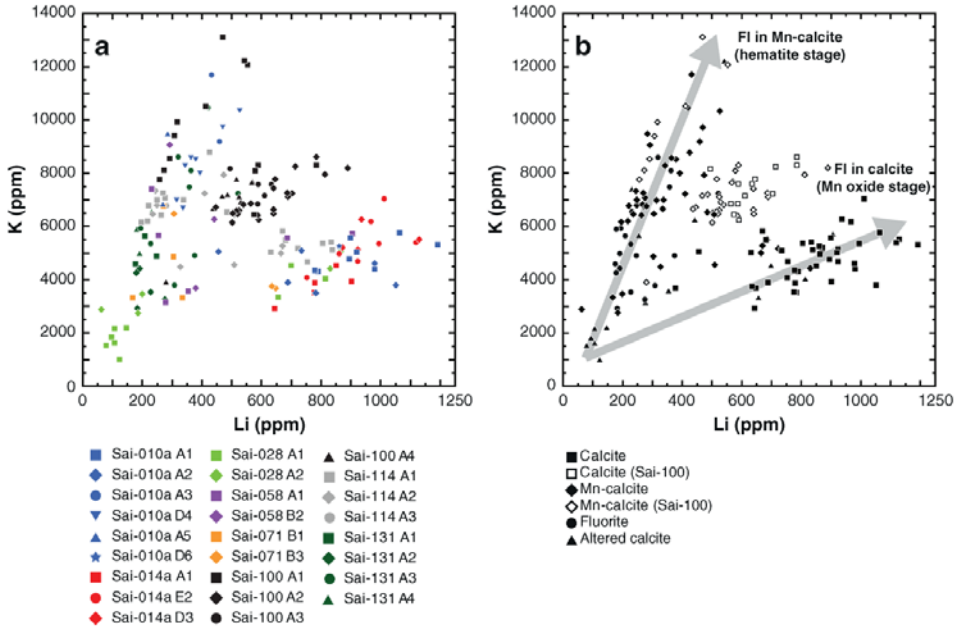

Fig. 6. (a) Plot illustrating the variation of K and Li concentrations of fluid inclusions, grouped according to petrographically defined fluid inclusion assemblages (FIAs). (b) Dataset sorted by host mineral phase (based on conventional petrography and BSE imaging). The data show two distinct trends with different K/Li ratios that are correlated with their respective host mineral. Both trends have one common end point at low K and Li concentrations.

types occurring in the Sailauf veins (Fusswinkel et al., 2013b). Fig. 5 shows a detailed image of one FIA from sample Sai-114 both in transmitted light and in the corresponding BSE image. The dark gray areas correspond to calcite from the Mn oxide stage, which is in turn replaced by more porous Mn-calcite from the hematite stage. The latter can be identified by its lighter gray color. During initial fluid inclusion petrography, all inclusions on this healed fracture had been assigned to the same FIA. The BSE image yields better information on the host carbonate of each individual fluid inclusion and thus on their paragenetic context. The lowermost FI is hosted by pure calcite from the Mn oxide stage, whereas the other FIs are hosted by a Mn-calcite alteration zone related to the hematite stage. BSE imaging only visualizes carbonate compositions at the sample surface, and the Mn-calcite alteration front could well extend more into calcite at depth. Notwithstanding this complication, we used BSE imaging to verify the host-carbonate composition of fluid inclusions from those FIAs that showed unclear textural relations. We found that even though utmost care was exerted in constraining the FIAs based on petrographic criteria alone, individual fluid inclusions

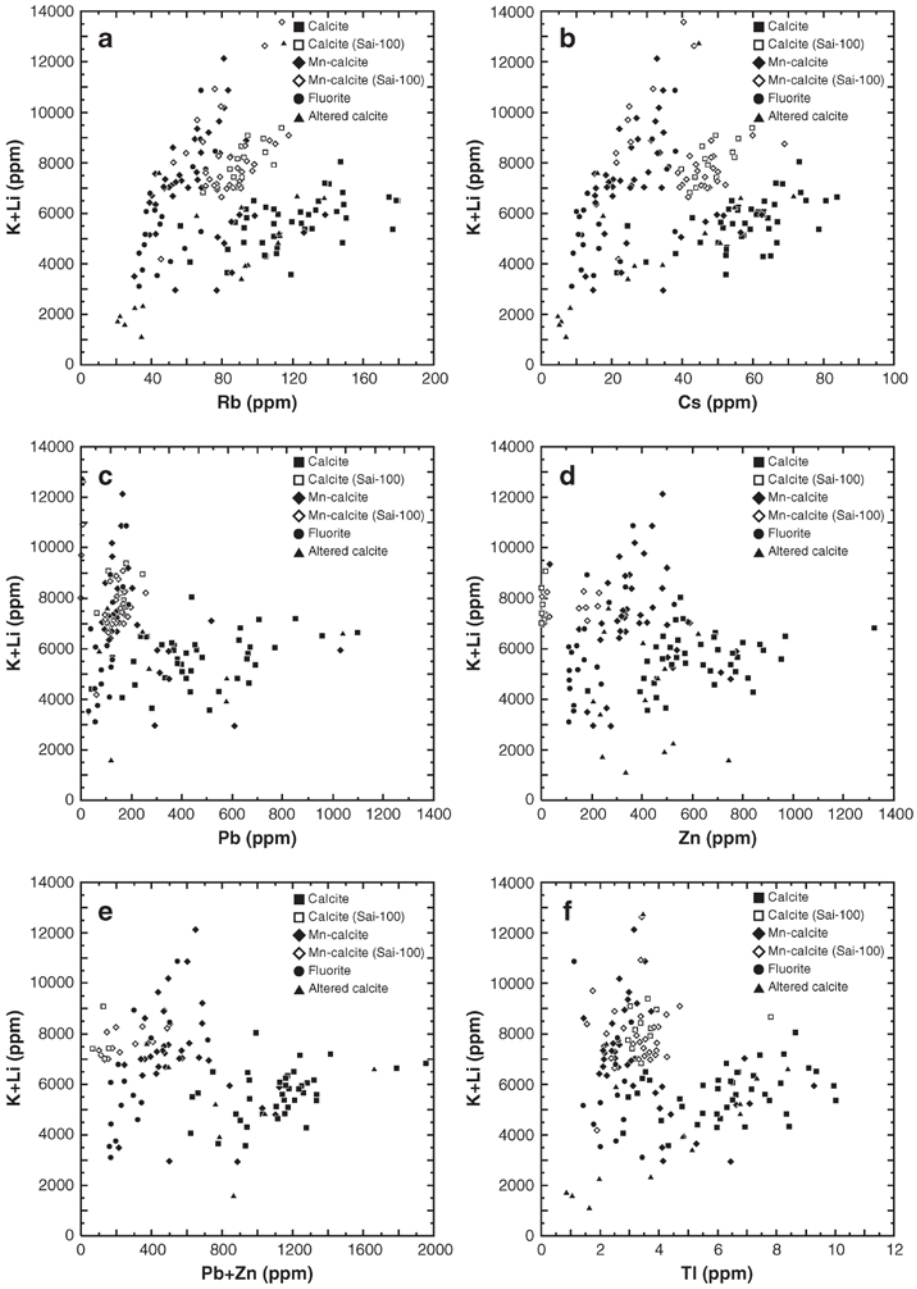

Fig. 7. Fluid inclusion compositions in variation diagrams of (K + Li) vs. Rb (a), Cs (b), Pb (c), Zn (d), (Pb + Zn) (e) and Tl (f). Data points that are absent in some plots had one element below the limit of detection.

belonging to different fluid pulses and thus hosted in complexly intergrown carbonate types had sometimes been assigned to the same FIA.

5.4. LA-ICPMS microanalysis of fluid inclusions

A total number of 189 fluid inclusions were successfully measured by LA-ICPMS, out of which 24 were hosted in fluorite and the remaining ones in calcite. LA-ICPMS analysis was done with a multi-element menu that included Li, Na, K, Rb, Cs, Mg, Ca, Sr, Ba, B, Fe, Mn, Zn, Pb, Cu, Tl, As, S, Cl and Br. The element suite included elements commonly enriched in hydrothermal Fe–Mn-deposits (see Fusswinkel et al., 2013b for a summary), elements enriched in base-metal vein type mineralization throughout the Spessart district (Okrusch et al., 2007; Wagner et al., 2010) and fluid-mobile elements like Li, B, Rb and Cs which provide insight into fluid–rock interaction processes (e.g. Aquilina et al., 1997; Reyes and Trompetter, 2012). Ag and Sb were initially included in the element suite, but discarded later in order to optimize detection limits and analytical precision for those elements that could always be detected in the fluid inclusions. Mn was not determined in all inclusions, because high Mn concentrations in the host calcites did not permit successful quantification in the FI. Average values of FIAs are listed in Table 3 and the complete dataset comprising concentration values, limits of detection and analytical errors for the fluid inclusions as well as concentration data for the host minerals is given in the electronic supplementary material. Where available, concentrations of Ag and Sb are also included. Two representative LA-ICPMS spectra are provided in the appendix. The host mineral concentration data show somewhat elevated Mg and Sr concentrations in the carbonates, while Cs and Rb were often below the limits of detection. Most fluid inclusion assemblages have consistent concentrations (small 1σ standard deviations) for elements such as Li, B, K, Rb, Cs, Cl and Br within the same FIA. Interestingly, this is well observed in samples Sai-010a, Sai-014a and Sai-100 where the FIAs could be readily assigned to the different carbonate generations (calcite from the Mn oxide stage, Mn-calcite from the hematite stage) by petrographic criteria. For the remaining samples and FIAs, the element concentrations of the alkali and alkaline earth metals are somewhat less consistent, as shown by much higher standard deviations. This observation can be related to different host carbonate associations of individual FIs within these FIAs that could only be identified by BSE imaging and will be described in more detail below. Trace element concentrations in the host carbonates do not show systematic variation trends that could be related to the different carbonate generations.

Mg and Sr, which are commonly enriched in carbonate phases, were found to be heterogeneously distributed in the host minerals as shown by variations in the depth dependent ICPMS signals. Therefore, the calculated matrix concentrations before and after the inclusion signal differed significantly, which made reliable quantification of concentrations in the fluid inclusions very difficult. For such cases, the concentrations of both elements were not included in the final fluid inclusion dataset. Ba and As concentrations also vary strongly and rather unsystematically throughout almost all samples and FIA, for unknown reasons. In some cases the Ba and As signals showed a well-defined peak synchronous with the Cl and Na signals, whereas in other cases the count rates would not return to background values immediately after the fluid inclusion peak. It cannot be ruled out that the latter is related to ablation of undetected barite or arsenate daughter crystals in the fluid inclusions that had precipitated on the inclusion walls. Because we used an aperture to adjust laser spot diameters to the fluid inclusion size, the complete fluid inclusion content was ablated and no fractionation caused by missing the daughter phases should have occurred. Therefore, the calculated Ba and As values have been accepted as best estimates for their true concentrations. Determination of S concentrations by means of LA-ICPMS faces substantial analytical challenges due to very high background signal levels (Seo et al., 2011), which in most cases rendered quantification of S concentrations in our samples impossible.

The K and Li concentrations are positively correlated, forming three distinct data arrays in K–Li space (Fig. 6) and one of them is solely defined by data from sample Sai-100, which is therefore singled out in all compositional plots by open symbols. Some texturally defined FIAs contain fluid inclusions that plot on the two main trend lines in K–Li space, whereas FIs from other FIAs consistently lie on just one of these trends (Fig. 6a). The location of FIs on the different trend lines correlates with the type of host carbonate, i.e. calcite from the Mn oxide stage, Mn-calcite from the hematite stage and partly altered calcite from the Mn oxide stage (Fig. 6b). This readily explains the larger standard deviations observed for most elements in those FIAs where detailed BSE imaging demonstrates that FIs are hosted by different carbonate types. In these cases, the individual FIs that have been assigned to one FIA based on petrographic grounds belong in fact to different FIAs. Conversely, in samples with clear FIA age relations (Sai-010a, Sai-014a) all individual fluid inclusions have similar K/Li ratios and thus lower standard deviations for most elements.

Table 4
Stable isotope data of carbonate minerals, Sailauf Mn–Fe–As mineralization.

Sample	Mineral	Mineralization	$\delta^{13}C_{V\text{-}PDB}$ (‰)	$\delta^{18}O_{V\text{-}SMOW}$ (‰)
Sai-001	Ca-rhodochrosite	Pre-ore stage	18.2	−5.2
Sai-003	Calcite	Mn oxide stage	25.9	−3.3
	Mn-calcite	Hematite stage	19.7	−5.1
Sai-005	Mn-calcite	Hematite stage	14.7	−4.5
	Ca-rhodochrosite	Alteration stage	16.1	−5.8
Sai-011	Calcite	Mn oxide stage	26.4	−2.5
	Ca-rhodochrosite	Hematite stage	17.3	−3.7
Sai-013	Mn-calcite	Hematite stage	15.5	−4.0
	Ca-rhodochrosite	Alteration stage	16.1	−5.1
	Ca-rhodochrosite	Alteration stage	17.1	−3.8
Sai-014	Mn-calcite	Hematite stage	15.1	−5.3
	Mn-calcite	Hematite stage	15.0	−4.5
Sai-015	Mn-calcite	Hematite stage	14.7	−4.5
	Ca-rhodochrosite	Alteration stage	16.1	−5.8
Sai-026	Mn-calcite	Hematite stage	16.3	−5.1
	Ca-rhodochrosite	Alteration stage	16.9	−3.6
Sai-031	Calcite	Mn oxide stage	23.6	−2.9
	Ca-rhodochrosite	Alteration stage	17.4	−4.1
Sai-033	Mn-calcite	Hematite stage	15.8	−3.5
	Ca-rhodochrosite	Alteration stage	17.2	−3.9
Sai-039	Calcite	Mn oxide stage	23.7	−2.8
Sai-051	Mn-calcite	Hematite stage	15.7	−3.5
	Mn-calcite	Hematite stage	17.2	−3.4
	Ca-rhodochrosite	Alteration stage	16.8	−5.3
Sai-061	Calcite	Mn oxide stage	26.6	−3.0
	Mn-calcite	Hematite stage	24.1	−3.3
Sai-065	Fe-calcite	Hematite stage	18.1	−1.5
Sai-079	Mn-calcite	Hematite stage	15.3	−3.7
	Mn-calcite	Hematite stage	17.6	−3.2
	Fe-calcite	Hematite stage	16.2	−5.0
Sai-080	Ca-rhodochrosite	Alteration stage	17.2	−4.1
Sai-084	Fe-calcite	Hematite stage	16.2	−4.9
Sai-086	Calcite	Mn oxide stage	26.5	−3.2
	Calcite	Mn oxide stage	25.4	−2.8
	Calcite	Mn oxide stage	25.8	−3.0
Sai-087	Calcite	Mn oxide stage	27.1	−2.7
	Mn-calcite	Hematite stage	16.2	−3.7
	Mn-calcite	Hematite stage	16.6	−3.7
Sai-092	Calcite	Mn oxide stage	24.1	−2.8
	Mn-calcite	Hematite stage	20.2	−3.5
Sai-094	Mn-calcite	Hematite stage	15.6	−3.4
	Ca-rhodochrosite	Alteration stage	17.9	−4.1
Sai-100	Calcite	Mn oxide stage	25.9	−2.0
	Mn-calcite	Hematite stage	17.1	−3.1
Sai-102	Calcite	Mn oxide stage	25.8	−2.7
	Calcite	Mn oxide stage	25.9	−2.6
Sai-114	Calcite	Mn oxide stage	26.9	−2.8
	Calcite	Mn oxide stage	26.8	−2.5
	Calcite	Mn oxide stage	26.6	−2.4
	Mn-calcite	Hematite stage	16.1	−3.2
	Mn-calcite	Hematite stage	15.6	−3.7
Sai-117	Ca-rhodochrosite	Alteration stage	16.9	−4.6
Sai-118	Fe-calcite	Hematite stage	16.4	−5.3

Fig. 7 shows (K + Li) concentrations plotted against concentrations of Rb, Cs, Pb, Zn, Pb + Zn and Tl, revealing clear correlations. The fluid inclusions that are most Li-rich are also most strongly enriched in Rb, Cs, Pb, Zn and Tl. The Zn concentrations are extremely low in most fluid inclusions measured in sample Sai-100, whereas their Pb and Tl concentrations are similar to those observed in fluorite and hematite stage Mn-calcite.

6. Stable isotope data

The 54 samples that were analyzed for carbon and oxygen isotope composition comprise carbonates from the Mn oxide stage (pure calcite), hematite stage (Mn-calcite and Fe-calcite) and the subsequent alteration stage (Ca-rhodochrosite II). One additional sample (Ca-rhodochrosite I) is from the early pre-ore stage. The stable isotope data of the carbonates are listed in Table 4, and are plotted in Fig. 8. The pure calcite of the Mn oxide stage has remarkably constant $\delta^{13}C$ values between −3.2 and −2.0‰, and the $\delta^{18}O$ values of calcite range between 23.6 and 27.1‰ (Fig. 8). The Mn-calcite from the hematite stage has lower $\delta^{13}C$ and $\delta^{18}O$ values, which are in the range of −5.3 to −3.1‰ and 14.7 to 17.6‰, respectively. Three data points of Mn-calcite from the hematite stage plot in between the tight clusters formed by most carbonate data from the two main ore stages. This can be explained by very fine intergrowths of the two carbonate types in these samples that were impossible to separate. Three data of the Fe-calcite from the hematite stage (that occurs only locally inside the veins) have consistent $\delta^{13}C$ and $\delta^{18}O$ values in the range of −5.3 to −4.9‰ and 16.2 to 16.4‰, respectively. One data point of this Fe-calcite is shifted towards slightly higher values. Ca-rhodochrosite from the pre-ore stage and the alteration stage are compositionally similar to Mn-calcite from the hematite stage in $\delta^{18}O$, but have $\delta^{13}C$ values that are as low as −5.8‰. The $\delta^{13}C$ and $\delta^{18}O$ values of Ca-rhodochrosite II from the latest alteration stage appear to be positively correlated.

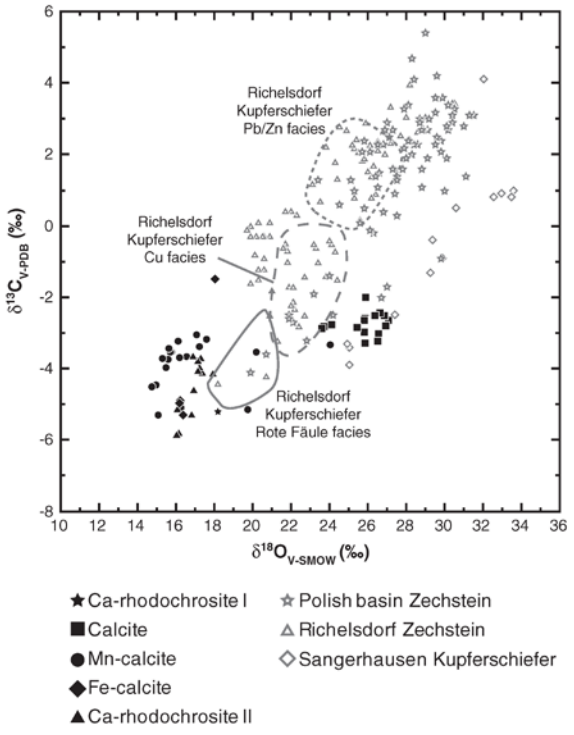

Fig. 8. Variation of the carbon and oxygen isotope data of hydrothermal carbonates from Sailauf compared to sedimentary carbonates from the Zechstein sedimentary rocks (Bechtel and Püttmann, 1991; Bechtel et al., 2000a). The hydrothermal carbonates fall into two distinct groups that correspond to the mineralization stages. The carbonates from the pre-ore stage, the hematite stage and the late alteration stage cluster in a field with lower $\delta^{18}O$ values, while carbonates from the Mn oxide stage have distinctly higher $\delta^{18}O$.

All analyzed hematite samples from the hematite stage display relatively homogeneous oxygen isotopic compositions, with $\delta^{18}O$ values ranging from −4.8 to −2.5‰ (Table 5). The Mn oxides braunite and hausmannite have $\delta^{18}O$ values in the range of −0.3 to 3.4‰ and −2.7 to −2.5‰, respectively. Celadonite occurs in the pre-ore and the hematite stage (but not in the Mn oxide stage), and samples of both types were analyzed for their hydrogen and oxygen isotopic composition (Table 5). The $\delta^{18}O$ values of all celadonites show little variation between 13.2 and 15.5‰, whereas the variation in δD is much larger and spans values between −98 and −9‰.

7. Discussion and conclusions

7.1. Fluid evolution of the Sailauf hydrothermal system

The textural association of the two chemically contrasting fluid compositions with a particular host carbonate (i.e., calcite and Mn-calcite) relates them to the two main mineralization events, the Mn oxide and hematite stage. Fluid inclusions with low K/Li ratios (the flat trend in Fig. 6b) occur in pure calcite and represent the fluid of the Mn oxide stage, whereas inclusions with high K/Li ratios (the steeper trend in Fig. 6b) are hosted in Mn-calcite and represent the fluid of the hematite stage. Very few fluid inclusions are hosted in Mn-calcite of the hematite stage, but have compositional characteristics that resemble the Mn oxide stage fluid. These fluid inclusions are interpreted as relicts of Mn stage fluids that were not affected by the carbonate alteration during the hematite stage. Sample Sai-100 belongs to the Mn oxide mineralization stage, but the fluid compositions are located on an intermediate trend in K–Li space that might reflect a transitional stage during the evolution of the hydrothermal system.

Table 5
Stable isotope data of celadonite and oxide minerals, Sailauf Mn–Fe–As mineralization.

Sample	Mineral	Mineralization	$\delta^{18}O_{V\text{-}SMOW}$ (‰)	$\delta D_{V\text{-}SMOW}$ (‰)
Sai-001	Celadonite	Pre-ore stage	15.5	−9
Sai-002	Celadonite	Pre ore stage	13.7	−58
Sai-013	Hematite	Hematite stage	−4.1	
Sai-014	Braunite	Mn oxide stage	0.1	
Sai-015	Braunite	Mn oxide stage	2.9	
Sai-027	Hematite	Hematite stage	−4.4	
Sai-028	Celadonite	Pre-ore stage	14.2	−22
	Hematite	Pre-ore stage	−3.8	
Sai-030	Celadonite	Pre-ore stage	13.3	−31
Sai-044	Hematite	Hematite stage	−3.5	
Sai-052	Hematite	Hematite stage	−4.8	
Sai-056	Braunite	Mn oxide stage	0.6	
	Hausmannite	Mn oxide stage	−2.7	
Sai-058	Hausmannite	Mn oxide stage	−2.5	
Sai-065	Hematite	Hematite stage	−3.5	
Sai-067	Braunite	Mn oxide stage	−0.2	
Sai-071	Hematite	Hematite stage	−3.4	
Sai-075	Braunite	Mn oxide stage	−0.1	
Sai-076	Hematite	Hematite stage	−2.9	
Sai-079	Hematite	Hematite stage	−2.5	
Sai-083	Braunite	Mn oxide stage	0.1	
Sai-084	Hematite	Hematite stage	−2.9	
Sai-087	Hematite	Hematite stage	−2.5	
Sai-092	Braunite	Mn oxide stage	−0.1	
Sai-093	Braunite	Mn oxide stage	0.0	
Sai-097	Braunite	Mn oxide stage	0.3	
Sai-098	Braunite	Mn oxide stage	−0.3	
Sai-100	Braunite	Mn oxide stage	3.4	
Sai-116	Celadonite	Pre-ore stage	13.2	−98

Fig. 7 shows plots of earth alkaline metals, base metals and Tl against K + Li concentrations. Alkali metals are typical indicators of fluid–rock interaction processes along the flow path and at the site of mineral deposition, because they are essential structural components of major rock-forming minerals (Aquilina et al., 1997; Ridley and Diamond, 2000). Thallium behaves similar to the alkali elements in S-undersaturated systems (McGoldrick et al., 1979). This is shown by the trends in plots of (K + Li) vs. Rb, Cs and Tl (Fig. 7a, b and f). Comparable variation trends also are displayed by the base metals, when plotted as a function of (K + Li) (Fig. 7c, d, e). The trends converge towards a common origin at low metal concentrations, suggesting that they represent mixing vectors between metal-bearing fluids and a common metal-depleted end-member. Sample Sai-100 appears to be the only exception to this general pattern. While the Pb concentrations are similar to those identified in fluids associated with Mn-calcite from the hematite stage, the Zn concentrations are much lower. This may indicate that the fluids have lost a major part of the Zn by mineral precipitation. The bulk salinities are approximately the same for all fluid inclusions, and the observed major and trace element differences (Figs. 6 and 7) cannot be caused by salinity variations and effects of chloride complexation (Hanor, 1994, 2001; Yardley, 2005).

The compositional trends in K–Li space of the fluids that reflect the two principal mineralization stages clearly indicate differences in fluid origin, whereas the base metal systematics indicate mixing processes between metal-depleted and metal-enriched end-member fluids. The K concentrations are not a good proxy for the fluid sources, because they are mainly affected by temperature and fluid–mineral equilibria (Henley et al., 1984; Hanor, 1994, 2001; Dolejš and Wagner, 2008). Alteration reactions of K-feldspar to illite release K into solution, whereas precipitation of K-feldspar or celadonite may reduce K concentrations in hydrothermal fluids. Based on critical data evaluation, Ridley and Diamond (2000) grouped K among the transitional elements that record fluid–rock interaction processes along the flow path and wallrock reactions close to the site of ore deposition.

The much more fluid-mobile alkali element Li is less sensitive to fluid–rock interaction, and together with B provides information on the fluid source (Ridley and Diamond, 2000). Reyes and Trompetter (2012) studied the mobility of Li and B during hydrothermal alteration processes as a function of temperature, rock type, solution chemistry and the secondary minerals precipitated. They demonstrated that distinct aqueous Li/B ratios resulted from equilibration with different source rock lithologies. They found that B is more mobile than Li at all temperatures and records sources of aqueous solutions, while Li mobility is more strongly affected by temperature and fluid–mineral equilibria. Because the fluid inclusion homogenization temperatures from both mineralization stages are very similar, temperature effects should not have affected the Li budget and the Li–B systematics can be used with confidence to trace the sources of the two different fluid types (Figs. 6 and 7).

Fig. 9 shows the Li–B relationships of fluid inclusions from Sailauf, compared to geothermal and basinal brines, different types of ore fluids and the seawater evaporation trajectory. Fluid inclusion data from calcite veins hosted by Permian Rotliegend red beds (Lüders et al., 2005) plot close to the fluids from the Mn oxide stage at high Li and B concentrations. Conversely, fluids from Irish-type Pb–Zn deposits (Wilkinson et al., 2005), from basement hosted hydrothermal Pb–Zn veins (Fusswinkel et al., 2013a) and from the Soultz-sous-Forêts geothermal site (Pauwels et al., 1993) plot near the hematite stage fluids at lower Li and B concentrations. Oil-field brines (Kharaka et al., 1987) have much lower Li concentrations but relatively high B concentrations. Interestingly, fluids from metamorphic quartz veins in the Pyrenees (Banks et al., 1991; McCaig et al., 2000) have variable Li–B compositions. Formation of the veins involved density-driven ingression of hypersaline brines into underlying sedimentary rocks and compositionally variable basement lithologies, where fluid compositions were extensively modified by reaction with these different rock types (Banks et al., 1991; McCaig et al., 2000; Leisen et al., 2012). The variability in Li and B concentrations reflects prolonged residence times in different host rocks. Taken together, the Li/B data demonstrate that the Sailauf Mn oxide stage fluids closely resemble fluids found in fracture mineralization in Rotliegend sedimentary rocks (Lüders et al., 2005). Conversely, fluids associated with hematite stage mineralization are compositionally comparable to basement interacted fluids (basement-hosted Pb–Zn veins in the Schwarzwald, Soultz-sous-Forêts granite reservoir fluids).

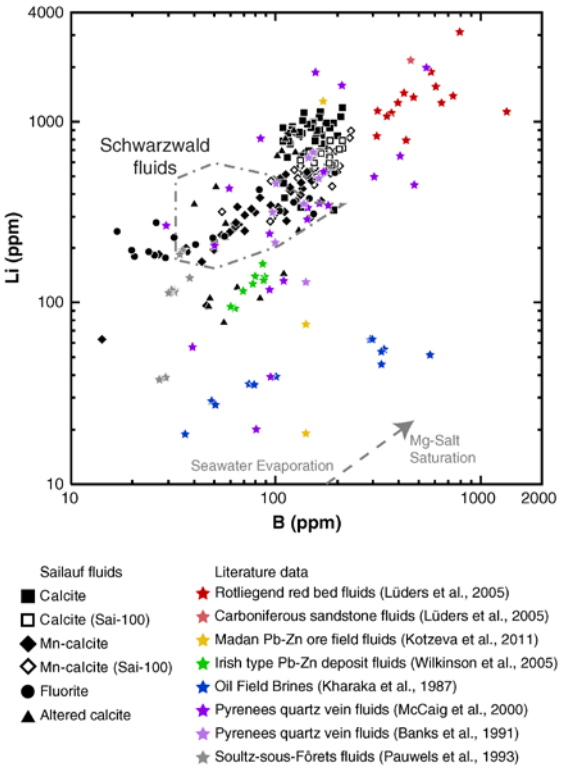

Fig. 9. Variation of Li and B concentrations of fluid inclusions from Sailauf, compared to data of other crustal fluids and the seawater evaporation trajectory (McCaffrey et al., 1987). The fluid inclusions of the Mn oxide stage have the highest Li and B concentrations, while fluid inclusions related to the hematite stage have lower concentrations of both elements. The Mn oxide stage fluids are compositionally closest to fluids from Rotliegend sediments (Lüders et al., 2005), whereas the hematite stage fluids compare well to typical post-Variscan basement-hosted Pb-Zn ore fluids ('Schwarzwald fluids' in the figure, Fusswinkel et al., 2013a).

Similar conclusions can be drawn from base metal data. Fig. 10 compares the Pb and Zn concentrations of fluid inclusions from Sailauf to literature data for different Pb–Zn ore deposits (Kostova et al., 2004; Wilkinson et al., 2005; Kotzeva et al., 2011), oil-field brines (Carpenter et al., 1974; Kharaka et al., 1987), basement-hosted Pb–Zn veins (Fusswinkel et al., 2013a), and fluids from red bed sedimentary rocks of the Rotliegend (Lüders et al., 2005). The Pb and Zn concentration data are generally arranged on linear trends, reflecting the dominant metal solubility controls by temperature, salinity and sulfide mineral equilibria (Yardley, 2005). The hematite stage fluid inclusions from Sailauf and few fluid inclusions from the Mn oxide stage overlap with a trend close to a Pb/Zn ratio of 0.4, which is commonly observed for many crustal fluids (Yardley, 2005). By contrast, most fluid inclusions from the Mn oxide mineralization show anomalous Pb enrichment, similar to the Pb enrichments described by Lüders et al. (2005) from the Rotliegend red bed fluids of the North German basin.

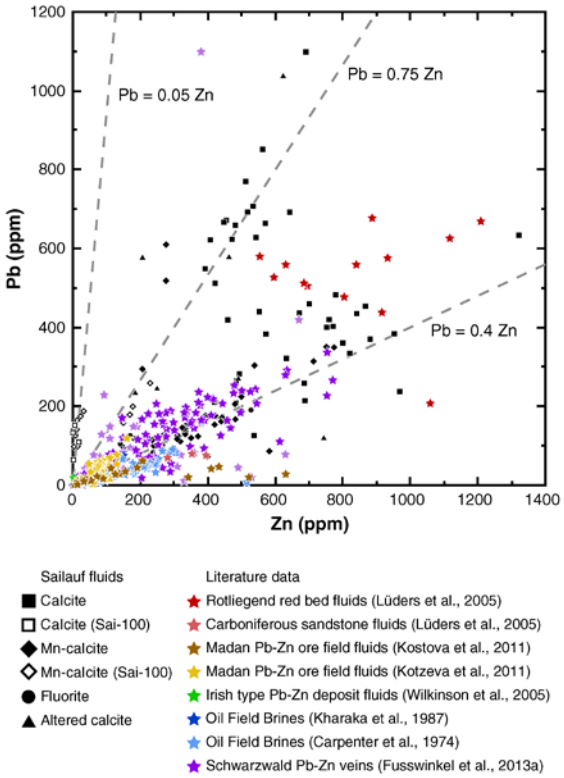

Fig. 10. Pb and Zn concentrations of fluid inclusions from Sailauf, compared to LA-ICPMS data for basement-hosted Pb–Zn veins from the Schwarzwald (SW Germany) and other literature data. The fluid inclusions from the hematite stage fall on the flat trend line that is considered typical for rock-buffered crustal fluids (Yardley, 2005). By contrast, most of the fluid inclusions from the Mn oxide stage have very high Pb/Zn ratios (steep trend), consistent with the generally anomalous chemical composition of these fluids. They compare best to Pb-enriched fluids from Permian Rotliegend sediments (Lüders et al., 2005).

Halogen systematics are a powerful tool for tracing fluid sources because of the conservative behavior of Cl, Br and I during fluid–rock interaction (Rittenhouse, 1967; Böhlke and Irwin, 1992; Kesler et al., 1996; Gleeson et al., 2001; Stoffell et al., 2008; Fusswinkel et al., 2013a). The molar Cl/Br ratios of all fluid inclusions from Sailauf are fairly constant, in the range of 50–200. Higher values up to 400 occur only in some fluorite-hosted inclusions (sample Sai-131). When plotted in coordinates of molar Cl/Br and Na/Br ratios (Fig. 11a), most data are located in a narrow elongated field below the seawater evaporation trajectory, and the fluids from the Mn oxide and hematite mineralization stage cannot be distinguished by their Cl/Br data. Only fluid inclusions from sample Sai-131 have somewhat higher Cl/Br ratios that plot to the left of the seawater evaporation trend. Following a critical evaluation of classical diagrams for fluid halogen data, Engle and Rowan (2013) recently proposed an alternative approach that overcomes shortcomings such as mathematical artifacts and spurious correlations. They suggested the use of isometric log ratio plots and we illustrate our fluid inclusion data in such a diagram in Fig. 11b. Like the conventional element ratio plot (Fig. 11a), the isometric log ratio plot demonstrates that the Sailauf fluids are enriched in Br relative to the seawater evaporation trajectory (lower z1 values), while fluorite-hosted fluid inclusions plot within the Na-depletion field (lower z2 values). This Na depletion could reflect alteration reactions involving sodic clay minerals that have lowered the Na/Cl ratio relative to evaporated seawater.

The Sailauf fluid inclusion data do not point to mixing processes between fluids with strongly differing Cl/Br ratios. The linear relationships in Fig. 11 could indicate some extent of fluid mixing between a strongly Br enriched brine and a Na-depleted fluid, but there is no systematic variation between the fluids associated with the Mn oxide and hematite ore stage. The general features of all fluid inclusions such as the high salinities, Cl/Br ratios below seawater, and Cl/Br and Na/Br ratios close to the seawater evaporation trajectory suggest that they were derived from evaporated seawater. This interpretation is in good agreement with the regional geological setting. The Frankenberg-Schlüchtern Zechstein subbasin that is located NE of the Spessart district contains abundant evaporitic sediments and the first halite bearing units occur around 30 km to the NE of Sailauf (Trusheim, 1964; Becker and Bechstädt, 2006). Therefore we conclude that the fluids responsible for the Sailauf mineralization originate from residual evaporitic fluids of Zechstein age that infiltrated into the underlying host rock sequences.

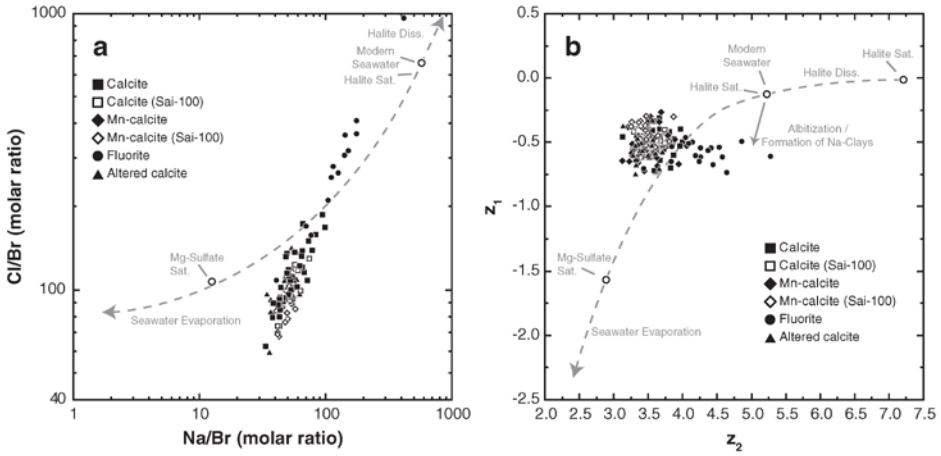

Fig. 11. (a) Plot of the molar Cl/Br and Na/Br ratios of fluid inclusions from Sailauf, compared to the sea water evaporation trajectory (McCaffrey et al., 1987) and the halite dissolution trend. The fluid inclusions hosted by different carbonate minerals form a narrow linear trend at Cl/Br ratios below the sea water line. (b) Log ratio plot of halogen data (Engle and Rowan, 2013), which illustrates that most fluid inclusions are enriched in Br (lower z2 values). These were mixed with a fluid that had lower Na/Cl ratios than evaporated seawater (lower z1 values).

Fluid–rock interaction with different lithologies (Variscan gneisses and granites of the basement, red beds of the Permian Rotliegend) resulted in extensive modification of the major cation chemistry, but did not alter the Cl/Br ratios and the Li and B concentrations.

7.2. Stable isotope systematics

The calcites from the Mn-oxide stage have distinctly higher $\delta^{18}O$ and slightly higher $\delta^{13}C$ values than the Mn-calcite and Fe-calcite of the hematite stage and the Ca-rhodochrosite of the pre-ore and alteration stages. The oxygen isotope data point to different fluid sources for the two mineralization stages, because the differences in fluid inclusion homogenization temperatures are too small to explain the shift in $\delta^{18}O$. Calculation of the isotopic composition of the ore fluid requires sufficiently accurate paleotemperature data. The mineralization temperatures can be estimated from pressure corrected fluid inclusion homogenization temperatures, using independent information on pressure. Okrusch et al. (2011) estimate a thickness of roughly 1450 m for the sedimentary units that were overlying the Sailauf hydrothermal vein system at the time of formation. Assuming lithostatic pressure conditions and using isochores calculated from the microthermometric data (Bodnar and Vityk, 1994), the trapping conditions for the Mn oxide and hematite stage are estimated as 170(±10) °C and 150(±10) °C, respectively. Assuming hydrostatic pressure conditions the trapping temperatures are 162(±10) °C and 142(±10) °C, less than 10 °C higher than the measured homogenization temperatures. By comparison, oxygen isotope equilibrium temperatures of 70–114 °C are obtained for texturally coexisting hematite and Mn-calcite pairs, using published fractionation factors for calcite-H_2O (Friedman and O'Neil, 1977) and hematite-H_2O (Bao and Koch, 1999). The difference of about 70–100 °C compared to the pressure-corrected homogenization temperatures can be explained by disagreement on the hematite-water fractionation factor at lower temperatures (Bao and Koch, 1999) or partial isotopic equilibrium during mineral precipitation. Therefore, the pressure-corrected fluid inclusion temperatures are accepted as best estimate of the mineralization temperatures.

The isotope composition of the ore fluid ($\delta^{18}O_{H2O}$ and δD_{H2O}) relative to V-SMOW has been calculated from the measured values for carbonate minerals and celadonite. Fractionation factors used were calcite-H_2O (Friedman and O'Neil, 1977) for calcite, Mn-calcite and Fe-calcite, and illite-H_2O (Capuano, 1992; Sheppard and Gilg, 1996) as an approximation for celadonite (Odin et al., 1988). In addition, salt effect corrections were applied (Truesdell, 1974; Horita et al., 1993; Chacko et al., 2001), because the fluids of the hematite and Mn oxide stage are sodic–calcic brines. The calculation assumed an average bulk fluid composition of 2.6 mol/kg NaCl, 1.1 mol/kg $CaCl_2$ and 0.2 mol/kg KCl, based on the microthermometric and LA-ICPMS data. The $\delta^{18}O_{H2O}$ and δD_{H2O} values that were calculated from the celadonite and carbonate data are shown in Fig. 12, and compared to fluid compositions from post Variscan basement-hosted Pb–Zn veins and reference data. The global meteoric water line and standard mean ocean water serve as reasonable approximations for the Permian waters (Knauth and Beeunas, 1986). The calculated $\delta^{18}O_{H2O}$ values for the hematite stage carbonates and pre-ore stage celadonite are in good agreement and are in a narrow range of 2.1 to 5.0‰, whereas the δD_{H2O} values vary widely between −79 and 10‰. By contrast, the Mn oxide stage carbonates were precipitated from high $\delta^{18}O$ fluids (approximately 13–17‰). The three hematite stage Mn-calcite samples with intermediate $\delta^{18}O_{V\text{-}SMOW}$ values are most likely caused by intergrowths with Mn oxide stage calcite. The $\delta^{18}O$ values of the Mn oxide stage fluids can be straightforwardly explained by evaporation or fluid–rock interaction at rock-buffered conditions (Holser, 1979; Sheppard, 1986). Taken together, the stable isotope data are best explained by fluids that originated from residual evaporitic brines, which were modified by extensive interaction with different host rock lithologies that involved Variscan crystalline basement and Permian red bed sediments.

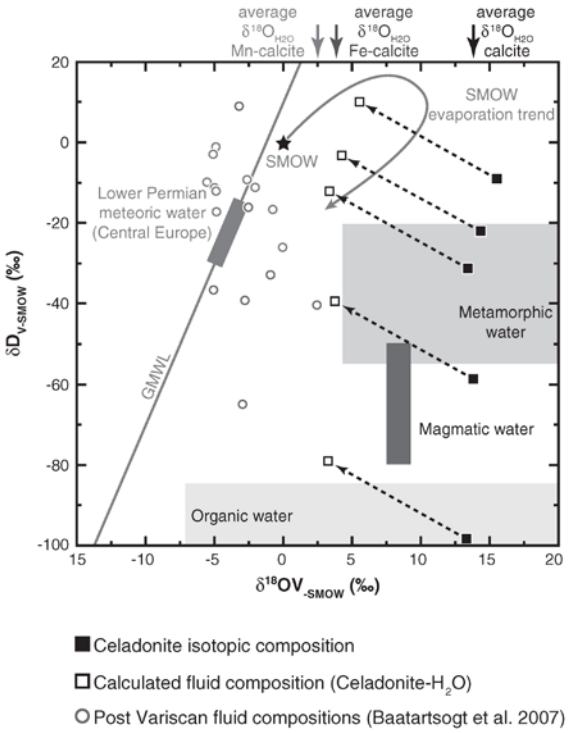

Fig. 12. Calculated oxygen and hydrogen isotope composition of the fluids from the Sailauf Mn–Fe–As mineralization, obtained from measured $\delta^{18}O$ and δD values of celadonite and fluid inclusion homogenization temperatures using fractionation factors from Sheppard and Gilg (1996) and Capuano (1992). For comparison, the global meteoric water line (GMWL), reference data of fluids related to hydrothermal post-Variscan Pb–Zn–Ba–F vein-type mineralization (Baatartsogt et al., 2007) and the sea water evaporation trend (Holser, 1979) are shown. Arrows indicate average fluid $\delta^{18}O_{H2O}$ values, calculated from measured carbonate isotopic composition data and fluid inclusion temperatures using the calcite-H_2O fractionation factors of Friedman and O'Neil (1977).

7.3. Fluid sources

The systematic variations in fluid chemistry that correlate with the two main mineralization stages (Mn oxide and hematite stage) demonstrate that the Sailauf hydrothermal system has experienced two major periods of fluid flow and fluid mixing. The Li/B and Pb/Zn ratios of the hematite stage fluids are compositionally similar to basement-interacted fluids that are often invoked to have formed basement- or sediment-hosted Pb–Zn ore deposits (Muchez et al., 2005). Conversely, the Mn oxide stage fluids are compositionally anomalous and can only be compared to fluids from fracture mineralization in Permian (Rotliegend) volcaniclastic red bed sediments (Lüders et al., 2005).

The Sailauf rhyolite body is situated on a basement high that formed a narrow elongated ridge during Rotliegend times. Abundant Rotliegend red bed clastic rocks occur in trough structures few kilometers NW and SE of Sailauf (Trusheim, 1964). Organic-matter rich dolomites of the marginal facies of the Zechstein directly overly the hydrothermal Mn–Fe–As veins and the Kupferschiefer appears below the dolomites few kilometers towards the NE (in the direction of the deepening basin). The Kupferschiefer and the overlying dolomites are commonly mineralized by stratabound Cu–Pb–Zn–(Ag) ores (Okrusch et al., 2007; Wagner et al., 2010). Both the Variscan crystalline basement and the Permian to Mesozoic sedimentary rocks are crosscut by NW–SE striking fault systems, which were activated during post-Variscan extensional tectonics (Ziegler, 1987). The faults are frequently

mineralized with quartz and barite, whereas hydrothermal Cu–Co–Ni–As–Fe–Bi ore mineralization is restricted to vein sections that crosscut Zechstein sedimentary rocks and the uppermost parts of the crystalline basement (Wagner et al., 2010). Comparable structurally controlled vein ores that crosscut the Cu–Ag mineralized Kupferschiefer are frequently observed in the Mansfeld and Sangerhausen ore districts of the Harz, Germany (Vaughan et al, 1989).

It has been long recognized that significant base metal enrichment in Kupferschiefer ore bodies can only be explained by input from external hydrothermal metal sources. The major Kupferschiefer ore districts in Germany and Poland are related to underlying highly oxidized rocks. They typically occur on basement highs and above Permian (Rotliegend) red bed sediments with underlying volcanic rocks (Jowett, 1986). The most widely accepted model for Kupferschiefer type mineralization suggests that metal-bearing late-diagenetic sodic–calcic formation waters from the Rotliegend volcaniclastics convected upwards along the flanks of basement highs. The reducing organic matter-bearing Kupferschiefer sedimentary rocks acted as geochemical trap and caused Cu deposition (Jowett, 1986; Oszczepalski, 1999). The exact timing of the main Cu mineralization still remains controversial (Symons et al., 2011). The critical importance of post-depositional metal enrichment involving hydrothermal fluids derived from Rotliegend sedimentary rocks, however, has been emphasized by many geochemical, mass balance and fluid flow modeling studies (Rentzsch, 1974; Jowett, 1986; Bechtel and Püttmann, 1991; Cathles et al., 1993; Oszczepalski, 1999; Bechtel et al., 2000b). Conversely, Blundell et al. (2003) proposed that metal bearing brines forming Kupferschiefer mineralization in the Lubin basin in Poland were injected into Rotliegend sequences from the basement and then transported laterally updip through the red beds to the sites of deposition near basement highs. Episodic fluid expulsion from the basement would be triggered by earthquake-induced normal fault reactivation (Muir-Wood and King, 1993).

The sediment-hosted Cu mineralization in the Spessart is not directly underlain by red bed sedimentary and volcanosedimentary rocks of the Rotliegend (Wagner and Lorenz, 2002; Okrusch et al., 2007; Wagner et al., 2010). Therefore, accepting metal-bearing brines from the Rotliegend as the principal ore fluids, the formation of these Kupferschiefer deposits must have involved fluid flow along the major NW–SE striking fault zones that host all known hydrothermal veins. This along-fault fluid flow that is dictated by the geological setting would be analogous to the forced brine convection model that has been proposed for the major Mount Isa Cu deposit in Australia (Matthäi et al., 2004).

The contrasting fluid compositions that have been found in the two major mineralization stages of the Sailauf hydrothermal vein system closely resemble metal-bearing Rotliegend brines (Mn oxide stage) and typical basement-derived Pb–Zn brines (hematite stage). Because the hydrothermal veins are located immediately below the basement-cover unconformity, the trapped fluids were not modified by interaction with the chemically reactive Zechstein rocks. The contrasting chemistries of Mn oxide and hematite stage fluids suggest that the hydrothermal system experienced two distinct periods of fluid flow that relate to different hydrological regimes.

The first fluid flow event (Mn oxide stage) records compositionally anomalous and highly oxidizing fluids derived from red bed sedimentary rocks of the Rotliegend that were introduced via forced brine convection along major faults. Whether these fluids originated as basement fluids that were injected into Rotliegend sequences prior to lateral flow towards the Spessart basement high, or if they represent Rotliegend interacted formation waters cannot be discriminated from the data at hand. By contrast, the second fluid flow event involved typical Pb–Zn enriched basement-interacted brines that would flow upwards during seismically-induced episodic fluid flow events focused within fault zones (Muir-Wood and King, 1993).

The Sailauf Mn–Fe–As veins therefore belong to a hydrothermal feeder system which records fluids derived from Rotliegend red beds and later fluids that were sourced from basement rocks. The early fluids that carry the signature of Rotliegend formation waters could then represent an analog of the ore fluids of Kupferschiefer type Cu mineralization. Although little is known about the chemical composition of Kupferschiefer ore solutions, the Cu concentrations of the Sailauf fluids (<10 ppm) appear very low. Mass balance calculations that estimated the volumes of fluids and source rocks required for Kupferschiefer deposit formation (Cathles et al., 1993; Blundell et al., 2003) assumed minimum Cu concentrations of 60 to 130 ppm in the main ore fluid. We note, however, that the Mn oxide minerals at Sailauf contain Cu concentrations that are one to two orders of magnitude higher than in the fluid inclusions (e.g., up to 300 ppm in braunite). Because Mn oxide minerals are very effective in co-precipitating Cu from aqueous solutions (Hewett, 1972), the fluid inclusions trapped in calcite from the Mn oxide stage may not represent the unmodified primary Cu ore fluid. Notwithstanding this complication, our dataset illustrates that the combination of detailed petrography and multi-element fluid inclusion microanalysis makes it possible to discriminate red bed and basement sourced fluids. Our data provide additional constraints on the composition of the principal ore fluids involved in formation of sediment-hosted Cu and Pb–Zn deposits in other ore districts.

Acknowledgments

This project was made possible by funding from the German Research Foundation (DFG), grant WA 1526/6-1. We thank Indra Gill-Kopp for preparation of excellent thin sections for fluid inclusion microthermometry as well as Heinrich Taubald and Bernd Steinhilber for stable isotope analysis. Furthermore, we thank Kalin Kouzmanov and an anonymous reviewer for constructive comments, and David Hilton for the editorial handling of this manuscript.

Appendix A. Supplementary data

Supplementary data to this article can be found online at http://dx.doi.org/10.1016/j.chemgeo.2013.10.026.

References

Aquilina, L., Pauwels, H., Genter, A., Fouillac, C., 1997. Water–rock interaction processes in the Triassic sandstone and the granitic basement of the Rhine Graben: geochemical investigation of a geothermal reservoir. Geochim. Cosmochim. Acta 61, 4281–4295.
Audétat, A., Günther, D., Heinrich, C.A., 1998. Formation of a magmatic–hydrothermal ore deposit: insights with LA-ICP-MS analysis of fluid inclusions. Science 279, 2091–2094.
Baatartsogt, B., Schwinn, G., Wagner, T., Taubald, H., Beitter, T., Markl, G., 2007. Contrasting paleofluid systems in the continental basement: a fluid inclusion and stable isotope study of hydrothermal vein mineralization, Schwarzwald district, Germany. Geofluids 7, 123–147.
Bakker, R.J., Baumgartner, M., 2012. Unexpected phase assemblages in inclusions with ternary H_2O-salt fluids at low temperatures. Cent. Eur. J. Geosci. 4, 225–237.
Banks, D.A., Davies, G.R., Yardley, B.W.D., McCaig, A.M., Grant, N.T., 1991. The chemistry of brines from an Alpine thrust system in the Central Pyrenees: an application of fluid inclusion analysis to the study of fluid behaviour in orogenesis. Geochim. Cosmochim. Acta 55, 1021–1030.
Bao, H., Koch, P.L., 1999. Oxygen isotope fractionation in ferric oxide–water systems: low temperature synthesis. Geochim. Cosmochim. Acta 63, 599–613.
Bayerisches Geologisches Landesamt, Geologische Karte von Bayern 1:500000. Bayerisches Geologisches Landesamt, München, (1996).
Bechtel, A., Püttmann, W., 1991. The origin of the Kupferschiefer-type mineralization in the Richelsdorf hills, Germany, as deduced from stable isotope and organic geochemical studies. Chem. Geol. 91, 1–18.
Bechtel, A., Gratzer, R., Püttmann, W., Oszczepalski, S., 2000a. Geochemical and isotopic composition of organic matter in the Kupferschiefer of the Polish Zechstein basin: relation to maturity and base metal mineralization. Int. J. Earth Sci. 89, 72–89.
Bechtel, A., Shieh, Y.N., Elliott, W.C., Oszczepalski, S., Hoernes, S., 2000b. Mineralogy, crystallinity and stable isotopic composition of illitic clays within the Polish Zechstein basin: implications for the genesis of Kupferschiefer mineralization. Chem. Geol. 163, 189–205.
Becker, F., Bechstädt, T., 2006. Sequence stratigraphy of a carbonate-evaporite succession (Zechstein 1, Hessian Basin, Germany). Sedimentology 53, 1083–1120.
Behr, H.J., Gerler, J., 1987. Inclusions of sedimentary brines in post-Variscan mineralizations in the Federal Republic of Germany—a study by neutron-activation analysis. Chem. Geol. 61, 65–77.

Behr, H.J., Horn, E.E., Frentzel-Beyme, K., Reutel, C., 1987. Fluid inclusion characteristics of the Variscan and post-Variscan mineralizing fluids in the Federal Republic of Germany. Chem. Geol. 61, 273–285.

Blundell, D., Karnkowski, P., Alderton, D., Oszczepalski, S., Kucha, H., 2003. Copper mineralization of the Polish Kupferschiefer: a proposed basement fault-fracture system of fluid flow. Econ. Geol. 98, 1487.

Bodnar, R.J., Vityk, M.O., 1994. Interpretation of microthermometric data for H_2O–NaCl fluid inclusions. In: De Vivo, B., Frezzotti, M. (Eds.), Fluid inclusions in minerals: Methods and applications. Pontignano, Siena, pp. 117–130.

Böhlke, J.K., Irwin, J.J., 1992. Laser microprobe analyses of Cl, Br, I, and K in fluid inclusions: implications for sources of salinity in some ancient hydrothermal fluids. Geochim. Cosmochim. Acta 56, 203–225.

Boiron, M.C., Cathelineau, M., Richard, A., 2010. Fluid flows and metal deposition near basement/cover unconformity: lessons and analogies from Pb–Zn–F–Ba systems for the understanding of Proterozoic U deposits. Geofluids 10, 270–292.

Capuano, R.M., 1992. The temperature dependence of hydrogen isotope fractionation between clay minerals and water: evidence from a geopressured system. Geochim. Cosmochim. Acta 56, 2547–2554.

Carpenter, A.B., Trout, M.L., Pickett, E.E., 1974. Preliminary report on the origin and chemical evolution of lead- and zinc-rich oil field brines in central Mississippi. Econ. Geol. 69, 1191–1206.

Cathles, L.M., Oszczepalski, S., Jowett, E.C., 1993. Mass-balance evaluation of the late diagenetic hypothesis for Kupferschiefer Cu mineralization in the Lubin basin of southwestern Poland. Econ. Geol. 88, 948–956.

Chacko, T., Cole, D.R., Horita, J., 2001. Equilibrium oxygen, hydrogen and carbon isotope fractionation factors applicable to geologic systems. Rev. Mineral. Geochem. 43, 1–81.

Derome, D., Cathelineau, M., Fabre, C., Boiron, M.C., Banks, D.A., Lhomme, T., Cuney, M., 2005. Mixing of sodic and calcic brines and uranium deposition at McArthur River, Saskatchewan, Canada: a Raman and laser-induced breakdown spectroscopic study of fluid inclusions. Econ. Geol. 100, 1529–1545.

Dolejš, D., Wagner, T., 2008. Thermodynamic modeling of non-ideal mineral-fluid equilibria in the system Si–Al–Fe–Mg–Ca–Na–K–H–O–Cl at elevated temperatures and pressures: implications for hydrothermal mass transfer in granitic rocks. Geochim. Cosmochim. Acta 72, 526–553.

Dombrowski, A., Okrusch, M., Henjes-Kunst, F., 1994. Geothermobarometry and geochronology on mineral assemblages of orthogneisses and related metapelites of the Spessart crystalline complex, NW Bavaria, Germany. Chem. Erde 54, 85–101.

Dombrowski, A., Okrusch, M., Richter, P., Henjes-Kunst, F., Höhndorf, A., Kröner, A., 1995. Orthogneisses in the Spessart Crystalline Complex, north-west Bavaria: Silurian granitoid magmatism at an active continental margin. Geol. Rundsch. 84, 399–411.

Engle, M.A., Rowan, E.L., 2013. Interpretation of Na–Cl–Br systematics in sedimentary basin brines: comparison of concentration, element ratio, and isometric log-ratio approaches. Math. Geosci. 45, 87–101.

Friedman, I., O'Neil, J.R., 1977. Compilation of stable isotope fractionation factors of geochemical interest. U.S. Geol. Surv. Prof. Paper (440-KK).

Fusswinkel, T., Wagner, T., Wälle, M., Wenzel, T., Heinrich, C.A., Markl, G., 2013a. Fluid mixing forms basement-hosted Pb–Zn deposits: insight from metal and halogen geochemistry of individual fluid inclusions. Geology 41, 679–682.

Fusswinkel, T., Wagner, T., Wenzel, T., Wälle, M., Lorenz, J., 2013b. Evolution of unconformity-related Mn–Fe–As vein mineralization, Sailauf (Germany): insight from major and trace elements in oxide and carbonate minerals. Ore Geol. Rev. 50, 28–51.

Garven, G., Appold, M.S., Toptygina, V.I., Hazlett, T.J., 1999. Hydrogeologic modeling of the genesis of carbonate-hosted lead–zinc ores. Hydrogeol. J. 7, 108–126.

Gleeson, S.A., Wilkinson, J.J., Stuart, F.M., Banks, D.A., 2001. The origin and evolution of base metal mineralising brines and hydrothermal fluids, South Cornwall, UK. Geochim. Cosmochim. Acta 65, 2067–2079.

Goldhaber, M.B., Church, S.E., Doe, B.R., Aleinikoff, J.N., Brannon, J.C., Podosek, F.A., Mosier, E.L., Taylor, C.D., Gent, C.A., 1995. Lead and sulfur isotope investigation of Paleozoic sedimentary rocks from the southern Midcontinent of the United States; implications for paleohydrology and ore genesis of the Southeast Missouri lead belts. Econ. Geol. 90, 1875–1910.

Goldstein, R.H., Reynolds, T.J., 1994. Systematics of fluid inclusions in diagenetic minerals. Society for Sedimentary Geology Short Course Series, 31.

Groves, D.I., Goldfarb, R.J., Gebre-Mariam, M., Hagemann, S., Robert, F., 1998. Orogenic gold deposits: a proposed classification in the context of their crustal distribution and relationship to other gold deposit types. Ore Geol. Rev. 13, 7–27.

Guillong, M., Heinrich, C.A., 2007. Sensitivity enhancement in laser ablation ICP-MS using small amounts of hydrogen in the carrier gas. J. Anal. At. Spectrom. 22, 1488–1494.

Guillong, M., Meier, D., Allan, M., Heinrich, C.A., Yardley, B., 2008. SILLS: A MATLAB-based program for the reduction of laser ablation ICP-MS data of homogeneous materials and inclusions. Mineralogical Association of Canada Short Course Series, 40 328–333.

Günther, D., Frischknecht, R., Heinrich, C.A., Kahlert, H.J., 1997. Capabilities of an argon fluoride 193 nm excimer laser for laser ablation inductively coupled plasma mass spectometry microanalysis of geological materials. J. Anal. At. Spectrom. 12, 939–944.

Günther, D., Audétat, A., Frischknecht, R., Heinrich, C.A., 1998. Quantitative analysis of major, minor and trace elements in fluid inclusions using laser ablation-inductively coupled plasma mass spectrometry. J. Anal. At. Spectrom. 13, 263–270.

Halter, W.E., Pettke, T., Heinrich, C.A., Rothen-Rutishauser, B., 2002. Major to trace element analysis of melt inclusions by laser-ablation ICP-MS: methods of quantification. Chem. Geol. 183, 63–86.

Hanor, J.S., 1994. Physical and chemical controls on the composition of waters in sedimentary basins. Mar. Pet. Geol. 11, 31–45.

Hanor, J.S., 2001. Reactive transport involving rock-buffered fluids of varying salinity. Geochim. Cosmochim. Acta 65, 3721–3732.

Hedenquist, J.W., Lowenstern, J.B., 1994. The role of magmas in the formation of hydrothermal ore deposits. Nature 370, 519–527.

Heinrich, C.A., Pettke, T., Halter, W.E., Aigner-Torres, M., Audétat, A., Günther, D., Hattendorf, B., Bleiner, D., Guillong, M., Horn, I., 2003. Quantitative multi-element analysis of minerals, fluid and melt inclusions by laser-ablation inductively-coupled-plasma mass-spectrometry. Geochim. Cosmochim. Acta 67, 3473–3497.

Henley, R.W., Truesdell, A.H., Barton, P.B., 1984. Fluid–mineral equilibria in hydrothermal systems. Rev. Econ. Geol. 1.

Hewett, D., 1972. Manganite, hausmannite, braunite; features, modes of origin. Econ. Geol. 67, 83.

Hitzman, M., Kirkham, R., Broughton, D., Thorson, J., Selley, D., 2005. The sediment-hosted stratiform copper ore system. In: Hedenquist, J.W., Thompson, J.F.H., Goldfarb, R.J., Richards, J.P. (Eds.), Economic Geology 100th Anniversary Volume. Society of Economic Geologists, Littleton CO, pp. 609–642.

Holser, W., 1979. Trace elements and isotopes in evaporites. Mar. Miner. 6, 295–436.

Horita, J., Cole, D.R., Wesolowski, D.J., 1993. The activity–composition relationship of oxygen and hydrogen isotopes in aqueous salt solutions: II. Vapor–liquid water equilibration of mixed salt solutions from 50 to 100 °C and geochemical implications. Geochim. Cosmochim. Acta 57, 4703–4711.

Jowett, E.C., 1986. Genesis of Kupferschiefer Cu–Ag deposits by convective flow of Rotliegende brines during Triassic rifting. Econ. Geol. 81, 1823–1837.

Käding, K.C., 2005. The Zechstein in the stratigraphical scale of Germany 2002. Newsl. Stratigr. 41, 123–127.

Kesler, S.E., Martini, A.M., Appold, M.S., Walter, L.M., Huston, T.J., Fuman, F.C., 1996. Na–Cl–Br systematics of fluid inclusions from Mississippi Valley-type deposits. Appalachian Basin: constraints on solute origin and migration paths. Geochim. Cosmochim. Acta 60, 225–233.

Kharaka, Y.K., Maest, A.S., Carothers, W.W., Law, L.M., Lamothe, P.J., Fries, T.L., 1987. Geochemistry of metal-rich brines from central Mississippi Salt Dome basin, U.S.A. Appl. Geochem. 2, 543–561.

Knauth, L.P., Beeunas, M.A., 1986. Isotope geochemistry of fluid inclusions in Permian halite with implications for the isotopic history of ocean water and the origin of saline formation waters. Geochim. Cosmochim. Acta 50, 419–433.

Kostova, B., Pettke, T., Driesner, T., Petrov, P., Heinrich, C.A., 2004. LA ICP-MS study of fluid inclusions in quartz from the Yuzhna Petrovitsa deposit, Madan ore field, Bulgaria. Swiss Bull. Mineral. Petrol. 84, 25–36.

Kotzer, T., Kyser, T., 1995. Petrogenesis of the Proterozoic Athabasca Basin, northern Saskatchewan, Canada, and its relation to diagenesis, hydrothermal uranium mineralization and paleohydrogeology. Chem. Geol. 120, 45–89.

Kotzeva, B.G., Guillong, M., Stefanova, E., Piperov, N.B., 2011. LA-ICP-MS analysis of single fluid inclusions in a quartz crystal (Madan ore district, Bulgaria). J. Geochem. Explor. 108, 163–175.

Kroner, U., Mansy, J.L., Mazur, S., Aleksandrowski, P., Hann, H.P., Huckriede, H., Lacquement, F., Lamarche, J., Ledru, P., Pharaoh, T.C., Zedler, H., Zeh, A., Zulauf, G., 2008. Variscan tectonics. In: McCann, T. (Ed.), The Geology of Central Europe. Geological Society, London, pp. 599–664.

Leach, D., Sangster, D., Kelley, K., Large, R., Garven, G., Allen, C., Gutzmer, J., Walters, S., 2005. Sediment-hosted lead–zinc deposits: a global perspective. Econ. Geol. 100, 561–607.

Leisen, M., Boiron, M.C., Richard, A., Dubessy, J., 2012. Determination of Cl and Br concentrations in individual fluid inclusions by combining microthermometry and LA-ICPMS analysis: implications for the origin of salinity in crustal fluids. Chem. Geol. 330–331, 197–206.

Lüders, V., Möller, P., 1992. Fluid evolution and ore deposition in the Harz mountains (Germany). Eur. J. Mineral. 4, 1053–1068.

Lüders, V., Reutel, C., Hoth, P., Banks, D.A., Mingram, B., Pettke, T., 2005. Fluid and gas migration in the North German Basin: fluid inclusion and stable isotope constraints. Int. J. Earth Sci. 94, 990–1009.

Matthäi, S.K., Heinrich, C.A., Driesner, T., 2004. Is the Mount Isa copper deposit the product of forced brine convection in the footwall of a major reverse fault? Geology 32, 357–360.

McCaffrey, M.A., Lazar, B., Holland, H.D., 1987. The evaporation path of seawater and the coprecipitation of Br^- and K^+ with halite. J. Sediment. Res. 57, 928–937.

McCaig, A.M., Tritlla, J., Banks, D.A., 2000. Fluid mixing and recycling during Pyrenean thrusting: evidence from fluid inclusion halogen ratios. Geochim. Cosmochim. Acta 64, 3395–3412.

McCann, T., Kiersnowski, H., Krainer, K., Vozárová, A., Peryt, T.M., Oplustil, S., Stollhofen, H., Schneider, J.L., Wetzel, A., Boulvain, F., Dusar, M., Török, Á., Haas, J., Tait, J., Körner, F., 2008. Permian. In: McCann, T. (Ed.), The Geology of Central Europe. The Geological Society, London, pp. 531–597.

McGoldrick, P.J., Keays, R.R., Scott, B.B., 1979. Thallium: a sensitive indicator of rock/seawater interaction and of sulfur saturation of silicate melts. Geochim. Cosmochim. Acta 43, 1303–1311.

Muchez, P., Heijlen, W., Banks, D.A., Blundell, D., Boni, M., Grandia, F., 2005. Extensional tectonics and the timing and formation of basin-hosted deposits in Europe. Ore Geol. Rev. 27, 241–267.

Muir-Wood, R., King, G.C.P., 1993. Hydrological signatures of earthquake strain. J. Geophys. Res. Solid Earth 98, 22035–22068.

Neumann, E.R., Wilson, M., Heeremans, M., Spencer, E.A., Obst, K., Timmerman, M.J., Kirstein, L., 2004. Late Carboniferous–Permian rifting and magmatism in southern

Scandinavia, the North Sea and northern Germany: A review. Geol. Soc. Lond. Spec. Publ. 223, 11–40.
Odin, G.S., Desprairies, A., Fullagar, P.D., Bellon, H., Decarreau, A., Froehlich, F., Zelvelder, M., 1988. Nature and geological significance of celadonite. In: Odin, G.S. (Ed.), Green marine clays; oolitic ironstone facies, verdine facies, glaucony facies and celadonite-bearing facies; a comparative study. Dev. Sedimentol, 45, pp. 337–398.
Okrusch, M., Richter, P., 1986. Orthogneisses of the Spessart crystalline complex, Northwest Bavaria: indicators of the geotectonic environment? Geol. Rundsch. 75, 555–568.
Okrusch, M., Weber, K., 1996. Der Kristallinkomplex des Vorspessart. Z. Geol. Wiss. 24, 141–174.
Okrusch, M., Lorenz, J., Weyer, S., 2007. The genesis of sulfide assemblages in the former Wilhelmine mine, Spessart, Bavaria, Germany. Can. Mineral. 45, 723–750.
Okrusch, M., Geier, G., Lorenz, J., 2011. Spessart. Geologische Entwicklung und Struktur, Gesteine und Minerale. Sammlung geologischer Führer Band 106. Gebr. Bornträger, Stuttgart.
Oszczepalski, S., 1999. Origin of the Kupferschiefer polymetallic mineralization in Poland. Mineral. Deposita 34, 599–613.
Pauwels, H., Fouillac, C., Fouillac, A.M., 1993. Chemistry and isotopes of deep geothermal saline fluids in the Upper Rhine Graben: origin of compounds and water–rock interactions. Geochim. Cosmochim. Acta 57, 2737–2749.
Raffensperger, J.P., Garven, G., 1995. The formation of unconformity-type uranium ore deposits; 2, Coupled hydrochemical modeling. Am. J. Sci. 295, 639–696.
Rentzsch, J., 1974. The Kupferschiefer in comparison with the deposits of the Zambian Copperbelt. In: Bartholomé, P. (Ed.), Gisements Stratiformes et Provinces Cuprifères. Société Géologique de Belgique, Liege, pp. 395–418.
Reyes, A.G., Trompetter, W.J., 2012. Hydrothermal water–rock interaction and the redistribution of Li, B and Cl in the Taupo Volcanic Zone, New Zealand. Chem. Geol. 314–317, 96–112.
Richard, A., Banks, D.A., Mercadier, J., Boiron, M.C., Cuney, M., Cathelineau, M., 2011. An evaporated seawater origin for the ore-forming brines in unconformity-related uranium deposits (Athabasca Basin, Canada): Cl/Br and δ^{37}Cl analysis of fluid inclusions. Geochim. Cosmochim. Acta 75, 2792–2810.
Richard, A., Rozsypal, C., Mercadier, J., Banks, D.A., Cuney, M., Boiron, M.C., Cathelineau, M., 2012. Giant uranium deposits formed from exceptionally uranium-rich acidic brines. Nat. Geosci. 5, 142–146.
Ridley, J.R., Diamond, L.W., 2000. Fluid chemistry of orogenic lode gold deposits and implications for genetic models. Rev. Econ. Geol. 13, 141–162.
Rittenhouse, G., 1967. Bromine in oil-field waters and its use in determining possibilities of origin of these waters. AAPG Bull. 51, 2430–2440.
Rumble, D., Hoering, T., 1994. Analysis for oxygen and sulfur isotope ratios in oxide and sulfide minerals by spot heating with a carbon dioxide laser in a fluorine atmosphere. Acc. Chem. Res. 27, 237–241.
Sangster, D., 1990. Mississippi Valley-type and sedex lead–zinc deposits: a comparative examination. Transactions of the Institution of Mining and Metallurgy, 99 21–42.
Schlegel, T.U., Wälle, M., Steele-MacInnis, M., Heinrich, C.A., 2012. Accurate and precise quantification of major and trace element compositions of calcic–sodic fluid inclusions by combined microthermometry and LA-ICPMS analysis. Chem. Geol. 334, 144–153.
Seo, J.H., Guillong, M., Aerts, M., Zajacz, Z., Heinrich, C.A., 2011. Microanalysis of S, Cl, and Br in fluid inclusions by LA-ICP-MS. Chem. Geol. 284, 35–44.
Sharp, Z., 1990. A laser-based microanalytical method for the in situ determination of oxygen isotope ratios of silicates and oxides. Geochim. Cosmochim. Acta 54, 1353–1357.
Sheppard, S.M.F., 1986. Characterization and isotopic variations in natural waters. Rev. Mineral. Geochem. 16, 165–183.
Sheppard, S.M.F., Gilg, H.A., 1996. Stable isotope geochemistry of clay minerals. Clay Miner. 31, 1–24.
Staude, S., Bons, P.D., Markl, G., 2009. Hydrothermal vein formation by extension-driven dewatering of the middle crust: an example from SW Germany. Earth Planet. Sci. Lett. 286, 387–395.
Steele-MacInnis, M., Bodnar, R.J., Naden, J., 2011. Numerical model to determine the composition of H_2O–NaCl–$CaCl_2$ fluid inclusions based on microthermometric and microanalytical data. Geochim. Cosmochim. Acta 75, 21–40.
Stoffell, B., Appold, M.S., Wilkinson, J.J., McClean, N.A., Jeffries, T.E., 2008. Geochemistry and evolution of Mississippi Valley-Type mineralizing brines from the Tri-State and Northern Arkansas districts determined by LA-ICP-MS microanalysis of fluid inclusions. Econ. Geol. 103, 1411–1435.
Sweeney, M., Binda, P., Vaughan, D., 1991. Genesis of the ores of the Zambian Copperbelt. Ore Geol. Rev. 6, 51–76.
Symons, D.T., Kawasaki, K., Walther, S., Borg, G., 2011. Paleomagnetism of the Cu–Zn–Pb-bearing Kupferschiefer black shale (Upper Permian) at Sangerhausen, Germany. Mineral. Deposita 46, 137–152.
Truesdell, A.H., 1974. Oxygen isotope activities and concentrations in aqueous salt solutions at elevated temperatures: consequences for isotope geochemistry. Earth Planet. Sci. Lett. 23, 387–396.
Trusheim, F., 1964. Über den Untergrund Frankens: Ergebnisse von Tiefbohrungen in Franken und Nachbargebieten, 1953–1960. Geol. Bavarica, 54 (92 pp.).
Vaughan, D., Sweeney, M., Friedrich, G., Diedel, R., Haranczyk, C., 1989. The Kupferschiefer; an overview with an appraisal of the different types of mineralization. Econ. Geol. 84, 1003–1027.
Vennemann, T.W., O'Neil, J.R., 1993. A simple and inexpensive method of hydrogen isotope and water analyses of minerals and rocks based on zinc reagent. Chem. Geol. 103, 227–234.
Wagner, T., Lorenz, J., 2002. Mineralogy of complex Co–Ni–Bi vein mineralisation, Bieber deposit, Spessart, Germany. Mineral. Mag. 66, 385–407.
Wagner, T., Okrusch, M., Weyer, S., Lorenz, J., Lahaye, Y., Taubald, H., Schmitt, R.T., 2010. The role of the Kupferschiefer in the formation of hydrothermal base metal mineralization in the Spessart ore district, Germany: insight from detailed sulfur isotope studies. Mineral. Deposita 45, 217–239.
Wilkinson, J.J., 2010. A review of fluid inclusion constraints on mineralization in the Irish ore field and implications for the genesis of sediment-hosted Zn–Pb deposits. Econ. Geol. 105, 417–442.
Wilkinson, J.J., Everett, C.E., Boyce, A.J., Gleeson, S.A., Rye, D.M., 2005. Intracratonic crustal seawater circulation and the genesis of subseafloor zinc–lead mineralization in the Irish orefield. Geology 33, 805–808.
Wilkinson, J.J., Stoffell, B., Wilkinson, C.C., Jeffries, T.E., Appold, M.S., 2009. Anomalously metal-rich fluids form hydrothermal ore deposits. Science 323, 764–767.
Yardley, B.W.D., 2005. Metal concentrations in crustal fluids and their relationship to ore formation. Econ. Geol. 100, 613–632.
Ziegler, P., 1987. Late Cretaceous and Cenozoic intra-plate compressional deformations in the Alpine foreland—a geodynamic model. Tectonophysics 137, 389–420.

FIA	FI	Size (µm)	Li (ppm)	Na (ppm)	K (ppm)	Rb (ppm)	Cs (ppm)	Mg (ppm)	Ca (ppm)	Sr (ppm)	Ba (ppm)	B (ppm)	Fe (ppm)	Mn (ppm)	Zn (ppm)	Pb (ppm)	Cu (ppm)	Ag (ppm)	Tl (ppm)	As (ppm)	Sb (ppm)	S (ppm)	Cl (ppm)	Br (ppm)	T_m (i) (°C)	T_H (HH) (°C)
Sai-010a D4 (conc.)	01	40	390	59800	8000	79	33	<0.1	43700	2190	150	130	n.a.	n.a.	360	150	4.1	n.a.	<0.04	330	n.a.	<8	208600	4930	-26.2	-2.9
	02	35	340	59000	8270	52	26	880	42900	1720	100	94	n.a.	n.a.	260	99	4.5	n.a.	1.4	220	n.a.	<8.9	185000	3590	-26.0	-8.5
	03	40	470	58800	<12	81	33	<0.08	43500	2210	1.6	150	n.a.	n.a.	370	120	3.8	n.a.	2.7	280	n.a.	<5.1	224500	5340	-26.1	-7.5
	04	35	340	58800	6670	61	25	<0.1	43500	1550	<0.4	100	n.a.	n.a.	240	100	<0.2	n.a.	<0.05	180	n.a.	<8.4	194300	4480	-26.1	-7.6
	05	35	360	58700	8570	65	27	1770	43500	2290	120	170	n.a.	n.a.	350	120	<0.05	n.a.	2.8	370	n.a.	<3.2	237600	3910	-26.1	-7.7
	06	50	530	58700	10300	83	35	1060	43500	2540	250	140	n.a.	n.a.	440	160	<0.08	n.a.	3.5	480	n.a.	<4.4	250900	5060	-26.1	-7.3
	07	50	310	58900	6980	57	22	970	43400	1660	22	79	n.a.	n.a.	320	110	3.6	n.a.	2.5	240	n.a.	<2.6	177300	2480	-26.1	-7.3
	08	45	380	59000	8510	94	31	700	43400	2250	3	83	n.a.	n.a.	330	140	4.2	n.a.	3.7	130	n.a.	<6.9	223600	5390	-26.1	-7.0
Average			390	59000	8190	72	29	1080	43400	2050	92	120			330	130	4.0		2.8	280			212700	4400	-26.1	-7.0
SD			70	400	1200	15	5	410	230	360	91	30			60	20	0.4		0.8	110			26000	1010	0.1	1.6
Sai-010a D6 (conc.)	01		860	63300	5270	130	56	10300	38800	3680	18	110	n.a.	n.a.	<0.4	370	6.0	n.a.	6.5	6.9	n.a.	<8.6	194400	4790	-25.4	-7.0
Sai-014a A1 (conc.)	02	55	780	57000	3530	110	65	140	45400	<0.009	51	120	n.a.	n.a.	390	550	5.7	n.a.	6.9	<0.08	n.a.	<1.5	190800	3080	-26.5	-7.4
	03	40	680	56500	4940	150	65	360	46000	<0.01	85	110	n.a.	n.a.	470	620	<0.06	n.a.	5.8	<0.1	n.a.	<2.7	242500	4010	-26.6	-7.2
	04	30	640	55900	2920	120	52	430	46600	1740	66	130	n.a.	n.a.	420	510	<0.08	n.a.	4.3	<0.2	n.a.	<3.4	204400	3880	-26.7	-7.4
	05	30	780	56400	3870	110	53	<0.06	46000	1720	67	110	n.a.	n.a.	450	670	3.7	n.a.	6.1	<0.1	n.a.	<2.9	180800	3060	-26.7	-7.4
	06	30	900	56500	3930	150	67	<0.07	46000	1650	82	120	n.a.	n.a.	410	620	<0.09	n.a.	5.3	<0.2	n.a.	<3.6	177500	2540	-26.6	-7.4
	07	30	850	56500	4530	130	59	210	46000	1420	5.2	130	n.a.	n.a.	520	690	2.9	n.a.	7.8	<0.3	n.a.	<7	189800	4610	-26.6	-7.1
	08	30	980	56500	4390	180	79	750	46400	2100	53	150	n.a.	n.a.	640	690	3.6	n.a.	10	<0.2	n.a.	<5.1	213400	5350	-26.6	-7.1
Average			800	56800	4010	140	63	380	46100	1730	58	120			470	620	4.0		7.0				199900	3790	-26.6	-7.3
SD			120	800	670	30	9	240	400	250	27	14			90	70	1.2		1.9				22600	980	0.1	0.1
Sai-014a D3 (conc.)	01	40	1130	61200	5520	170	84	460	41000	2910	140	160	n.a	n.a.	690	1100	<0.09	n.a	9.1	<0.1	n.a	<3.4	251900	3270	-25.8	-7.1
	02	40	920	61900	5140	120	61	<0.03	40300	1590	90	150	n.a	n.a	510	770	4.9	n.a	8.1	<0.07	n.a	<1.8	199900	2970	-25.8	-7.1
	03	35	870	65400	5210	150	63	750	36200	<0.02	150	130	n.a.	n.a.	460	670	<0.06	n.a.	6.5	<0.1	n.a.	<2.5	180800	2910	-25.1	-8.1
	04	25	940	63000	6270	140	67	220	39000	2100	110	120	n.a	n.a	560	850	6.2	n.a	8.3	<0.1	n.a	<2.5	237800	3890	-25.7	-7.1
	06	25	910	61600	<14	120	60	<0.08	40400	810	<0.3	94	n.a.	n.a.	500	260	<0.1	n.a.	6.3	<0.2	n.a.	<4.6	235100	4320	-25.5	-7.5
Average			960	62600	5540	140	67	480	39400	1850	120	130			540	730	5.6		7.7				221100	3470	-25.5	-7.4
SD			100	1700	520	20	10	270	1900	880	30	30			90	310	0.9		1.2				29600	610	0.3	0.4
Sai-014a E2 (conc.)	01	30	990	63400	5360	150	66	<0.05	38900	2220	15	150	n.a.	n.a.	540	630	4.1	n.a	7.2	<0.1	n.a	<2.3	205400	2530	-25.5	-6.4
	02	40	860	62800	4960	150	64	160	39600	1820	87	130	n.a.	n.a.	570	660	4.5	n.a.	7.2	<0.2	n.a.	360	207900	3380	-25.6	-6.3
	04	50	920	63400	4690	120	58	210	38900	1710	15	110	n.a.	n.a.	480	660	6.0	n.a.	7.6	<0.2	n.a.	<3.3	189900	2680	-25.5	-6.5
	05	30	1010	63500	7040	150	73	500	38900	2220	38	130	n.a.	n.a.	550	440	<0.1	n.a.	8.6	<0.2	n.a.	<4.1	230900	4500	-25.5	-6.6
	06	35	750	64700	4080	100	50	<0.06	38100	1830	45	120	n.a.	n.a.	460	420	4.4	n.a.	6	<0.1	n.a.	<2.7	173300	3360	-25.5	-6.3
	07	35	970	61800	6190	140	68	280	40600	1700	100	140	n.a.	n.a.	530	710	3.4	n.a.	7.4	<0.2	n.a.	<3	212900	4250	-25.4	-4.7
	08	30	1120	62600	5390	180	75	400	39600	<0.03	160	140	n.a.	n.a.	830	960	<0.08	n.a.	9.4	<0.2	n.a.	<3.7	280700	5310	-25.7	-6.6
Average			950	63200	5390	140	65	310	39200	1920	66	131			570	640	4.5		7.6			360	214400	3720	-25.5	-6.2
SD			120	900	960	30	9	140	800	240	53	13			120	180	1.0		1.1				34400	1010	0.1	0.6

FIA	FI	Size (µm)	Li (ppm)	Na (ppm)	K (ppm)	Rb (ppm)	Cs (ppm)	Mg (ppm)	Ca (ppm)	Sr (ppm)	Ba (ppm)	B (ppm)	Fe (ppm)	Mn (ppm)	Zn (ppm)	Pb (ppm)	Cu (ppm)	Ag (ppm)	Tl (ppm)	As (ppm)	Sb (ppm)	S (ppm)	Cl (ppm)	Br (ppm)	T_m (i) (°C)	T_h (HH) (°C)
Sai-028 A1 (conc.)	01	40	120	59200	1000	34	7	<0.1	37800	1540	30	65	n.a.	n.a.	340	<0.04	<0.1	n.a.	1.6	<0.4	n.a.	<4.2	200900	4730	-25.1	-19.5
	02	30	96	56600	1840	22	4.7	2960	40400	1720	16	47	n.a.	n.a.	490	140	3.6	n.a.	1.5	<0.3	n.a.	<3	176400	4390	-25.5	-20.1
	03	35	150	61200	2200	35	9.6	<0.1	35200	4190	17	110	n.a.	n.a.	1580	250	5.6	n.a.	3.7	<0.3	n.a.	<3.9	269400	6260	-24.8	-20.1
	04	35	79	63500	1530	25	5.1	7250	31500	2470	22	56	n.a.	n.a.	740	120	2.2	n.a.	1	<0.2	n.a.	<2	190800	3950	-24.3	-22.1
	05	50	110	62000	2160	30	8.2	2410	35400	1690	31	47	n.a.	n.a.	520	77	3.5	n.a.	2	<0.2	n.a.	<2.7	181000	3710	-24.8	-18.1
	06	95	700	51700	4530	110	46	<0.02	45200	1580	9.8	110	n.a.	n.a.	490	270	2.8	n.a.	6.8	<0.04	n.a.	<0.7	184800	4970	-26.2	-21.5
	07	55	660	51700	3330	95	34	9550	46700	1010	2.2	100	n.a.	n.a.	410	<0.01	1.8	n.a.	4.9	<0.07	n.a.	<1.1	178300	2920	-26.5	-18.4
	08	60	110	57100	1640	21	5.7	2430	41900	1630	2.4	84	n.a.	n.a.	240	28	1.6	n.a.	0.85	<0.08	n.a.	<1.4	169900	4660	-25.8	-15.9
	09	40	810	53700	4040	110	51	<0.03	46200	1700	130	110	n.a.	n.a.	460	580	2.8	n.a.	6.8	<0.07	n.a.	<1.4	169800	4440	-26.5	-14.6
Average			320	57400	2470	54	19	4920	40000	1950	29	81			590	210	3.0		3.2				191300	4450	-25.5	-18.9
SD			310	4400	1210	39	19	3290	5400	920	39	28			400	190	1.3		2.4				30900	920	0.7	2.3
Sai-028 A2 (conc.)	01	70	34	53700	1300	27	6.4	3280	48100	1510	47	23	n.a.	n.a.	400	72	2.2	n.a.	2	0.45	n.a.	130	188400	4350	-26.9	-10.1
	03	35	180	55300	2750	77	35	<0.06	48100	2110	<0.2	27	n.a.	n.a.	280	610	<0.09	n.a.	6.5	<0.2	n.a.	<3.7	174500	5050	-27.0	-4.7
	04	55	62	53300	2890	53	15	2040	50700	1380	51	74	n.a.	n.a.	210	290	2.2	n.a.	4.2	9	n.a.	17	165900	5180	-27.5	-2.9
	07	30	870	59500	5080	140	63	<0.07	42900	2430	<0.2	120	n.a.	n.a.	810	1030	<0.1	n.a.	9.3	<0.2	n.a.	<3.3	186900	4560	-26.1	-6.8
	08	45	830	59300	4420	130	57	<0.2	42900	1410	16	130	n.a.	n.a.	520	600	<0.2	n.a.	7.1	<0.4	n.a.	<6.8	188100	4700	-26.1	-7.3
	09	30	200	53400	3450	86	23	<0.06	50700	2570	18	36	n.a.	n.a.	260	330	<0.08	n.a.	5.3	<0.1	n.a.	<2.7	203400	5040	-27.5	-2.6
Average			380	55800	3320	86	33	2660	47200	1900	33	58			410	490	2.2		5.7	5		74	187900	4810	-26.8	-5.7
SD			380	2900	1340	44	23	880	3600	540	19	52			220	330	0.0		2.5	6		80	9200	330	0.6	2.6
Sai-058 A1 (conc.)	01	40	910	55200	5720	140	57	940	47200	3700	250	120	n.a	n.a.	620	1040	3.4	n.a	8.4	1610	n.a	<2	193300	3540	-26.8	-7.8
	02	50	350	57900	3590	93	26	<0.1	43800	1180	67	40	n.a	n.a	210	580	0.7	n.a	4.8	<0.3	n.a	<6.6	211500	4240	-26.2	-9.3
	03	50	280	57900	3150	91	24	<0.08	43800	960	60	57	n.a.	n.a.	230	270	<0.1	n.a.	5.1	<0.2	n.a.	<3.7	207500	4300	-26.2	-9.3
	04	30	230	51800	7400	44	16	790	51100	1780	11	56	n.a	n.a	270	110	4.7	n.a	2.2	23	n.a	<3.6	215200	3390	-27.5	-7.4
	05	35	250	60200	5670	66	18	<0.05	42700	1600	64	130	n.a.	n.a.	45	74	2.7	n.a.	2.5	20	n.a.	<2.2	239500	5790	-26.1	-5.0
	06	30	690	51600	5570	91	55	<0.04	51600	1480	270	120	n.a.	n.a.	400	720	<0.06	n.a.	7.3	<0.1	n.a.	<2.7	165700	3360	-27.6	-6.5
Average			450	55800	5180	88	33	870	46700	1780	120	87			300	470	2.9		5.1	550			205500	4100	-26.7	-7.6
SD			280	3500	1570	32	18	110	3900	980	110	40			200	380	1.7		2.5	920			24600	930	0.6	1.5
Sai-058 B2 (conc.)	01	65	870	64300	6000	130	55	580	38400	1920	310	160	n.a.	n.a.	590	510	<0.05	n.a.	7.9	<0.08	n.a.	<1.6	215500	5050	-25.4	-4.9
	02	30	440	61500	6250	120	72	790	41900	2710	86	51	n.a.	n.a.	250	250	<0.6	n.a.	3.7	<0.7	n.a.	<14	197400	5370	-26.0	-2.6
	03	40	380	56800	3690	62	30	<0.04	44000	1480	130	110	n.a.	n.a.	460	170	3.3	n.a.	2.8	<0.1	n.a.	<2	185900	4710	-26.2	-11.7
	04	30	320	56700	11900	56	23	120	44100	1990	150	190	n.a.	n.a.	65	51	<0.09	n.a.	1.4	<0.1	n.a.	<2.7	206500	4530	-26.2	-12.1
	05	30	96	55300	2400	77	21	<0.06	48100	2620	35	46	n.a.	n.a.	260	520	<0.08	n.a.	<0.02	<0.2	n.a.	<2.9	212800	5910	-27.0	-4.6
	06	35	290	58300	9060	66	22	910	42700	1740	57	150	n.a.	n.a.	34	64	<0.2	n.a.	2.9	<0.2	n.a.	<3.8	202500	4830	-26.0	-11.1
Average			400	58800	6600	85	37	600	43200	2080	130	120			280	260	3.0		4				203400	5070	-26.1	-7.8
SD			260	3400	3490	32	21	350	3200	490	100	60			220	210	0.0		2				10800	510	0.5	3.9

FIA	FI	Size (µm)	Li (ppm)	Na (ppm)	K (ppm)	Rb (ppm)	Cs (ppm)	Mg (ppm)	Ca (ppm)	Sr (ppm)	Ba (ppm)	B (ppm)	Fe (ppm)	Mn (ppm)	Zn (ppm)	Pb (ppm)	Cu (ppm)	Ag (ppm)	Tl (ppm)	As (ppm)	Sb (ppm)	S (ppm)	Cl (ppm)	Br (ppm)	T_m (i) (°C)	T_H (HH) (°C)
Sai-071 B1 (conc.)	01	30	330	63200	3320	83	21	<0.1	31100	1330	<0.3	130	n.a.	n.a.	490	280	<0.5	<0.07	8.9	<0.2	<0.1	<20	185500	6650	-24.2	-22.1
	02	20	270	55800	6760	88	29	5650	31700	<0.1	<0.7	51	n.a.	n.a.	590	<0.3	<1	<0.2	6.9	<0.4	<0.2	<43	146300	5050	-22.1	-24.5
	08	30	170	37900	3330	30	13	3890	24200	1300	33	43	n.a.	n.a.	180	32	<0.5	<0.1	4.1	<0.2	<0.1	<21	89000	2160	-12.6	-24.9
	10	20	300	42300	4870	42	18	<0.5	25600	1570	<0.9	70	n.a.	n.a.	340	<0.4	<1.4	<0.2	6.6	<0.5	<0.4	<56	105000	2130	-14.6	-24.7
Average			270	49800	4570	61	20	4770	28200	1400	33	74			400	160			6.6				131500	4000	-18.4	-24.0
SD			70	11700	1630	29	7	1250	3800	150	0	39			180	180			2.0				43400	2240	4.9	1.1
Sai-071 B3 (conc.)	01	15	310	57000	6470	36	13	<0.3	44700	1050	<0.5	100	n.a.	n.a.	150	96	<0.8	<0.2	2.9	48	<0.2	<34	127300	2640	-26.3	-8.2
	02	20	650	53900	3690	100	52	1780	48600	1030	19	71	n.a.	n.a.	180	<1.2	<3.6	<0.8	8.4	<1.9	<0.9	<170	166600	3050	-27.4	-6.1
	03	40	630	52200	3770	110	38	2630	50500	450	<2.3	110	n.a.	n.a.	130	45	<3.2	<0.6	5.3	<1.3	<0.8	<140	222200	3780	-27.1	-4.9
	09	20	320	54100	11100	48	24	<0.3	48800	2200	22	110	n.a.	n.a.	420	180	<0.9	<0.2	7.3	<0.4	<0.2	<37	213200	2440	-27.0	-6.3
Average			480	54300	6260	74	32	2210	48200	1180	21	98			220	110			6.0	48			182300	2980	-27.0	-6.4
SD			190	2000	3460	37	17	600	2500	730	2	18			140	70			2.4	0			44000	590	0.4	1.2
Sai-071 B4 (conc.)	03	25	80	54900	1730	46	13	<0.3	48600	1160	<0.8	<1.6	n.a.	n.a.	190	240	<0.9	<0.2	4.3	<0.4	<0.2	<40	133800	3100	-27.1	-2.6
Sai-100 A1 (conc.)	01	40	570	64600	6450	91	44	21	38900	2000	29	190	n.a.	n.a.	0.8	130	11.0	n.a.	3.2	<0.2	n.a.	<3.8	174800	3060	-25.5	-1.8
	02	40	290	64600	8540	69	25	<0.1	38900	870	<0.3	96	n.a.	n.a.	<0.5	<0.06	5.9	n.a.	1.8	<0.4	n.a.	<8.3	161100	4730	-25.5	-1.8
	03	40	260	64600	7750	52	21	<0.2	38900	950	31	63	n.a.	n.a.	<0.5	1.5	2.0	n.a.	2.2	<0.5	n.a.	<9.3	165800	4200	-25.5	-1.8
	04	30	550	77400	12100	100	43	0.58	23000	2030	<0.2	150	n.a.	n.a.	<0.2	11	13.0	n.a.	3.4	5.3	n.a.	<4.4	192100	6350	-23.4	-10.0
	05	30	780	64600	8300	94	49	<0.06	38900	2380	46	180	n.a.	n.a.	18	110	11.0	n.a.	3	<0.2	n.a.	<4.7	187500	4690	-23.4	-10.0
	06	35	270	64600	8120	60	21	<0.1	38900	680	17	63	n.a.	n.a.	<0.5	<0.05	5.8	n.a.	1.6	<0.5	n.a.	<9.8	159200	4540	-25.5	-1.8
	07	35	540	78500	12200	110	45	<0.05	22100	2530	75	180	n.a.	n.a.	<0.1	10	14.0	n.a.	3.5	8.6	n.a.	<3	204000	7660	-25.5	-1.8
	08	30	310	75300	9400	66	25	23	25600	1360	27	99	n.a.	n.a.	<0.2	3.8	4.9	n.a.	1.8	<0.2	n.a.	<4.6	175600	4620	-23.3	-9.5
	09	35	410	77500	10500	76	32	29	23000	1570	52	120	n.a.	n.a.	<0.2	9.5	12.0	n.a.	3.4	<0.2	n.a.	<3.4	216600	5100	-23.7	-9.1
	10	25	590	65100	8290	110	48	37	38200	2470	89	190	n.a.	n.a.	<0.3	140	10.0	n.a.	2.5	<0.3	n.a.	<5.2	213900	4040	-23.4	-9.7
	11	30	470	80500	13100	110	40	<0.06	19500	950	<0.1	94	n.a.	n.a.	<0.2	2.3	5.8	n.a.	<0.01	<0.2	n.a.	<3.8	210400	6830	-25.4	-2.2
	12		320	80500	9920	79	25	<0.1	19500	180	<0.3	54	n.a.	n.a.	<0.5	1	<0.3	n.a.	<0.03	<0.5	n.a.	<9.4	210900	5720	-25.4	-2.2
	13		580	65000	8100	93	47	28	38400	2430	120	180	n.a.	n.a.	<0.2	120	4.1	n.a.	3.4	<0.2	n.a.	<3.3	209800	4430	-25.4	-2.2
Average			460	70990	9440	85	36	23	31100	1570	54	128			9	49	8.3		2.7	7			190900	5080	-24.7	-4.9
SD			160	7200	2000	20	11	12	8800	790	34	53			12	61	4.0		0.7	2			21500	1250	1.0	3.8

FIA	FI	Size (µm)	Li (ppm)	Na (ppm)	K (ppm)	Rb (ppm)	Cs (ppm)	Mg (ppm)	Ca (ppm)	Sr (ppm)	Ba (ppm)	B (ppm)	Fe (ppm)	Mn (ppm)	Zn (ppm)	Pb (ppm)	Cu (ppm)	Ag (ppm)	Tl (ppm)	As (ppm)	Sb (ppm)	S (ppm)	Cl (ppm)	Br (ppm)	T_m (i) (°C)	T_h (HH) (°C)
Sal-100 A2 (conc.)	01	35	810	65000	7950	110	69	25	38500	2600	170	230	n.a.	n.a.	<0.1	150	n.a	n.a.	4.3	<0.1	n.a.	n.a	208400	4710	-25.5	-1.9
	02	35	640	65700	6480	90	52	<0.02	37800	2180	<0.04	150	n.a.	n.a.	<0.07	130	n.a.	n.a.	3.3	<0.07	n.a.	n.a.	172900	5540	-25.8	-1.9
	03	35	690	62800	7120	89	49	20	40800	2350	160	180	n.a.	n.a.	8.2	170	n.a	n.a.	3.5	<0.1	n.a.	n.a	193400	2960	-25.8	-1.9
	04	35	520	62800	6510	77	39	<0.06	40800	2460	52	170	n.a.	n.a.	<0.2	100	n.a.	n.a.	2.4	<0.2	n.a.	n.a.	166200	4060	-25.8	-2.0
	05	35	590	62700	6410	91	47	<0.04	40800	2390	150	200	n.a.	n.a.	120	170	n.a.	n.a.	3.3	13	n.a.	n.a.	181000	3490	-25.8	-2.0
	06	30	500	62700	6510	86	48	<0.07	40800	1420	35	140	n.a.	n.a.	12	140	n.a.	n.a.	4.3	<0.3	n.a.	n.a.	186700	4820	-25.7	-5.4
	07	30	640	62300	7430	94	58	<0.06	40400	2820	47	180	n.a.	n.a.	3.3	140	n.a.	n.a.	1.8	<0.3	n.a.	n.a.	186700	4850	-25.7	-5.4
	08	40	520	62300	6580	71	46	<0.05	40400	1060	41	130	n.a.	n.a.	14	110	n.a.	n.a.	4.3	<0.4	n.a.	n.a.	202800	5410	-25.4	-2.0
	09	40	500	65300	6140	80	42	21	38100	2130	15	160	n.a.	n.a.	<0.1	110	n.a	n.a.	2.5	2.1	n.a.	n.a	170500	4280	-25.4	-2.0
	10	35	520	65300	6600	84	40	<0.03	38100	1960	110	150	n.a.	n.a.	<0.1	110	n.a	n.a.	3.5	<0.1	n.a.	n.a	173100	4150	-25.7	-1.8
	11	40	540	63300	6820	73	41	31	40200	1400	28	120	n.a.	n.a.	3.8	98	n.a	n.a.	3.9	1.5	n.a.	<3.5	190300	4420	-25.8	-1.8
	12	40	640	63000	6640	90	50	110	40600	2210	120	180	n.a.	n.a.	32	190	n.a	n.a.	3.7	8.4	n.a.	n.a	214400	3970	-25.8	-1.8
	13	40	450	63000	6720	77	39	<0.1	40600	1100	44	150	n.a.	n.a.	14	99	n.a	n.a.	3.9	<0.5	n.a.	n.a	182100	4120	-25.4	-2.0
	14	30	520	63000	6460	83	44	86	40600	1630	11	130	n.a.	n.a.	7.3	130	n.a.	n.a.	3.7	<0.5	n.a.	n.a.	171500	4230	-25.5	-2.0
	15	40	890	65200	8200	120	60	<0.04	38200	3030	120	230	n.a.	n.a.	<0.2	170	n.a.	n.a.	4.7	<0.2	n.a.	n.a.	235400	4760	-25.7	-1.6
	16	50	690	64500	7260	98	44	<0.09	38900	3060	140	200	n.a.	n.a.	<0.4	140	8.5	n.a.	3.2	<0.3	n.a.	n.a.	188600	4060	-25.3	-2.0
	17	45	710	63700	8240	100	56	<0.03	39900	2380	180	210	n.a.	n.a.	23	250	8.8	n.a.	3.9	<0.09	n.a.	n.a.	188500	4490	-25.4	-2.0
	18	45	590	65000	6250	69	42	<0.03	37800	1840	120	150	n.a.	n.a.	<0.1	110	8.9	n.a.	3.4	1.6	n.a.	n.a	162100	3650	-25.4	-2.0
	19	55	780	65200	8610	110	60	27	38200	2580	170	210	n.a.	n.a.	<0.1	180	13.0	n.a.	3.6	<0.1	n.a.	<1.8	205300	5680	-25.6	-1.8
	20	50	670	65200	8530	110	49	<0.05	38200	2600	<0.1	170	n.a.	n.a.	<0.1	120	7.0	n.a.	2.9	<0.1	n.a.	<2.2	180400	5470	-25.5	-1.9
	21	45	700	64300	7230	110	47	<0.05	39200	2130	170	200	n.a.	n.a.	<0.1	170	12.0	n.a.	3.7	<0.1	n.a.	<2.6	218500	3960	-25.4	-1.9
	22		560	64600	6860	91	50	27	38900	2160	23	190	n.a.	n.a.	1.9	65	9.3	n.a.	3.1	<0.1	n.a.	<2.4	192800	4350	-25.5	-1.9
	23		640	65200	7770	100	54	22	38200	1840	54	140	n.a.	n.a.	0.98	92	7.1	n.a.	3.4	<0.2	n.a.	<2.7	196900	4770	-25.4	-1.9
Average			620	64000	7100	91	49	41	39400	2140	93	170			20	140	9.3		3.5	5			189900	4440	-25.6	-2.2
SD			110	1200	760	14	8	33	1200	560	61	30			33	40	2.1		0.7	5			18100	670	0.2	1.0
Sal-100 A3 (conc.)	01	30	590	64500	6850	87	44	<0.03	38900	2100	110	190	n.a	n.a	5.8	150	9.4	n.a	3.1	1.4	n.a	<2.7	177100	3070	-25.5	-2.1
	02	35	630	63300	7590	92	55	35	40300	2520	120	180	n.a.	n.a.	n.a	160	7.4	n.a.	3.7	2.1	n.a.	n.a.	198500	3240	-25.7	-2.0
	03	45	590	63800	7580	89	46	<0.06	39600	2350	75	180	n.a.	n.a.	<0.3	130	5.2	n.a.	3.2	<0.3	n.a.	<4.6	194900	3500	-25.6	-2.2
	04	40	610	63300	7150	84	40	<0.05	40300	<0.02	130	130	n.a	n.a.	5.3	140	4.6	n.a	2.9	<0.2	n.a	<3.7	194200	3700	-25.7	-2.0
	05	25	490	65800	8170	91	46	<0.05	37600	2070	480	160	n.a.	n.a.	<0.1	19	9.9	n.a.	7.8	<0.1	n.a.	<2.5	177100	5350	-25.3	-2.3
Average			580	64100	7470	89	46	35	39300	2260	180	170			6	120	7.3		4.1	2			188400	3770	-25.6	-2.1
SD			50	1100	500	3	5	0	1100	210	170	20			0	60	2.4		2.1	0			10400	910	0.1	0.1

FIA	FI	Size (µm)	Li (ppm)	Na (ppm)	K (ppm)	Rb (ppm)	Cs (ppm)	Mg (ppm)	Ca (ppm)	Sr (ppm)	Ba (ppm)	B (ppm)	Fe (ppm)	Mn (ppm)	Zn (ppm)	Pb (ppm)	Cu (ppm)	Ag (ppm)	Tl (ppm)	As (ppm)	Sb (ppm)	S (ppm)	Cl (ppm)	Br (ppm)	T_m (i) (°C)	T_H (HH) (°C)
Sai-100 A4 (conc.)	01	30	520	60800	7770	78	42	<0.07	42900	1510	18	180	n.a.	n.a.	170	180	2.7	n.a.	4	25	n.a.	<5.8	192600	4180	-26.1	-2.3
	02	30	530	60600	7120	91	50	<0.05	43000	1830	53	200	n.a.	n.a.	180	200	<0.1	n.a.	3.9	20	n.a.	<3.3	192500	4860	-26.2	-1.4
	03	45	440	60300	6680	76	45	<0.05	43500	1050	<0.1	190	n.a.	n.a.	180	200	<0.2	n.a.	<0.02	<0.2	n.a.	<3.8	173800	3840	-25.8	-2.0
	04	45	570	62500	7690	85	49	41	41000	1580	23	130	n.a.	n.a.	23	180	3.7	n.a.	3.8	<0.3	n.a.	<6.6	198500	4780	-25.8	-2.0
	05	40	280	62500	3910	45	22	66	41000	1300	9.5	94	n.a.	n.a.	<0.3	62	<0.2	n.a.	1.9	<0.3	n.a.	<5.6	146700	2380	-25.8	-2.0
	06	30	530	62500	6910	79	46	35	41000	1780	110	160	n.a.	n.a.	13	160	11.0	n.a.	3.5	<0.2	n.a.	<4.5	182700	3860	-26.5	-2.5
	07	30	490	58300	7200	97	44	<0.1	45400	1580	110	130	n.a.	n.a.	220	180	6.5	n.a.	3.3	6.9	n.a.	<7.2	175900	4180	-26.5	-2.5
	08	30	570	58300	7660	85	48	<0.09	45400	2050	150	210	n.a.	n.a.	230	260	<0.2	n.a.	2.8	<0.3	n.a.	<5.6	208300	4180	-26.5	-2.5
	09		470	58300	7140	71	39	34	45400	1000	19	160	n.a.	n.a.	150	160	<0.4	n.a.	3.1	<0.5	n.a.	<9.6	183600	4810	-26.5	-2.5
Average			490	60500	6890	79	43	44	43200	1520	62	162			146	180	6.0		3.3	17			183800	4120	-26.2	-2.2
SD			90	1800	1180	15	9	15	1900	350	54	38			80	50	3.7		0.7	9			17700	760	0.3	0.4
Sai-114 A1 (conc.)	01	35	800	60600	5370	110	60	3460	42400	1730	180	160	n.a.	n.a.	870	450	4.2	n.a.	6	<0.3	n.a.	<5	193800	4630	-26.2	-1.0
	02	45	420	59500	8760	72	35	3150	43500	1970	78	130	n.a.	n.a.	500	190	5.0	n.a.	3.3	78	n.a.	<2.7	207200	4400	-26.2	-4.6
	03	40	340	54000	7000	66	26	<0.09	46300	1880	28	66	n.a.	n.a.	390	180	5.5	n.a.	2.4	<0.3	n.a.	<5.8	194100	5290	-26.5	-13.6
	07	50	670	59000	5830	98	54	<0.06	45100	1530	10	150	n.a.	n.a.	480	260	3.5	n.a.	3.5	<0.2	n.a.	<3.9	190200	3940	-26.5	-0.4
	08	80	680	61200	5490	94	53	2010	42700	500	1.1	160	n.a.	n.a.	630	320	4.1	n.a.	3.7	<0.06	n.a.	<1.4	187900	4950	-26.1	-1.0
	09	60	480	57700	6540	68	34	3060	45400	1840	43	100	n.a.	n.a.	390	170	4.5	n.a.	3.2	<0.1	n.a.	<2.5	195500	5440	-26.5	-4.8
	11	65	260	55900	6420	52	20	1680	46800	2000	41	65	n.a.	n.a.	330	140	6.6	n.a.	2.6	13	n.a.	<2.2	179800	3500	-26.7	-6.9
	12	40	250	53700	6990	54	19	520	49100	1960	89	70	n.a.	n.a.	330	140	6.3	n.a.	2.2	38	n.a.	<2.7	196800	3440	-27.1	-7.1
	14	30	200	54800	6160	42	15	<0.07	48000	1380	75	51	n.a.	n.a.	230	110	<0.2	n.a.	2.2	11	n.a.	<4.5	174000	3290	-26.9	-7.0
	15	40	270	55900	7250	56	18	<0.03	46800	1990	97	66	n.a.	n.a.	320	150	6.7	n.a.	2.1	28	n.a.	<2.5	200900	4450	-26.7	-6.9
	16	30	220	55800	6760	47	16	550	46800	1450	69	49	n.a.	n.a.	240	120	3.3	n.a.	2.1	10	n.a.	<5.2	181300	3910	-26.7	-6.8
	19	35	830	59500	5420	100	56	<0.06	44500	1860	120	200	n.a	n.a.	800	360	<0.2	n.a	3.4	<0.2	n.a	<4.5	213200	2790	-26.4	-0.7
	21	65	630	58200	5030	87	51	3730	45700	1780	<0.04	150	n.a	n.a	540	130	2.9	n.a	3.3	<0.09	n.a	<1.8	172300	3860	-26.6	-1.3
	23	50	220	55200	6210	39	15	750	47400	1430	77	50	n.a.	n.a.	310	120	7.8	n.a.	2	13	n.a.	<2.5	180100	3390	-26.8	-7.2
	24	55	280	55100	7070	48	20	2010	48300	1810	7.9	64	n.a	n.a	330	130	<0.09	n.a	2.1	<0.1	n.a	<2.2	183100	4210	-27.0	-4.6
	25	50	720	59900	5180	99	52	2050	43900	1980	120	170	n.a.	n.a.	770	350	3.4	n.a.	4.1	1.8	n.a.	<1.5	188000	3700	-26.3	-1.3
	26	55	840	56500	5130	110	61	870	46600	1840	11	170	n.a.	n.a.	700	460	2.8	n.a.	5.5	<0.1	n.a.	<2.3	191000	5690	-26.7	-5.1
	27	35	750	58100	4680	93	52	<0.02	44900	2020	<0.06	170	n.a	n.a.	570	380	2.1	n.a	4.7	<0.06	n.a	<1.4	190100	4220	-26.4	-5.5
Average			490	57300	6190	74	37	1990	45800	1700	65	110			490	230	4.6		3.2	24			190000	4170	-26.6	-4.8
SD			240	2300	1030	25	18	1160	1900	370	50	50			200	1200	1.7		1.2	24			10800	800	0.3	3.3

FIA	FI	Size (µm)	Li (ppm)	Na (ppm)	K (ppm)	Rb (ppm)	Cs (ppm)	Mg (ppm)	Ca (ppm)	Sr (ppm)	Ba (ppm)	B (ppm)	Fe (ppm)	Mn (ppm)	Zn (ppm)	Pb (ppm)	Cu (ppm)	Ag (ppm)	Tl (ppm)	As (ppm)	Sb (ppm)	S (ppm)	Cl (ppm)	Br (ppm)	T_m (i) (°C)	T_n (HH) (°C)
Sai-114 A2 (conc.)	01		250	55200	6800	50	19	<0.03	47800	2190	100	65	n.a.	n.a.	420	150	7.9	n.a.	2.5	<0.1	n.a.	<2	198200	4330	-25.9	-5.7
	02		510	59800	4550	78	40	10800	41200	1570	92	110	n.a.	n.a.	710	310	3.8	n.a.	4	<0.09	n.a.	<1.9	171800	4050	-25.8	-10.6
	03		240	54900	6470	40	15	4290	47900	1580	28	54	n.a.	n.a.	310	130	5.5	n.a.	2.1	15	n.a.	<2.3	192200	3780	-26.9	-6.6
	04		660	58100	5000	85	47	<0.08	45800	1290	71	140	n.a.	n.a.	500	160	2.4	n.a.	3.9	9.1	n.a.	<5.9	196200	5300	-26.6	-1.7
	05		330	60400	4480	81	24	12400	41900	1420	<0.09	76	n.a.	n.a.	750	350	2.4	n.a.	4.4	14	n.a.	<2.5	180400	4150	-25.9	-7.2
	06		410	57400	7230	66	30	<0.03	46800	1660	130	120	n.a.	n.a.	440	170	8.8	n.a.	2.5	<0.1	n.a.	<2.3	172800	2710	-26.8	-0.2
	07		670	58900	5280	90	50	<0.09	45100	1820	130	170	n.a.	n.a.	540	300	<0.2	n.a.	3.1	5.1	n.a.	<5.5	170500	2740	-26.5	-1.0
	08		510	58100	6440	77	39	<0.05	45800	2060	140	140	n.a.	n.a.	500	220	<0.1	n.a.	3.1	<0.1	n.a.	<3.2	184800	2710	-26.6	-1.8
	09		240	57500	7330	42	15	<0.04	44500	1730	87	61	n.a.	n.a.	340	160	4.0	n.a.	2.7	17	n.a.	<3	202800	3890	-26.3	-8.4
	10		470	58500	7930	68	34	<0.03	44700	2170	170	130	n.a.	n.a.	480	210	6.7	n.a.	2.4	520	n.a.	<2.3	204700	3900	-26.4	-4.1
Average			430	57900	6150	68	31	9200	45200	1750	110	110			500	220	5.2		3.1	100			187400	3760	-26.5	-4.7
SD			160	1800	1240	18	13	4300	2200	310	40	40			140	80	2.4		0.8	210			13100	830	0.4	3.4
Sai-114 A3 (conc.)	01		280	55400	6780	47	20	15400	41900	1190	<0.09	110	n.a.	n.a.	580	87	<0.09	n.a.	1.8	<0.1	n.a.	<2.5	182900	3460	-25.7	-19.6
Sai-131 A1 (conc.)	01	30	180	60200	4590	36	12	1380	42100	1350	29	29	<5.4	460	110	<0.1	n.a.	n.a.	n.a.	1.3	n.a.	<7	220600	1210	-26.0	-6.8
	02	50	210	60500	5650	46	11	1350	41800	1350	22	40	<13	200	120	<0.2	n.a	n.a.	n.a.	<0.7	n.a.	820	218500	510	-25.9	-6.9
	05	35	250	60600	4900	39	11	2300	41800	2090	29	17	<7.2	480	110	<0.07	n.a	n.a.	n.a.	5.8	n.a.	<10	241100	1490	-25.9	-6.7
Average			213	60400	5050	40	11	1680	41900	1600	27	29		380	110					4		820	226700	1070	-25.9	-6.8
SD			40	200	550	5	1	540	200	430	4	12		156	10					3			12500	510	0.0	0.1
Sai-131 A2 (conc.)	01	50	230	57100	3530	35	11	1960	45500	1700	22	32	<3.5	260	130	68	<0.06	n.a.	2.5	<0.1	n.a.	<1.7	176900	1780	-26.5	-6.9
	04	55	280	57100	3270	43	15	2160	45500	1790	18	26	<7.1	100	130	32	<0.1	n.a	2	<0.2	n.a	<3.4	201700	<13	-26.5	-7.0
	07	65	180	57700	2920	33	8.7	1240	44800	1180	18	25	280	300	110	59	<0.1	n.a	3.4	<0.2	n.a	<3.1	207200	1820	-26.3	-7.0
	12	80	190	58200	4420	59	16	1490	44200	1780	42	37	<5.6	410	240	83	<0.08	n.a.	2.8	<0.2	n.a.	<2.4	252800	1170	-26.5	-6.8
	15		180	57700	4260	33	9	1760	44800	1710	29	20	<4.2	390	110	57	<0.05	n.a	1.8	<0.1	n.a	220	190500	1620	-26.4	-6.8
Average			210	57600	3680	41	12	1720	45000	1630	26	28	280	290	140	60			2.5			220	205800	1600	-26.4	-6.9
SD			40	500	640	11	3	370	600	260	10	7		120	60	19			0.6				26700	300	0.1	0.1

FIA	FI	Size (µm)	Li (ppm)	Na (ppm)	K (ppm)	Rb (ppm)	Cs (ppm)	Mg (ppm)	Ca (ppm)	Sr (ppm)	Ba (ppm)	B (ppm)	Fe (ppm)	Mn (ppm)	Zn (ppm)	Pb (ppm)	Cu (ppm)	Ag (ppm)	Tl (ppm)	As (ppm)	Sb (ppm)	S (ppm)	Cl (ppm)	Br (ppm)	T_m (i) (°C)	T_H (HH) (°C)
Sai-131 A3 (conc.)	01	40	310	58300	3790	51	22	<0.1	45600	2710	270	150	<5.8	<0.4	<0.2	120	<0.06	n.a.	<0.02	<0.1	n.a.	<2.4	164000	<8.7	-26.6	-1.3
	02	40	360	58400	8090	76	38	260	45600	1700	140	130	<15	1070	330	170	4.4	n.a.	3.1	1.3	n.a.	66	190900	1170	-26.6	-1.1
	03	30	420	58300	10500	68	38	<0.1	45600	2300	190	83	<9	<0.6	360	180	<0.1	n.a.	1.1	<0.2	n.a.	<3.8	213200	1700	-26.6	-1.5
	04	25	190	53800	5930	42	12	1080	49400	1780	36	20	<24	710	140	100	<0.3	n.a.	2.8	<0.5	n.a.	<10	198600	<38	-27.2	-5.6
	05	25	370	55400	4910	68	38	160	48600	1410	91	150	<24	100	220	120	<0.3	n.a.	2	<0.5	n.a.	<10	180100	2550	-27.1	-2.2
	06	30	360	54200	7490	64	36	150	48900	1180	110	120	<35	120	270	130	<0.4	n.a.	2.6	<0.8	n.a.	<16	170100	1810	-27.1	-5.9
	07	35	230	53200	5340	45	16	830	50000	2050	47	49	<17	1530	170	130	<0.2	n.a.	2.6	3.6	n.a.	<7.9	181400	1330	-27.3	-5.9
	08	45	320	58900	8620	68	31	<0.6	45000	1160	110	100	<29	<2.2	180	120	<0.3	n.a.	<0.09	<0.6	n.a.	<13	217100	<46	-26.5	-1.2
	09	25	520	58900	7240	71	36	680	45000	2180	190	190	<10	4340	530	190	<0.1	n.a.	2.6	22	n.a.	<4.2	173300	2030	-26.5	-1.3
Average			340	56600	6880	61	30	530	47100	1830	132	110		1330	280	140	4.4		2.4	9		66	187600	1770	-26.8	-2.9
SD			100	2400	2090	12	10	390	2100	530	75	53		1590	130	30			0.7	11			18800	500	0.3	2.1
Sai-131 A4 (conc.)	01	60	230	57900	6560	39	13	1030	44600	1650	36	56	<5.7	16	170	40	<0.06	n.a.	2.5	<0.1	n.a.	<2.4	222000	1780	-26.3	-6.7
	02	40	190	56600	4960	36	11	2040	45900	1940	29	24	<17	480	150	83	<0.2	n.a.	1.4	<0.4	n.a.	<7.4	175100	730	-26.5	-6.8
	04	35	260	56800	<65	45	14	750	45800	1140	<0.8	<2.1	<31	12	<0.9	50	<0.4	n.a.	<0.1	<0.6	n.a.	<14	184400	<46	-26.5	-6.7
	05	35	170	56800	<26	41	13	1390	45800	1440	<0.3	<1.1	<12	340	<0.4	44	<0.1	n.a.	<0.04	<0.2	n.a.	<5.4	235900	4680	-26.5	-6.7
	06	35	180	56700	5900	37	9.9	2100	45900	1860	28	<1.7	<24	430	110	59	<0.3	n.a.	<0.06	<0.5	n.a.	<10	218000	2860	-26.5	-6.9
	07		260	60500	4130	47	3.3	420	42100	2180	22	21	<7.3	280	<0.6	<0.1	n.a	n.a.	n.a.	<0.4	n.a.	<11	199700	1400	-26.0	-6.6
Average			220	57600	5400	41	11	1290	45000	1700	29	34		260	140	55			2.0				205900	2330	-26.4	-6.8
SD			40	1500	1070	4	4	690	1500	373	6	19		200	30	17			0.8				23500	1620	0.2	0.1
Limits of detection (3σ background)																										
Sai-010a A1 (LOD)	01	35	0.07	0.1	7.4	0.04	0.02	0.06	17	0.02	0.2	0.4			0.2	0.03	0.08		0.02	0.1		3.7	170	9.9		
	02	25	0.1	0.2	12	0.07	0.03	0.09	26	0.03	0.2	0.6			0.2	0.05	0.1		0.03	0.2		5.7	260	15		
	03	30	0.1	0.2	13	0.07	0.03	0.1	28	0.03	0.3	0.7			0.2	0.03	0.1		0.04	0.2		6.4	290	17		
	05	50	0.1	0.2	9.5	0.05	0.02	0.08	21	0.03	0.2	0.5			0.2	0.05	0.09		0.03	0.2		4.7	210	12		
	09	60	0.2	0.2	15	0.08	0.04	0.1	29	0.03	0.2	0.7			0.3	0.05	0.1		0.03	0.2		7	330	18		
	11	40	0.08	0.1	7.2	0.04	0.02	0.06	14	0.009	0.1	0.3			0.2	0.02	0.07		0.02	0.1		3.4	170	8.9		
	12	35	0.2	0.3	17	0.09	0.04	0.2	34	0.04	0.4	0.8			0.4	0.04	0.1		0.03	0.3		8.2	400	21		
	13	30	0.6	0.8	54	0.3	0.1	0.3	95	0.1	0.9	2.6			1	0.2	0.5		0.1	0.8		23	1200	59		
Sai-010a A2 (LOD)	01	40	0.2	0.9	12	0.1	0.05	1.5	42	0.07	0.4	1			4.5	0.3	0.7	0.09	0.05	0.3	0.1	28	330	40		
	02	30	0.2	0.8	9.8	0.08	0.04	1.1	34	0.05	0.3	0.8			3.5	0.2	0.5	0.06	0.03	0.2	0.1	23	270	33		
	06	25	0.2	0.8	9.5	0.07	0.04	1.4	38	0.05	0.3	1			4.1	0.3	0.6	0.07	0.04	0.3	0.1	23	260	33		
	07	25	0.3	1.2	14	0.1	0.05	1.7	56	0.1	0.5	1.4			6	0.3	0.9	0.07	0.06	0.4	0.2	35	400	50		
	08	30	0.2	0.8	10	0.07	0.04	1	34	0.05	0.3	0.8			3.3	0.2	0.6	0.1	0.08	0.2	0.1	23	280	33		
	10		0.2	0.8	9.8	0.06	0.04	1.2	32	0.06	0.3	0.7			3.3	0.2	0.5	0.06	0.04	0.3	0.1	22	270	32		
Sai-010a A3 (LOD)	04	30	1.2	1.5	97	0.5	0.2	0.8	190	0.2	2.3	4.9			2.1	0.3	0.7		0.2	1.7		46	2200	120		
	06	30	0.06	0.09	6.1	0.03	0.02	0.04	13	0.01	0.1	0.3			0.1	0.02	0.04		0.01	0.09		3	140	7.7		
Sai-010a A5 (LOD)	01	20	0.4	1.3	17	0.1	0.07	2.6	55	0.1	0.3	1.4			5.2	0.3	0.9	0.2	0.07	0.4	0.2	37	450	54		
	02	25	0.4	1.3	17	0.1	0.07	2.2	54	0.09	0.5	1.5			5.3	0.3	0.8	0.2	0.1	0.4	0.2	37	460	55		

FIA	FI	Size (µm)	Li (ppm)	Na (ppm)	K (ppm)	Rb (ppm)	Cs (ppm)	Mg (ppm)	Ca (ppm)	Sr (ppm)	Ba (ppm)	B (ppm)	Fe (ppm)	Mn (ppm)	Zn (ppm)	Pb (ppm)	Cu (ppm)	Ag (ppm)	Tl (ppm)	As (ppm)	Sb (ppm)	S (ppm)	Cl (ppm)	Br (ppm)	T_m (i) (°C)	T_h (HH) (°C)
Sai-010a D4 (LOD)	01	40	0.2	0.2	17	0.07	0.04	0.1	33	0.04	0.4	0.9			0.3	0.07	0.2		0.04	0.3		8	380	21		
	02	35	0.2	0.3	19	0.1	0.04	0.1	36	0.05	0.4	0.9			0.3	0.07	0.1		0.05	0.3		8.9	430	23		
	03	40	0.1	0.2	12	0.06	0.02	0.08	21	0.03	0.2	0.6			0.2	0.05	0.1		0.03	0.2		5.1	260	14		
	04	35	0.2	0.3	19	0.1	0.04	0.1	35	0.04	0.4	1			0.4	0.08	0.2		0.05	0.3		8.4	430	22		
	05	35	0.06	0.09	7.3	0.03	0.02	0.05	13	0.02	0.1	0.3			0.2	0.03	0.05		0.01	0.1		3.2	170	8.5		
	06	50	0.05	0.1	10	0.05	0.02	0.07	18	0.03	0.2	0.5			0.2	0.02	0.08		0.02	0.2		4.4	220	12		
	07	50	0.06	0.08	5.9	0.03	0.01	0.03	11	0.01	0.1	0.2			0.1	0.01	0.04		0.01	0.09		2.6	130	6.9		
	08	45	0.2	0.2	16	0.07	0.03	0.09	28	0.03	0.3	0.7			0.3	0.05	0.1		0.04	0.2		6.9	350	18		
Sai-010a D6 (LOD)	01		0.2	0.3	20	0.1	0.04	0.1	37	0.05	0.3	0.9			0.4	0.08	0.2		0.04	0.3		8.6	440	23		
Sai-014a A1 (LOD)	02	55	0.03	0.06	3.8	0.02	0.007	0.03	6.9	0.009	0.07	0.2			0.07	0.008	0.03		0.01	0.08		1.5	92	4.6		
	03	40	0.07	0.1	7.3	0.04	0.02	0.06	13	0.01	0.1	0.4			0.2	0.03	0.06		0.01	0.1		2.7	170	8.6		
	04	30	0.08	0.1	9.3	0.05	0.02	0.08	16	0.03	0.1	0.5			0.2	0.03	0.08		0.02	0.2		3.4	210	11		
	05	30	0.09	0.1	7.8	0.02	0.01	0.06	13	0.02	0.1	0.4			0.2	0.02	0.06		0.01	0.1		2.9	180	8.8		
	06	30	0.09	0.1	9.9	0.05	0.02	0.07	17	0.02	0.1	0.4			0.2	0.02	0.09		0.02	0.2		3.6	220	11		
	07	30	0.2	0.2	19	0.1	0.04	0.1	33	0.04	0.3	0.8			0.4	0.04	0.2		0.04	0.3		7	420	21		
	08	30	0.1	0.2	14	0.06	0.03	0.1	23	0.04	0.3	0.8			0.3	0.04	0.1		0.02	0.2		5.1	300	15		
Sai-014a D3 (LOD)	01	40	0.09	0.1	11	0.04	0.02	0.08	16	0.03	0.2	0.5			0.2	0.03	0.09		0.02	0.1		3.4	200	10		
	02	40	0.04	0.07	6.1	0.03	0.01	0.03	9	0.01	0.1	0.3			0.1	0.02	0.05		0.006	0.07		1.8	110	5.8		
	03	35	0.05	0.09	7.1	0.03	0.02	0.05	12	0.02	0.1	0.3			0.1	0.02	0.06		0.01	0.1		2.5	140	7.6		
	04	25	0.07	0.09	7.8	0.03	0.01	0.05	12	0.02	0.1	0.4			0.1	0.02	0.06		0.02	0.1		2.5	140	7.6		
	06	25	0.1	0.2	14	0.06	0.03	0.08	22	0.02	0.3	0.8			0.3	0.04	0.1		0.03	0.2		4.6	280	14		
Sai-014a E2 (LOD)	01	30	0.1	0.1	8.4	0.03	0.02	0.05	12	0.02	0.1	0.3			0.2	0.01	0.07		0.02	0.1		2.3	150	7.8		
	02	40	0.1	0.1	14	0.05	0.02	0.1	20	0.03	0.2	0.6			0.2	0.04	0.1		0.03	0.2		3.8	240	13		
	04	50	0.09	0.1	12	0.05	0.02	0.07	18	0.02	0.2	0.5			0.2	0.03	0.1		0.004	0.2		3.3	210	11		
	05	30	0.1	0.2	15	0.07	0.03	0.07	23	0.04	0.2	0.7			0.3	0.03	0.1		0.04	0.2		4.1	270	14		
	06	35	0.1	0.1	10	0.04	0.02	0.06	15	0.02	0.1	0.4			0.2	0.02	0.08		0.02	0.1		2.7	180	9.1		
	07	35	0.09	0.1	11	0.04	0.02	0.06	16	0.03	0.2	0.5			0.2	0.03	0.06		0.02	0.2		3	190	9.9		
	08	30	0.08	0.1	13	0.05	0.02	0.09	19	0.03	0.2	0.5			0.3	0.04	0.08		0.03	0.2		3.7	220	12		
Sai-028 A1 (LOD)	01	40	0.1	0.2	12	0.06	0.03	0.1	26	0.03	0.2	0.6			0.3	0.04	0.1		0.03	0.4		4.2	270	16		
	02	30	0.07	0.1	8.8	0.05	0.02	0.07	18	0.02	0.2	0.5			0.2	0.03	0.08		0.02	0.3		3	200	12		
	03	35	0.1	0.2	12	0.05	0.03	0.1	24	0.03	0.2	0.7			0.3	0.05	0.1		0.03	0.3		3.9	260	15		
	04	35	0.06	0.08	5.9	0.03	0.01	0.04	12	0.01	0.1	0.3			0.1	0.02	0.05		0.01	0.2		2	130	7.6		
	05	50	0.06	0.1	8	0.03	0.02	0.07	15	0.02	0.1	0.5			0.2	0.03	0.07		0.02	0.2		2.7	170	10		
	06	95	0.02	0.02	2	0.008	0.003	0.02	3.8	0.004	0.03	0.1			0.04	0.005	0.02		0.004	0.04		0.7	43	2.5		
	07	55	0.03	0.05	3.4	0.01	0.008	0.03	6.3	0.009	0.06	0.2			0.09	0.01	0.03		0.01	0.07		1.1	73	4.2		
	08	60	0.04	0.05	4.3	0.02	0.009	0.03	7.6	0.01	0.08	0.2			0.09	0.01	0.04		0.01	0.08		1.4	93	5.2		
	09	40	0.04	0.05	4.4	0.02	0.007	0.03	7.7	0.01	0.06	0.2			0.08	0.01	0.03		0.009	0.07		1.4	88	5.2		
Sai-028 A2 (LOD)	01	70	0.2	0.2	19	0.06	0.04	0.1	31	0.03	0.3	0.8			0.3	0.07	0.1		0.04	0.3		5.9	400	22		
	03	35	0.09	0.1	12	0.05	0.02	0.06	20	0.02	0.2	0.6			0.2	0.04	0.09		0.03	0.2		3.7	250	14		
	04	55	0.09	0.1	10	0.04	0.02	0.07	17	0.02	0.2	0.5			0.2	0.02	0.07		0.01	0.2		3.2	220	12		
	07	30	0.1	0.1	12	0.05	0.02	0.07	19	0.02	0.2	0.6			0.2	0.04	0.1		0.03	0.2		3.3	230	13		
	08	45	0.2	0.3	24	0.09	0.05	0.2	37	0.05	0.4	1			0.4	0.05	0.2		0.05	0.4		6.8	470	26		
	09	30	0.1	0.1	12	0.05	0.02	0.06	18	0.03	0.2	0.5			0.2	0.03	0.08		0.02	0.1		2.7	210	12		

FIA	FI	Size (µm)	Li (ppm)	Na (ppm)	K (ppm)	Rb (ppm)	Cs (ppm)	Mg (ppm)	Ca (ppm)	Sr (ppm)	Ba (ppm)	B (ppm)	Fe (ppm)	Mn (ppm)	Zn (ppm)	Pb (ppm)	Cu (ppm)	Ag (ppm)	Tl (ppm)	As (ppm)	Sb (ppm)	S (ppm)	Cl (ppm)	Br (ppm)	T_m (i) (°C)	T_H (HH) (°C)
Sai-058 A1 (LOD)	01	40	0.05	0.1	7.3	0.03	0.02	0.05	11	0.02	0.09	0.4			0.1	0.02	0.06		0.01	0.09		7	170	6.8		
	02	50	0.3	0.2	24	0.1	0.05	0.1	34	0.05	0.3	1.1			0.4	0.08	0.2		0.04	0.3		6.6	420	22		
	03	50	0.2	0.1	14	0.06	0.03	0.08	19	0.03	0.2	0.6			0.2	0.05	0.1		0.02	0.2		3.7	240	13		
	04	30	0.1	0.1	13	0.06	0.03	0.09	19	0.03	0.2	0.6			0.2	0.03	0.1		0.02	0.2		3.6	220	12		
	05	35	0.06	0.09	8.4	0.03	0.02	0.05	11	0.02	0.1	0.3			0.1	0.02	0.07		0.009	0.1		2.2	140	7.7		
	08	30	0.09	0.1	9.6	0.04	0.02	0.04	13	0.01	0.2	0.4			0.1	0.02	0.06		0.02	0.1		2.7	160	9		
Sai-058 B2 (LOD)	01	65	0.04	0.08	6	0.03	0.01	0.03	8.6	0.01	0.1	0.3			0.08	0.02	0.05		0.008	0.08		1.6	110	5.6		
	02	30	0.9	1.4	7.3	0.2	0.1	0.6	200	0.2	1.2	2.1			1	0.2	0.6		0.2	0.7		14	920	57		
	03	40	0.07	0.09	7.4	0.03	0.01	0.04	11	0.01	0.1	0.3			0.1	0.02	0.05		0.01	0.1		2	130	6.9		
	04	30	0.06	0.1	11	0.04	0.02	0.06	15	0.02	0.2	0.5			0.2	0.03	0.09		0.02	0.1		2.7	180	9.7		
	05	30	0.08	0.1	11	0.04	0.02	0.06	15	0.02	0.2	0.4			0.2	0.03	0.08		0.02	0.2		2.9	190	10		
	06	35	0.1	0.2	15	0.06	0.03	0.09	23	0.04	0.3	0.7			0.2	0.05	0.2		0.03	0.2		3.8	260	13		
Sai-071 B1 (LOD)	01	30	0.2	0.7	13	0.08	0.04	0.1	29	0.06	0.3	0.7			2.1	0.1	0.5	0.07	0.07	0.2	0.1	20	240	34		
	02	20	0.3	1.4	24	0.2	0.08	0.3	62	0.1	0.7	1.5			4.8	0.3	1	0.2	0.1	0.4	0.2	43	530	71		
	08	30	0.2	0.7	11	0.08	0.04	0.2	30	0.06	0.4	0.8			2.4	0.2	0.5	0.1	0.07	0.2	0.1	21	250	33		
	10	20	0.5	1.8	31	0.2	0.1	0.5	82	0.2	0.9	2.2			6.3	0.4	1.4	0.2	0.2	0.5	0.4	56	680	91		
Sai-071 B3 (LOD)	01	15	0.3	1.1	16	0.1	0.06	0.3	51	0.1	0.5	1.4			4.4	0.3	0.8	0.2	0.1	0.4	0.2	34	420	54		
	02	20	1.3	5.7	97	0.6	0.3	1.5	240	0.4	2.9	7.1			19	1.2	3.6	0.8	0.5	1.9	0.9	170	2100	290		
	03	40	1.2	4.5	80	0.6	0.2	1.1	200	0.3	2.3	4.9			15	1	3.2	0.6	0.5	1.3	0.8	140	1700	230		
	09	20	0.4	1.1	16	0.1	0.09	0.3	55	0.09	0.5	1.4			4.6	0.3	0.9	0.2	0.1	0.4	0.2	37	450	58		
Sai-071 B4 (LOD)	03	25	0.3	1.3	25	0.2	0.08	0.3	59	0.09	0.8	1.6			4.1	0.3	0.9	0.2	0.09	0.4	0.2	40	500	70		
Sai-100 A1 (LOD)	01	40	0.06	0.08	10	0.05	0.02	0.06	14	0.01	0.1	0.4			0.2	0.02	0.1		0.006	0.2		3.6	220	19		
	02	40	0.1	0.2	22	0.1	0.05	0.1	31	0.04	0.3	0.9			0.5	0.06	0.3		0.02	0.4		8.3	470	42		
	03	40	0.2	0.2	25	0.1	0.05	0.2	35	0.04	0.3	1			0.5	0.06	0.3		0.02	0.5		9.3	530	47		
	04	30	0.09	0.1	12	0.05	0.02	0.05	17	0.03	0.2	0.4			0.2	0.03	0.2		0.02	0.2		4.4	240	22		
	05	30	0.09	0.1	12	0.04	0.02	0.06	17	0.03	0.2	0.4			0.2	0.02	0.2		0.02	0.2		4.7	260	23		
	06	35	0.2	0.2	25	0.08	0.04	0.1	35	0.07	0.4	0.9			0.5	0.05	0.4		0.05	0.5		9.8	540	49		
	07	35	0.06	0.07	7.8	0.03	0.01	0.05	11	0.02	0.1	0.3			0.1	0.03	0.1		0.02	0.2		3	170	15		
	08	30	0.1	0.1	12	0.06	0.02	0.09	17	0.03	0.2	0.4			0.2	0.05	0.2		0.02	0.2		4.6	260	23		
	09	35	0.06	0.08	8.9	0.04	0.02	0.04	13	0.02	0.1	0.3			0.2	0.03	0.1		0.02	0.2		3.4	190	17		
	10	25	0.09	0.1	14	0.06	0.03	0.08	19	0.04	0.2	0.6			0.3	0.03	0.2		0.009	0.3		5.2	290	26		
	11	30	0.07	0.09	9.9	0.05	0.02	0.06	14	0.02	0.1	0.4			0.2	0.03	0.1		0.01	0.2		3.8	210	19		
	12		0.2	0.2	24	0.1	0.05	0.1	34	0.06	0.3	0.9			0.5	0.08	0.3		0.03	0.5		9.4	510	46		
	13		0.07	0.06	8.6	0.04	0.02	0.05	12	0.03	0.1	0.4			0.2	0.02	0.1		0.01	0.2		3.3	180	16		

FIA	FI	Size (μm)	Li (ppm)	Na (ppm)	K (ppm)	Rb (ppm)	Cs (ppm)	Mg (ppm)	Ca (ppm)	Sr (ppm)	Ba (ppm)	B (ppm)	Fe (ppm)	Mn (ppm)	Zn (ppm)	Pb (ppm)	Cu (ppm)	Ag (ppm)	Tl (ppm)	As (ppm)	Sb (ppm)	S (ppm)	Cl (ppm)	Br (ppm)	T_m (i) (°C)	T_h (HH) (°C)
Sai-100 A2 (LOD)	01	35	0.03	0.05	4.5	0.02	0.01	0.02	9.1	0.02	0.1	0.3			0.1	0.02			0.005	0.1			180	11		
	02	35	0.02	0.03	2.7	0.01	0.005	0.02	5.1	0.008	0.04	0.1			0.07	0.009			0.002	0.07			100	6.4		
	03	35	0.04	0.06	5.4	0.03	0.01	0.05	9.8	0.02	0.08	0.3			0.2	0.02			0.01	0.1			200	13		
	04	35	0.05	0.07	6.3	0.04	0.01	0.06	12	0.02	0.1	0.3			0.2	0.02			0.01	0.2			230	15		
	05	35	0.04	0.06	6.4	0.03	0.01	0.04	12	0.02	0.1	0.3			0.2	0.04			0.01	0.2			230	15		
	06	30	0.08	0.1	11	0.06	0.02	0.07	19	0.03	0.2	0.5			0.3	0.07			0.02	0.3			390	25		
	07	30	0.1	0.1	10	0.06	0.03	0.06	19	0.03	0.2	0.6			0.3	0.06			0.01	0.3			370	24		
	08	40	0.1	0.1	14	0.07	0.03	0.05	25	0.04	0.3	0.7			0.4	0.07			0.01	0.4			500	32		
	09	40	0.04	0.05	4.8	0.03	0.009	0.03	8.6	0.01	0.09	0.2			0.1	0.02			0.009	0.1			170	11		
	10	35	0.04	0.05	4.8	0.02	0.008	0.03	8.5	0.009	0.08	0.2			0.1	0.01			0.006	0.1			170	11		
	11	40	0.07	0.08	8.6	0.04	0.02	0.04	12	0.03	0.1	0.4			0.2	0.03			0.008	0.2		3.5	190	18		
	12	40	0.1	0.1	13	0.05	0.02	0.09	22	0.04	0.2	0.6			0.3	0.05			0.02	0.3			440	29		
	13	40	0.2	0.2	20	0.08	0.03	0.1	34	0.06	0.3	0.9			0.4	0.07			0.03	0.5			690	45		
	14	30	0.2	0.2	20	0.08	0.03	0.1	35	0.06	0.3	0.9			0.4	0.08			0.03	0.5			710	46		
	15	40	0.06	0.07	6.9	0.03	0.01	0.04	12	0.02	0.09	0.4			0.2	0.03			0.02	0.2			240	16		
	16	50	0.1	0.2	16	0.07	0.03	0.09	25	0.04	0.3	0.8			0.4	0.06	0.3		0.03	0.3			390	18		
	17	45	0.04	0.04	4.5	0.02	0.008	0.03	6.8	0.009	0.08	0.2			0.08	0.02	0.07		0.008	0.09			110	5		
	18	45	0.03	0.05	5.2	0.02	0.01	0.03	7.6	0.01	0.07	0.2			0.1	0.02	0.08		0.01	0.1			120	5.8		
	19	55	0.03	0.06	4.7	0.02	0.01	0.04	7.6	0.01	0.08	0.2			0.1	0.02	0.08		0.005	0.1		1.8	110	9.1		
	20	50	0.04	0.07	5.7	0.03	0.01	0.05	9.3	0.02	0.1	0.3			0.1	0.02	0.09		0.007	0.1		2.2	130	11		
	21	45	0.05	0.07	6.7	0.04	0.01	0.05	11	0.02	0.09	0.3			0.1	0.02	0.1		0.02	0.1		2.6	150	13		
	22		0.05	0.05	6.2	0.02	0.01	0.04	9.6	0.01	0.06	0.2			0.2	0.03	0.1		0.01	0.1		2.4	140	12		
	23		0.08	0.07	7	0.03	0.02	0.05	10	0.02	0.1	0.3			0.2	0.02	0.1		0.02	0.2		2.7	160	13		
Sai-100 A3 (LOD)	01	30	0.06	0.07	7.2	0.03	0.02	0.03	11	0.02	0.1	0.3			0.2	0.02	0.1		0.01	0.1		2.7	150	13		
	02	35															0.1									
	03	45	0.09	0.1	12	0.04	0.03	0.06	17	0.03	0.2	0.5			0.3	0.04	0.2		0.02	0.3		4.6	260	23		
	04	40	0.07	0.08	9.6	0.04	0.02	0.05	14	0.02	0.1	0.4			0.2	0.02	0.2		0.01	0.2		3.7	200	18		
	05	25	0.04	0.06	6.6	0.03	0.01	0.05	10	0.02	0.09	0.3			0.1	0.02	0.1		0.01	0.1		2.5	140	12		
Sai-100 A4 (LOD)	01	30	0.1	0.1	15	0.06	0.03	0.07	19	0.03	0.2	0.6			0.3	0.03	0.3		0.03	0.3		5.8	310	30		
	02	30	0.06	0.07	8.6	0.03	0.02	0.05	11	0.02	0.1	0.4			0.2	0.02	0.1		0.02	0.2		3.3	180	17		
	03	45	0.08	0.08	9.6	0.04	0.02	0.05	13	0.02	0.1	0.4			0.1	0.03	0.2		0.02	0.2		3.8	200	19		
	04	45	0.1	0.1	16	0.06	0.03	0.09	23	0.04	0.2	0.6			0.3	0.03	0.2		0.01	0.3		6.6	350	32		
	05	40	0.1	0.1	14	0.05	0.03	0.08	19	0.03	0.2	0.5			0.3	0.03	0.2		0.01	0.3		5.6	300	27		
	06	30	0.09	0.08	11	0.05	0.02	0.07	15	0.03	0.2	0.4			0.2	0.03	0.2		0.02	0.2		4.5	240	22		
	07	30	0.1	0.2	18	0.08	0.03	0.1	24	0.04	0.3	0.7			0.4	0.06	0.3		0.03	0.3		7.2	380	36		
	08	30	0.09	0.1	14	0.06	0.02	0.09	19	0.03	0.2	0.5			0.3	0.05	0.2		0.02	0.3		5.6	300	28		
	09		0.2	0.2	24	0.1	0.04	0.2	33	0.06	0.4	0.9			0.5	0.09	0.4		0.05	0.5		9.6	510	48		

FIA	FI	Size (μm)	Li (ppm)	Na (ppm)	K (ppm)	Rb (ppm)	Cs (ppm)	Mg (ppm)	Ca (ppm)	Sr (ppm)	Ba (ppm)	B (ppm)	Fe (ppm)	Mn (ppm)	Zn (ppm)	Pb (ppm)	Cu (ppm)	Ag (ppm)	Tl (ppm)	As (ppm)	Sb (ppm)	S (ppm)	Cl (ppm)	Br (ppm)	T_m (i) (°C)	T_H (HH) (°C)
Sai-114 A1 (LOD)	01	35	0.1	0.1	12	0.05	0.01	0.06	18	0.04	0.2	0.6			0.3	0.03	0.2		0.02	0.3		5	260	15		
	02	45	0.04	0.06	6.4	0.03	0.01	0.03	8.9	0.01	0.1	0.3			0.09	0.02	0.1		0.009	0.1		2.7	140	7.8		
	03	40	0.1	0.1	14	0.07	0.02	0.09	20	0.04	0.2	0.7			0.3	0.04	0.3		0.03	0.3		5.8	300	17		
	07	50	0.07	0.09	9.4	0.05	0.02	0.06	13	0.02	0.2	0.4			0.2	0.02	0.2		0.01	0.2		3.9	200	11		
	08	80	0.02	0.03	3.4	0.01	0.006	0.02	4.5	0.007	0.06	0.1			0.08	0.009	0.06		0.005	0.06		1.4	70	4		
	09	60	0.03	0.05	6.4	0.02	0.01	0.04	8.6	0.02	0.08	0.3			0.1	0.01	0.1		0.008	0.1		2.5	130	7.4		
	11	65	0.04	0.05	5.7	0.03	0.01	0.03	7.5	0.01	0.07	0.2			0.1	0.01	0.09		0.01	0.1		2.2	110	6.5		
	12	40	0.04	0.05	7	0.03	0.01	0.04	9.1	0.01	0.1	0.3			0.1	0.02	0.1		0.008	0.1		2.7	140	7.9		
	14	30	0.07	0.1	12	0.05	0.03	0.07	15	0.03	0.2	0.4			0.2	0.03	0.2		0.01	0.2		4.5	230	13		
	15	40	0.05	0.06	6.5	0.03	0.009	0.03	8.2	0.02	0.1	0.2			0.1	0.02	0.09		0.01	0.1		2.5	130	7.4		
	16	30	0.1	0.1	14	0.07	0.02	0.08	18	0.03	0.2	0.6			0.3	0.04	0.2		0.01	0.3		5.2	270	16		
	19	35	0.07	0.09	12	0.05	0.03	0.06	15	0.03	0.2	0.5			0.2	0.03	0.2		0.03	0.2		4.5	230	13		
	21	65	0.03	0.03	4.7	0.02	0.01	0.03	6	0.01	0.04	0.2			0.09	0.008	0.07		0.007	0.09		1.8	93	5.5		
	23	50	0.05	0.06	6.8	0.03	0.01	0.04	8.7	0.02	0.07	0.3			0.1	0.02	0.1		0.01	0.1		2.5	130	7.8		
	24	55	0.04	0.04	5.9	0.02	0.009	0.04	7.3	0.01	0.09	0.2			0.1	0.02	0.09		0.004	0.1		2.2	110	6.7		
	25	50	0.02	0.03	4.1	0.02	0.007	0.02	5.2	0.01	0.05	0.1			0.09	0.01	0.05		0.005	0.07		1.5	79	4.7		
	26	55	0.04	0.05	6.4	0.03	0.01	0.03	8.3	0.01	0.1	0.2			0.1	0.01	0.08		0.005	0.1		2.3	120	7.3		
	27	35	0.03	0.03	3.8	0.02	0.007	0.02	4.6	0.009	0.06	0.1			0.07	0.009	0.05		0.002	0.06		1.4	71	4.2		
Sai-114 A2 (LOD)	01		0.02	0.04	5.2	0.02	0.008	0.03	7	0.01	0.09	0.2			0.1	0.02	0.07		0.01	0.1		2	100	6		
	02		0.03	0.04	5.1	0.02	0.008	0.03	6.5	0.008	0.09	0.2			0.09	0.02	0.08		0.008	0.09		1.9	100	5.9		
	03		0.03	0.05	6.1	0.02	0.01	0.03	7.5	0.01	0.08	0.2			0.1	0.01	0.09		0.009	0.1		2.3	120	6.9		
	04		0.1	0.1	17	0.07	0.02	0.08	20	0.04	0.2	0.6			0.3	0.04	0.2		0.02	0.3		5.9	310	19		
	05		0.04	0.05	7	0.03	0.02	0.03	8.5	0.02	0.09	0.2			0.1	0.02	0.1		0.01	0.1		2.5	130	7.8		
	06		0.04	0.04	6.5	0.03	0.01	0.03	8	0.009	0.09	0.2			0.1	0.01	0.08		0.004	0.1		2.3	120	7.2		
	07		0.1	0.1	16	0.06	0.03	0.09	18	0.04	0.2	0.5			0.3	0.05	0.2		0.01	0.3		5.5	290	17		
	08		0.07	0.06	9.1	0.04	0.01	0.05	11	0.02	0.1	0.3			0.2	0.02	0.1		0.01	0.1		3.2	170	9.9		
	09		0.05	0.06	8.8	0.03	0.01	0.04	11	0.02	0.1	0.3			0.1	0.01	0.1		0.01	0.1		3	160	9.4		
	10		0.04	0.05	6.7	0.03	0.01	0.03	7.9	0.01	0.09	0.2			0.1	0.02	0.09		0.005	0.1		2.3	120	7.2		
Sai-114 A3 (LOD)	01		0.05	0.05	7.2	0.03	0.01	0.04	8.4	0.01	0.09	0.2			0.1	0.02	0.09		0.01	0.1		2.5	130	7.6		
Sai-131 A1 (LOD)	01	30	0.2	0.2	14	0.1	0.03	0.1	61	0.04	0.3	0.8	5.4	0.8	0.5	0.1				0.3		7	310	20		
	02	50	0.7	0.5	33	0.2	0.1	0.1	140	0.2	1.3	2.1	13	1.8	1.1	0.2				0.7		17	680	45		
	05	35	0.2	0.3	19	0.1	0.04	0.1	83	0.09	0.6	1.2	7.2	1	0.6	0.07				0.4		10	420	27		
Sai-131 A2 (LOD)	01	50	0.09	0.09	4.1	0.03	0.01	0.04	21	0.02	0.1	0.4	3.5	0.3	0.2	0.02	0.06		0.02	0.1		1.7	150	6.6		
	04	55	0.1	0.1	8.1	0.05	0.03	0.09	39	0.02	0.2	0.7	7.1	0.5	0.3	0.04	0.1		0.03	0.2		3.4	290	13		
	07	65	0.2	0.1	8	0.05	0.02	0.08	35	0.03	0.2	0.6	6.8	0.5	0.3	0.04	0.1		0.03	0.2		3.1	250	11		
	12	80	0.2	0.1	7.9	0.04	0.02	0.08	34	0.02	0.1	0.4	5.6	0.4	0.2	0.03	0.08		0.02	0.2		2.4	180	9.8		
	15		0.1	0.1	7.8	0.02	0.007	0.05	28	0.02	0.1	0.4	4.2	0.3	0.1	0.02	0.05		0.01	0.1		2.1	130	6.7		
Sai-131 A3 (LOD)	01	40	0.2	0.2	10	0.04	0.01	0.1	36	0.03	0.2	0.4	5.8	0.4	0.2	0.03	0.06		0.02	0.1		2.4	150	8.7		
	02	40	0.4	0.4	26	0.08	0.03	0.2	95	0.06	0.3	1.1	15	1.1	0.4	0.07	0.1		0.04	0.3		6.4	400	23		
	03	30	0.3	0.2	16	0.05	0.02	0.1	57	0.03	0.2	0.6	9	0.6	0.3	0.05	0.1		0.02	0.2		3.8	250	14		
	04	25	0.7	0.6	45	0.1	0.05	0.3	160	0.08	0.6	1.8	24	1.7	0.6	0.1	0.3		0.07	0.5		10	660	38		
	05	25	0.6	0.6	45	0.1	0.05	0.5	150	0.09	0.4	1.8	24	1.7	0.7	0.1	0.3		0.06	0.5		10	650	36		
	06	30	1.1	1.1	70	0.2	0.1	0.6	240	0.2	0.8	2.9	35	2.6	1.2	0.2	0.4		0.1	0.8		16	970	57		
	07	35	0.6	0.5	36	0.1	0.04	0.2	120	0.07	0.4	1.3	17	1.3	0.5	0.09	0.2		0.06	0.4		7.9	480	28		
	08	45	1.1	0.9	62	0.2	0.08	0.6	200	0.1	0.8	2.6	29	2.2	0.8	0.1	0.3		0.09	0.6		13	800	46		
	09	25	0.3	0.3	20	0.06	0.03	0.1	64	0.04	0.2	1	10	0.7	0.4	0.06	0.1		0.04	0.2		4.2	260	15		

FIA	FI	Size (µm)	Li (ppm)	Na (ppm)	K (ppm)	Rb (ppm)	Cs (ppm)	Mg (ppm)	Ca (ppm)	Sr (ppm)	Ba (ppm)	B (ppm)	Fe (ppm)	Mn (ppm)	Zn (ppm)	Pb (ppm)	Cu (ppm)	Ag (ppm)	Tl (ppm)	As (ppm)	Sb (ppm)	S (ppm)	Cl (ppm)	Br (ppm)	T_m (i) (°C)	T_h (HH) (°C)
Sai-131 A4 (LOD)	01	60	0.2	0.2	13	0.03	0.01	0.1	36	0.02	0.1	0.5	5.7	0.4	0.2	0.02	0.06		0.02	0.1		2.4	140	7.4		
	02	40	0.5	0.6	36	0.1	0.04	0.3	110	0.06	0.5	1.2	17	1.3	0.5	0.09	0.2		0.06	0.4		7.4	460	26		
	04	35	1.1	1	65	0.2	0.09	0.5	200	0.1	0.8	2.1	31	2.2	0.9	0.2	0.4		0.1	0.6		14	810	46		
	05	35	0.3	0.4	26	0.08	0.03	0.2	82	0.05	0.3	1.1	12	0.9	0.4	0.04	0.1		0.04	0.2		5.4	320	18		
	06	35	0.6	0.7	54	0.1	0.06	0.4	160	0.09	0.5	1.7	24	1.7	0.7	0.1	0.3		0.06	0.5		10	600	34		
	07		0.3	0.2	19	0.1	0.07	0.1	80	0.08	0.5	1.3	7.3	1	0.6	0.1				0.4		11	400	26		
Analytical errors (1σ)																										
Sai-010a A1 (1σ error)	01	35	12	69	55	2.3	1.3		7500	17	7.4	8.1			12	5.6	2.4		0.5	1.4		37	2500	91		
	02	25	18	97	140	3.6	2	50	13000	27	8.5	14			19	8.2	1.3		0.8			76	4200	180		
	03	30	19	110	160	3.8	2.1	55	14000	31	3.7	14			18	7.6	1.5		0.8			86	4600	210		
	05	50	17	92	62	3.2	1.7	23	6800	19	5.5	11			18	7.7	0.7		0.9			34	3000	94		
	09	60	17	96	130	3.3	1.8		10000	24	8.3	13			19	8.8	1.7		0.8	2.9			3800	160		
	11	40	14	72	98	2.8	1.5	60	12000	25	3.3	10			17	6.9	1		0.5	1.7		56	3000	120		
	12	35	23	110	220	4	2.2	77	16000	36	12	18			20	9.7	1.7		0.9	4		110	5700	260		
	13	30	16	78	130	3.4	1.8	36	4800	17	5.6	12			17	4.9	1.1		0.7			55	3600	140		
Sai-010a A2 (1σ error)	01	40	8.1	69	32	1.6	0.8	58	3000	10	6.3	7.4			14	3.9	1.4	0.2	0.3	1.9	0.2	64	2000	110		
	02	30	18	110	120	3.8	2.3	220	13000	32	9.8	17			49	9.4		0.3	0.7	3.2	1	280	4700	450		
	06	25	19	130	150	4.1	2		18000	39	15	24			64	11	7.5		0.8	4.3	1.7		5800	570		
	07	25	29	170	110	5.2	3	180	13000	32	6.3	23			54	16		0.9	1.3			260	5700	430		
	08	30	23	150	110	4.6	2.7	270	15000	32	11	20			46	11		0.5	1.4				5200	390		
	10		16	110	61	3.2	2	150	7900	21	5.4	13			27	6.5	2.9	0.4	0.6	1.1	0.5	130	3300	220		
Sai-010a A3 (1σ error)	04	30	19	140	260	4	2	37	7900	26	6.8	18			17	5.7	1.9		0.7	4.3			7000	330		
	08	30	13	80	130	2.3	1.1	80	15000	31	7.7	9.9			12	4.2	1.2		0.5	6.9		76	4000	170		
Sai-010a A5 (1σ error)	01	20	24	260	240	6.4	3.6	580	29000	63	26	36			75	12	7.5	1.2	1.8	20	1.5		10000	830		
	02	25	19	200	190	4.8	2.7		20000	45		25			63	11		0.9	1.7	15			7700	630		
Sai-010a D4 (1σ error)	01	40	16	130	270	3.8	1.9		19000	35	14	18			19	6.5	2.4		0.6	11			7000	310		
	02	35	9.7	83	120	2.1	1.1	51	8400	16	7.4	8.6			9.3	3.3	1		0.4	5.8		58	3500	140		
	03	40	10	76	100	2.3	1.1	53	8600	17	2.4	9.6			10	3.4	1		0.4	6.1		49	3100	120		
	04	35	18	160	520	4.1	2.2	250	36000	66	15	27			21	7.5			1.4	18		260	12000	600		
	05	35	8.7	74	98	1.9	1	64	11000	20	7.2	9.6			9.7	3.3	1		0.4	6.3		49	3100	110		
	06	50	12	89	160	2.7	1.3	88	15000	27	12	12			13	4.4	1.6		0.6	8.8		79	4400	180		
	07	50	3.7	33	45	0.9	0.4	30	4800	8.6	2.1	3.2			4.2	1.4	0.4		0.2	2.5		22	1400	50		
	08	45	9.3	78	120	2.4	1.1	58	8300	17	3	9.3			10	3.5	1		0.5	4.3		55	3400	130		
Sai-010a D6 (1σ error)	01		20	110	180	4	1.9	150	13000	35	4.6	12			77	12	2.4		1.2	6.3		85	4800	210		
Sai-014a A1 (1σ error)	02	55	9.1	54	88	1.8	1.1	36	13000		4.5	7.3			7.8	9	0.7		0.5				2700	110		
	03	40	14	84	150	3.4	1.7	54	17000	39	7.6	11			13	10	1.6		0.8	4		66	4600	180		
	04	30	17	100	140	3.7	1.9	41	14000	27	7.6	13			15	11	1.7		0.8	3.6		56	4500	160		
	05	30	11	65	94	2.3	1.2	26	9700	19	5.4	7.6			9.6	6.6	1.1		0.6			36	2800	110		
	06	30	11	62	150	2.5	1.4		13000	26	6.1	11			16	7.7			0.7				3800	170		
	07	30	9	50	56	1.8	1	13	3300	8.5	1.4	6			7.8	5.2	0.5		0.5			21	1800	64		
	08	30	15	84	140	3.6	1.9	35	11000	29	6.3	12			14	10	1.4		0.9	4		56	4000	170		

FIA	FI	Size (μm)	Li (ppm)	Na (ppm)	K (ppm)	Rb (ppm)	Cs (ppm)	Mg (ppm)	Ca (ppm)	Sr (ppm)	Ba (ppm)	B (ppm)	Fe (ppm)	Mn (ppm)	Zn (ppm)	Pb (ppm)	Cu (ppm)	Ag (ppm)	Tl (ppm)	As (ppm)	Sb (ppm)	S (ppm)	Cl (ppm)	Br (ppm)	T_m (i) (°C)	T_H (HH) (°C)
Sai-014a D3 (1σ error)	01	40	20	98	320	4.3	2.3	79	25000	46	11	18			18	13	2.3		1	5.9			6500	300		
	02	40	7.4	41	68	1.5	0.8		6600	13	3.6	5.1			7	4.6	0.7		0.4			25	1800	67		
	03	35	12	71	110	2.6	1.3	47	12000	25	6.9	8.1			10	7.3	1.3		0.6			45	3100	120		
	04	25	16	87	180	3.3	1.8	50	18000	33	7.6	12			15	10	2		0.8				4300	180		
	06	25	13	110	170	3.8	2		13000	29	3.7	13			16	9	1.9		0.8				4200	170		
Sai-014a E2 (1σ error)	01	30	11	57	80	2.2	1.1	23	6700	14	2	6.5			9.4	5.7	1		0.5				2200	78		
	02	40	12	68	110	2.6	1.3	33	7700	18	4.9	8			11	6.7	1		0.6	2		33	2700	110		
	04	50	9.9	54	100	1.9	1	29	7500	16	3.4	6.8			7.9	5.3	0.7		0.5	2.6		30	2300	92		
	05	30	19	96	230	3.7	2.1	74	15000	31	6.6	13			16	8.1			0.9				4900	200		
	06	35	14	84	170	2.7	1.4		14000	31	4.9	8.9			13	7.2	1.4		0.6	3.5		51	3700	160		
	07	35	17	91	180	3.4	1.9	37	14000	26	7.6	12			14	9.6	1.7		0.8	3		55	4100	160		
	08	30	21	110	290	4.5	2.2	78	22000	53	12	19			22	15	3.1		0.9				6400	280		
Sai-028 A1 (1σ error)	01	40	5.6	80	120	1.5	0.6	83	10000	21	4.4	9.3			19	6	1.4		0.5	6.4		46	3600	160		
	02	30	4.3	67	110	1.1	0.4	100	10000	22	4.1	7.9			20	5.8	1.5		0.5				3100	140		
	03	35	5.2	70	81	1.4	0.5	100	7400	19	4.4	7.9			22	5.2	1.1		0.5	3.5		31	3000	120		
	04	35	3.5	66	80	1.1	0.4	150	9900	22	3.4	5.2			24	5.2	1.4		0.5			34	2600	110		
	05	50	1.8	29	19	0.5	0.2	14	1700	3.9	1.3	2.2			4.8	1.3	0.3		0.1				890	29		
	06	95	5	29	30	1	0.5		5500	8.6	1	3.2			7.1	2.6	0.6		0.3				1100	42		
	07	55	5.7	34	20	1.1	0.5	47	3200	4.7	0.7	3.4			6.4	1	0.5		0.3	3.6		8.2	1100	30		
	08	60	3.2	48	40	0.7	0.3	30	5600	8.7	1	4.4			6	1.5	0.4		0.2	2.4			1600	57		
	09	40	7.2	40	51	1.4	0.7	32	6400	11	3.8	4.7			7.8	3.9	0.6		0.4			19	1600	65		
Sai-028 A2 (1σ error)	01	70	1.1	29	23	0.5	0.2	14	1300	3.7	1.6	1.6			4.1	1	0.3		0.1	0.4		7.3	960	33		
	03	35	8.3	91	160	2.7	1.4		14000	20	3.3	8.4			12	8.9	1		0.8			54	4100	190		
	04	55	2.1	38	43	0.9	0.4	28	3600	6.2	2.3	2.4			4.2	2.6	0.4		0.3	1		14	1400	56		
	07	30	29	170	410	5.8	2.9	280	34000	44	22	25			34	18	3.5		1.4			130	7500	370		
	08	45	13	72	76	2.5	1.3	37	4500	9.5	2.3	8			11	6.7	0.7		0.6	1.5			2500	94		
	09	30	7.8	90	170	2.8	1.1		13000	21	4.2	5.7			11	7			0.6	3.3		43	4200	170		
Sai-058 A1 (1σ error)	01	40	8.3	43	54	1.7	0.8	16	5200	11	5.7	5.2			7.7	5.5	0.6		0.4	7.7		19	1600	56		
	02	50	8.4	71	110	2.3	0.9		6400	9.7	5	6.5			7.1	6.4	1		0.6	1.9			2900	120		
	03	50	12	110	160	3.6	1.5	75	15000	19	7.2	11			13	8			0.8			57	4900	200		
	04	30	6	59	100	1.4	0.7	18	7100	11	2.5	5.7			7	2.7	1		0.3	1.9		28	2500	93		
	05	35	7.5	78	140	2.1	0.8	35	13000	16	5.6	9.3			4.2	2.9	1.1		0.4	2.3		42	3500	140		
	08	30	15	85	180	2.9	1.7		16000	30	13	11			28	11	1.9		0.8	6.2			4100	180		
Sai-058 B2 (1σ error)	01	65	8.6	47	79	1.7	0.9	23	7800	10	6.5	5.6			8.1	5.1	0.6		0.4	1.2		25	2000	78		
	02	30	14	110	43	3.9	2.4	27	6300	18	8.9	8.5			13	6.2	1.5		0.7	1.7		40	4000	180		
	03	40	6.6	55	78	1.5	0.8	55	7600	9.9	5.5	5.7			10	2.8	0.6		0.3			25	2100	82		
	04	30	8.3	79	150	2	1	17	12000	17	8	11			4.9	2.2	1.5		0.5				3500	150		
	05	30	5.1	79	230	2.3	1		19000	25	4.9	11			11	7	1.6		0.7			69	4900	230		
	06	35	8.3	78	130	2.2	0.9	35	8800	13	5	10			4	2.9	1.4		0.4	1.9		38	3200	130		
Sai-071 B1 (1σ error)	01	30	25	260	600	7.5	2.9	850	56000	120		49			130	20			4.4		3.7		15000	1700		
	02	20	24	250	490	7.6	3.5	280	38000	68		28			110	12	18		2.8			950	13000	1500		
	08	30	7.2	81	56	1.8	0.9	73	6700	15	4.7	7.4			16	2.7	2.6	0.2	0.8	1.2	0.4	100	2400	180		
	10	20	22	200	290	5.1	2.6	290	22000	48	3.9	30			66	8.5	12		2.4	5.2	3		8400	890		

FIA	FI	Size (μm)	Li (ppm)	Na (ppm)	K (ppm)	Rb (ppm)	Cs (ppm)	Mg (ppm)	Ca (ppm)	Sr (ppm)	Ba (ppm)	B (ppm)	Fe (ppm)	Mn (ppm)	Zn (ppm)	Pb (ppm)	Cu (ppm)	Ag (ppm)	Tl (ppm)	As (ppm)	Sb (ppm)	S (ppm)	Cl (ppm)	Br (ppm)	T_m (i) (°C)	T_h (HH) (°C)
Sai-071 B3 (1σ error)	01	15	12	130	79	2.6	1.3	65	7900	17	11	14			25	5.4	3.8		0.9	6.7	0.9		3700	270		
	02	20	17	120	110	4.1	2.3	35	3400	12	4.9	11			22	3.6			1.5		0.7	170	4000	320		
	03	40	33	220	320	8	3.9	110	14000	22	8.2	29			65	7.3	12	2.3	2.2	7.3	2.8	530	9900	950		
	09	20	16	160	120	3.7	2.1	200	13000	29	7.5	17			45	8.7			1.8	2.9		230	5800	390		
Sai-071 B4 (1σ error)	03	25	8.6	170	220	4	1.7	95	16000	24	4	15			41	11	7.7		1.7				6200	650		
Sai-100 A1 (1σ error)	01	40	4.3	34	36	1.1	0.6	2.8	2500	6.9	2.2	4			1.6	1.8	0.7		0.3	0.8		15	1200	81		
	02	40	7.7	83	85	2.4	1.1	5.8	5200	13	2.5	7.3			1.7	1.1	1.3		0.4				2800	200		
	03	40	4.7	54	52	1.4	0.7	2.6	2600	7.3	2.8	4				0.4	0.7		0.2			19	1800	120		
	04	30	7.3	65	62	2.1	1	5.5	4600	12	1.2	6.3				0.8	1.3		0.4	1.5			2100	140		
	05	30	8.3	59	62	2.3	1.2	5	4300	13	3.4	7.2			2.8	2.7	1.2		0.4	1.2		25	2300	150		
	06	35	6.9	78	98	2.1	1	5.7	5300	13	3.3	5.1					1.5		0.3				3000	220		
	07	35	8.1	73	63	2.4	1.2	6.5	6200	15	4.6	7.3			2.2	0.9	1.5		0.4	1.9		24	2400	160		
	08	30	7.5	88	72	2.3	1.1	6.4	5700	14	4.2	6.9				0.9	1.4		0.4	1.7		28	2700	170		
	09	35	6.7	70	76	1.9	1	6.9	6600	15	4	8.2				1	1.5		0.4				2600	170		
	10	25	8.2	65	75	2.3	1.2	6.2	5500	14	5.1	7.5				2.9	1.4		0.3	1.9			2500	160		
	11	30	8.4	87	93	2.7	1.2	7.4	7700	18	2.4	6.2			2.1	0.5	1.4		0.3	2.1		38	3000	210		
	12		13	150	280	4.1	1.9		16000	36	7.1	13				2.3			0.9				7500	600		
	13		6.8	54	44	1.8	1	4.4	3900	11	4.9	6				2.2	0.8		0.3			17	1800	100		
Sai-100 A2 (1σ error)	01	35	7.4	50	36	1.8	1.1	5.1	4700	13	5.4	6.3			1.6	2.3			0.3	1.2			2100	110		
	02	35	6.2	47	44	1.5	0.9		7300	15	3.3	6.3			6.8	2.3			0.3	3.4			2200	130		
	03	35	6.6	47	29	1.5	0.9	4.4	3400	9.9	5	5.4			2.2	2.3			0.3	1			1700	80		
	04	35	14	110	110	3.4	1.9	20	15000	36	7.9	13			5.1	4.8			0.6	4.1			5400	310		
	05	35	8.1	63	77	2.1	1.1	12	8400	20	6.5	9.1			9.1	3.3			0.4	2.9			3400	200		
	06	30	8.1	66	47	2.1	1.2	5.6	4100	11	3.2	6.7			1.8	3			0.4	1.6			2500	140		
	07	30	19	130	130	4.9	2.9	19	14000	37	9.6	16			9.3	6.1			0.9				6000	350		
	08	40	13	100	120	3.3	1.9		9500	24	7	12			3.4	4.3			0.7	3.5			5700	330		
	09	40	6.6	57	31	1.7	0.9	5	3800	11	2.5	5.8			1.6	2.2			0.3	0.9			1800	95		
	10	35	14	110	120	3.4	1.9		17000	40	10	13				4.4			0.7	4.4			5400	320		
	11	40	9.7	79	63	2.3	1.4	8.1	6000	16	3.9	7.9			2.3	3.2	1.2		0.5	1.9		26	2500	160		
	12	40	5.3	43	33	1.4	0.8	5	2200	8.5	4	4.9			2.7	2.2			0.3	1.1			1700	89		
	13	40	17	140	260	4.3	2.6	42	18000	50	6.8	16			8.9	6.4			0.9	7.5			10000	650		
	14	30	5.6	46	31	1.4	0.8	4.2	1600	6.9	1.4	4.5			1.2	2			0.3	1.4			1600	87		
	15	40	6.7	44	25	1.6	0.9		2200	9.1	5.4	5.9				2.3			0.3				1600	75		
	16	50	8.8	65	75	2.2	1.1		4800	16	6.6	8.3			4.6	3	1.4		0.4				2600	98		
	17	45	5.5	39	26	1.4	0.8	14	3000	8.2	4.5	4.6			2.5	2.3	0.7		0.2	0.8			1200	39		
	18	45	4.6	37	23	1	0.6	3	2600	6.9	3.3	3.7				1.4	0.6		0.2	0.6			1100	33		
	19	55	6.7	47	29	1.8	1.1	3.9	3400	10	5.8	5.8			1.2	2.6	0.9		0.3	0.8		10	1500	84		
	20	50	15	110	98	4	2.1	14	13000	31		12			3.4	5.2	2.1		0.7	3		41	4000	250		
	21	45	5.3	39	27	1.4	0.7	3.2	2600	7.5	4.1	4.6				1.9	0.8		0.2				1300	69		
	22		4.1	33	20	1.1	0.6	2.2	1900	5.9	1.4	3.7			0.7	1	0.6		0.2			7.4	1000	54		
	23		6.7	50	33	1.8	1	5.3	3200	8.4	3.9	4.9			0.7	2	0.8		0.3				1600	85		
Sai-100 A3 (1σ error)	01	30	6.2	50	43	1.6	0.9		4300	13	4.4	5.6			1.7	2.6	0.9		0.3	1.2			1700	98		
	02	35	6.2	47	45	1.5	0.9	11	4500	13	4.2	5.2			6.1	2.5	1		0.3	1.1			1700	100		
	03	45	7.2	57	61	1.9	1	9.7	4600	12	4	5.4				2.6	1.2		0.3			25	2100	140		
	04	40	11	83	130	2.6	1.4		12000	23	7.8	9			3.3	3.9	1.9		0.5				4000	290		
	05	25	15	130	200	4.1	2.2	40	23000	41	20	15			4.3	3.8	3.3		1.2	5			6000	440		

FIA	FI	Size (μm)	Li (ppm)	Na (ppm)	K (ppm)	Rb (ppm)	Cs (ppm)	Mg (ppm)	Ca (ppm)	Sr (ppm)	Ba (ppm)	B (ppm)	Fe (ppm)	Mn (ppm)	Zn (ppm)	Pb (ppm)	Cu (ppm)	Ag (ppm)	Tl (ppm)	As (ppm)	Sb (ppm)	S (ppm)	Cl (ppm)	Br (ppm)	T_m (i) (°C)	T_H (HH) (°C)
Sai-100 A4 (1σ error)	01	30	12	97	120	3	1.7	30	9000	25	7.2	11			9.6	5.4	2.2		0.6	3.7		52	3800	270		
	02	30	11	91	210	3.1	1.7	66	17000	38	9.8	11			11	6	3.5		0.5	5.3			5200	430		
	03	45	23	190	400	6.4	3.8		38000	87	16	25			24	13	5.9		1.2	11		180	10000	830		
	04	45	5.7	44	36	1.5	0.8	3.1	2000	6.6	1.8	6.9			2.2	2.2	1		0.3			14	1500	89		
	05	40	5.7	55	67	1.5	0.9	7.1	4700	11	1.8	16			5.1	1.9			0.3				2100	150		
	06	30	5.5	44	38	1.4	0.8	4.1	2700	8.3	4.1	4.8			2.7	2.2	0.8		0.3	1			1500	90		
	07	30	10	86	96	3.1	1.6	11	6600	17	7.5	8.9			9.4	4.6	1.5		0.5	2.4			3200	220		
	08	30	11	81	96	2.7	1.6	12	7500	19	8.5	10			9.2	5	1.7		0.5	2.5		41	3200	210		
	09		11	89	84	2.8	1.6	8.5	4900	14	3.8	10			8.3	4.4	1.2		0.5	1.7			3100	200		
Sai-114 A1 (1σ error)	01	35	6.2	40	31	1.5	0.9	27	2200	6.7	4.6	4.4			9	3.2	0.7		0.3	0.9		13	1400	49		
	02	45	3.9	34	31	1	0.6	27	2900	7.1	3.5	3.6			6.3	1.9	0.6		0.2	2			1200	44		
	03	40	5.9	54	62	1.7	0.8	46	4300	12	4.8	4.9			11	3.3	1.3		0.4	1.7		27	2200	89		
	07	50	8.3	59	52	2.1	1.2	40	4600	11	2.1	6.4			12	3.8	1		0.4			23	2100	76		
	08	60	3.1	21	15	0.7	0.4	18	1700	4.2	0.5	2.4			5.1	1.6	0.3		0.1			6.3	690	24		
	09	60	3.6	29	19	0.9	0.5	23	1600	5.5	1.7	2.6			6.1	1.7	0.5		0.2	0.8		7.3	930	31		
	11	65	3.1	33	35	0.9	0.4	21	3400	7.9	2	2.6			4.9	1.7	0.6		0.2	1.2		15	1200	48		
	12	40	5	54	84	1.5	0.8	50	8100	17	5.1	4.8			8	2.8	1.4		0.3	2.6			2500	110		
	14	30	8.8	90	170	2.3	1.1		14000	30	8.2	8.5			13	4.6	2.5		0.4	4.7			4500	210		
	15	40	5.1	55	53	1.5	0.7	38	5700	13	4.8	4.4			7.6	2.8	1		0.3	2			2000	75		
	16	30	5.7	67	66	1.8	0.8	28	4900	13	5.2	4.6			8.6	3.2	1.1		0.3	2.2			2400	90		
	19	35	12	77	100	2.6	1.6	79	8400	20	7.4	10			19	5.8			0.5	2.1			3200	130		
	21	65	3.8	27	16	0.9	0.6	22	1700	5.7	1	2.8			6.7	1.8	0.4		0.2	1		6.2	830	26		
	23	50	3.7	44	31	1.1	0.5	23	3000	7.9	3.6	3			6.1	1.9	0.7		0.2	1			1400	45		
	24	55	3.5	37	31	1	0.5	26	3100	8	1.2	2.9			5.2	1.7	0.7		0.2			12	1200	45		
	25	50	5	34	31	1.2	0.7	28	3700	9	3.3	3.9			7.2	2.5	0.6		0.2	0.7			1200	43		
	26	55	5.9	37	23	1.4	0.8	13	2200	6.8	1.1	3.9			7.2	3.1	0.4		0.3	0.5		8.5	1200	40		
	27	35	7.6	51	67	1.8	1		8700	17	5.2	6			18	4.2	1		0.4	1.8			2100	88		
Sai-114 A2 (1σ error)	01		6.6	71	91	1.9	0.9	150	11000	22	6.9	5.7			25	4.1	1.7		0.4				3000	120		
	02		6.5	53	48	1.7	0.9	83	5900	10	4.5	5			14	3.8	1		0.3	4.4		20	1800	67		
	03		2.9	33	34	0.8	0.4	23	3300	7.3	2.7	2.5			5.1	1.6	0.7		0.2	1.1		14	1200	45		
	04		10	70	130	2.4	1.4	110	8200	17	6	7.6			21	4.3	1.8		0.4	2.8		49	3300	160		
	05		5.2	53	47	1.7	0.7	74	4800	10	1	4			15	4.1	0.8		0.4	1.5			1800	64		
	06		6.7	59	80	1.7	0.9	76	8000	17	6.6	5.9			14	3.7	1.3		0.3	2.3			2300	97		
	07		11	78	120	2.7	1.6		7900	19	8.3	9.2			17	6	1.4		0.5	2.7		45	3100	140		
	08		9.1	72	110	2.3	1.2		10000	20	8	7.6			15	4.6	1.7		0.4	2.6		46	3000	130		
	09		5.7	66	81	1.6	0.7	75	7000	13	5.3	4.8			14	3.4	1.2		0.3	2.2			2500	99		
	10		6.8	57	58	1.7	0.9		5800	12	6.4	5.6			11	3.6	1		0.3	6.2			2000	72		
Sai-114 A3 (1σ error)	01		8.1	83	150	2.1	1.1	190	15000	19	1.7	8.1			29	4	4		0.5	21			3900	170		
Sai-131 A1 (1σ error)	01	30	6.2	73	99	1.7	0.8	18	9600	10	5.1	6.7	61	7.4	7.2	2.8				2.9			3300	160		
	02	50	13	140	140	3.6	1.4	28	11000	18	7	10		9.7	12	4.2						76	5100	220		
	05	35	6.7	67	60	1.6	0.7	17	4500	11	3.4	4.4		5.5	5.6	2.3				1.6			2300	91		
Sai-131 A2 (1σ error)	01	50	3.5	32	18	0.6	0.3	8	2800	4.2	1.7	2.4		1.9	2.8	0.9	1.8		0.2	0.8		8.3	1100	37		
	04	55	8.3	69	66	1.6	0.8	19	8400	9.7	4.8	7.4	85	4.6	6.8	1.6	4.3		0.3			29	3200	110		
	07	65	5.9	61	39	1.1	0.5	12	5400	6.5	2.3	3.8	57	3.8	4.5	1.6	0.5		0.3	1.3		17	2100	66		
	12	60	9.5	95	130	2.3	0.9	30	15000	14	4.9	6.6	160	6.9	7.9	2.7	6.3		0.4	4.3		47	4100	200		
	15		3.5	38	31	0.8	0.2	9.9	3500	4.1	1.4	2.1	35	2.4	2.5	0.8	0.5		0.1			9.7	1000	31		

FIA	FI	Size (µm)	Li (ppm)	Na (ppm)	K (ppm)	Rb (ppm)	Cs (ppm)	Mg (ppm)	Ca (ppm)	Sr (ppm)	Ba (ppm)	B (ppm)	Fe (ppm)	Mn (ppm)	Zn (ppm)	Pb (ppm)	Cu (ppm)	Ag (ppm)	Tl (ppm)	As (ppm)	Sb (ppm)	S (ppm)	Cl (ppm)	Br (ppm)	T_m (i) (°C)	T_h (HH) (°C)
Sai-131 A3 (1σ error)	01	40	25	200	310	3.6	2.3	78	42000	32	27	26	410	58		8.2	20		0.9	8.2		93	6700	270		
	02	40	8.8	66	79	1.5	0.8	9.7	4600	6.9	5	6.7		6.7	7.2	2.5	0.7		0.3	1.2		20	2000	68		
	03	30	20	150	440	3.7	2.1	63	35000	23	16	29	370	32	20	5.8	13		1.2				7300	380		
	04	25	13	120	280	2.1	1	35	15000	14	5.4	12	190	15	9.6	3.6	1.7		0.6			69	5200	240		
	05	25	17	130	270	2.8	1.5	26	14000	13	7.9	16	180	10	12	3.9	1.3		0.5			65	4700	220		
	06	30	20	150	360	3.2	1.9	30	16000	14	10	19		14	15	5			0.6	5.3		86	6100	300		
	07	35	7.7	70	82	1.3	0.6	14	4600	8	3.4	5.2		8.6	5.6	2.3	0.7		0.3	1.3		20	2000	67		
	08	45	35	250	1100	5.6	3	91	53000	29	19	43	690	40	27	7.7	5		1.8				16000	850		
	09	25	18	120	330	2.7	1.4	42	22000	16	11	17	260	25	17	4.5	11		0.6	6.7		76	5100	250		
Sai-131 A4 (1σ error)	01	60	5.7	53	53	0.8	0.3	12	3800	5	1.8	3.5	37	1.6	3.6	0.8	1		0.2			11	1400	37		
	02	40	7.7	81	85	1.2	0.5	21	4600	8.4	3	5.4	56	5.4	5.6	2			0.3			19	2100	62		
	04	35	34	310	1700	6.1	2.2	130	65000	33	8.8	54		57	26	6.8	6.8					370	23000	1200		
	05	35	36	350		5.6	2.2	170	80000	42	14		840	41	24	6.7	13		1.4			280	17000	830		
	06	35	20	190	510	2.9	1.1	62	23000	20	7.8	17		19	11	3.7			0.8	5.7		100	7200	330		
	07		18	160	330	4.7	2.5	36	29000	30	11	20		18	11	1.6							8400	470		
Host compositions																										
Sai-010a A1 (host comp)	01		1	63	31	0.2	0.07	120	400443	110	5.8	b.d.	b.c.	b.d.	1.7	1.5	0.6	b.d.	0.03	0.3	b.d.	310	330	7.7		
	02		0.4	32	65	0.09	b.d.	130	400443	110	1.2	0.9	b.c.	b.d.	1	1.3	b.d	b.d.	b.d.	0.3	b.d.	320	270	14		
	03		0.4	23	50	b.d.	0.1	130	400443	130	b.d	b.d.	b.c.	b.d.	0.8	0.9	b.d	b.d.	b.d.	0.3	b.d.	300	320	b.d.		
	05		0.2	20	20	0.07	0.02	84	400443	120	0.8	b.d.	b.c.	b.d.	0.6	0.8	b.d	b.d.	b.d.	2.6	b.d.	320	320	b.d.		
	09		2.4	180	72	0.4	0.2	220	400443	130	0.4	1.3	b.c.	b.d.	3.1	2.4	b.d	b.d.	b.d.	1.7	b.d.	510	450	21		
	11		0.2	9.9	72	b.d.	b.d.	230	400443	110	0.6	b.d.	b.c.	b.d.	0.8	0.5	2	b.d.	b.d.	0.1	b.d.	360	240	11		
	12		1	70	110	0.2	b.d.	190	400443	130	b.d	1.3	b.c.	b.d.	1.4	1.3	b.d.	b.d.	b.d.	0.6	b.d.	430	230	21		
	13		1.5	66	400	b.d.	b.d.	360	400443	110	3.9	b.d.	b.c.	b.d.	4.3	5.3	b.d.	b.d.	b.d.	b.d.	b.d.	260	810	48		
Sai-010a A2 (host comp)	01		b.d.	38	b.d.	b.d.	b.d.	290	393081	110	b.d	b.d.	b.c.	b.d.	b.d	0.6	b.d.	b.d.	b.d.	b.d.	b.d.	150	b.d.	b.d.		
	02		1.7	18	49	0.2	b.d	300	393081	120	b.d	b.d.	b.c.	b.d.	b.d	0.7	b.d	b.d.	b.d.	b.d.	b.d.	150	b.d.	b.d.		
	06		b.d.	17	33	b.d.	b.d	220	393081	100	b.d	b.d.	b.c.	b.d.	b.d	b.d.	b.d	b.d	b.d.	b.d.	b.d	230	b.d.	b.d.		
	07		b.d.	32	b.d.	0.4	0.4	160	393081	110	b.d	b.d.	b.c.	b.d.	b.d	9.8	b.d.	b.d.	0.1	b.d.	b.d.	120	b.d.	b.d.		
	08		1.1	140	17	0.2	0.2	360	393081	94	b.d	b.d.	b.c.	b.d.	b.d	1.4	b.d	b.d	b.d.	0.6	b.d	180	620	b.d.		
	10		b.d.	b.d.	13	b.d.	b.d.	340	400443	95	b.d	b.d.	b.c.	b.d.	b.d	b.d.	b.d.	b.d	b.d.	b.d.	b.d.	140	260	b.d.		
Sai-010a A3 (host comp)	04		2.2	180	b.d.	b.d.	b.d.	110	400443	140	b.d	b.d.	b.c.	b.d.	b.d	1.6	b.d.	b.d.	b.d.	b.d.	b.d.	570	1200	b.d.		
	06		0.5	74	29	0.09	0.02	220	400443	100	0.4	b.d.	b.c.	b.d.	0.7	0.7	b.d.	b.d.	b.d.	0.7	b.d.	310	320	7.4		
Sai-010a A5 (host comp)	01		1	180	41	0.3	0.1	410	393081	100	1.4	2	b.c	b.d.	b.d	0.7	b.d	b.d	b.d.	1.8	b.d	150	810	b.d		
	02		1.6	230	84	0.3	b.d	410	393081	100	19	b.d.	b.c.	b.d.	b.d	1.4	b.d	b.d	b.d.	3.1	0.5	190	b.d.	b.d.		

FIA	FI	Size (µm)	Li (ppm)	Na (ppm)	K (ppm)	Rb (ppm)	Cs (ppm)	Mg (ppm)	Ca (ppm)	Sr (ppm)	Ba (ppm)	B (ppm)	Fe (ppm)	Mn (ppm)	Zn (ppm)	Pb (ppm)	Cu (ppm)	Ag (ppm)	Tl (ppm)	As (ppm)	Sb (ppm)	S (ppm)	Cl (ppm)	Br (ppm)	T_m (i) (°C)	T_H (HH) (°C)
Sai-010a D4 (host comp)	01		b.d.	9.1	100	b.d.	b.d	400	400443	74	b.d	b.d.	b.d.	b.d.	0.9	0.4	b.d	b.d.	b.d.	0.4	b.d.	390	380	16		
	02		b.d.	19	93	b.d.	b.d.	310	400443	74	b.d	b.d.	b.d.	b.d.	0.3	0.2	b.d.	b.d.	b.d.	0.6	b.d.	340	410	17		
	03		0.2	39	28	b.d.	b.d	330	400443	76	0.3	b.d.	b.d.	b.d.	0.6	0.3	b.d	b.d.	b.d.	1.5	b.d.	350	190	b.d.		
	04		0.9	120	58	0.1	0.05	310	400443	73	0.5	b.d.	b.d.	b.d.	0.8	0.4	b.d.	b.d.	b.d.	0.9	b.d.	280	390	14		
	05		0.1	21	b.d.	b.d.	b.d.	300	400443	76	0.3	b.d.	b.d.	b.d.	1	0.2	b.d.	b.d.	b.d.	0.2	b.d.	300	240	b.d.		
	06		b.d.	9.1	100	b.d.	b.d.	400	400443	74	b.d	b.d.	b.d.	b.d.	0.9	0.4	b.d.	b.d.	b.d.	0.4	b.d.	390	380	16		
	07		b.d.	b.d.	b.d.	b.d.	b.d.	b.d.	b.d.	b.d.	b.d	b.d.	b.d.	b.d.	b.d	b.d.	b.d.	b.d.	b.d.	b.d.	b.d.	b.d.	b.d.	b.d.		
	08		0.3	76	89	0.09	b.d.	410	400443	77	b.d	b.d.	b.d.	b.d.	0.6	0.4	b.d.	b.d.	b.d.	0.5	b.d.	430	390	17		
Sai-010a D6 (host comp)	01		1	53	120	0.1	0.04	1100	400443	190	0.4	b.d.	b.d.	b.d.	180	9.8	0.3	b.d.	0.07	3.3	b.d.	350	290	19		
Sai-014a A1 (host comp)	02		0.3	25	79	b.d.	0.01	91	400443	480	0.4	0.4	b.d.	b.d.	0.4	12	b.d	b.d.	b.d.	0.7	b.d.	230	350	8.9		
	03		0.5	37	52	0.08	0.04	98	400443	140	0.5	b.d.	b.d.	b.d.	1	9	b.d	b.d.	0.02	0.5	b.d.	260	400	13		
	04		1	75	51	0.2	0.09	85	400443	99	0.2	b.d.	b.d.	b.d.	0.8	2.2	b.d.	b.d.	b.d.	0.7	b.d.	210	480	5.8		
	05		0.8	63	110	0.1	0.05	52	400443	80	b.d	b.d.	b.d.	b.d.	0.6	1.3	b.d.	b.d.	b.d.	0.3	b.d.	240	450	18		
	06		3.5	210	290	0.3	0.2	110	400443	110	b.d	b.d.	b.d.	b.d.	2.1	4	b.d.	b.d.	b.d.	4.4	b.d.	330	1400	51		
	07		3.5	210	290	0.3	0.2	110	400443	110	b.d	b.d.	b.d.	b.d.	2.1	4	b.d.	b.d.	b.d.	4.4	b.d.	330	1400	51		
	08		0.4	35	140	0.09	0.09	68	400443	140	0.7	1.6	b.d.	b.d.	0.5	4.5	b.d	b.d.	b.d.	0.9	b.d.	230	530	26		
Sai-014a D3 (host comp)	01		b.d.	10	55	b.d.	b.d.	84	400443	93	b.d	b.d.	b.d.	b.d.	0.4	1	b.d.	b.d.	b.d.	0.5	b.d.	300	140	b.d.		
	02		b.d.	b.d.	b.d.	b.d.	b.d	b.d	b.d.	b.d.	b.d	b.d.	b.d.	b.d.	b.d	b.d.	b.d	b.d.	b.d.	b.d.	b.d.	b.d	b.d.	b.d.		
	03		0.3	17	54	b.d.	b.d.	170	400443	160	b.d	b.d.	b.d.	b.d.	0.4	2.8	b.d.	b.d.	b.d.	0.7	b.d.	260	510	14		
	04		0.2	14	52	0.07	b.d.	63	400443	86	b.d	b.d.	b.d.	b.d.	0.7	0.9	b.d.	b.d.	b.d.	0.4	b.d.	270	180	12		
	06		0.2	21	60	b.d.	b.d.	130	400443	190	0.6	4.1	b.d.	b.d.	0.8	4.3	b.d.	b.d.	b.d.	0.2	b.d.	220	150	12		
Sai-014a E2 (host comp)	01		0.3	20	96	b.d	b.d	82	400443	100	b.d	b.d	b.d	b.d	b.d	1.2	b.d	b.d	b.d	b.d	b.d	240	300	b.d		
	02		b.d.	2.8	59	b.d.	b.d.	190	400443	130	b.d	b.d.	b.d.	b.d.	0.8	1.6	b.d.	b.d.	b.d.	1.6	b.d.	270	140	12		
	04		0.3	23	22	b.d	0.04	100	400443	97	b.d	b.d	b.d	b.d	0.7	1	b.d	b.d	b.d	1.1	b.d	230	200	b.d		
	05		b.d.	0.4	39	b.d.	b.d.	250	400443	110	b.d	b.d.	b.d.	b.d.	0.4	0.8	b.d.	b.d.	b.d.	0.2	b.d.	240	250	b.d.		
	06		0.8	8.3	b.d.	0.05	b.d.	110	400443	110	0.2	b.d.	b.d.	b.d.	0.3	1.4	b.d.	b.d.	b.d.	0.5	b.d.	220	160	6.8		
	07		0.6	44	40	0.08	0.03	60	400443	86	0.1	b.d.	b.d	b.d.	0.4	1.1	b.d	b.d	b.d.	0.3	b.d	270	350	7.3		
	08		0.2	23	b.d.	b.d.	b.d.	59	400443	81	0.4	1	b.d.	b.d.	2.3	2.1	0.2	b.d.	b.d.	4.1	b.d.	270	270	b.d.		
Sai-028 A1 (host comp)	01		b.d.	11	70	b.d.	b.d	600	400443	140	0.2	b.d.	b.d.	b.d.	17	5.5	0.2	b.d	0.04	5.3	b.d	280	660	10		
	02		0.2	34	87	b.d.	b.d.	790	400443	98	b.d	b.d.	b.d.	b.d.	11	2.8	0.07	b.d.	0.03	2.3	b.d.	250	680	6		
	03		b.d.	9.4	110	b.d.	b.d.	1100	400443	170	b.d	b.d.	b.d.	b.d.	40	9.1	0.3	b.d.	b.d.	7.8	b.d.	380	810	24		
	04		b.d.	17	b.d.	b.d.	b.d.	1900	400443	150	0.2	b.d.	b.d.	b.d.	25	4.3	0.1	b.d.	0.04	3.3	b.d.	240	350	4.3		
	05		0.08	29	36	0.03	b.d.	370	400443	54	b.d	3.7	b.d.	b.d.	8.2	0.7	b.d.	b.d.	0.02	2.9	b.d.	240	560	8.5		
	06		0.4	52	21	0.1	0.02	1100	400443	57	0.1	1.4	b.d.	b.d.	6.1	0.7	0.2	b.d.	0.007	9.1	b.d.	160	470	6		
	07		b.d.	6.1	16	0.02	b.d.	1500	400443	31	b.d	b.d.	b.d.	b.d.	7.9	0.3	0.2	b.d.	b.d.	16	b.d.	180	430	3.5		
	08		b.d.	54	24	b.d.	b.d.	180	400443	51	b.d	b.d.	b.d.	b.d.	1.5	0.3	b.d.	b.d.	b.d.	1.8	b.d.	190	480	6.1		
	09		0.2	23	12	0.05	0.02	180	400443	57	0.1	0.3	b.d.	b.d.	3.4	1	0.04	b.d.	b.d.	3.4	b.d.	160	410	5		

FIA	FI	Size (µm)	Li (ppm)	Na (ppm)	K (ppm)	Rb (ppm)	Cs (ppm)	Mg (ppm)	Ca (ppm)	Sr (ppm)	Ba (ppm)	B (ppm)	Fe (ppm)	Mn (ppm)	Zn (ppm)	Pb (ppm)	Cu (ppm)	Ag (ppm)	Tl (ppm)	As (ppm)	Sb (ppm)	S (ppm)	Cl (ppm)	Br (ppm)	T_m (i) (°C)	T_m (HH) (°C)
Sai-028 A2 (host comp)	01		0.2	63	140	0.09	b.d.	420	400443	43	b.d.	b.d.	b.d.	b.d.	0.6	0.5	b.d.	b.d.	b.d.	0.3	b.d.	250	460	17		
	03		0.1	20	18	0.03	b.d.	390	400443	40	b.d.	b.d.	b.d.	b.d.	0.6	0.3	b.d.	b.d.	b.d.	0.3	b.d.	190	520	7.3		
	04		0.2	24	62	b.d.	b.d.	490	400443	42	b.d.	b.d.	b.d.	b.d.	0.7	0.6	b.d.	b.d.	b.d.	0.5	b.d.	230	340	15		
	07		0.1	38	b.d.	0.08	b.d.	390	400443	35	b.d.	0.7	b.d.	b.d.	1.7	1	b.d.	b.d.	b.d.	1.1	b.d.	230	580	7.3		
	08		0.3	35	80	0.06	b.d.	450	400443	42	b.d.	b.d.	b.d.	b.d.	0.6	0.5	b.d.	b.d.	b.d.	0.6	b.d.	230	510	17		
	09		0.1	85	71	0.2	0.05	440	400443	43	b.d.	b.d.	b.d.	b.d.	0.6	0.4	b.d.	b.d.	b.d.	0.7	b.d.	230	1000	28		
Sai-058 A1 (host comp)	01		0.09	6.3	65	b.d.	b.d.	150	400443	51	0.5	b.d.	b.d.	b.d.	1.4	0.8	b.d.	b.d.	b.d.	2.1	b.d.	170	250	15		
	02		b.d.	3.8	82	b.d.	b.d.	140	400443	33	b.d.	b.d.	b.d.	b.d.	0.4	0.3	b.d.	b.d.	b.d.	0.5	b.d.	240	240	14		
	03		b.d.	3.8	82	b.d.	b.d.	140	400443	33	b.d.	b.d.	b.d.	b.d.	0.4	0.3	b.d.	b.d.	b.d.	0.5	b.d.	240	240	14		
	04		0.04	4.3	64	b.d.	b.d.	70	400443	34	b.d.	b.d.	b.d.	b.d.	0.2	0.3	b.d.	b.d.	b.d.	0.2	b.d.	210	260	12		
	05		b.d.	0.2	b.d.	b.d.	b.d.	44	400443	25	b.d.	b.d.	b.d.	b.d.	b.d.	0.1	b.d.	b.d.	b.d.	0.1	b.d.	200	240	6.2		
	08		b.d.	12	60	b.d.	b.d.	190	400443	97	b.d.	b.d.	b.d.	b.d.	15	3.7	0.1	b.d.	b.d.	2.1	b.d.	250	300	13		
Sai-058 B2 (host comp)	01		b.d.	0.3	21	b.d.	b.d.	58	400443	29	b.d.	0.2	b.d.	b.d.	0.08	0.2	b.d.	b.d.	b.d.	0.09	b.d.	190	170	5.4		
	02		b.d.	2	b.d.	b.d.	b.d.	65	400443	38	b.d.	b.d.	b.d.	b.d.	b.d.	0.3	b.d.	b.d.	b.d.	b.d.	b.d.	240	b.d.	46		
	03		b.d.	0.3	21	b.d.	b.d.	58	400443	29	b.d.	0.2	b.d.	b.d.	0.08	0.2	b.d.	b.d.	b.d.	0.09	b.d.	190	170	5.4		
	04		5	1100	180	1	0.5	19	400443	71	2.5	4	b.d.	b.d.	0.6	0.3	0.1	b.d.	0.05	0.3	b.d.	260	2000	86		
	05		b.d.	3.7	77	b.d.	b.d.	18	400443	37	b.d.	b.d.	b.d.	b.d.	0.3	0.2	b.d.	b.d.	b.d.	0.2	b.d.	180	210	11		
	06		0.1	40	17	0.05	b.d.	150	400443	26	b.d.	b.d.	b.d.	b.d.	0.2	0.2	b.d.	b.d.	b.d.	0.3	b.d.	280	240	15		
Sai-071 B1 (host comp)	01		b.d.	6.2	34	b.d.	b.d.	1300	400443	100	b.d.	b.d.	b.d.	b.d.	9.5	0.9	b.d.	b.d.	b.d.	b.d.	b.d.	230	500	b.d.		
	02		b.d.	26	56	b.d.	b.d.	340	400443	54	b.d.	b.d.	b.d.	b.d.	6.9	0.3	b.d.	b.d.	b.d.	12	b.d.	500	320	b.d.		
	08		b.d.	3.4	35	b.d.	b.d.	810	400443	76	b.d.	b.d.	b.d.	b.d.	8.7	0.6	b.d.	b.d.	b.d.	0.3	b.d.	190	370	b.d.		
	10		b.d.	16	300	b.d.	0.4	1000	400443	130	b.d.	b.d.	b.d.	b.d.	b.d.	2.9	b.d.	b.d.	b.d.	b.d.	b.d.	390	b.d.	b.d.		
Sai-071 B3 (host comp)	01		b.d.	b.d.	b.d.	b.d.	b.d.	b.d.	b.d.	b.d.	b.d.	b.d.	b.d.	b.d.	b.d.	b.d.	b.d.	b.d.	b.d.	b.d.	b.d.	b.d.	b.d.	b.d.		
	02		b.d.	5.2	290	b.d.	b.d.	190	400443	44	b.d.	b.d.	b.d.	b.d.	9.6	0.8	b.d.	b.d.	b.d.	b.d.	b.d.	390	b.d.	b.d.		
	03		b.d.	25	190	b.d.	b.d.	660	400443	59	b.d.	b.d.	b.d.	b.d.	31	0.7	b.d.	b.d.	b.d.	2.1	b.d.	580	640	b.d.		
	09		0.2	50	57	0.1	b.d.	2400	400443	69	b.d.	b.d.	b.d.	b.d.	28	0.7	0.6	b.d.	b.d.	0.4	b.d.	230	430	b.d.		
Sai-071 B4 (host comp)	03		b.d.	7.4	130	b.d.	b.d.	40	400443	21	b.d.	b.d.	b.d.	b.d.	5.8	0.6	b.d.	b.d.	b.d.	b.d.	b.d.	260	380	b.d.		

FIA	FI	Size (µm)	Li (ppm)	Na (ppm)	K (ppm)	Rb (ppm)	Cs (ppm)	Mg (ppm)	Ca (ppm)	Sr (ppm)	Ba (ppm)	B (ppm)	Fe (ppm)	Mn (ppm)	Zn (ppm)	Pb (ppm)	Cu (ppm)	Ag (ppm)	Tl (ppm)	As (ppm)	Sb (ppm)	S (ppm)	Cl (ppm)	Br (ppm)	T_m (i) (°C)	T_m (HH) (°C)
Sai-100 A1 (host comp)	01		2.6	210	78	0.4	0.2	11	400443	110	1.1	b.d.	b.d.	b.d.	1.1	0.8	b.d.	b.d.	0.03	0.8	b.d.	410	860	89		
	02		2.6	210	78	0.4	0.2	11	400443	110	1.1	b.d.	b.d.	b.d.	1.1	0.8	b.d.	b.d.	0.03	0.8	b.d.	410	860	89		
	03		2.6	210	78	0.4	0.2	11	400443	110	1.1	b.d.	b.d.	b.d.	1.1	0.8	b.d.	b.d.	0.03	0.8	b.d.	410	860	89		
	04		0.3	36	b.d.	b.d.	b.d.	13	400443	89	b.d.	b.d.	b.d.	b.d.	1.3	0.2	b.d.	b.d.	b.d.	0.5	b.d.	360	320	b.d.		
	05		1.4	110	55	0.2	0.09	12	400443	95	0.3	b.d.	b.d.	b.d.	b.d.	0.6	b.d.	b.d.	b.d.	0.4	b.d.	390	850	45		
	06		1.4	110	55	0.2	0.09	12	400443	95	0.3	b.d.	b.d.	b.d.	b.d.	0.6	b.d.	b.d.	b.d.	0.4	b.d.	390	850	45		
	07		0.5	87	35	0.09	0.09	10	400443	89	0.1	0.3	b.d.	b.d.	0.7	0.09	b.d.	b.d.	b.d.	0.5	b.d.	290	390	27		
	08		4.8	1500	130	0.7	0.3	12	400443	110	0.2	2	b.d.	b.d.	b.d.	0.3	b.d.	b.d.	0.05	0.5	b.d.	370	2900	110		
	09		0.4	69	b.d.	0.07	b.d.	11	400443	100	0.2	b.d.	b.d.	b.d.	1.5	0.1	b.d.	b.d.	b.d.	0.6	b.d.	330	560	26		
	10		0.2	28	19	b.d.	b.d.	11	400443	89	b.d.	b.d.	b.d.	b.d.	2	0.2	b.d.	b.d.	b.d.	0.6	b.d.	370	420	b.d.		
	11		0.8	220	54	0.09	0.07	9.6	400443	130	b.d.	b.d.	b.d.	b.d.	b.d.	0.1	b.d.	b.d.	0.03	0.4	b.d.	330	640	34		
	12		0.8	220	54	0.09	0.07	9.6	400443	130	b.d.	b.d.	b.d.	b.d.	b.d.	0.1	b.d.	b.d.	0.03	0.4	b.d.	330	640	34		
	13		12	23	13	b.d.	0.03	12	400443	110	0.3	0.4	b.d.	b.d.	2.1	0.2	0.1	b.d.	b.d.	1.2	b.d.	290	350	14		
Sai-100 A2 (host comp)	01		0.1	18	20	b.d.	0.02	11	400443	120	0.4	b.d.	b.d.	b.d.	1.6	0.2	b.d.	b.d.	b.d.	0.4	b.d.	b.d.	720	17		
	02		0.05	8.5	19	0.02	b.d.	17	400443	81	0.4	0.6	b.d.	b.d.	3.8	0.3	b.d.	b.d.	0.01	1.5	b.d.	b.d.	510	16		
	03		0.3	23	b.d.	0.05	0.04	15	400443	100	b.d.	b.d.	b.d.	b.d.	2.6	0.2	b.d.	b.d.	b.d.	0.5	b.d.	b.d.	830	23		
	04		0.3	23	b.d.	0.05	0.04	15	400443	100	b.d.	b.d.	b.d.	b.d.	2.6	0.2	b.d.	b.d.	b.d.	0.5	b.d.	b.d.	830	23		
	05		0.3	39	28	0.05	0.05	20	400443	110	0.1	0.4	b.d.	b.d.	1.5	0.4	b.d.	b.d.	b.d.	3.8	b.d.	b.d.	830	20		
	06		0.3	39	28	0.05	0.05	20	400443	110	0.1	0.4	b.d.	b.d.	1.5	0.4	b.d.	b.d.	b.d.	3.8	b.d.	b.d.	830	20		
	07		3.4	82	61	0.3	0.2	18	400443	140	0.6	1	b.d.	b.d.	0.3	0.5	b.d.	b.d.	0.009	0.7	b.d.	b.d.	2000	67		
	08		3.4	82	61	0.3	0.2	18	400443	140	0.6	1	b.d.	b.d.	0.3	0.5	b.d.	b.d.	0.009	0.7	b.d.	b.d.	2000	67		
	09		0.8	60	33	0.09	0.04	21	400443	130	0.8	1.2	b.d.	b.d.	11	0.7	b.d.	b.d.	0.008	1.2	b.d.	b.d.	750	20		
	10		0.8	60	33	0.09	0.04	21	400443	130	0.8	1.2	b.d.	b.d.	11	0.7	b.d.	b.d.	0.008	1.2	b.d.	b.d.	750	20		
	11		0.06	11	21	b.d.	b.d.	19	400443	120	b.d.	0.3	b.d.	b.d.	0.4	0.3	b.d.	b.d.	b.d.	0.7	b.d.	250	300	13		
	12		1.4	130	b.d.	0.3	0.1	42	400443	170	b.d.	1.1	b.d.	b.d.	0.8	1.1	b.d.	b.d.	0.03	3.8	b.d.	b.d.	1300	b.d.		
	13		1.4	130	b.d.	0.3	0.1	42	400443	170	b.d.	1.1	b.d.	b.d.	0.8	1.1	b.d.	b.d.	0.03	3.8	b.d.	b.d.	1300	b.d.		
	14		1.4	130	b.d.	0.3	0.1	42	400443	170	b.d.	1.1	b.d.	b.d.	0.8	1.1	b.d.	b.d.	0.03	3.8	b.d.	b.d.	1300	b.d.		
	15		3.1	390	96	0.5	0.2	28	400443	160	0.9	0.8	b.d.	b.d.	2	1.4	b.d.	b.d.	0.03	1.2	b.d.	b.d.	2200	61		
	16		1	98	95	0.1	0.05	99	400443	160	0.7	3.8	b.d.	b.d.	0.8	2.5	b.d.	b.d.	b.d.	32	b.d.	b.d.	560	75		
	17		0.4	69	34	0.09	0.02	160	400443	69	0.2	b.d.	b.d.	b.d.	3.4	0.5	b.d.	b.d.	b.d.	0.5	b.d.	b.d.	360	16		
	18		0.09	6.4	39	0.03	b.d.	12	400443	84	b.d.	b.d.	b.d.	b.d.	0.9	0.1	b.d.	b.d.	b.d.	0.5	b.d.	b.d.	370	9		
	19		0.7	120	43	0.08	0.04	12	400443	88	0.5	15	b.d.	b.d.	1.4	0.5	0.08	b.d.	0.008	0.4	b.d.	240	430	19		
	20		0.7	120	43	0.08	0.04	12	400443	88	0.5	15	b.d.	b.d.	1.4	0.5	0.08	b.d.	0.008	0.4	b.d.	240	430	19		
	21		0.2	17	55	b.d.	0.08	23	400443	100	b.d.	3.1	b.d.	b.d.	3.3	0.7	b.d.	b.d.	b.d.	3.8	b.d.	320	330	18		
	22		0.6	75	49	0.07	0.04	11	400443	92	0.4	0.6	b.d.	b.d.	0.9	0.3	b.d.	b.d.	b.d.	0.4	b.d.	290	430	21		
	23		1.1	100	35	0.2	0.08	25	400443	76	0.3	0.6	b.d.	b.d.	0.2	0.6	b.d.	b.d.	b.d.	3.6	b.d.	210	350	13		

FIA	FI	Size (µm)	Li (ppm)	Na (ppm)	K (ppm)	Rb (ppm)	Cs (ppm)	Mg (ppm)	Ca (ppm)	Sr (ppm)	Ba (ppm)	B (ppm)	Fe (ppm)	Mn (ppm)	Zn (ppm)	Pb (ppm)	Cu (ppm)	Ag (ppm)	Tl (ppm)	As (ppm)	Sb (ppm)	S (ppm)	Cl (ppm)	Br (ppm)	T_m (i) (°C)	T_m (HH) (°C)
Sai-100 A3 (host comp)	01		0.1	3.1	21	0.04	b.d.	63	400443	160	b.d.	0.4	b.d.	b.d.	0.3	2.1	b.d.	b.d.	b.d.	0.3	b.d.	300	280	13	
	02		b.d.	1.3	b.d.	b.d.	b.d.	52	400443	140	b.d.	b.d.	b.d.	b.d.	0.3	1.5	b.d.	b.d.	b.d.	0.2	b.d.	300	200	20	
	03		0.2	29	41	0.06	b.d.	40	400443	97	b.d.	b.d.	b.d.	b.d.	b.d.	0.8	b.d.	b.d.	b.d.	0.5	b.d.	460	470	b.d.	
	04		0.08	1.9	30	b.d.	b.d.	23	400443	76	b.d.	b.d.	b.d.	b.d.	b.d.	0.3	b.d.	b.d.	b.d.	0.4	b.d.	390	430	b.d.	
	05		0.2	13	26	0.03	b.d.	26	400443	76	0.1	b.d.	b.d.	b.d.	1.1	0.3	b.d.	b.d.	b.d.	0.4	b.d.	280	310	b.d.	
Sai-100 A4 (host comp)	01		0.9	160	65	0.1	0.07	78	400443	100	0.3	0.4	b.d.	b.d.	0.9	1.2	b.d.	b.d.	0.01	0.5	b.d.	300	560	25	
	02		0.06	9.5	46	0.04	b.d.	140	400443	100	0.2	b.d.	b.d.	b.d.	0.6	0.5	b.d.	b.d.	b.d.	0.5	b.d.	290	250	b.d.	
	03		0.9	74	54	0.2	0.09	120	400443	120	0.2	b.d.	b.d.	b.d.	1	1.2	b.d.	b.d.	0.01	0.5	b.d.	300	440	23	
	04		5.4	280	150	0.8	0.5	19	400443	110	b.d.	32	b.d.	b.d.	3.3	1.5	2	b.d.	b.d.	80	b.d.	500	1200	110	
	05		5.4	280	150	0.8	0.5	19	400443	110	b.d.	32	b.d.	b.d.	3.3	1.5	2	b.d.	b.d.	80	b.d.	500	1200	110	
	06		1.8	170	85	0.3	0.2	19	400443	100	b.d.	0.9	b.d.	b.d.	0.5	1	b.d.	b.d.	0.03	1.1	b.d.	440	680	76	
	07		1.3	170	58	0.3	0.08	24	400443	100	0.4	0.7	b.d.	b.d.	2	1	b.d.	b.d.	b.d.	0.8	b.d.	370	640	46	
	08		1.3	170	58	0.3	0.08	24	400443	100	0.4	0.7	b.d.	b.d.	2	1	b.d.	b.d.	b.d.	0.8	b.d.	370	640	46	
	09		1.3	170	58	0.3	0.08	24	400443	100	0.4	0.7	b.d.	b.d.	2	1	b.d.	b.d.	b.d.	0.8	b.d.	370	640	46	
Sai-114 A1 (host comp)	01		1.2	65	56	0.2	0.09	1300	400443	81	0.3	b.d.	b.d.	b.d.	10	1.2	b.d.	b.d.	b.d.	0.6	b.d.	440	570	29	
	02		1.4	280	97	0.3	0.1	810	400443	85	0.7	b.d.	b.d.	b.d.	5.9	1.2	b.d.	b.d.	b.d.	2.4	b.d.	350	790	40	
	03		3.1	300	59	0.4	0.1	980	400443	92	3.1	b.d.	b.d.	b.d.	12	3	b.d.	b.d.	0.04	0.7	b.d.	380	860	28	
	07		2.9	380	57	0.4	0.2	740	400443	79	0.5	0.9	b.d.	b.d.	13	2.8	b.d.	b.d.	0.03	0.4	b.d.	370	820	29	
	08		0.2	25	19	0.05	0.03	650	400443	100	0.2	0.3	b.d.	b.d.	0.6	0.4	b.d.	b.d.	b.d.	0.4	b.d.	220	280	6.7	
	09		0.05	2.7	18	0.03	b.d.	2100	400443	150	b.d.	b.d.	b.d.	b.d.	38	2.9	0.2	b.d.	0.03	3.2	b.d.	340	240	b.d.	
	11		0.5	67	40	0.06	0.03	340	400443	78	b.d.	b.d.	b.d.	b.d.	1.1	0.6	b.d.	b.d.	b.d.	0.8	b.d.	310	400	16	
	12		0.4	110	14	0.08	0.04	350	400443	84	0.2	b.d.	b.d.	b.d.	0.9	0.6	b.d.	b.d.	b.d.	0.4	b.d.	340	420	15	
	14		1.2	35	56	0.1	b.d.	630	400443	110	0.3	b.d.	b.d.	b.d.	1.9	0.7	b.d.	b.d.	b.d.	0.5	b.d.	410	450	34	
	15		0.2	37	20	0.03	0.02	390	400443	79	b.d.	0.2	b.d.	b.d.	0.5	0.7	b.d.	b.d.	b.d.	0.3	b.d.	250	290	11	
	16		0.1	14	25	b.d.	b.d.	350	400443	98	0.2	0.7	b.d.	b.d.	1.7	0.9	b.d.	b.d.	0.01	3.6	b.d.	350	230	15	
	19		0.2	16	31	b.d.	b.d.	630	400443	89	b.d.	b.d.	b.d.	b.d.	4.2	0.8	b.d.	b.d.	b.d.	0.3	b.d.	380	300	23	
	21		0.08	12	9.9	0.04	b.d.	1300	400443	190	0.2	b.d.	b.d.	b.d.	40	6.5	0.2	b.d.	0.05	5.7	b.d.	220	270	b.d.	
	23		0.6	140	24	0.2	0.04	520	400443	87	0.4	0.6	b.d.	b.d.	1.1	0.6	b.d.	b.d.	b.d.	0.3	b.d.	260	520	20	
	24		0.5	110	22	0.07	0.03	560	400443	94	0.2	b.d.	b.d.	b.d.	1.2	0.8	0.1	b.d.	0.005	2.4	b.d.	280	400	15	
	25		0.4	48	12	0.07	0.04	510	400443	96	0.3	b.d.	b.d.	b.d.	1	0.6	b.d.	b.d.	b.d.	0.7	b.d.	220	300	7	
	26		0.5	78	25	0.09	0.03	280	400443	110	0.4	b.d.	b.d.	b.d.	0.9	0.7	b.d.	b.d.	0.005	0.4	b.d.	220	360	14	
	27		0.4	43	15	0.08	0.02	1900	400443	79	0.2	0.2	b.d.	b.d.	20	0.9	b.d.	b.d.	0.02	0.3	b.d.	190	270	11	

FIA	FI	Size (μm)	Li (ppm)	Na (ppm)	K (ppm)	Rb (ppm)	Cs (ppm)	Mg (ppm)	Ca (ppm)	Sr (ppm)	Ba (ppm)	B (ppm)	Fe (ppm)	Mn (ppm)	Zn (ppm)	Pb (ppm)	Cu (ppm)	Ag (ppm)	Tl (ppm)	As (ppm)	Sb (ppm)	S (ppm)	Cl (ppm)	Br (ppm)	T_m (i) (°C)	T_m (HH) (°C)
Sai-114 A2 (host comp)	01		0.6	110	40	0.1	0.04	1900	400443	84	0.3	b.d.	b.d.	b.d.	20	0.9	0.1	b.d.	b.d.	0.7	b.d.	230	430	15		
	02		0.2	32	22	0.03	0.02	1700	400443	38	b.d.	0.2	b.d.	b.d.	8.7	0.4	0.2	b.d.	b.d.	7.9	b.d.	230	250	b.d.		
	03		1	120	36	0.2	0.07	390	400443	80	1.2	0.3	b.d.	b.d.	3.2	0.9	b.d.	b.d.	b.d.	0.7	b.d.	270	550	18		
	04		1.3	120	48	0.2	0.1	1500	400443	84	0.3	b.d.	b.d.	b.d.	21	1.7	b.d.	b.d.	b.d.	0.6	b.d.	340	570	b.d.		
	05		0.06	1.2	b.d.	b.d.	b.d.	1800	400443	63	b.d.	b.d.	b.d.	b.d.	16	0.2	b.d.	b.d.	b.d.	0.3	b.d.	260	250	b.d.		
	06		0.5	49	16	0.08	0.02	870	400443	93	0.6	b.d.	b.d.	b.d.	9.3	1.4	b.d.	b.d.	b.d.	1.2	b.d.	270	380	b.d.		
	07		0.4	42	b.d.	b.d.	b.d.	1500	400443	94	0.6	0.7	b.d.	b.d.	10	1.1	b.d.	b.d.	0.02	0.8	b.d.	360	400	b.d.		
	08		0.4	57	16	b.d.	b.d.	610	400443	65	0.6	b.d.	b.d.	b.d.	4.2	0.7	b.d.	b.d.	b.d.	0.6	b.d.	300	290	b.d.		
	09		0.8	240	23	0.2	0.03	1200	400443	59	0.5	b.d.	b.d.	b.d.	16	1	0.1	b.d.	0.02	0.6	b.d.	300	480	b.d.		
	10		0.07	23	11	0.04	b.d.	1200	400443	61	0.1	b.d.	b.d.	b.d.	10	1.3	b.d.	b.d.	0.006	0.5	b.d.	260	310	b.d.		
Sai-114 A3 (host comp)	01		0.2	31	23	b.d.	b.d.	1300	400443	33	b.d.	b.d.	b.d.	b.d.	13	0.7	0.4	b.d.	b.d.	19	b.d.	250	320	b.d.		
Sai-131 A1 (host comp)	01		0.5	110	77	b.d.	0.04	18	513364	10	b.d.	b.d.	90	2.2	b.d.	b.d.	b.d.	b.d.	b.d.	1	b.d.	430	970	94		
	02		b.d.	96	280	b.d.	b.d.	17	513364	11	b.d.	b.d.	98	b.d.	b.d.	b.d.	b.d.	b.d.	b.d.	2.3	b.d.	740	2000	220		
	05		b.d.	b.d.	92	b.d.	b.d.	14	513364	6.5	b.d.	b.d.	110	b.d.	b.d.	b.d.	b.d.	b.d.	b.d.	0.5	b.d.	580	320	51		
Sai-131 A2 (host comp)	01		2.8	620	92	0.4	0.1	44	513364	28	0.9	b.d.	59	3.7	1.3	0.6	2.7	b.d.	b.d.	1.2	b.d.	340	4000	170		
	04		3.2	520	180	0.9	0.2	43	513364	36	0.6	b.d.	57	3.5	b.d.	0.3	b.d.	b.d.	b.d.	0.7	b.d.	410	4300	170		
	07		0.2	60	90	0.06	b.d.	16	513364	7.1	b.d.	b.d.	58	b.d.	0.2	0.09	b.d.	b.d.	b.d.	0.8	b.d.	350	600	55		
	12		1.3	430	b.d.	0.4	0.07	46	513364	28	0.3	b.d.	81	3.9	0.5	0.4	b.d.	b.d.	b.d.	1.5	b.d.	290	2100	120		
	15		0.2	21	b.d.	b.d.	0.02	34	513364	9.7	0.2	b.d.	77	b.d.	0.1	0.05	1.4	b.d.	b.d.	2.1	b.d.	180	85	23		
Sai-131 A3 (host comp)	01		1.7	210	b.d.	0.3	0.2	43	513364	37	2.5	1.3	76	59	1	0.3	0.2	b.d.	b.d.	1.3	b.d.	250	630	b.d.		
	02		0.2	60	90	0.06	b.d.	16	513364	7.1	b.d.	b.d.	58	b.d.	0.2	0.09	b.d.	b.d.	b.d.	0.8	b.d.	350	600	55		
	03		b.d.	40	b.d.	0.1	0.05	37	513364	14	0.7	b.d.	85	5.2	b.d.	b.d.	b.d.	b.d.	b.d.	0.8	b.d.	330	b.d.	16		
	04		1.3	300	b.d.	0.2	b.d.	47	513364	22	b.d.	b.d.	74	12	1.3	0.5	b.d.	b.d.	b.d.	1.4	b.d.	300	560	35		
	05		b.d.	92	b.d.	b.d.	b.d.	39	513364	13	b.d.	b.d.	83	b.d.	b.d.	0.3	b.d.	b.d.	b.d.	1.4	b.d.	250	550	b.d.		
	06		b.d.	22	150	b.d.	b.d.	41	513364	12	b.d.	b.d.	66	b.d.	b.d.	b.d.	b.d.	b.d.	b.d.	1.6	b.d.	330	b.d.	32		
	07		b.d.	58	b.d.	b.d.	b.d.	39	513364	14	0.7	b.d.	90	2.8	b.d.	0.2	b.d.	b.d.	b.d.	1.3	b.d.	320	410	30		
	08		b.d.	1.5	b.d.	b.d.	b.d.	37	513364	9.8	b.d.	b.d.	79	b.d.	b.d.	b.d.	b.d.	b.d.	b.d.	2.6	b.d.	360	b.d.	b.d.		
	09		b.d.	68	140	b.d.	b.d.	40	513364	15	b.d.	b.d.	72	9	b.d.	b.d.	b.d.	b.d.	b.d.	3.2	b.d.	170	420	b.d.		
Sai-131 A4 (host comp)	01		b.d.	14	b.d.	b.d.	0.01	40	513364	7.5	0.1	b.d.	70	b.d.	b.d.	0.02	0.7	b.d.	b.d.	0.6	b.d.	170	58	4.3		
	02		1.7	330	b.d.	0.2	b.d.	60	513364	25	b.d.	b.d.	86	5.5	1.1	0.4	b.d.	b.d.	b.d.	1.2	b.d.	390	990	28		
	04		b.d.	130	b.d.	b.d.	b.d.	41	513364	10	b.d.	b.d.	74	b.d.	b.d.	b.d.	b.d.	b.d.	b.d.	1.6	b.d.	320	550	36		
	05		0.5	86	b.d.	b.d.	b.d.	45	513364	11	b.d.	b.d.	83	b.d.	b.d.	0.1	0.3	b.d.	b.d.	1.2	b.d.	280	310	12		
	06		b.d.	73	b.d.	b.d.	b.d.	46	513364	11	0.9	b.d.	78	b.d.	b.d.	b.d.	0.3	b.d.	b.d.	1.1	b.d.	230	210	23		
	07		b.d.	14	140	b.d.	b.d.	16	513364	10	b.d.	b.d.	110	b.d.	b.d.	b.d.	b.d.	b.d.	b.d.	1.8	b.d.	560	500	54		

Summary of fluid inclusion data (Sailauf)

FIA	FI	Size (µm)	Li (ppm)	Na (ppm)	K (ppm)	Rb (ppm)	Cs (ppm)	Mg (ppm)	Ca (ppm)	Sr (ppm)	Ba (ppm)	B (ppm)	Fe (ppm)	Mn (ppm)	Zn (ppm)	Pb (ppm)	Cu (ppm)	Ag (ppm)	Tl (ppm)	As (ppm)	Sb (ppm)	S (ppm)	Cl (ppm)	Br (ppm)	T_m (i) (°C)	T_m (HH) (°C)
Concentration data																										
Sai-010a A1 (conc.)	01	35	780	62600	4350	110	57	<0.06	40500	1870	150	160	n.a.	n.a.	670	440	<0.08	n.a.	4.8	<0.1	n.a.	<3.7	203400	4080	-25.7	-3.5
	02	25	980	61500	4400	130	65	670	40800	1860	<0.2	180	n.a.	n.a.	750	400	<0.1	n.a.	6.5	<0.2	n.a.	<5.7	197800	4000	-25.7	-6.7
	03	30	900	63100	5570	130	63	<0.1	39900	1700	<0.3	160	n.a.	n.a.	690	260	<0.1	n.a.	6.7	<0.2	n.a.	<6.4	181800	5110	-25.6	-4.0
	05	50	920	62600	5020	130	63	400	40500	2450	<0.2	180	n.a.	n.a.	880	370	<0.09	n.a.	10	<0.2	n.a.	<4.7	212900	5070	-25.7	-3.5
	09	60	790	63400	4310	110	57	<0.1	39800	1370	<0.2	160	n.a.	n.a.	770	400	<0.1	n.a.	6.3	<0.2	n.a.	<7	193000	3480	-25.6	-2.9
	11	40	1060	62700	5770	150	74	<0.06	40500	2840	9.3	210	n.a.	n.a.	1320	630	<0.07	n.a.	6.3	<0.1	n.a.	<3.4	182100	3380	-25.7	-3.2
	12	35	890	61600	4780	120	67	<0.2	41800	1950	170	160	n.a.	n.a.	780	480	<0.1	n.a.	6	8.3	n.a.	<8.2	213500	5020	-25.9	-2.9
	13	30	1190	59800	5320	180	81	1750	43700	3500	30	210	n.a.	n.a.	970	240	0.7	n.a.	6.7	<0.8	n.a.	<23	196400	5530	-26.2	-2.9
Average			940	62200	4940	130	66	940	41000	2200	90	180			860	400	0.7		6.7	8			197600	4500	-25.8	-3.7
SD			140	1200	570	20	8	710	1300	700	80	20			210	120			1.5				12100	800	0.2	1.2
Sai-010a A2 (conc.)	01	40	460	57800	5050	57	24	1060	45000	1740	150	110	n.a.	n.a.	420	210	<0.7	<0.09	3	32	<0.1	<28	155100	2070	-26.4	-5.8
	02	30	780	60700	3510	100	63	<1.05	42900	2850	140	160	n.a.	n.a.	840	440	<0.5	<0.06	6	13	<0.1	<23	144000	2970	-26.1	-2.3
	06	25	730	61900	5100	94	43	<1.38	42200	2240	<0.3	170	n.a.	n.a.	760	420	<0.6	<0.07	6	5.4	<0.1	<23	153800	3800	-26.0	0.1
	07	25	1050	61100	3790	92	45	1040	42300	1240	9	160	n.a.	n.a.	820	330	<0.9	<0.07	5.5	<0.4	<0.2	<35	189700	2280	-26.0	-2.8
	08	30	980	61000	4620	110	54	870	42400	1910	110	190	n.a.	n.a.	950	380	<0.6	<0.1	6.6	<0.2	<0.1	<23	169800	2980	-26.0	-3.3
	10		690	55500	3890	83	53	1680	48800	2370	38	140	n.a.	n.a.	690	210	<0.5	<0.06	4.1	<0.3	<0.1	<22	150700	3290	-27.1	-1.2
Average			780	59700	4330	89	47	1160	43900	2060	89	160			750	330			5.2	17			160500	2900	-26.3	-2.5
SD			210	2500	670	18	13	350	2600	560	63	30			180	100			1.4	14			16600	640	0.4	1.8
Sai-010a A3 (conc.)	04	30	460	60800	9190	78	32	1010	42500	2390	<2.3	130	n.a.	n.a.	310	130	<0.7	n.a.	3	<1.7	n.a.	<46	232300	7340	-26.0	-3.4
	06	30	430	60800	11700	81	33	1830	42500	2510	110	120	n.a.	n.a.	480	170	5.0	n.a.	3.2	370	n.a.	<3	237100	5610	-26.0	-3.4
Average			450	60800	10450	80	33	1420	42500	2450	110	125			400	150	5.0		3.1	370			234700	6480	-26.0	-3.4
SD			20	0	1780	2	1	580	0	90		10			120	30			0.1				3400	1220	0.0	0.0
Sai-010a A5 (conc.)	01	20	270	57800	6840	51	25	2280	44600	1810	110	80	n.a.	n.a.	300	92	<0.9	0.25	1.9	220	1.1	<37	165300	3720	-26.3	-7.5
	02	25	280	60000	9490	53	27	<2.15	41800	1980	<0.5	58	n.a.	n.a.	410	140	<0.8	<0.2	<0.1	180	<0.2	<37	193700	2100	-26.0	0.1
Average			275	58900	8170	52	26	2280	43200	1900	110	69			360	120		0.3	1.9	200	1		179500	2910	-26.2	-3.7
SD			10	1600	1870	1	1	0	1980	120	0	16			80	30		0.0	0.0	30	0		20100	1150	0.2	3.8